IMPERIAL COLLEGE LONDON
Department of Materials

Towards Controlling the Coercivity in Molecular Thin Films for Spintronic Applications

Thesis submitted for the degree of
DOCTOR OF PHILOSOPHY

Hsiang-Han Tseng

Abstract

Organic semiconductors have attracted worldwide interest for the past two decades. The properties of these molecules can be easily manipulated and exploited, and furthermore benefit from chemical versatility, mechanical flexibility and low cost. This has led to a remarkable success in the field of plastic electronics and molecules have found numerous device applications such as photovoltaic cells (PV), organic light emitting diode (OLED), organic field effect transistor (OFET) and sensors. Organic semiconductors have recently become of considerable interest for spintronic applications, due to the long spin relaxation times and magneto-resistive effects observed in these systems.

In order to fully exploit the advantages of these molecules for spintronic applications, it is essential to explore molecular routes towards all organic spin valves and search for molecule-based magnets as alternatives to conventional spin injector/detector such as $La_{0.67}Sr_{0.33}MnO_3$ (LMSO) and Co. The scope of this thesis is to investigate the way to control the functional properties and in particular the magnetic interactions and coercivities in molecular thin films, with an emphasis on the charge-transfer salt, [MnTPP][TCNQ], and a ferromagnetic system, FePc (including mixed H_2Pc:FePc), respectively, fabricated by organic molecular beam deposition (OMBD). Although the magnetic couplings are currently limited to cryogenic temperature, it is shown that it is possible to engineer exotic physical properties in these mixed films, where the magnetism seen as an intrinsic property to the functional molecules shows a strong dependence on the local chemical structure and spatial displacement for the magnetic ions, which can be manipulated by addition of electron acceptor and non-magnetic substituent. Compared to conventional magnetic semiconductors, this approach is a molecular route towards tuneable magnetic properties, allowing one to directly control the magnetic interactions by varying the film composition via co-deposition, a desirable property that is obtained in the film form and readily exploited in all organic spintronic applications.

Declaration of Authorship

I hereby declare that this thesis is a presentation of my research work which includes nothing from the work performed in collaboration unless specified in the text, and contributions of others if involved are indicated with due reference to literature.

Hsiang-Han Tseng

Date: 15th November 2015

Copyright

The copyright of this thesis rests with the author and is made available under a Creative Commons Attribution Non-Commercial No Derivatives licence. Researchers are free to copy, distribute or transmit the thesis on the condition that they attribute it, that they do not use it for commercial purposes and that they do not alter, transform or build upon it. For any reuse or redistribution, researchers must make clear to others the licence terms of this work

Publication

The following publication is directly related to the work presented in this thesis:

Hsiang-Han Tseng, Michele Serri, Nicholas M. Harrison and Sandrine Heutz
"Thin film properties of tetracyanoquinodimethane (TCNQ) with novel templating effects"

J. Mater. Chem. C, 2015,3, 8694-8699, DOI: 10.1039/C5TC01778E (2015)

Which has the abstract: The morphological and structural properties of films based on the strong electron acceptor molecule, 7,7,8,8,-tetracyanoquinodimethane (TCNQ) are presented and the influence of growth rate and the nature of the substrate are investigated. On weakly-interacting substrates, TCNQ films grown by Organic Molecular Beam Deposition (OMBD) exhibit randomly oriented micron-sized islands with significant curvature and three preferential orientations suggested by diffraction from (022), (021) and (020) planes. Pre-coating with 3,4,9,10-perylenetetracarboxylic dianhydride (PTCDA) is shown to result in morphological and structural modifications to the TCNQ films, characterized by uniform rectangular-shaped micron-sized islands, with the preferential molecular orientation reduced to only (020), compared to the films on bare substrates. We rationalise the interactions between TCNQ and PTCDA based on the match between the displacement of the perylene-H atoms/anhydride groups in PTCDA and that of the CN groups in TCNQ. These results suggest an alternative approach for using templating to control the molecular orientation in organic heterostructures.

Acknowledgement

My thesis would not be complete without acknowledging all the people that make it possible with their contributions. I first want to express my deepest thanks to my supervisor Dr Sandrine Heutz, for giving me an opportunity and confidence, and introduced me to the field of molecular magnetism. Sandrine's knowledge, encouragement and enthusiasm are key motivations along my PhD. I also want to thank Prof Nicholas Harrison for his invaluable advice and insights from a theoretical point of view.

I wish to thank my colleagues in Heutz group. I am grateful for Din, Zhenlin and Leo in the initial stage of the PhD. Jimmy, Alex, Sharon, Jasvir, Ryun, Peter and Roland always made time and supported me throughout my PhD. I appreciate all the help that was offered. I would like to thank Michele for his guidance in the first years of my PhD. I am also thankful to Luke for his comments and discussions on magnetism and spintronics, and the members of the Natalie Stingelin's Group.

I am indebted to Richard Sweeney, Dr Richard Thorogate, Dr Mahmoud Ardakani, Dr Robert Palgrave and Benjamin Chan for their assistance with the experimental equipment and data analysis. My appreciation and gratitude goes to my friends in London, particularly Stephen, Romi, Monica, Bin, Jing, Evgeniy, Taylor, Andrei and Georg. Finally my upmost gratitude goes to my parents, for raising, caring and loving me, endlessly and unconditionally, and for the patience and support they have always been giving me. Through them I learnt the courage and persistence I need to have for tackling challenging problems in science.

Contents

1. Introduction and Literature Review ····· 28

1.1 Organic Spintronics ····· 33

1.1.1 Spintronics ····· 33

1.1.2 Organic Spintronics ····· 35

1.1.3 All-organic spintronic devices ····· 37

1.2 Molecule-based magnets ····· 39

1.2.1 Magnetism ····· 39

1.2.2 Spin Hamiltonian ····· 42

1.2.3 Magnetic dipole-dipole interaction ····· 43

1.2.4 Exchange interaction ····· 43

1.3 Charge-Transfer Salt and Metal Phthalocyanines ····· 44

1.3.1 7,7,8,8,-Tetracyanoquinodimethane (TCNQ) ····· 44

1.3.2 Manganese tetraphenylporphyrin chloride (MnTPPCl) ····· 49

1.3.3 Transition metal phthalocyanines (MPcs) ····· 53

1.4 Thesis Layout ····· 58

2. Experimental methods ····· 61

2.1 Sample preparation ····· 61

2.2 OMBD growth ····· 61

2.3 Thickness calibration ····· 63

2.4 Ex-situ Characterizations ····· 66

2.4.1 UV/Visible Absorption Spectroscopy ····· 66

2.4.2 Infrared Spectroscopy ····· 69

2.4.3 X-ray photoelectron Spectroscopy ····· 71

2.4.4 Scanning electron microscopy ····· 72

2.4.5 Atomic force microscopy ····· 73

2.4.6 X-ray diffraction ····· 76

2.4.7 Superconducting quantum interference device (SQUID) magnetometry 80

3. TCNQ thin films 85

3.1 TCNQ on the weakly interacting substrates 85
3.1.1 UV/Visible spectroscopy of the films 85
3.1.2 Morphology and structure of the films 86

3.2 TCNQ on PTCDA 92
3.2.1 UV/Visible spectroscopy of the films 92
3.2.2 Morphology and structure of the films 93

4. MnTPPCl thin films 100

4.1 As-deposited films 100
4.1.1 UV/Visible spectroscopy of the films 100
4.1.2 Morphology and structure of the films 106
4.1.3 X-ray Photoelectron Spectroscopy 108
4.1.4 Magnetic characterization of the films 115

4.2 Degradation of the films 117

5. Co-deposited [MnTPPCl][TCNQ] 129

5.1 UV/Visible spectroscopy of the films 129

5.2 Infrared Spectroscopy of the films 133

5.3 X-ray Photoelectron Spectroscopy 138

5.4 Morphology and structure of the films 146

5.5 Magnetic characterization of the films 149

6. FePc in mixed films and spin-valve structures 157

6.1 Mixed H_2Pc:FePc films 160
6.1.1 Morphology of the films 160
6.1.2 Structure of the films 162

6.1.3 Magnetic characterization of the films 165

6.2 Substrate effects on FePc films 168

6.2.1 Morphology of Al 168

6.2.2 Structure of Al 170

6.2.3 Morphological and structural properties of FePc on Al 171

6.3 FePc in spin-valve structures 175

6.3.1 Morphology of the films 175

6.3.2 Structure of the films 179

6.3.3 Magnetic characterization of the films 181

7. Conclusions 190

8. Bibliography 196

Appendix 214

A.1 Electronic absorption spectra of MnTPPCl films 214

A.2 IR spectrum 218

A.3 FePc thin films 219

List of Figures

Figure 1.1 Structure of 1D polymeric-chain ferrimagnet formed by [MnTPP(Br)][TCNE] (a), where dark grey, light grey, dark purple, light purple and yellow spheres represent carbon, hydrogen, manganese, nitrogen and bromine atoms, respectively, shown with solvent molecules omitted [16], and (b) The 1D coordination polymeric ferrimagnetic chain of alternating unpaired spins, Mn (S = 2, long arrows) and TCNE (s = 1/2, short arrows), in which the N atom of TCNE is attached to (S = 2) the Mn atom of MnTPP(Br) via *trans*-μ-*N*-σ bonding [16]; right panel: schematic diagram illustrating the coupling arising from bonding between d_z^2-like Mn(III) and π^* TCNE. 29

Figure 1.2 Magnetization as a function of the applied field, M(H) curves measured from [MnTPP(Br)][TCNE] at 2 K, 3 K and 4 K, respectively, adapted from [14]. 30

Figure 1.3 Schematics show the canted antiferromagnetic couplings along and between the chains of alternating S = 2 (long arrow) and s = 1/2 (short arrow) (a), and a different canted antiferromagnetic coupling of S = 2 (long arrow) and s = 1/2 (short arrow) along and parallel to the chain (b) adapted from [14]. 31

Figure 1.4 Schematic representation of the spin-valve behaviours in a tri-layer spin valve with a non-magnetic spacer sandwiched by two ferromagnetic layers (FM_1 and FM_2) with different coercivities, as depicted by the thin and thick arrows, respectively. The light grey rectangles correspond to the electrical contacts for the spin valve. When the magnetizations in the two ferromagnetic layers are parallel to each other (left panel in (a)) the spins in the anti-parallel alignment can travel through the sandwiched structure, giving rise to a higher conductivity and lower resistance. By contrast, electrons in the right panel in (a) undergo collisions in the either ferromagnetic layer, resulting in a higher overall resistance (adapted from [35]). In this case, the observed MR would be in a positive value, since the parallel configuration of the spin valve yields the low resistance state, and (b): the

sandwiched structure comprises of ferromagnetic layers with different coercivities, decoupled by the non-magnetic spacer. 34

Figure 1.5 The inverse of the magnetic susceptibility (χ^{-1}) for paramagnetic, antiferromagnetic and ferromagnetic behaviour shown as the red, black and blue lines, respectively. 41

Figure 1.6 Hysteresis curves of a paramgent and a ferromagnet below its Curie temperature. The coercive field, H_{cr}, saturation magnetization, M_s, and remanent magnetization, M_r, are indicated, and arrows are shown to illustrate the directionality and history dependence of the behaviour. 42

Figure 1.7 Absorption spectrum of TCNQ in dichloromethane with a concentration of 2.5×10^{-5} M. 45

Figure 1.8 Experimentally observed packing motifs of dimerized TCNE (a) σ-dimer, (b) π-dimer 1, (c) π-dimer 2, and (d) σ-$[TCNQ\text{-}TCNQ]^{2-}$. 46

Figure 1.9 IR spectrum of the TCNQ film deposited onto KBr substrate. 47

Figure 1.10 The schematics representing (a) molecular structure of TCNQ, and (b) the unit cell of TCNQ projected on the *a*-*c* plane (viewed along the *b*-axis) adopted from [98], where dark grey, light grey and light purple spheres represent carbon, hydrogen and nitrogen atoms, respectively. 48

Figure 1.11 The molecular structure of MnTPPCl. 49

Figure 1.12 Absorption spectrum of MnTPPCl in dichloromethane with the concentration of 10^{-5} M. 50

Figure 1.13 IR spectrum of the MnTPPCl film on KBr substrate. 52

Figure 1.14 The molecular structure of FePc. 53

Figure 1.15 The crystalline structures (a) and (c) based on the herringbone arrangement found in the β-phase [126], and (b) and (d) depicted the α-phase structure determined by Hoshino *et al.*, adapted from [127]. 54

Figure 1.16 Schematics showing, (a) the definitions for the stacking axis, the stacking angle (φ) and the relative displacement between the Pcs in the molecular column, and different relative displacements arising from the molecular orientations adopted by (b) the α-phase and (c) the β-phase, respectively. 55

Figure 1.17 Schematics for the *3d* orbitals of the metal ions, and the electronic ground state of Fe(II)Pc and Mn(III)TPPCl, respectively. 57

Figure 2.1 Schematic showing the OMBD growth chamber. The three-shelve cassette allows for multiple depositions and using a mask without breaking the vacuum, and the substrate temperature during the growth is controlled by the lamp. The distance between the substrate and the source is approximately 70 cm. The film homogeneity is optimized by rotating the substrate holder (cassette) during the deposition. 62
Figure 2.2 Profiles of cross-sections made on two MnTPPCl thin films on silicon, with their thicknesses measured by AFM, corresponding to (a) 79.8 nm and (b) 39.5 nm, respectively. 64
Figure 2.3 Optical absorption spectra of α- and β-CuPc on kapton substrate. Note that the high frequency oscillations on the α-CuPc are due to the substrate..... 67
Figure 2.4 Davydov splitting, adapted from [139]. 68
Figure 2.5 Schematics for ATR-IR. 70
Figure 2.6 Schematic depicting the photoelectric process in XPS. 72
Figure 2.7 Schematics of atomic force microscopy. 74
Figure 2.8 Typical behaviour of the force an AFM tip experiences as a function of distance to the substrate. 75
Figure 2.9 The effects of free oscillations (black solid curve) and oscillations on surface (black dashed curve) experienced by the tip, adopted from [141]. 75
Figure 2.10 Schematics of a 3D unit cell structure with the crystal axes. 77
Figure 2.11 Illustrating Bragg's law for reflections from the planes in a crystal. 77
Figure 2.12 Schematics of an X-ray diffractometer with Bragg-Brentano geometry..... 78
Figure 2.13 Schematics depicting the texture mode provided by XRD with Schulz geometry. 80
Figure 2.14 Schematics showing the SQUID magnetometry. 81
Figure 2.15 powder sample for SQUID measurement. 82
Figure 2.16 SQUID sample preparation (a) left: a mask to delimit the area where film is deposited; right: the film (green) deposited on the kapton substrate (yellow), and (b) the film on kapton rolled and inserted into the sample straw. 83
Figure 3.1 Optical spectra of (1) TCNQ solution in dicholoromethane (DCM) with a concentration of $.5x10^{-3}$ M, 80 nm thick TCNQ films deposited on glass at the rate of (2) 1.0 Å/s, and (3) 0.37 Å/s, respectively. 86

Figure 3.2 Optical micrographs of the 80 nm thick TCNQ films grown at the rate of (a) 0.37 Å/s, and (b) the same area observed with a cross polariser, and at the rate of (c) 1.0 Å/s and (d) (d) the same area observed with a cross polariser. The scale bars in (a), (b), (c) and (d) are 20 μm. 87

Figure 3.3 SEM micrographs of the 80 nm thick TCNQ films deposited at the rate of (a) and (b) 0.37 Å/s, and (c) and (d) 1.0 Å/s on bare silicon substrates. 88

Figure 3.4 AFM micrographs of the 80 nm thick TCNQ films deposited on glass at the rate of 0.37 Å/s (a) and (c), and 1.0 Å/s (b) and (d) on bare glass (substrates). The inner panels in (a) and (c) show the corresponding phase images. The height profile along the purple line in (a) and (c) reveals the TCNQ grain height, plotted below the figures. The area between the TCNQ islands highlighted by the yellow boxes in (a) and (b) are shown in (c) and (d). The scale bars are 2 μm in (a) and (b), and 200 nm in (c) and (d), respectively. 89

Figure 3.5 X-ray diffraction (XRD) patterns of (a) TCNQ powder, 80 nm thick TCNQ films deposited on glass at the rate of (b) 1.0 Å/s, (c) 0.37 Å/s, and on a 20 nm thick PTCDA film, (d) 0.37 Å/s, with the diffraction pattern of a 20 nm thick PTCDA film shown in (e). Inset: the ψ curve at $2\theta = 25.3°$ obtained on the TCNQ film deposited onto PTCDA shown in blue circles, plotted with the Gaussian fit (magenta) with FWHM = 8.8°. 90

Figure 3.6 The optical spectra of (1) a 20 nm thick PTCDA film, (2) a 80 nm thick TCNQ film, (3) a simulated spectrum based on the sum of optical absorption recorded from a 20 nm thick PTCDA film, and that of a 80 nm thick TCNQ film, and (4) the 80 nm thick TCNQ film deposited onto 20 nm thick PTCDA film. All the samples are grown on glass substrate..... 93

Figure 3.7 Optical micrographs of (a) the 80 nm thick TCNQ film grown at the rate of 0.37 Å/s on glass substrate pre-coated with a 20 nm thick PTCDA film (which is deposited at the rate of 0.2 Å/s), and (b) the same area observed with a cross polariser. The scare bars in (a) and (b) are 20 μm, respectively. 94

Figure 3.8 SEM micrographs on the 80 nm thick TCNQ film deposited at the rate of 0.37 Å/s on the 20 nm thick PTCDA layer on silicon substrate. The scare bars are 10 μm in (a) and 1.0 μm in (b), respectively. 94

Figure 3.9 AFM micrographs of (a) a 20 nm thick PTCDA film deposited on glass substrate, (b), (c) and (d): the 80 nm thick TCNQ deposited at the rate of 0.37 Å/s on glass

pre-coated with a 20 nm thick PTCDA film. The inner panel in (a), (b) and (c) represent the corresponding phase images, and the height profiles in (a), (b) and (d) are depicted by the purple line, plotted below the figures. The area uncovered by the rectangular-shaped islands highlighted by the yellow and green boxes are show in (c) and (d). The scale bars are 200 nm in (a) and (d), 400 nm in (c) and 2 μm in (b). 95

Figure 3.10 The schematics of (a) the TCNQ crystal structure obtained from [98] with its (020), (021) and (022) diffracting planes, and the corresponding unit cell axes given in the upper-right, (b) the (020) plane of TCNQ parallel to the (102) plane of PTCDA, which is characterized by the face-on orientation when grown at room temperature, (c) upper panel: the lattice of TCNQ on its (020) plane highlighted by the green box; lower panel: the (102) plane of PTCDA shown in the wireframe style except for the oxygen atom represented by the red spheres, and a similar lattice highlighted in the red box to depict the displacement of the perylene H atoms on parallel PTCDA molecules; (d) top-view: possible molecular arrangement of the TCNQ unit cell along its (020) direction projected onto the PTCDA layer adopting (102) orientation, using the same scale as in (c). Grey, red and white spheres represent carbon, oxygen and hydrogen atoms. Both purple and yellow are used to represent nitrogen atoms, and the latter is used to mark those are the out-of-plane and thus close to the (102) plane of PTCDA. 98

Figure 4.1 Optical spectra of a 100 nm thick MnTPPCl film deposited at the rate of 0.9 Å/s on glass that is recorded immediately after the film deposition (black solid line), and the MnTPPCl solution (green dotted line) in dichloromethane, with the concentration of 10^{-5} M, B-band, VI, V_a, V, IV (Q-band) and III used to label the absorption band following the notations from Boucher [104] as previously summarized in Table 1.2 in section (1.3.2). 101

Figure 4.2 Optical spectra recorded from the as-deposited MnTPPCl films deposited at the rate of 0.9 Å/s on glass substrates, with the thickness of (a) 100 nm, (b) 75 nm, (c) 50 nm, (d) 33 nm, and (e) 25 nm, respectively, with the absorption intensity normalized to 1 nm thick for comparison. Inset: the optical spectra of the MnTPPCl films of 100 nm, 75 nm, 50 nm, 33 nm and 25 nm without normalization to the absorption intensity. 102

Figure 4.3 The optical spectrum of the100 nm thick as-deposited MnTPPCl film deposited at the rate of 0.9 Å/s (black solid line) plotted in the scale of energy (eV), presented with the eight Gaussian functions used for deconvolution, with the cumulative fit shown in black dotted line..... 104

Figure 4.4 SEM micrographs of (a) the 100 nm MnTPPCl film deposited at the rate of 0.9 Å/s onto silicon, and (b) a cross-section of the same film (with the scale bar of 100 nm). The black area at the bottom corresponds to vacuum..... 106

Figure 4.5 AFM micrographs of a 100 nm thick MnTPPCl film deposited at the rate of 0.9 Å/s on glass substrate with the scale bars of 400 nm in (a) and 200 nm in (b), respectively. 107

Figure 4.6 XRD scans of (a) a 100 nm thick MnTPPCl films deposited at the rate of 0.9 Å/s on (1) glass substrate, (2) on glass substrate pre-coated with a 20 nm thick PTCDA layer, and (b) on kapton. A. The solid grey line plotted to index the diffraction peak at $2\theta = 27.6°$ due to (102) plane of PTCDA. 108

Figure 4.7 XPS survey scans of the MnTPPCl powder (black), and the 125 nm thick as-deposited MnTPPCl film grown at the rate of 0.9 Å/s on silicon substrate (red). 109

Figure 4.8 High resolution of XPS core-level spectra of (a), (c), (e) and (g) the MnTPPCl powder and (b), (d), (f) and (h) MnTPPCl film. The photoemission lines are deconvoluted with the Voigt peak shape and the background is subtracted with the Shirley algorithm..... 111

Figure 4.9 Colour scheme for the molecular structure of MnTPPCl and the chemically distinctive carbon atoms, adapted from [119]. 114

Figure 4.10 (a) Field dependent magnetization curves, $M(H)$, at 2 K (black), 4.2 K (red), 8 K (blue) and 10 K (magenta) of the MnTPPCl powder, the solid line representing a paramagnetic spin $S = 2$, $g = 2$, $T = 2$ K (black), (b) the net moment as a as a function of the ratio of field over temperature (H/T) of the MnTPPCl powder, at 2 K (black), 4.2 K (red), 8 K (blue) and 10 K (magenta), (c) magnetic susceptibility as a function of temperature $\chi(T)$ of the MnTPPCl powder (open black circle) with the Curie-Weiss expression (red), and (d) inverse magnetic susceptibility as a function of temperature $1/\chi$ (open black circle) fitted with the Curie-Weiss fit (red) applied between 14 and 120 K. 116

Figure 4.11 Optical spectra of the 100 nm thick MnTPPCl film deposited at the rate of 0.9 Å/s on glass, recorded under different times and conditions, (1) as-deposited, (2) 28 days, (3) nearly 2 years after the film deposition, and (4) the MnTPPCl solution in dichloromethane (DCM), with the concentration of 10^{-5} M. All the spectra are normalized to the absorption intensity of the B-band, λ = 375 nm. 118

Figure 4.12 Optical spectra of the 100 nm MnTPPCl film obtained right after the growth (black) and stored in the glovebox for 6 months (red). 119

Figure 4.13 Optical spectra of the MnTPPCl solutions under ambient conditions (green), with a concentration of 10^{-5} M in dichloromethane, and in a sealed cuvette purged with Ar for 20 mins with a concentration of 1.25×10^{-5} M in dicholoromethane (black). All the spectra are normalized to the absorbance in the respective Soret band, λ = 478 nm. The position for the same band in the as-deposited MnTPPCl film is λ = 484 nm. 120

Figure 4.14 Electronic absorption spectra of the MnTPPCl films deposited at the rate of 0.9 Å/s on glass, with the thickness of (a) 100 nm (b) 75 nm (c) 50 nm (d) 33 nm, and (e) 25 nm, recorded at different time intervals shown in black, red, blue, magenta, olive and cyan curves with labels, (1) as-deposited, (2) 7 days, (3) 14 days (4) 21 days (5) 28 days, and (6) approximately after two years after film deposition. The films were stored under ambient conditions in the absence of light during the course of this study. 121

Figure 4.15 Optical spectra of a 100 nm thick MnTPPCl film recorded at different time intervals, corresponding to (a) as-deposited, (b) 7 days, (c) 14 days, (d) 21 days, (e) 28 days, and (f) approximately 2 years after film deposition stored under dark and ambient conditions, plotted in the scale of eV and shown with the individual Gaussian functions that are to deconvolute the spectra. Peak4 and Peak5 correspond to the Soret features for Mn(III)- and Mn(II)-porphyrins, respectively. 122

Figure 4.16 The areas for Peak4 (λ = 484 nm, Mn(III), shown in red rectangle) and Peak5 (λ = 447 nm, Mn(II), shown in blue circle) extracted from the optical spectra recorded from the 100 nm thick MnTPPCl film by deconvolution with the Gaussian components (see text), plotted as a function of time, and the sum (shown in black triangle) obtained by adding the peak areas for Peak4 and Peak5, plotted as a function of time. 124

Figure 4.17 The decease of % Mn(II) contained in the MnTPPCl films with the thickness of 25 nm (black rectangle), 33 nm (red circle), 50 nm (blue triangle), 75 nm (magenta triangle) and 100 nm (green diamond) plotted in logarithm as a function of time. 126

Figure 5.1 Optical spectra of (1) the co-deposited [MnTPPCl][TCNQ] film on glass substrate (an equivalent thickness of 100 nm for MnTPPCl, by using the deposition rates of 0.9 Å/s and 0.26 Å/s for MnTPPCl and TCNQ, respectively), (2) the 100 nm thick as-deposited MnTPPCl film grown at the rate of 0.9 Å/s on glass substrate, (3) the MnTPPCl solution dissolved in dichloromethane (DCM), with a concentration of 10^{-5} M,(4) the TCNQ solution dissolved in dichloromethane (DCM), with a concentration of $2.5x10^{-3}$ M and (5) the 80 nm thick TCNQ film deposited at the rate of 0.37 Å/s on glass. 130

Figure 5.2 (1) Optical spectra of the co-deposited [MnTPPCl][TCNQ] film on glass substrate (an equivalent thickness of 100 nm for MnTPPCl, with a 1 to 1 ratio between MnTPPCl and TCNQ obtained by using the deposition rates of 0.9 Å/s and 0.26 Å/s for MnTPPCl and TCNQ, respectively), (2) the solution spectrum of a co-deposited [MnTPPCl][TCNQ] film grown on glass with the same deposition parameters used as in (1) fully dissolved in dichloromethane (DCM), (3) the sum of the optical spectra recorded from the MnTPPCl and TCNQ solution by combining (4): normalized solution spectrum of MnTPPCl with a concentration of 10^{-5} M in DCM and (5): the normalized solution spectrum of TCNQ with a concentration of $6.25x10^{-4}$ M in DCM. 131

Figure 5.3 (a) IR spectra of the 80 nm TCNQ film grown at the rate of 0.37 Å/s (black), the 100 nm MnTPPCl film grown at the rate of 0.9 Å/s (red), the co-deposited [MnTPPCl][TCNQ] films with 1:1 ratio obtained two sets of deposition rates, corresponding to MnTPPCl = 0.9 Å/s, TCNQ = 0.26 Å/s (blue), MnTPPCl = 0.1 Å/s and TCNQ = 0.03 Å/s (magenta), where an equivalent thickness of 100 nm for MnTPPCl was used in the two depositions. (b) is a zoom on the key region for the finger-printing, and (c) the IR spectra of the 100 nm H_2TPP film (orange), and the co-deposited [H_2TPP][TCNQ] film (an equivalent thickness of 100 nm for H_2TPP) (purple) with 1:1 ratio between H_2TPP and TCNQ obtained at the deposition rates of H_2TPP =0.9 Å/s and TCNQ = 0.29 Å/s, respectively. All the films are deposited onto KBr (100), shown the vertical lines

to label the ν(C≡N) stretching in the nitrile group in neutral (purple solid) and ionized bound state (grey solid), and ν(C-C) stretching (grey dotted) and σ(C-H) deformation (bending) (purple dotted) in benzene..... 134

Figure 5.4 Transition metal complex upon reaction with TCNQ, or similar polynitriles resulting in single coordination (a) σ- or as a bridging ligand to bond to metal via (b) $\mu_{-1,1}$, TCNQ cis-bonding, (c) $\mu_{-1,2}$, TCNQ trans-bonding, and (d) μ_4 TCNQ bonding, respectively. 135

Figure 5.5 XPS survey scans of the MnTPPCl powder (black), the 125 nm thick as-deposited MnTPPCl film grown at the rate of 0.9 Å/s on silicon substrate (red), and the co-deposited [MnTPPCl][TCNQ] film on silicon substrate, (an equivalent thickness of 200 nm for MnTPPCl, with a 1 to 1 ratio obtained by using MnTPPCl = 0.45 Å/s, TCNQ = 0.13 Å/s, respectively) (blue)..... 139

Figure 5.6 High resolution of XPS core-level (a) Cl2p (b) Mn2p (c) C1s and (d) N1s spectra of the co-deposited [MnTPPCl][TCNQ] film. The photoemission lines are deconvoluted with the Voigt peak shape and the background is subtracted with the Shirley algorithm..... 141

Figure 5.7 Colour scheme used for MnTPPCl (adapted from [119]) and the chemically distinctive carbon atoms (left). The blue, orange, red and green spheres represent the carbons in the phenyl group, meso-bridged, and the two nitrogen-bonded, namely N_α and N_β; (right) the molecular structure of TCNQ (adapted from [98]), where the carbon atoms in different chemical environments are labelled in blue, orange and green, accordingly. 144

Figure 5.8 SEM micrographs of (a) the co-deposited [MnTPPCl][TCNQ] film on silicon substrate, (an equivalent thickness of 100 nm for MnTPPCl, with a 1 to 1 ratio between MnTPPCl and TCNQ obtained by using the deposition rates of MnTPPCl = 0.9 Å/s and TCNQ = 0.26 Å/s, respectively), and (b) a cross-section of the film (with the scale bar of 200 nm). The black area on the top of (b) corresponds to vacuum..... 146

Figure 5.9 AFM micrographs of the co-deposited [MnTPPCl][TCNQ] films on glass substrate, with an equivalent thickness of 100 nm for MnTPPCl used for the two depositions. (a) corresponds to a film with 1 to 1 ratio obtained by using the deposition rates of MnTPPCl = 0.9 Å/s and TCNQ = 0.26 Å/s, respectively, with the corresponding phase image in (b), whereas (c) represents a 1 to 1 ratio between

MnTPPCl and TCNQ for the film obtained at a lower set of deposition rates, using MnTPPCl = 0.1 Å/s, TCNQ = 0.03 Å/s, respectively, and the corresponding phase image in (d). The scale bars are 400 nm in (a) and (b), and 200 nm in (c) and (d), respectively. 147

Figure 5.10 XRD scans of (1) the co-deposited [MnTPPCl][TCNQ] film (with an equivalent thickness of 200 nm for MnTPPCl, and a 1 to 1 ratio between MnTPPCl and TCNQ is obtained by using the deposition rates of MnTPPCl = 0.9Å/s and TCNQ = 0.26Å/s), and (2) the co-deposited [MnTPPCl][TCNQ] film (an equivalent thickness of 100 nm for MnTPPCl, with a 1 to 1 ratio between MnTPPCl and TCNQ obtained by using the deposition rates of MnTPPCl = 0.1 Å/s, TCNQ = 0.03 Å/s, respectively). Both films are deposited on glass substrate. 149

Figure 5.11 (a) Isothermal magnetization curves as a function of the applied field, $M(H)$, at 2 K (black open circle), 4.2 K (red open circle), 8 K (blue open circle) and 10 K (magenta open circle) of the co-deposited [MnTPPCl][TCNQ] film (an equivalent thickness of 200 nm for MnTPPCl, with a 1 to 1 ratio between MnTPPCl and TCNQ obtained by using the deposition rates of MnTPPCl = 0.45 Å/s and TCNQ = 0.13 Å/s, respectively), and magnetization at 2 K (black circle) obtained from MnTPPCl powder, shown with the Brillouin fit with $S = 2$, $S = 3/2$, and 1/2 with $g = 2$ at 2 K (black, red and purple solid line), and (b) the net moment as a as a function of the ratio of field over temperature (H/T) of the co-deposited [MnTPPCl][TCNQ] film,..... 150

Figure 5.12 (a) Differential susceptibility as a function of temperature $\chi(T)$ of the co-deposited [MnTPPCl][TCNQ] film (with an equivalent thickness of 200 nm for MnTPPCl and a 1 to 1 ratio by using the deposition rates of MnTPPCl = 0.45 Å/s, TCNQ = 0.13 Å/s, respectively) (open black circle) with the Curie-Weiss fit (red), inset: inverse differential susceptibility as a function of temperature $1/\chi$ (open black circle) fitted with the Curie-Weiss law (red), (b) $\chi T(T)$ product as a function of temperature of the co-deposited [MnTPPCl][TCNQ] film, (c) $\chi T(T)$ product as a function of temperature of the co-deposited [MnTPPCl][TNCQ] film shown with χT ($T = 2$ - 94 K) simulated by the isotropic Heisenberg dimer model ($S = 2$ and $s = 1/2$, $g = 1.96$, intra-dimer coupling constant $(J/k_B) \sim -100$ K and $zJ'/k_B \sim -5$ K for inter-dimeric interactions) (red), and (d) inverse differential susceptibility as a

function of temperature χ^{-1}(T) of the co-deposited [MnTPPCl][TCNQ] film (black open square), shown with χ^{-1}(T) simulated by the isotropic Heisenberg dimer model (S = 2 and s = 1/2, g = 1.96) (see text). 152

Figure 6.1 Schematics depicting (a) an all organic spin valve, or all phthalocyanine spin valve, consisting of Al/FePc/H_2Pc/FePc/Al. The molecular ferromagnet, FePc, can be utilized as a spin injector and detector with different coercivities, decoupled by a thin layer of H_2Pc as the non-magnetic spacer. (b), (c) and (d); three multi-layers similar to the device structure given in (a), but fabricated with only one layer of FePc, (b) 25 nm FePc on 50 nm Al, (c) 25 nm FePc/25 nm H_2Pc/50 nm Al, and (d) 15 nm FePc/35 nm H_2Pc/50 nm Al. All the multi-layered structures for magnetic characterizations are grown on kapton substrate. 159

Figure 6.2 AFM micrographs of 100 nm thick films of mixed H_2Pc:FePc (H_2Pc = 10%) on (a) and (b) silicon substrate, (d) and (e) on kapton. The scale bars in (a) and (d) are 200 nm, and 100 nm for (b) and (e), respectively; (c) and (f) corresponding to the watershed mark used for (b) and (e) to extract the average lateral grain size of the mixed H_2Pc:FePc films. 161

Figure 6.3 AFM micrograph of 100 nm thick films of mixed H_2Pc:FePc films (H_2Pc = 50 %) on (a) and (b) silicon substrate, (d) and (e) on kapton. The scale bars in (a) and (d) are 200 nm, whereas those for (b) and (e) are 100 nm, respectively; (c) and (f) corresponding to the watershed mark used for (b) and (e) to extract the average lateral grain size of the H_2Pc:FePc films..... 162

Figure 6.4 XRD scans of (a) a 50 nm thick FePc film, and 100 nm thick films of mixed H_2Pc:FePc containing (b) 10 % of H_2Pc, and (c) 50 % of H_2Pc. All the films are deposited on silicon substrate, and the data are offset for clarity. The light grey lines plotted to index the (100) diffraction peak at $2\theta = 6.9°$ and the 2^{nd} order diffraction at $2\theta = 13.8°$. 163

Figure 6.5 Isothermal magnetization curves as a function of the applied field, $M(H)$, measured at the temperature of 2 K for the neat 25 nm FePc film (black solid curve), 100 nm thick films of mixed H_2Pc:FePc, with ratios of 10 % (red solid curve) and 50 % of H_2Pc (blue solid curve), respectively, shown with the Brillouin fit for a spin S = 1 with g = 2. The magnetic moment is expressed in the unit of μ_B per Fe atom. Inner panel: no hysteresis loop can be observed for the mixed film consisting of 50 % of H_2Pc. 165

Figure 6.6 Schematics show possible film configuration for the H_2Pc:FePc films, based on the number of FePc molecules that are likely to be found in the molecular column at the given concentration of H_2Pc; top panel: mixed H_2Pc:FePc film containing 50 % FePc, and lower panel: 90 % FePc. The blue, and white spheres represent FePc and metal-free H_2Pc, respectively. 167

Figure 6.7 AFM micrographs of Al films deposited at the rate of 0.2 Å/s by using OMBD on glass with a thickness of 100 nm (a) and 50 nm (b), and 100 nm thick films on (c) silicon and (d) kapton substrates, and the height profile along the green line in (a), (b), (c) and (d) reveals the Al grain height, plotted below the figures. The respective RMS measured for each sample corresponds to 4.6, 2.4, 4.4 and 5.5 nm for (a), (b), (c) and (d), respectively, and the scale bars in all figures are 300 nm. 169

Figure 6.8 the XRD scan of a 50 nm thick Al film deposited at the rate of 0.2 Å/s at room temperature on silicon covered by its native oxide. 170

Figure 6.9 AFM micrographs of the 50 nm thick Al films deposited at the rate of 0.2 Å/s (a) on silicon substrate, (d) and (g) on glass substrates, 50 nm thick FePc films on (b) silicon and (e) and (h) on glass substrates, and 50 nm thick FePc films on substrates coated with 50 nm thick Al films deposited at the rate of 0.2 Å/s (c) on silicon substrate and (f) and (i) on glass substrates. The height profile along the purple line in (g), (h) and (i) reveals the grain height, plotted below the figures, and the watershed mark used to estimate the average grain size of 50 nm FePc films (h) on glass, and (i) on 50 nm thick Al deposited on glass, respectively. The scale bars in (g), (h) and (i) are 100 nm, whereas a scale bar of 200 nm is used in the rest of the images. 172

Figure 6.10 XRD scans of the 50 nm thick FePc films deposited on 50 nm thick Al films (red solid curves), the 50 nm Al film (black solid curves), and the 50 nm FePc films (blue solid curves) on (a) glass, and (b) silicon substrate, with the light grey line plotted to index the (100) diffraction peak at $2\theta = 6.9°$. The deposition rates for FePc and Al are 0.5 Å/s and 0.2 Å/s, respectively. No background subtraction is applied and the data are offset for clarity. The step size and time per step used for the XRD measurements are 0.033° and 50 second, respectively. 174

Figure 6.11 AFM micrograph of (a) the 25 nm thick FePc film deposited at the rate of 0.5 Å/s on glass, and the height profile along the purple line in (a) reveals the FePc grain

height, plotted below the figure, with the scale bar of 100 nm included. (b)The watershed mark for (a) used to extract the average lateral grain size of the 25 nm FePc film. 176

Figure 6.12 AFM micrographs of multi-layered structures, 25 nm FePc on 50 nm Al on (a) glass, (d) and (g) kapton substrate, 25 nm FePc/25 nm H_2Pc on 50 nm Al on (b) glass, (e) and and (h) on kapton substrate, and 15 nm FePc/35 nm H_2Pc on 50 nm Al on (e) glass substrate, (f) and (i) on kapton substrate. The deposition rates for FePc, H_2Pc and Al are 0.5 Å/s, 0.5 Å/s and 0.2 Å/s, respectively. The figures shown with the watershed mark below (a), (b), (c), (g), (h) and (i) are used to extract the average lateral grain size of the corresponding films. Except for (g), (h) and (i) where the scale bars of 100 nm is used, the scale bars given in the rest are 200 nm..... 177

Figure 6.13 XRD scans of the 25 nm FePc (black solid curves), 25 nm FePc/50 nm Al (red solid curves), 25 nm FePc/25 nm H_2Pc/50 nm Al (blue solid curves), and 15 nm FePc/35 nm H_2Pc/50 nm Al (magenta solid curves) on (a) glass and (b) kapton substrates, and a 50 nm FePc film on glass coated with a 50 nm thick Al (green solid curve), with the light grey line plotted to index the (100) diffraction peak at $2\theta = 6.9°$. The deposition rates for FePc, H_2Pc and Al are 0.5 Å/s, 0.5 Å/s and 0.2 Å/s, respectively. No background subtraction is applied and the data are offset for clarity. The step size is identical to what is used for other XRD measurements but the time per step is increased to 120 second to improve the diffraction signal. 179

Figure 6.14 The magnetization as a function of the applied field and temperature $M(H)$ and $M(T)$ curves for the 25 nm FePc films deposited onto (a), (c) and (e) bare kapton substrate, and (b), (d) and (f) on kapton coated with a first Al layer with a thickness of 50 nm. (c) and (d) temperature dependent magnetization $M(T)$ curves measured with zero-field cooled (ZFC) and field-cooled (FC) protocols under the applied field $H = 250$ Oe and 375 Oe, and (e) and (f) the differential susceptibility as a function of temperature; inner panel in (e) and (f): the inverse differential susceptibility ($1/\chi$) as a function of temperature fitted by the Curie-Weiss expression (solid red line). 182

Figure 6.15 The magnetization as a function of applied field and temperature $M(H)$ and $M(T)$ curves for (a), (c) and (e) for the 25 nm FePc/25 nm H_2Pc/50 nm Al, and (b), (d)

and (f) for 15 nm FePc/35 nm H_2Pc/50 nm Al. (c) and (d) temperature dependent magnetization $M(T)$ curves measured with zero-field cooled (ZFC) and field-cooled (FC) protocols under the applied field H = 250 Oe and 375 Oe, and (e) and (f) the differential susceptibility as a function of temperature; inner panel in (e) and (f): the inverse differential susceptibility ($1/\chi$) as a function of temperature fitted by the Curie-Weiss expression (solid red line). 183

Figure 6.16 (a) and (b) $M(H)$ curves of the 25 nm FePc/kapton, 25 nm FePc/Al, 25 nm FePc/25 nm H_2Pc/Al and 15 nm FePc/35 nm H_2Pc/Al measured at 2 K, (c) and (d) the virgin curves measured from the 25 nm FePc/25 nm H_2Pc/Al and 15 nm FePc/35 nm H_2Pc/Al at 2 K, normalized to the respective moments at H = 7 T, and (e) and (f) the M(T) curves measured with zero-field cooled (ZFC) protocols under the applied field H = 375 Oe obtained from the 25 nm FePc/kapton, 25 nm FePc/Al and 25 nm FePc/25 nm H_2Pc/Al and 15 nm FePc/35 nm H_2Pc/Al; inner panel in (e) and (f), the bifurcation points observed for 25 nm FePc/kapton, 25 nm FePc/Al, 25 nm FePc/25 nm H_2Pc/Al and 15 nm FePc/35 nm H_2Pc/Al, with approximately 3.5 K seen for the 25 nm and 15 nm FePc films grown on Al pre-coated with H_2Pc. 184

Figure 6.17 The observed coercivities (a) and the magnetization obtained under the applied field of 7 Tesla at 2 K (b) for the FePc multilayers as a function of lateral grain sizes determined by AFM. 187

List of Tables

Table 1.1 The vibrational frequency (in the unit of cm $^{-1}$) of C≡N stretching and C-H bending in TCNQ and the salts [92] observed for different oxidation states [82, 96].... 48

Table 1.2 Band assignments for the Mn(III) porphyrins proposed by Boucher [104]. 50

Table 2.1 Relevant values of the MnTPPCl films obtained from two film depositions. 64

Table 2.2 The deposition rates calculated for co-evaporation of MnTPPCl and TCNQ used in this work..... 65

Table 3.1 Texture coefficients of the 80 nm thick TCNQ films deposited onto bare substrates and PTCDA. 91

Table 4.1 Ratios of the absorption peaks at λ = 447 nm to 484 nm, calculated by using the respective peak heights obtained from the optical spectra recorded from the as-deposited MnTPPCl films with a thickness of 100, 75, 50, 33 and 25 nm. 103

Table 4.2 The extracted peak positions, heights, FWHMs and areas by fitting the optical spectrum with Gaussian functions as shown in Figure 4.3. Peak4 (the Soret band for Mn(III)) corresponds to the absorption at λ = 484 nm (2.57 eV), whereas Peak5 (λ = 447 nm, 2.77 eV) is absent in the MnTPPCl solution spectrum and only observed for the as-deposited MnTPPCl film. 105

Table 4.3 The relative amounts calculated for the Mn(III) and Mn(II) species in the as-deposited MnTPPCl films. 105

Table 4.4 The elements to manganese (Mn) ratios calculated for MnTPPCl (theoretical values), the MnTPPCl powder, and the 125 nm MnTPPCl film grown at the rate of 0.9 Å/s on silicon substrate after correcting for the empirical sensitivity factors. The photoemission lines of the XPS C1s, N1s, Cl2p and Mn2p peaks are fitted with the Voigt function (see Figure 4.8). 110

Table 4.5 Summary of the peak centers and areas extracted by using the Voigt function to deconvolute the C1s, N1s, Cl2p and Mn2p spectra recorded from the MnTPPCl powder and 125 nm thick MnTPPCl film. The relative quantities for the different chemically inequivalent C atoms listed in bracket are calculated without contribution from the π-π shake-up. 112

Table 4.6 The parameters extracted for the absorption bands at λ = 447 nm (2.77 eV) and λ = 484 nm (2.57 eV) in the optical spectra for a 100 nm thick MnTPPCl film recorded at different time intervals (see text). 123

Table 4.7 The relative amounts calculated for the Mn(III) and Mn(II) species. 126

Table 5.1 Summary of the CN vibration frequencies (in the unit of cm^{-1}), of TCNE radical anion (isolated and bound state), TCNQ in its neutral form and radical anion (isolated and bound state), and the observed frequencies for the co-deposited [MnTPPCl][TCNQ] films obtained by two sets of deposition rates. 137

Table 5.2 Summary of the element to manganese (Mn) ratios, of MnTPPCl powder, 125 nm thick as-deposited MnTPPCl film grown at the rate of 0.9 Å/s on silicon substrate, and the co-deposited [MnTPPCl][TCNQ] film on silicon substrate, (an equivalent thickness of 200 nm for MnTPPCl, with a 1 to 1 ratio between MnTPPCl and TCNQ obtained by using the deposition rates of MnTPPCl = 0.45 Å/s and TCNQ = 0.13 Å/s, respectively). The photoemission lines of the XPS C1s, N1s, Cl2p and Mn2p peaks are fitted with Voigt function (see Figure 5.6)..... 140

Table 5.3 The observed binding energies of C1s, N1s, Mn2p and Cl2p XPS profiles for the MnTPPCl powder, MnTPPCl film, and co-deposited [MnTPPCl][TCNQ] film. The XPS line-shape is fitted with the Voigt functions for the MnTPPCl powder, the 125 nm thick as-deposited MnTPPCl film grown at the rate of 0.9 Å/s, and the co-deposited [MnTPPCl][TCNQ] film (an equivalent thickness of 200 nm for MnTPPCl, with a 1 to 1 ratio between MnTPPCl and TCNQ obtained by using the deposition rates of MnTPPCl = 0.45 Å/s, TCNQ = 0.13 Å/s, respectively). Both the neat MnTPPCl film and the co-deposited [MnTPPCl][TCNQ] films were deposited on silicon substrate. The relative quantities for the different chemically inequivalent C atoms listed in bracket are calculated without contribution from the π-π shake-up. 142

Table 5.4 Binding energies for Mn 2p in similar compounds reported in the literature... 144

Table 6.1 Summary of the XRD patterns obtained from 100 nm thick films of mixed H_2Pc:FePc with a concentrations of 10 % and 50 % of H_2Pc deposited on silicon substrate, and the respective grain sizes calculated by the Sherrer analysis, 2θ(°) represents the peak center, whereas $w_{2\theta}$(°) corresponds to the peak width obtained from the full width half maximum (FWHM) of the Gaussian fit, expressed in the unit of degree. 164

Table 6.2 Diffraction peaks, intensities and the corresponding crystallographic planes observed for the Al crystal structure, adapted from [202]. 171

Table 6.3 Summary of the RMS values measured from the 50 nm FePc films deposited on glass, silicon and 50 nm Al films. 173

Table 6.4 Summary of the XRD patterns obtained from the 50 nm FePc films on glass and silicon substrate, and the respective grain sizes calculated by the Sherrer analysis, 2θ(°) represents the peak center, whereas $w_{2\theta}$(°) corresponds to the peak width obtained from the full width half maximum (FWHM) of the Gaussian fit, expressed in the unit of degree. 175

Table 6.5 Average lateral grain sizes (d) and roughness of multilayers based on FePc, H_2Pc and Al and 25 nm FePc observed by AFM (see text). 178

Table 6.6 Summary of the XRD pattern obtained from 25 nm and 50 nm FePc films, and multilayers based FePc, H_2Pc and Al. The grain size are calculated by the Sherrer analysis. 2θ(°) is the peak center, whereas $w_{2\theta}$(°) corresponds to the peak width extracted by full width maximum (FWHM) of the Gaussian fit, expressed in the unit of degree. 180

Table 6.7 Coercivities (H_{cr}), Curie-Weiss constants (T_c), the birfucation temperature (T_B) and the magnetization (M_s) under the applied field (H) = 7 T observed for the three multi-layered structures consisting of FePc, H_2Pc and Al grown on kapton substrate at 2 K (see text). 186

Glossary

Cp Cyclopentadienyl ($C_5H_5^-$)

Pc Phthalocyanine

H_2Pc Metal-free phthalocyanine

CuPc Copper Phthalocyanine

FePc Iron Phthalocyanine

PTCDA Perylene-3,4,9,10-tetracarboxylic dianhydride

TCNE Tetracyanoethylene

TCNQ 7,7,8,8,-tetracyanoquinodimethane

TTF…..tetrathiafulvalene

MnTPPCl Manganese tetraphenylporphyrin chloride

OEP Octaethylporphyrin

Nc Naphthalocyanine

SIA Single ion anisotropy

GMR Giant magnetoresistance

MTJ Magnetic tunnelling junction

TMR Tunnelling magnetoresistance

EPR Electron Paramagnetic Resonance

T6 sexithienyl

Alq_3 8-hydroxy-quinoline aluminium

$La_{0.7}Sr_{0.3}MnO_3$ (LSMO) Lanthanum strontium manganite

HOMO Highest occupied molecular orbital

LUMO Lowest unoccupied molecular orbital

SOMO Single occupied molecular orbital

DCM dichloromethane

OMAR organic magneto-resistance

OMBD Organic Molecular Beam Deposition

QCM Quartz crystal microbalance

SQUID Superconducting quantum interference device

SCE Saturated calomel electrode

MnPc Manganese phthalocyanine

F_{16}CoPc copper hexadecafluorophthalocyanine

1. Introduction and Literature Review

Molecular semiconductors are of both practical importance and fundamental interest. The optical, electronic, and magnetic properties in these materials can be controlled and combined through chemistry approaches, allowing for flexibility, tuneable characteristics, scalability and low temperature processing. In this context, molecular semiconductors are an ideal platform to realize magnets with tailored properties, by utilizing the molecular building blocks to combine with magnetic ions and/or organic radicals. Molecule-based magnets, whose functionalities have been expanded increasingly over the past four decades, have potential for spintronic applications, due to combination of semiconducting characteristics with the presence of an unpaired spin observed in these systems. The thesis will be centerd on the properties of molecular magnetic films. Hereafter the relevant literature will be reviewed and we will conclude with a detailed layout of the thesis.

Molecule-based magnets display extraordinary properties. In contrast to conventional inorganic magnets, organic magnets are distinguished by the magnetic coupling of the unpaired electrons (spins) residing in the *s-, p-* orbitals. In many cases, the magnetism is also due to transition metals or lanthanides bridged by organic ligands [1]. In the case of transition metal phthalocyanines (MPcs), α-FePc [2, 3] and β-MnPc [4-6], the resulting magnetic interactions are attributed to couplings between the unpaired spins carried by the central metal ions via the polyaromatic macrocycle.

The structure of molecule-based magnets mostly consists of carbon-based scaffolds, and as a result, structural motifs ranging from 0D (single-molecule magnets), 1D (elongated polymeric chains), 2D (plane/sheet structures), and 3D (3D network structures) can be readily achieved via synthetic chemistry routes. As with molecular electronics, molecule-based magnets offer attractive advantages including low cost, light weight, chemical tuneability, and mechanical flexibility [7, 8].

The field of molecule-based magnets attracted increasing interest since the discovery of the

first organic ferromagnet [$FeCp_2$][TCNE] (Cp = ferrocene and TCNE = tetracyanoethlyene) (T_c ~ 5 K) [9, 10]. [$FeCp_2$] can be also reacted with the structural analogue of TCNE,7,7,8,8,-tetracyanodimethane (TCNQ), resulting in [$FeCp_2$][TCNQ] [11]. Many magnetic charge-transfer salts are TCNE-based, which have the formula $M(TCNE)_x$, (where M = Mn, Fe, Co, Ni, Cd, *etc.*), including the well-known room temperature ferromagnet $V(TCNE)_x$ (x ~ 2) (T_c ~ 400 K), for which the central metal ion is coordinated by six nitrogen atoms with a bond length of 2.076°Å [12] forming a 3D network structure. Reacting TCNE with manganese tetraphenylporphyrin (MnTPP) leads to another charge-transfer salt, [MnTPP][TCNE], characterized by a 1D coordination polymeric ferrimagnetic chain, which exhibits unusually high coercivity and a large remanent magnetization corresponding to 27800 Oe and 11500 emu/mole at 2 K, respectively (Figure 1.2) [10, 13, 14], comparable to some of the largest values in the commercial magnets such as $SmCo_5$ (6k Oe) at room temperature [15].

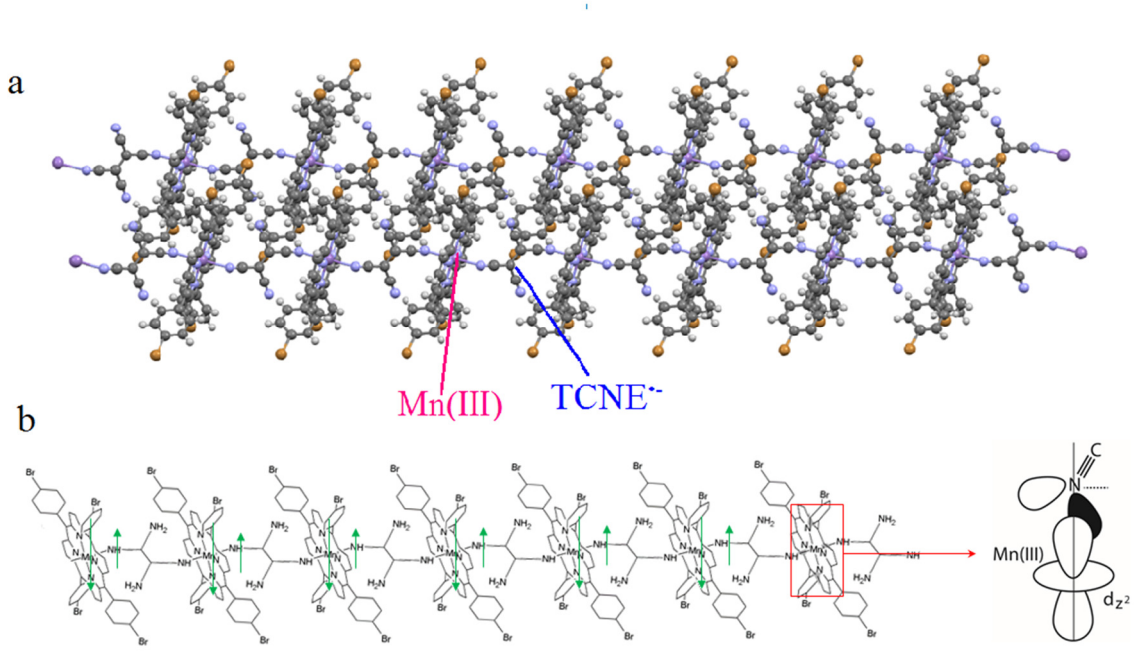


Figure 1.1 Structure of 1D polymeric-chain ferrimagnet formed by [MnTPP(Br)][TCNE] (a), where dark grey, light grey, dark purple, light purple and yellow spheres represent carbon, hydrogen, manganese, nitrogen and bromine atoms, respectively, shown with solvent molecules omitted [16], and (b) The 1D coordination polymeric ferrimagnetic chain of alternating unpaired spins, Mn (S = 2, long arrows) and TCNE (s = 1/2, short arrows), in which the N atom of TCNE is attached to (S = 2) the Mn atom of MnTPP(Br) via *trans-μ-N-σ* bonding [16]; right panel: schematic diagram illustrating the coupling arising from bonding between d_z^2-like Mn(III) and π^* TCNE.

Figure 1.1 (a) shows a schematic of $[MnTPP]^{+}[TCNE]^{\bullet-}$, with the structure typical among the [MnTPP][TCNE] family, the members of which have been extended by synthetic routes to systematically study and establish a relation between the function and structure for this class of materials, including [MnTPP(X)][TCNE] (X = F, Cl, Br and I) [14], [MnTPP(CF_3)][TCNE] [17], and MnTPP(OCH_3)][TCNE] [18]. Substitution with Mg [19] and Fe [20] for the central ion and using other macrocylic ligand like MnPc [21], Mn (II) octaethylporphyrin (OEP) [22], and Mn (II) naphthalocyanine (Nc) [23] is shown to result in the same type of 1D coordination polymeric chains with a similar linkage as seen in the $[Mn.TPP]^{+}[TCNE]^{\bullet-}$.

The magneto-structural properties of the [MnTPP][TCNE] family have been extensively studied by Epstein and Miller *et al* [13, 22, 24-26]. The magnetic order (T_c ~ 14 K) observed for this class of materials arises from the unpaired spins residing on the Mn ion (S = 2) aligning in an opposite direction to the spin residing on TCNE (s = 1/2), giving rise to the dominant antiferromagnetic intra-chain interaction, J_{intra}. Independent of temperature, the magnetization as a function of the applied field increases linearly at the low field regime (see Figure 1.2) characteristic of a canted antiferromagnet, then increases gradually after a rapid rise, revealing a transition to a new state with higher magnetization is brought about by the increasing field, suggesting the meta-magnetic-like behaviours.

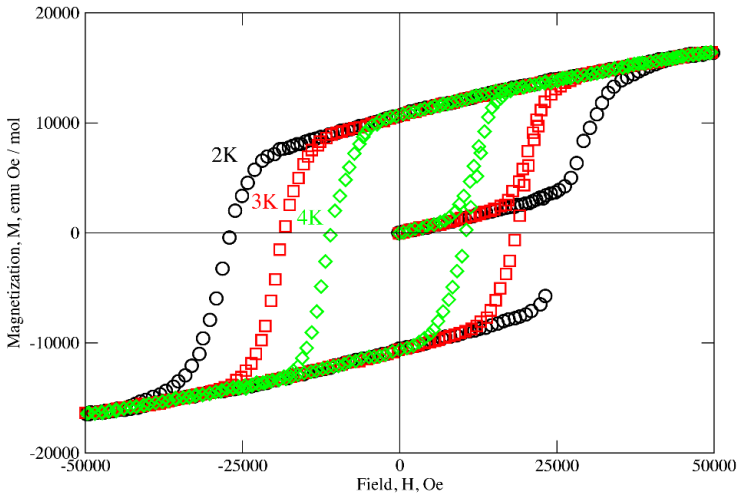


Figure 1.2 Magnetization as a function of the applied field, $M(H)$ curves measured from [MnTPP(Br)][TCNE] at 2 K, 3 K and 4 K, respectively, adapted from [14].

Below T_c, competition between the dipolar interactions and single ion anisotropy (SIA) on Mn(III) determines a canted antiferromagnetic ground state. Under the applied field the material switches over an energy barrier to a new canted state that stabilizes the total magnetic energy, and as the canting angle continuously changes as the field increases to saturate at the ferrimagnetic order. The field necessary to switch between different canted-angle states increases at low temperature, as the intensity of the dipolar interaction increases with decreasing temperature. The anomalously large coercivities and remanence in combination with the spin glass behaviours are unique features for this class of materials, and it is suggested that the magnetic ground state is stabilized by the large anisotropy arising from the sum of dipole-dipole interactions with the effects of single ion anisotropy from the Mn(II) site [14].

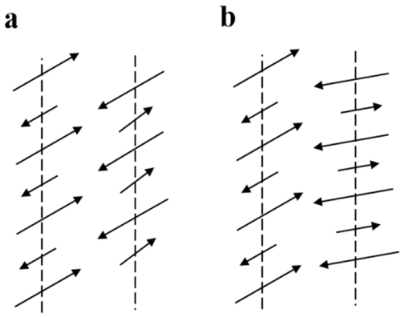


Figure 1.3 Schematics show the canted antiferromagnetic couplings along and between the chains of alternating $S = 2$ (long arrow) and $s = 1/2$ (short arrow) (a), and a different canted antiferromagnetic coupling of $S = 2$ (long arrow) and $s = 1/2$ (short arrow) along and parallel to the chain (b) adapted from [14].

The inverse magnetic susceptibility $\chi^{-1}(T)$ for [MnTPP][TCNE] can be fitted with the Curie-Weiss expression, yielding the effective θ, and θ' respectively for the two linear regions [24], and the minimum in the χT product characteristic of 1D ferrimagnetic behaviours [27-29] is not observed because of the high value of θ'. When a minimum of the χT product is present, the intra-chain interaction (J_{intra}) between the spin carriers Mn(III) and $TCNE^{\bullet-}$ can be modelled by the Seiden expression for a 1D uniform ferrimagnetic chain consisting of isolated (non-interacting) chains of alternating spins $S = 2$ (classical) and $s = 1/2$ (quantum) respectively [28]. This ferrimagnetic chain compound can be modelled by the Seiden expression [28], which can be written as the following, with Λ and δ as a function of JS/k_BT described according to the literature [28, 30]. S, s, g_S and g_s correspond to the spin state and

the g-factor for the two spins,

$$\chi_m = \frac{N\mu_B}{3\,k_B T}\left[{g_s}^2 S^2\left(\frac{S+1}{S}+\frac{2\delta}{1-\delta}\right)-4g_s g_s \Lambda_S S\frac{1}{1-\delta}\right.$$
$$\left.+\,{g_s}^2\left(s(s+1)+2\Lambda^2 s^2\frac{1}{1-\delta}\right)\right] \tag{1.1}$$

$$\gamma = -\frac{JS}{2k_B T} \tag{1.2}$$

$$a_0 = 4[\gamma^{-1}\sinh\gamma - \gamma^{-2}\cosh\gamma + \gamma^{-2}] \tag{1.3}$$

$$a_1 = 12[(\gamma^{-1}+12\gamma^{-3})\sinh\gamma - (5\gamma^{-2}+12\gamma^{-4})\cosh\gamma - \gamma^{-2}+12\gamma^{-4}] \tag{1.4}$$

$$b_0 = \gamma^{-1}(\cosh\gamma - 1) \tag{1.5}$$

$$b_1 = 3[(\gamma^{-1}+4\gamma^{-3})\cosh\gamma - 4\gamma^{-2}\sinh\gamma + \gamma^{-1} - 4\gamma^{-3}] \tag{1.6}$$

$$\delta = \frac{a_1}{3a_0} \tag{1.7}$$

$$\Lambda = 2\left[\frac{b_1}{3a_0}+\frac{b_0}{a_0}\right] \tag{1.8}$$

The Seiden expression has been very successful to capture the 1D intra-chain interactions observed for [MnTPP][TCNE] at high temperature (above ~ 50 K), though it deviates at low temperature as the 2D and/or 3D interactions (inter-chain) come to dominate [14, 24, 31]. Systematic studies on the magneto-structural correlation in the [MnTPP][TCNE] family reveal that the values of θ' and T_c, are sensitive to the distance between parallel chains and dihedral angle between the Mn - N - C, due to the direct exchange between Mn and N of TCNE, and variations in the magnetic behaviours depend on the substituted functional groups to the macrocyclic ring, and the type of solvents used for synthesis that causes solvent-induced pseudo-polymorphs [32].

The goal of this thesis is to achieve molecular films with controllable coercivities for spintronic applications through solvent-free approach by using Organic Molecular Beam Deposition (OMBD), with the focus on molecule-based magnets, [MnTPP][TCNE], which exhibits particularly high coercivities, and FePc, which has a lower coercivity but is potentially easier to process and integrate in multilayers. OMBD is a well-established growth method - it provides accurate control over the film deposition process under high vacuum conditions and the advantages include growth that is free of contamination, highly reproducible and comparable with co-deposition. The details for the film fabrication will be discussed in section (2.2) and (2.3).

Due to the low sublimation temperature (130-140 °C, 1.33×10^{-3} bar [33]) of TCNE, TCNQ is selected to co-evaporate with MnTPPCl, since they are the structural analogous to MnTPP and TCNE, respectively. The properties of the individual MnTPPCl and TCNQ films grown by OMBD are characterized, and which are then compared to those obtained from the co-deposited [MnTPPCl][TCNQ] films. The aim is to form MnTPP-TCNQ spin chains, by displacing Cl with TCNQ. The molecular ferromagnet, FePc, is particularly promising as a spin injector/detector. In FePc, the magnetic correlation and coercivity arise from the spin coupling interaction between the metal centers embedded in the molecular columns. In addition to the orientational modification, the influence of inclusion of a non-magnetic substituent, H_2Pc, as a function of concentration varied by simple co-evaporation is investigated. Such mixed films are shown to be an unconventional approach towards controllable coercivities by the molecular route.

1.1 Organic Spintronics

1.1.1 Spintronics

Spintronics is a multidisciplinary research field which studies spin-based phenomena such as detection, polarization and manipulation of electron and nuclear spin in the solid state. The field finds it beginning in the discovery of the giant-magnetoresistive effects (GMR) in 1988 [1, 2]. In addition to charge, the spin degree of freedom is exploited for data transmission and storage, offering decreased electric power, high sensitivity, and non-volatility [3]; this has been successfully utilized as for example read heads for hard drives

and random access memory. The GMR effects are observed in multilayers composed of alternating ferromagnets with different coercive fields, FM_1 and FM_2, respectively, separated by a nonmagnetic junction. The schematic of such a structure, also called spin valve, is shown in Figure 1.4.

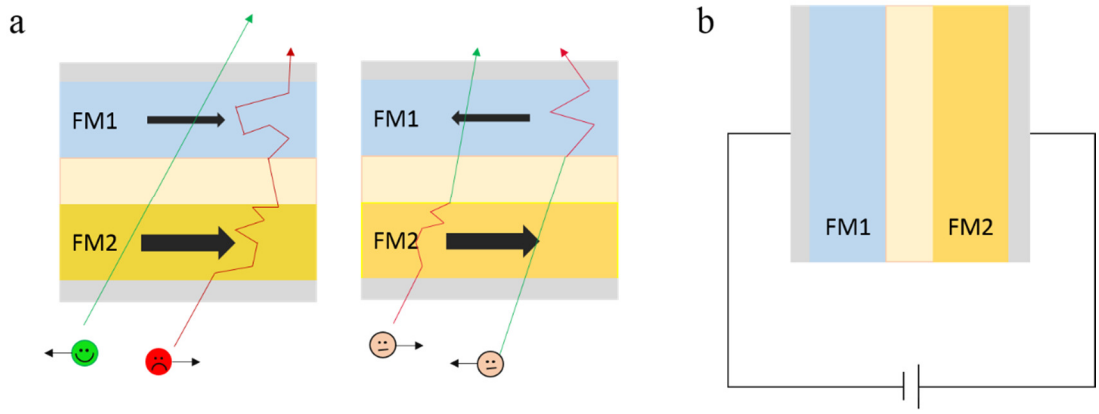


Figure 1.4 Schematic representation of the spin-valve behaviours in a tri-layer spin valve with a non-magnetic spacer sandwiched by two ferromagnetic layers (FM_1 and FM_2) with different coercivities, as depicted by the thin and thick arrows, respectively. The light grey rectangles correspond to the electrical contacts for the spin valve. When the magnetizations in the two ferromagnetic layers are parallel to each other (left panel in (a)) the spins in the anti-parallel alignment can travel through the sandwiched structure, giving rise to a higher conductivity and lower resistance. By contrast, electrons in the right panel in (a) undergo collisions in the either ferromagnetic layer, resulting in a higher overall resistance (adapted from [34]). In this case, the observed MR would be in a positive value, since the parallel configuration of the spin valve yields the low resistance state, and (b): the sandwiched structure comprises of ferromagnetic layers with different coercivities, decoupled by the non-magnetic spacer.

The operation of the spin valve consists of injection of a non-equilibrium spin population by an electrical current from the first ferromagnetic electrode through the non-magnetic barrier followed by spin detection. One of the key factors that determines the function of a spin valve is spin polarization (P_n), which is generally defined as [35],

$$P_n = \frac{N_\uparrow {\upsilon_\uparrow}^n - N_\downarrow {\upsilon_\downarrow}^n}{N_\uparrow {\upsilon_\uparrow}^n + N_\downarrow {\upsilon_\downarrow}^n} \tag{1.9}$$

where N_σ is the material's density of state (DOS) at the Fermi level (E_F) for spin σ (↑ for majority electrons and ↓ for minority) and υ_s corresponds to the spin-dependent Fermi velocity, with $n = 0$ for photoemission measurements and $n = 1$ and 2 for ballistic and

diffusion transport, respectively. No spins can be detected if the spin polarization is lost before the second electrode. Spin polarization arises as an electric current passes through a ferromagnetic material, leading to an imbalance between up electrons and down electrons in terms of spin alignment. Two physical parameters, spin relaxation time (τ_s) and diffusion length (λ_s) characterise the behaviour of spins as they pass through a material, corresponding respectively to the life-time and distance the spin travels before the polarization is lost. These quantities are of paramount importance as they depend on the materials choice and in turn define the upper bound for the thickness of the non-magnetic spacer, subsequently determining the ability for a spin valve to perform effectively.

Based on the GMR effect, current transport for the spin valve is controlled by the magnetizations in the two ferromagnetic layers, yielding respectively a high- and low-resistance state as the magnetization in the ferromagnetic layers changes from anti-parallel to parallel spin alignment. In this way, the resistance of the spin valve can be switched between the high-resistance state and the low-resistance one by external field. The magneto-resistance (MR) is quantified by the change in the percentile of the electrical resistance measured in the configuration under the external field H, compared to the other. The standard MR definition [35] is given below as,

$$\mathrm{MR} = \frac{R(H) - R(0)}{R(0)} \tag{1.10}$$

where $R(H)$ corresponds to the device resistance measured in the magnetic field, H. Positive MR is observed in a spin valve that has the low resistance state for the parallel configuration, whereas the negative MR refers to a low resistance state obtained from an anti-parallel configuration. In a magnetic tunnelling junction (MTJ), tunnelling magneto-resistive (TMR) effects can be observed as the spin current tunnels through a layer of insulating barrier sandwiched by the ferromagnetic electrodes [35].

1.1.2 Organic Spintronics

Over the last decades, considerable research in organic semiconductors [36] led to numerous technologically important optoelectronic applications, such as organic photovoltaic (PV) cells [37, 38], organic light-emitting diodes (OLEDs) [39-41] and organic field-effect

transistors (OFETs) [42-44], just to name a few. Spins in organic semiconductors were initially manipulated to harvest the singlet states in OLEDs, then the magneto-resistive effects in a hybrid organic spin valve with a molecular layer of sexithienyl (T_6) were reported by Dediu *et al.* in 2002, where a magneto-resistance (MR) ~ 30 % could be observed at room temperature [45]. Spin valve behaviour was also observed shortly after in p-conjugated molecule 8-hydroxy-quinoline aluminium (Alq_3) as the organic spacer to decouple the magnetic electrodes, $La_{0.7}Sr_{0.3}MnO_3$ (LSMO) and Co, respectively, with MR ~ 40 % at 11 K [46]. These pioneering experiments successfully demonstrate ease of fabrication and integration of organic semiconductors into existing technologies, and the potential organic semiconductors have to offer to spintronics. It should be mentioned that organic semiconductors exhibit organic magneto-resistance (OMAR), in absence of external magnetic stimulus, an intrinsic property originating from the hyperfine interactions [47]. The mechanisms for spin relaxation observed in these systems make organic semiconductors very attractive for spintronics applications, which can benefit from the immense functionalities, mechanical flexibility and low cost.

Largely composed of first row light weight elements such as C, N and O, molecular semiconductors have a the spin relaxation time (τ_s) is significantly longer than that of conventional semiconductors, due to from weak spin-orbit coupling and relatively low hyperfine interaction, making them particular attractive for spintronic applications. The values of τ_s observed for organic spin valves consisting of Alq_3 and rubrene are reported to be up to 1 second [46, 48], significantly longer than those of the inorganic semiconductors such as GaAs (~ 10^{-8} second) [49]. The spin diffusion length (λ_s) in organic semiconductors is limited by the charge mobility, which is one average orders of magnitude smaller compared the conventional semiconductors. For example, rubrene, known as one of the high mobility organic semiconductors, exhibits a mobility of 10 $cm^2 V^{-1} s^{-1}$, and a charge mobility of 0.4 $cm^2 V^{-1} s^{-1}$ has been reported for nanowires of copper phthalocyanine (CuPc) [50]. The diffusion length (λ_s) of Alq_3 as a layer buried in a functional spin valve has been measured by using low energy muon spin rotation spectroscopy [51].

The spin relaxation times of organic semiconductors can be measured by the electron paramagnetic resonance (EPR) technique [52], yet the effects of the physical-chemical properties on the spin relaxation times in relation to spin polarization in spintronic devices is difficult to estimate. The magneto-resistance observed for a multilayer stack represents a macroscopic property that comprises of the materials characteristics (*e.g.* structural, chemical

and electronic structure) in each individual component as well as the interface, and is subject to variations amongst devices, partly due to the inhomogeneous organic/metal interface.

Experimental and theoretical studies have indicated that the interface plays a fundamental role in the spin injection [53, 54], since the electronic structure changes with respect to the local molecular geometry/orientation and formation of chemical bonds when adsorbed on the magnetic electrode. This has been demonstrated by Barraud *et al.*, who showed the magneto-resistive effects in a nano-sized spin valve fabricated by nano-indentation processes with MR ~ 300 % at 11 K [55]. This paper contributed to elucidating the role of interface in determing the sign of magnetoresistance and the complex ferromagnetic metal-organic interface was labelled [56]. Interaction between the organic layer and the magnetic surface arises when brought in contact if close at the Fermi level, leading to new states formed by hybridization of the respective molecular orbitals and density of states. The molecular orbitals of the organic layer broaden in a spin-selective manner with respect to the spin polarized density states of the magnetic electrode, and the sign of MR can be explained by the strength of the interaction between the organic layer and the magnetic electrode [55].

In general, spin injection and MR can be enhanced by surface treatment to the magnetic electrode, for example adding an extra layer of oxide (*e.g.* Al_2O_3) [57] between the organic layer and electrode so as to minimize structural defects such as pin holes and interdiffusion into the organic layer that may cause the ferromagnetic electrodes to couple. Surface treatment can be used strategically to prevent formation of a dipole layer formed by the organic/metal interface to facilitate the current/spin injection. Improved MR signal is also reported by Sun *et. al.*, where a buffer layer consisting of magnetic nanodots is introduced at the interface between the organic layer and Co electrode [58].

1.1.3 All-organic spintronic devices

To date, most of the organic spin valves reported in the literature are fabricated with an organic layer as a non-magnetic spacer, sandwiched by ferromagnetic electrodes such as Co in combination with LSMO [46, 59, 60]. LSMO is a half-metal, and chemically stable, able to maintain spin polarization at room temperature [46, 61]. However, fabrication of LMSO often demands sophisticated epitaxial growth on a single crystal substrate that lacks mechanical flexibility, and conductivity mismatch can be an obstacle for spins to be injected

from the ferromagnetic metal into the organic medium [62]. This stimulates an active research in searching for molecule-based magnets for spin injector/detector towards all-organic spin valves. Remarkable progress has been made, and in 2011, magneto-resistive effects were reported by Li *et al.* for an all-organic spin valve based on the two ferromagnetic electrodes fabricated with a room temperature molecule-based ferromagnet, $V(TCNE)_x$ (x ~ 2) [63] (T_c ~ 400 K) [64], in which the magnetic order arises from antiferromagnetic coupling between the unpaired spins on V^{+3}, in the orbital of *3d* (t_{2g}), $S = 3/2$, and the unpaired electrons in the π^* orbital of $TCNE^{\bullet-}$ anion, $s = 1/2$ [65].

The all-organic spin valve device consists of stacks of two ferromagnetic layers of $V(TCNE)_x$ with different coercivities achieved by different fabrication processes, namely chemical vapour deposition (CVD) and molecular layer deposition (MLD), as spin injector and analyser, separated by a 10 nm thick layer of rubrene as the non-magnetic junction, with 50 nm and 30 nm Al respectively as the bottom and top electrodes. Spin injection from the first layer of $V(TCNE)_x$ through tunnelling is supported by the electrical characterization for the device, and the resistance exhibits the typical butterfly shape with the switching fields corresponding to the respective ferromagnetic layers, with a maximum negative MR of ~ 0.04 % observed at 100 K. The inverted spin-valve effects observed in the $V(TCNE)_x$ based spintronic devices is due to the shift in the respective energy levels in the two $V(TCNE)_x$ layers caused by the external bias, where the spin-selective tunnelling between the spin-polarized sub-bands of $TCNE^{\bullet-}\pi^*$ is allowed for the anti-parallel configuration [63]. The negative MR seen in this case is a consequence of the intrinsic features of the $V(TCNE)_x$ based spintronic devices, attributed to its unique electronic structure, and therefore the origin of the negative sign is different from what is reported by Barraud *et al.* [55]. This finding shows the potential organic semiconductors have towards realizing all organic spintronic applications at room temperature.

In addition to $V(TCNE)_x$, molecular films of the transition metal phthalocyanine family, could play a key role in spintronics, though currently the operation temperature of which is still limited. The magnetic coupling in CoPc is above the boiling temperature (77 K) of liquid nitrogen [66], and very recently MnPc has been shown to exchange bias to a ferromagnet, where the shift in the coercive field can still be observed at ~ 100 K [67, 68]. The materials properties for phthalocyanine and the individual components of charge transfer salts will be discussed in the following section. Spin-valve like behaviours have been observed at single

molecular level, based on a magnetic junction formed by Single Molecular Magnets (SMM) [69]. Spin filtering and magneto-resistive effects have been recently reported for carbon nanotube decorated with terbium phthalocyanine ($TbPc_2$) molecules [69]; this field attracts considerable research interest as fundamental questions in the underlying physics in these systems need to be addressed, demonstrating the broad potential these molecules have to integrate functional properties and chemical modifications on the nanometer-scale.

1.2 Molecule-based magnets

1.2.1 Magnetism

Magnetism is a cooperative property, and the magnetization observed in molecule-based magnets mainly arises from magnetic moments caused by the spin angular momentum of unpaired electrons carried by spin-bearing groups such as transition metal ions and/or radicals, referred to as spin centers. The effective magnetic moment of a spin center, m_{eff}, can be expressed as below,

$$m_{eff} = g_e\sqrt{S(S+1)}\,\mu_B \tag{1.11}$$

where g_e is the Landé g-factor, S is the spin quantum number (*e.g.* S is 1/2 for systems with one unpaired spin), and μ_B is the Bohr magneton. The magnetic properties of a material depend on the way a collection of spin centers interact. When the spin centers are not coupled, no magnetic order would be observed even at low temperature and therefore the molecule-based magnet behaves as a paramagnet. At low magnetic fields, the magnetization, M, of a paramagnet is proportional to the applied field (H) and the proportionality constant corresponds to the magnetic susceptibility, while more often the susceptibility expressed as,

$$\chi = \frac{\partial M}{\partial H} \tag{1.12}$$

Under weak fields (~200 to 500 Oe), the susceptibility for paramagnets is inverse proportional to temperature T,

$$\chi = \frac{C}{T} \tag{1.13}$$

$$C = \frac{\mu_0 N_A}{3k_B}\, {m_{eff}}^2 = \frac{\mu_0}{3k_B}\, {g_e}^2 S(S+1){\mu_B}^2 \tag{1.14}$$

where C is the Curie constant, which relates the effective moment carried by the spin center, defined by (1.14), where μ_0 corresponds to the vacuum permeability, required when in *SI* units.

The magnetic moment on a spin center increases with the field and reaches a saturation moment at very large fields, which can be calculated by the Brillouin function, $B_s(y)$, (1.15).

$$\langle m_B \rangle = g_e \mu_B S B_s\,(y) \tag{1.15}$$

$$B_s\,(y) = \frac{2S+1}{2S} coth\left[\frac{(2S+1)}{2S}\, y\right] - \frac{1}{2S}\, coth\left[\frac{y}{2S}\right] \tag{1.16}$$

$$y = \frac{g_e\, \mu_B S B}{k_B T} \tag{1.17}$$

, where k_B and T are the Boltzmann constant and temperature, respectively.

The situation is different when the spins in the molecule-based magnet are coupled and the interaction induces either a parallel or anti-parallel alignment between the neighbouring spins, corresponding to ferromagnetic and antiferromagnetic ordering, respectively. At high temperatures where the spin interaction is less than k_BT, under weak magnetic fields the susceptibility as a function of temperature can be expressed by the Curie-Weiss law as

$$\chi = \frac{C}{(T-\theta)} \tag{1.18}$$

, where θ corresponds to the Weiss temperature, which is a measure of the strength of the spin coupling in the material. A positive θ reveals the spin centers are coupled ferromagnetically, whereas presence of antiferromagnetic couplings is indicated by a negative θ, as shown in Figure 1.5. The plot of the inverse susceptibility as a function of temperature provides a simple way to distinguish the type of magnetic couplings exhibited by the magnets. The slope of the inverse susceptibility plotted as a function of temperature is

inverse the Curie constant C^{-1}, which can be related to (1.14). While the magnetic susceptibility as a function of temperature can be described by the Curie-Weiss formula, the spin-spin interactions are approximated by the mean field theory, and the internal magnetic field would cause further spin alignment and reduction for the ferromagnetic and antiferromagnetic ordered spins, respectively.

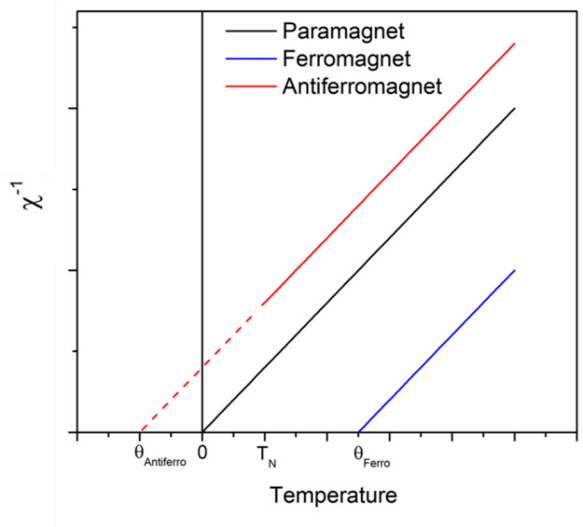


Figure 1.5 The inverse of the magnetic susceptibility (χ^{-1}) for paramagnetic, antiferromagnetic and ferromagnetic behaviour shown as the red, black and blue lines, respectively.

A system with coupled spins exhibits a magnetically ordered state, which can be observed below the transition temperature, and behaves like a paramagnetic material beyond the transition point. The transition temperature for a ferromagnet is called Curie temperature (T_c), and Néel temperature (T_N) for an antiferromagnet. While the Weiss temperature is similar to the Curie temperature for ferromagnets, the Weiss temperature (θ_{AFM}), determined for antiferromagnets tend to be different from the Néel temperature [70].

The magnetic response to the applied field is also very useful for characterising magnetic behaviours, and for, ferromagnets qunatities such as coercivity (coercive field), H_{cr}, and remanence, M_r can be defined (Figure 1.6). The coercivity is the required magnetic field to demagnetize a magnetic material which has been magnetically saturated. Whether a magnet is considered to be hard (H_{cr} > 1000 Oe) or soft (H_{cr} < 100 Oe) depends on the magnitude of its coercivity, and as a consequence it determines which conditions ($\mu_0 MH >> k_B T$) a magnet can be utilized for storage applications.

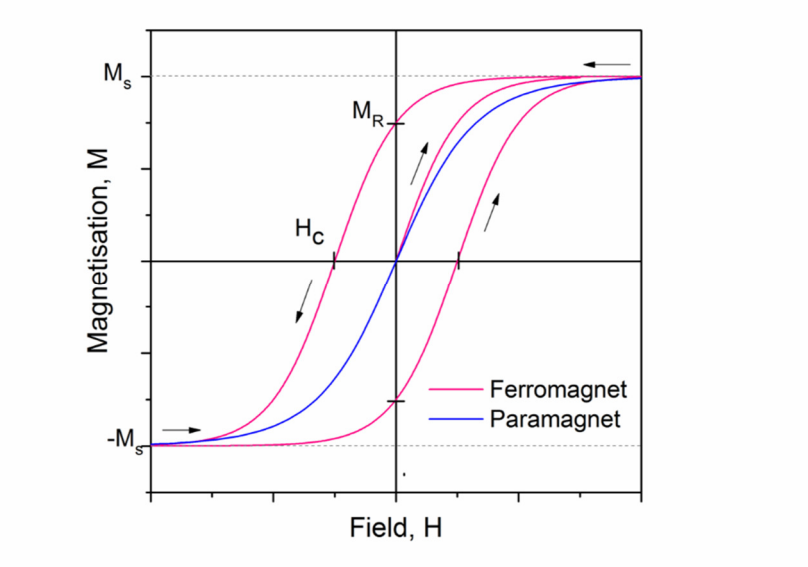


Figure 1.6 Hysteresis curves of a paramgent and a ferromagnet below its Curie temperature. The coercive field, H_{cr}, saturation magnetization, M_s, and remanent magnetization, M_r, are indicated, and arrows are shown to illustrate the directionality and history dependence of the behaviour.

1.2.2 Spin Hamiltonian

The magnetic phenomena discussed above are referred to as bulk properties of the molecule-based magnets, and the coupling mechanisms result from the interplay of various competitive interactions triggered by different types of couplings between the spin centers.

The spin Hamiltonian for molecule-based magnets can be represented as (1.19). The Zeeman Hamiltonian, $\mathcal{H}_{Zeeman}$, describes the interactions of the spins with the magnetic field. The effect of zero-field interaction, $\mathcal{H}_{ZFI}$, observed when the unpaired spins carried by the spin center is > 1/2.

$$\mathcal{H}_{\text{spin}} = \mathcal{H}_{\text{Zeeman}} + \mathcal{H}_{spin-spin} + \mathcal{H}_{ZFI} \tag{1.19}$$

The spin-spin coupling Hamiltonian, $\mathcal{H}_{\text{spin}-\text{spin}}$, describes the interactions between the spin centers, at *i* and *j* site, as shown in (1.20), where the pairwise interaction, $J_{ij,}$ also known as exchange, indicates the type and strength of coupling between the nearest adjacent sites, giving rise to ferromagnetic ($J > 0$) or antiferromagnetic ($J < 0$) order.

$$\mathcal{H}_{spin-spin} = -J_{ij}\, S_i \cdot S_j \tag{1.20}$$

However, the Heisenberg Hamiltonian (1.20) does not provide details on the spin alignment, which is essential to interpret the observed bulk properties in the molecule-based magnets. Several spin coupling mechanisms responsible for producing magnetic ordering ground states have been proposed, which are discussed in the following.

1.2.3 Magnetic dipole-dipole interaction

This dipole-dipole spin coupling, with energy *E* defined in (1.21), is a long distance interaction, attributed to the magnetic fields induced by the spins (with magnetic dipoles, μ_1 and μ_2), separated by a distance of *r*.

$$E = \frac{\mu_0}{4\pi r^3}\left[\mu_1 \cdot \mu_2 - \frac{3}{r^2}\,(\mu_1 \cdot r^2)(\mu_2 \cdot r^2)\right] \tag{1.21}$$

The strength of the magnetic dipolar interaction is typically estimated to be less than ~ 5 K, which is relatively weak and not sufficient to induce a long-range orderings observed for molecule-based magnets. Nevertheless, magnetic dipole-dipole interactions may help stabilize magnetic orderings in systems with ordering temperature less than 5 K and spin couplings between spin chains.

1.2.4 Exchange interaction

In contrast to magnetic dipole-dipole interaction, spins can couple in various pathways quantum mechanically as a result of exchange interaction governed by the Pauli exclusion principle. These spin coupling mechanisms responsible for the observed magnetic ordering in the molecule-based magnets include direct exchange, superexchange, and indirect exchange. First of all, direct exchange arises from coupling of the two magnetic spins residing in the neighbouring orbital; such coupling requires overlap between the singly occupied molecular orbitals (SOMO) as well as orthogonality. Direct exchange is responsible for the magnetic ordering observed in $V(TCNE)_x$ and [MnTPP][TCNE], where the spins of different

magnetic moments are coupled antiferromagnetically, but with different magnetic moment, resulting in the ferrimagnetic alignment.

As for phthalocyanines, the spins are localized in the cavity of the Pc ligand and separated by a relatively large distance in contrast to the charge-transfer salts, and subsequently superexchange and indirect exchanges are invoked to account for the observed magnetic orderings in these molecular systems. In superexchange the spin couplings occur via electron hopping from the transition metals via the non-magnetic Pc ligand, and as a consequence the magnetic structure in Pc systems is very sensitive to the stacking angle. This will be expanded upon for different Pcs in section (1.3.3).

1.3 Charge-Transfer Salt and Metal Phthalocyanines

1.3.1 7,7,8,8,-Tetracyanoquinodimethane (TCNQ)

While there exist many p-type molecular semiconductors, the options for n-type candidates remain limited, including most notably copper hexadecafluorophthalocyanine (F_{16}CuPc) [71], tetracyanoethylene (TCNE) [72], 7,7,8,8,-tetracyanoquinodimethane (TCNQ) [73] and F_4-TCNQ [74]. Due to the strong electron withdrawing ability (HOMO = -7.3 eV, LUMO = -4.8 eV, E_g = 2.5 eV) [73], TCNQ has been extensively utilized as an electron acceptor, either as a dopant [75] or a separate layer in molecular PV devices to facilitate the separation of the charge carriers, for instance in the heterostructures based on ZnPc/TCNQ and CuPc/TCNQ [73]. The n-type behaviour also allowed TCNQ to be used in n-type FETs [76, 77]. In addition, a wide range of charge-transfer salts based on TCNQ and TCNE were reported to display interesting physical properties, and an organic conductor, TTF-TCNQ, can be obtained as a mixture of TCNQ with tetrathiafulvalene (TTF) and heterointerface created by lamination [78]. The interest in the synthesis of TTF-TCNQ dates back to 1973 [79], and this high conductivity could be also observed at the interface between TTF and TCNQ [78].

Additionally, TCNE/TCNQ are important building blocks to form metal-organic frameworks (MOF)s. Owing to the complex chemistries and versatile structural motifs [80], TCNE/TCNQ can be used as linkers to form metal complexes. Alternatively, when TCNQ reduction occurs, the radical anion of TCNE/TCNQ can function as spin-bearing groups [81], attributing to the magnetic coupling with the ligated transition metal. For example, the

charge-transfer (CT) salt $V(TCNE)_x$, a room temperature molecular ferromagnet [64] has recently been applied to the organic spin-valve [63], and M(TCNQ) (M = Mn, Fe, Co and Ni) also reported to display unusual magnetic behaviours [82].

UV/Visible spectroscopy

The optical properties of TCNQ in both vapor-phase and solution have been well-characterized [83, 84]. In vapor-phase, absorption results from a single vibronic progression consisting of three components, with the maximum observed at a wavelength of 362 nm. The Franck-Condon factors for the vibronic transitions (0, 0) (λ = 362 nm), (0,1) (λ = 345 nm) and (0,2) (λ = 330 nm) were determined to be 0.656, 0.249 and 0.099, respectively [83].

The same kind of vibronic progression was also observed for the TCNQ solution spectrum, with a slightly red-shifted absorption maximum (λ_{max} = 402 nm) when dissolved in chloroform. The spectrum exhibiting very few electronic transitions can be related to the high symmetry of TCNQ (D_{2h}) [85]. Figure 1.7 presents the solution spectrum of TCNQ dissolved in DCM, where the absorption maximum corresponds well with the literature values [83, 84, 86].

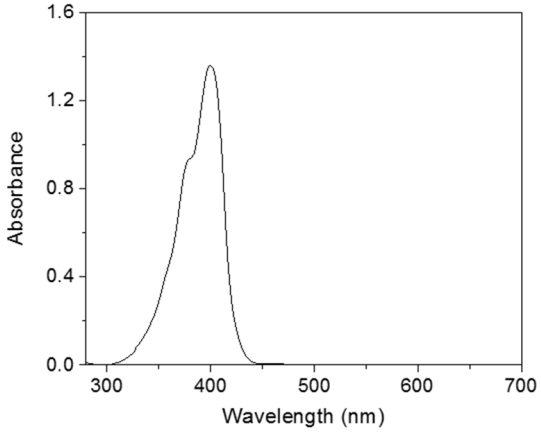


Figure 1.7 Absorption spectrum of TCNQ in dichloromethane with a concentration of $2.5x10^{-5}$ M.

When undergoing reduction, the optical spectrum of TCNQ exhibited changes mostly in the near IR range. The radical anions of TCNQ (in both monovalent and divalent) in solution

were observed, and the two different radical anions showed very different spectra, where absorption bands at about λ = 750 and 870 nm were expected for $TCNQ^{\bullet-}$ [87]. However, the optical spectrum can be complicated by other reactions accompanied by the TCNQ reduction such as dimerization. Various studies on the TCNQ solutions indicated that the strong electron acceptors with radical anions tend to form dimers, which showed absorption bands similar to that observed for $TCNQ^{\bullet-}$ [88]. In DCM, the monomeric $TCNQ^{\bullet-}$ exhibited a λ_{max} = 845 nm (log ε_M = 4.6), whereas two absorption peaks at λ = 643 and 870 nm (log ε_M = 4.5 and 4.1, respectively) were found to correspond to the dimeric species [88]. Dimerization of $TCNE^{\bullet-}$ (and TCNQ as well as other structurally similar compounds) in solid state has also been observed, and the monomeric and dimeric species exhibited a slightly red-shifted absorption maximum in comparison to the solution-phase [88]. Theoretical efforts showed that in electron-donor-acceptor systems a diamagnetic $[TCNQ\text{-}TCNQ]^{2-}$ dimer is in effect stabilized by the two anion radicals with an anti-parallel alignment [89, 90].

Infrared (IR) spectroscopy

The vibrational spectrum of TCNQ as well as that with salts have been investigated by IR spectroscopy [91, 92]. Overall, the spectrum of TCNQ is dominated by strong absorptions at 2226 cm^{-1} and 863 cm^{-1}, with other absorptions in the range of 3000-3300 cm^{-1} and 1000-1500 cm^{-1} corresponding to the presence of the functional groups, CH (aromatic) and C-C within the TCNQ molecule. The absorption at 2226 cm^{-1} is characteristic of ν(C≡N) stretching, whereas the band at 863 cm^{-1} corresponds to C-H bending (aromatic), and both observed from the TCNQ film deposited on KBr substrate (see Figure 1.9) appear to agree with the literature values for neutral TCNQ [91-93].

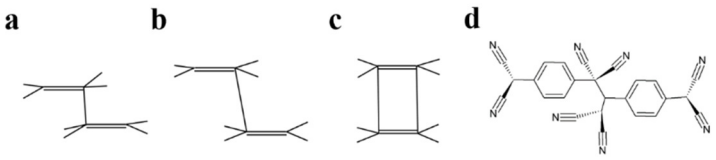


Figure 1.8 Experimentally observed packing motifs of dimerized TCNE (a) σ-dimer, (b) π-dimer 1, (c) π-dimer 2, and (d) σ-$[TCNQ\text{-}TCNQ]^{2-}$.

The change in the oxidation state has a strong influence on the molecular structure of TCNQ.

In $TCNQ^{\bullet-}$ the bond length of the C≡N groups is longer than those of neutral TCNQ, owing to the delocalization of the unpaired radical. Subsequently, a shift in the ν(C≡N) stretching towards lower wavenumber can be observed, as the bonding between CN groups is between triple bonding and π- bonding character. Thus, the shift (0-27 cm^{-1}) observed for ν(C≡N) stretching can be correlated with degree of the charge-transfer within the donor-acceptor systems [94, 95]. The splitting of ν(C≡N) stretching occurs in case of an asymmetric environment experienced by the CN groups [24, 80].

While ν(C≡N) stretching can be used to detect the presence of charge-transfer for TCNQ, it can also lead to ambiguous structural determination for TCNQ charge-transfer complexes. As with metals there are more than one type of metal-ligand coordination (σ-, μ-) arising from the nitrile to metal interactions, and dimerization of $TCNQ^{\bullet-}$ results in different types of isomers (σ-, π- $[TCNQ\text{-}TCNQ]^{2-}$), both of which cannot be identified by simply monitoring the ν(C≡N) stretching.

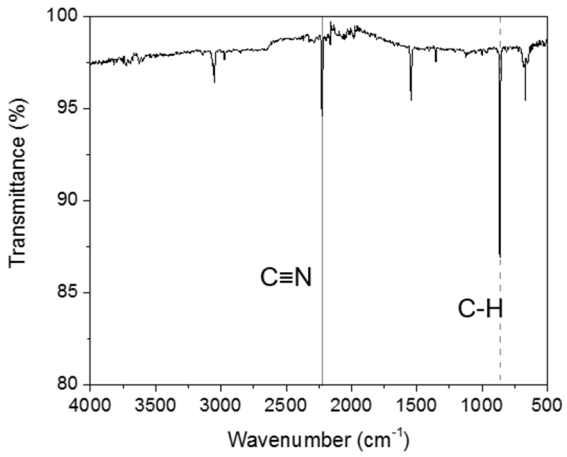


Figure 1.9 IR spectrum of the TCNQ film deposited onto KBr substrate.

Furthermore, the σ(C-H) out-of-plane bending is diagnostic for the oxidation state of TCNQ, which falls in the range between 800 and 900 cm^{-1}. The isomers of dimerized $TCNQ^{\bullet-}$ were characterized structurally [96, 97], with different absorption frequency for the σ(C-H) out-of-plane bending determined for $TCNQ^{0}$, $TCNQ^{\bullet-}$ and $[TCNQ\text{-}TCNQ]^{2-}$ [82, 96]. Therefore, when using IR spectrum to deduce the molecular environment of TCNQ in the charge-transfer systems, both the absorption frequencies of σ(C-H) out-of- plane bending and ν(C≡N) stretching should be taken into account, since the ionized TCNQ is subject to dimerize in

either solution or solid state.

Table 1.1 The vibrational frequency (in the unit of cm $^{-1}$) of C≡N stretching and C-H bending in TCNQ and the salts [92] observed for different oxidation states [82, 96].

	TCNQ	NaTCNQ	Na_2TCNQ	Na_3TCNQ
ν(C≡N)	2228	2197	2164	2035
		2166	2096	1901
	TCNQ	$TCNQ^{\bullet-}$	σ- $[TCNQ\text{-}TCNQ]^{2-}$	
σ(C-H)	864	819-830	802	

TCNQ crystalizes in the C2/c space group (a = 8.906, b = 7.060 and c = 16.395 Å with β = 98.54°) [98], and forms the typical herringbone structure in which the molecular columns of TCNQ stack along the b-axis with a tilt angle of ~ 66.7°, as shown in Figure 1.10 (b). In addition, the angle between the long molecular axis of TCNQ and the a-axis is around 48°. This configuration leads to the shortest distance in terms of the intermolecular contacts of the CN groups towards the H-donors of the adjacent TCNQ molecules, and hydrogen bonding is expected to be prominent amongst various intermolecular interactions involved in molecular packing for TCNQ.

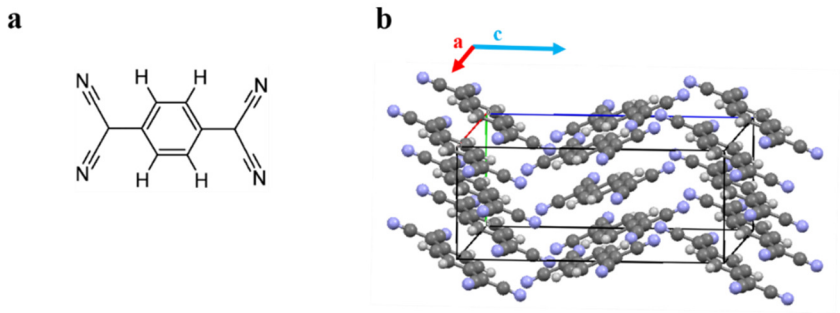


Figure 1.10 The schematics representing (a) molecular structure of TCNQ, and (b) the unit cell of TCNQ projected on the a-c plane (viewed along the b-axis) adopted from [98], where dark grey, light grey and light purple spheres represent carbon, hydrogen and nitrogen atoms, respectively.

The optical properties of TCNQ crystals (neutral TCNQ) are remarkably similar to those obtained in the vapor-phase and solutions, where the spectrum was found to mainly consist of vibronic transitions originating from the single electronic transition, $1B_{3u} \leftarrow 1A_{1g}$ [83, 85,

91]. Nevertheless, the spectrum of the crystal and amorphous film can be differentiated from that of the vapor-phase and solution by a much broader absorption band (spanning from ~ 2.0 to 4.5 eV), due to the quasi-metallic reflectance [83, 85]. Overall, the optical studies revealed optical anisotropy exhibited by the TCNQ single crystals [83, 85], and similar anisotropic effects were observed when investigated by polarized IR spectroscopy [91].

1.3.2 Manganese tetraphenylporphyrin chloride (MnTPPCl)

The simplest porphyrin is porphine, an aromatic compound of 11 pairs of π - electrons in conjugation in the macrocyclic ring. For tetraphenylporphyrins (TPP)s, the meso-positions are substituted with phenyl groups. Addition of the phenyl groups does not extend the conjugation of the porphyrin skeleton, and rotation of the phenyl groups is allowed as they are connected by C-C bond. Thus, this further adds to the structural flexibility for TPPs, in addition to the common saddled and ruffled geometry observed for the un-substituted porphyrins. The ability to undergo conformational changes renders them to have a significant role in biological processes in a cooperative manner with the metal ions as well as co-factors.

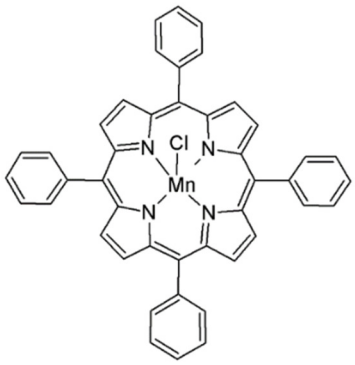


Figure 1.11 The molecular structure of MnTPPCl.

By releasing two protons, porphyrins reduce to porphyrinato (Por^{2-}), and with a central cavity of 90 pm, Por^{2-} can form complexes with various metal ions such as Mg^{2+}, Cr^{3+}, Mn^{3+}, Fe^{3+}, Co^{2+}, Ni^{2+}, Cu^{2+}, Zn^{2+}, Cd^{2+}, Sn^{4+}, Pb^{2+} [99] and others [11]. Ions with radii larger than 90 pm subsequently cause the porphyrin ring to deviate from the initial planar geometry, which is further distorted if an axial ligand is present, such as FeTPPCl and MnTPPCl [100].

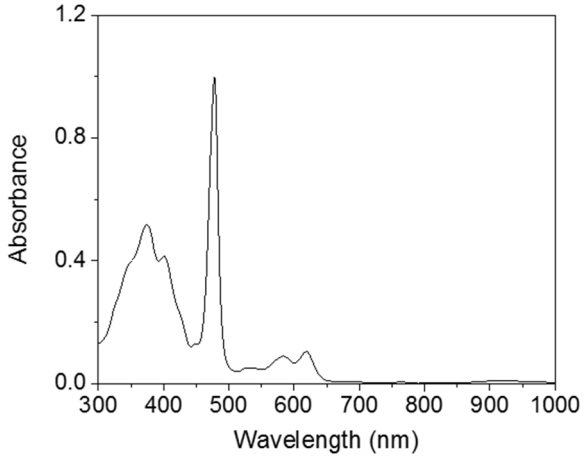


Figure 1.12 Absorption spectrum of MnTPPCl in dichloromethane with the concentration of 10^{-5} M.

The optical spectra of porphyrins exhibit very similar features, where the absorption bands can be explained by Gouterman's four-orbital model [101]. The spectra is characterized by strong absorption close to UV range, assigned as B-bands, and the bands between 500-900 nm with much lower oscillator strength are attributed to Q-type, both of which corresponding to π-π* transitions between the HOMO (a_1, a_2) and LUMO (e_g^*) of porphyrins [101, 102]. The low intensity of the Q-bands is a result of the nearly cancelled transition dipole. The B- and Q-bands are band assignments used to described different types of electronic transitions studied in molecular spectroscopy [103].

Table 1.2 Band assignments for the Mn(III) porphyrins proposed by Boucher [104].

	λ_{max} (nm)	transitions
I	~769	a_{1u}, $a_{2u} \rightarrow e_g$ (charge-transfer)
II	~667	$a_{2u} \rightarrow d_{z2}$ (charge-transfer)
III	~592	a_{1u}, $a_{2u} \rightarrow e_g$
IV	~559	a_{1u}, $a_{2u} \rightarrow e_g$*
V	~455	a'_{2u}, $b_{2u} \rightarrow e_g$ (charge-transfer)
V_a	~427	$a'_{2u} \rightarrow d_{z2}$ (charge-transfer)
VI	~370	a_{1u}, $a_{2u} \rightarrow e_g$* (charge-transfer) a'_{2u}, $b_{2u} \rightarrow e_g$ (charge-transfer)

The optical absorption of Mn(III) porphyrins is anomalous in comparison to those of other metalloporphyrins. In addition to a large blue shift for the B-band, the spectrum is dominated by intense charge-transfer bands, a consequence of large mixing between Mn(III) and the porphyrin ligand. The energy levels of the *d*-orbitals of Mn(III) are comparable with respect to the HOMO/LUMO of the porphyrin, and high-spin d^4 configuration allows for overlap between d_{xy} of Mn(III) and $e_g(\pi)$ of porphyrin, resulting in strong metal-ligand mixing. The absorption bands observed in the spectra of Mn(III) porphyrins with the corresponding assignments proposed by Boucher [104] are summarized in Table 1.2.

Changes in the Mn oxidation state were observed for Mn(III) porphyrins [105]. The optical studies on the vapour phase Mn(III)TPPCl indicated that the spectrum consisted of electronic absorptions corresponding to both Mn(II) and Mn(III), suggesting occurrence of self-reduction for Mn(III)TPPCl when vaporized [105]. In solutions, electrochemistry of Mn(III) porphyrins is regulated by the axial ligation, and reduction of Mn(III) to Mn(II) leads the absorption maximum to shift from $\lambda_{max} = 476$ to $\lambda_{max} = 444$ nm, corresponding to Mn(III)TPPCl and Mn(II)TPPCl$^-$, respectively [106]. The dioxygen adduct of Mn(II)TPP exhibits an optical spectrum similar to that observed for Mn(III)TPPCl, with the absorption maximum at $\lambda_{max} = 472$ nm [107], though the spin state of MnTPP(O_2) is $S = 3/2$, with a D value = -2.48 ± 0.07 cm $^{-1}$ [107]. The oxygenation of MnTPP, FeTPP and CoTPP was also investigated by vibrational spectroscopy [108, 109]. On Ag(111) MnTPPCl forms self-assembled monolayer in registry with the underlying three-fold symmetry. Annealing at ~ 423 K led to dissociation of the Cl ligand from Mn(III)TPPCl, with the porphyrin structure intact, both suggested from the XPS results [110]. Following annealing at 510 K Mn(III)TPPCl/Ag(111) with exposure to O_2, XPS suggested formation of Mn(III)TPPO via an homolytic cleavage pathway [111].

The vibrational properties of porphyrins have been well-studied. While D_{2h} can be used to describe the molecular symmetry of porphyrins, with TPPs structural approximations will need to be employed, as the phenyl groups are not perfectly perpendicular to the porphyrin core. Nevertheless, for vibrational properties the D_{4h} has been assigned to MTPPs (M = Ni(II), Fe(III), Mn(III) and Co(III)) [100, 112].

For porphyrin, a system of 37 atoms the in-plane degree of freedom (2n-3) is 71, which corresponds to,

$$\Gamma_{in\text{-}plane} = 9A_{1g} + 9B_{1g} + 8A_{2g} + 9B_{2g} + 18E_u$$

For instance, 169 normal mode is calculated for ZnTPP [100]. In addition to the vibrations related to the substituted phenyl groups, overall they have a relatively small impact on the vibrational frequencies of the porphyrin-core. Two additional bands appear at 803 and 1014 cm^{-1}, corresponding to the σ(C-H) deformation of the phenyl groups, and the coupling of vibrations of the phenyl groups to the pyrole-breathing mode, respectively.

However, the vibrations related to the porphyrin-core can be influenced by the central metal ion, as well as its oxidation state. For example, the displacement of Fe(II) and Fe(III) in TPP is deviated from the porphyrin plane since the size of these ions is larger than the cavity [100], which in turn causes dooming of the porphyrin to maintain the bonding between the metal and TPP ligand.

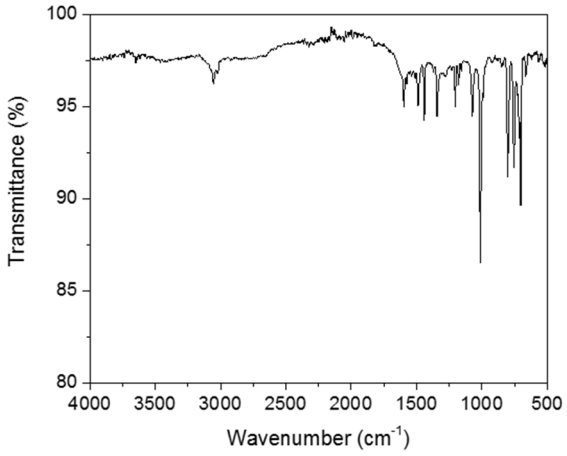


Figure 1.13 IR spectrum of the MnTPPCl film on KBr substrate.

Early studies [102, 113-115] indicated the electronic ground state of the 5-coordinate Mn(III) porphyrins to be high-spin (d^4), $S = 2$. The zero-field splitting (ZFS), D values, for Mn(III) porphyrins extracted from the magnetic susceptibility measurements are -2.3 cm^{-1} and -1.9 cm^{-1} for single crystals and powder, respectively [113-115]. EPR studies on single crystal of Mn(III)TPPCl showed a sizeable and negative D value, ranging between ~ 2 and 3 cm^{-1} [116, 117], with the g-values very close to 2 ($g_{\parallel} = 1.98(2)$, $g_{\perp} = 2.005(3)$ [118]). Low-temperature magnetic measurements on polycrystalline MnTPPCl [113] showed the saturation moment at high temperature slightly falls below the expected value (4 μ_B), and that M(H/T) for both MnTPPCl and MnTPPCl(py) deviated from $S = 2$, $g = 2$ Brillouin function

at high field. Meanwhile, the magnetization was found to be less suppressed for polycrystalline MnTPPCl(py). While the suppressed magnetization is related to the large and negative *D* value, the results suggested presence of antiferromagnetic exchange for magnetization in MnTPPCl [113].

Various structures have been published, and the solvate-free MnTPPCl structure belongs to trigonal system [119], differing from structures obtained with toluene [120] and acetone solvates [121]. The distance of Mn is ~ 0.27 Å above the porphyrin plane [102], which can be seen from solvate-free structure in [119]. Polymorphism in the porphyrin has been shown to be substrate-dependent, primarily attributed to the flexibility to switch between the doomed and ruffled geometry [122].

1.3.3 Transition metal phthalocyanines (MPcs)

Originally discovered as a pigment, Linstead *et al.* [123] determined the structure of phthalocyanines (Pcs) which are based on a macrocyclic ring composed of four iminoisoindoline units. It is an aromatic compound arising from the large conjugated system of 18 π - electrons. The central cavity of Pcs can accommodate various metal ions, which extensively influence the electronic structure, optical absorption and magnetic properties of Pcs.

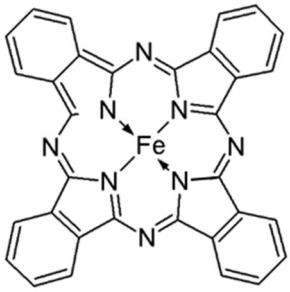


Figure 1.14 The molecular structure of FePc.

The simplest Pc is metal-free Pc, H_2Pc, and losing protons results in its reduced form, Pc^{-2}, which forms many complexes with divalent metal ions, including Mn(II), Fe(II), Co(II), Ni(II), Cu(II) and Zn(II). The square-planar Pcs are assigned to either D_{2h} or D_{4h} symmetry. For example, the molecular symmetry of divalent planar Pcs are assigned to D_{4h} but reduced

to D_{2h} for H_2Pc. The diameter of the central cavity of Pcs is ~ 1.6 Å [124], and as a consequence the size of the central ion can cause structural distortion so as to deviate from the Pc planar skeleton and reduce the molecular symmetry.

As a molecular solid, polymorphism is observed for Pcs, owing to the weak intermolecular interactions such as van der Waals responsible for molecular packing, subsequently Pcs crystalize into different polymorphic structures, such as the α, β, and η-phases etc. The α-phase (see Figure 1.15 (b)) can be prepared by acid-paste, grinding and by film deposition at room temperature, whereas gradient purification, and growth at elevated substrate temperature, can lead to the needle-like crystals in the β-phase (Figure 1.15(a)) [123]. The former is often obtained as fine particles, in contrast to the β-phase crystal, which is the thermodynamically stable form of Pcs. Although less common, a different structure, known as the η-phase, has been observed in CuPc nanowires [125]. Planar Pcs are isomorphic, and thus adopt the same structure in solid form.

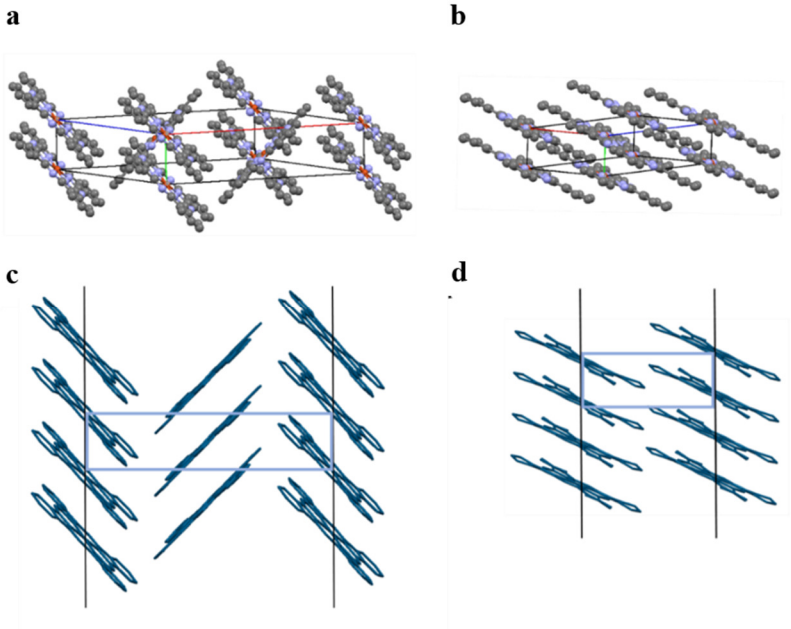


Figure 1.15 The crystalline structures (a) and (c) based on the herringbone arrangement found in the β-phase [126], and (b) and (d) depicted the α-phase structure determined by Hoshino *et al.*, adapted from [127].

Whilst chemically indistinguishable, the different crystalline structures displayed by the α- and β-phases lead to many unique physical properties exclusive to the solid state. The molecular columns of Pcs stack along its *b*-axis and structural determination showed that the

most distinctive difference between the α- and β-phase lies in the stacking angle, which is 26° for the α-phase, whereas a slightly larger molecular tilt corresponding to 45° is found for the β-phase. The β-phase belongs to monoclinic $P2_{1/a}$, space group, in which two molecules occupy the unit cell. For the α-phase two types of crystalline structures have been proposed. The former is the well-known herringbone structure, consisting of two types of molecular columns packed in the herringbone arrangement with respect to each other. Recently work by Hoshino re-determined the α-phase CuPc, revealing a different molecular arrangement, referred to as brickstack structure, with the unit cells occupied by one kind of molecular column.

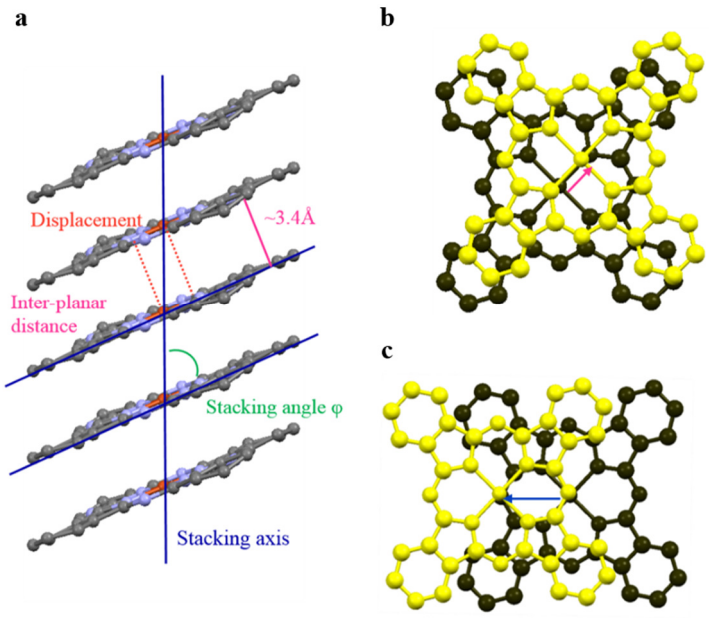


Figure 1.16 Schematics showing, (a) the definitions for the stacking axis, the stacking angle (φ) and the relative displacement between the Pcs in the molecular column, and different relative displacements arising from the molecular orientations adopted by (b) the α-phase and (c) the β-phase, respectively.

As the stacking angle increases from 26 to 45° for the α- and β-phase, the orientation of the Pc molecular columns is also shifted, subsequently inducing several changes in the spatial arrangements. The distance between the two Pc molecules, which is its inter-planar distance, corresponds to ~ 3.5 Å for the α-phase, slightly larger compared to ~ 3.3 Å for the β-phase. The direction in which Pcs of the same columns shift also differs, in turn giving rise to two types of overlap between the Pc molecules (Figure 1.16 (b) and (c)), and a difference in the

displacement of Pc in relation to the adjacent molecules. In the α-phase the central ion of the neighbouring Pc is displaced close to the α-nitrogen of the Pc molecule underneath, yet the parallel molecular shift in the β-phase results in the central ion to be located above the aza-nitrogen. The spatial variations in the molecular arrangements adopted by Pcs have significant influence on the magnetic properties, exhibiting a dependence of the stacking-angle.

The optical properties of Pcs are dominated by the organic ligand, and the corresponding spectrum can be characterized by intense absorptions in the near-UV range and relatively higher wavelength, corresponding to B- and Q-bands, arising from π-π^* transitions. The optical spectrum of metallophthalocyanines (MPcs) can be complicated by presence of charge-transfer bands due to mixing of the metal-organic ligand. For the thin films of Pcs, the optical spectrum often can retain the characteristic absorption bands, though very minor differences may appear, compared to that of the solution, such as broader peak widths, or band-splitting. These discrepancies are related to the short intermolecular distance that separate the molecules in the solid state, where molecules can form dimers and when excited give rise to Davydov splitting (see Figure 2.4).

Magnetic transitions in MPcs arise from the unpaired spins carried by the central ion, and for example, Mn(II)Pc (d^5) and Fe(II)Pc (d^6) correspond to the spin state of $S = 3/2$ and 1 [3, 128], respectively, whereas both Ni(II)Pc (d^8) and Zn(II)Pc (d^{10}) are diamagnetic [129]. The corresponding magnetic ground state is directly related to the electronic structure of the metal ion, determined by the relative energy alignments of the d-orbitals. In MPcs crystals, the five degenerate d-orbitals split into two degenerate (d_{xz}, d_{yz}), and three non-degenerate (d_x^2-d_y^2, d_z^2, d_{xy}) states, as a consequence of orthorhombic crystal-field splitting, due to strong axial ligands of the adjacent molecules. This results in a different ground state, ^3E_g, for Fe(II) in FePc crystals, instead of $^3A_{2g}$.

The magnetic properties of FePc have attracted much interest. Early magnetic studies suggested that α-FePc forms ferromagnetic coupling up to $T_c \sim 10$ K [3], whereas β-FePc behaves as a paramagnet [130]. On the contrary, MnPc displays antiferromagnetism in its α-phase [6], but switches to a ferromagnet for β-MnPc. Both MnPc and FePc are described as canted ferromagnets.

The dependence of molecular orientation on the type of magnetism displayed in the α- and β-phase of FePc and MnPc can be rationalized by the spatial variations between the two

phases, since the magnetic behaviour is a result of competition between different exchange mechanisms for the spin coupling in MPcs [66, 131, 132]. As discussed above, the stacking angle (φ), the displacement direction with respect to the MPc molecules stacked along the *b*-axis, and the distance between the parallel molecular column differ going from the α- to β-phase, as shown in Figure 1.16 (a) and (b). The stacking angle (φ), however, directly determines the distance between the magnetic ions within the molecular columns, and has a stronger impact on the magnetic coupling of MPcs, as seen in the case of CoPc, where the magnitude of the exchange energy is predicted to reach 400 K with a co-facial alignment between the two phthalocyanine molecules allowed by φ ~ 90° [66].

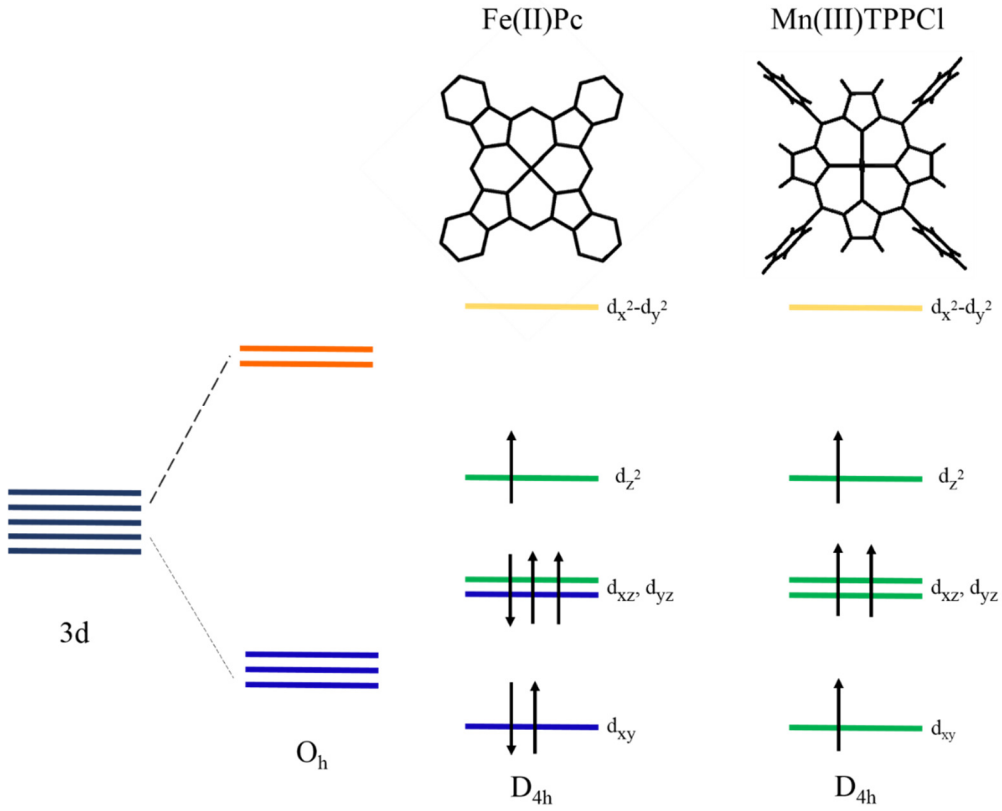


Figure 1.17 Schematics for the *3d* orbitals of the metal ions, and the electronic ground state of Fe(II)Pc and Mn(III)TPPCl, respectively.

In α-FePc crystals, Fe(II) ions couple ferromagnetically as linear chains along their *b*-axis, with presence of very weak antiferromagnetic inter-chain interactions, and the magnetic behaviour can be modelled by one-dimensional (1D) Ising chain [3]. The ZFC (zero-field cooled) - FC (field-cooled) temperature dependent magnetic studies on α-FePc crystals

observed bifurcation, suggesting irreversibility of the magnetization, a phenomenon similar to superparamagnetism and/or spin glass.

FePc displays easy-axis of magnetization along the plane (*xy*), with the magnetocrystalline anisotropy energy determined to be -1.18 meV [133]. X-ray magnetic circular dichroism (XMCD) suggests that the planar anisotropy of α-FePc orginates from the unusually large unquenched orbital moment [134]. The long range magnetic ordering for FePc is reflected by the hysteretic behaviour, $M(H)$, where the loop opens up at 2 K. The coercivity of FePc is influenced by the nature of the substrate, where the edge on orientation adopted by FePc on weakly interacting substrates is switched to face-on orientation when deposited on Au [135] or a thin layer of perylene-3,4,9,10-tetracarboxylic dianhydride (PTCDA). This has a strong influence on the field required to achieve saturation in the $M(H)$ curve.

Film texture and morphology are a crucial parameter for controlling the magnetic coupling. Films and nanostructures of FePc prepared by different fabrication methods have shown to give rise to different observed coercivities. The nanowires of FePc exhibit a coercivity up to 10000 Oe, attributed to the shape anisotropy [136], whereas increase in the FePc grain size in the films obtained at an elevated substrate temperature results in a larger coercivity compared to the film deposited at room temperature [137], suggesting the influence of the Fe spin chain lengths on the coercivity.

1.4 Thesis Layout

In the previous sections, a literature review on the molecular magnets that can be ideal candidates for spintronic applications is provided. Chapters of the thesis develop as follows. Chapter 2 covers the experimental methods applied to fabricate double-layers, co-deposited films and multi-layers, followed by introduction on the relevant *ex-situ* techniques to characterize the thin film properties.

Chapter 3 introduces the film properties of TCNQ, used in the following chapter as an acceptor to react with MnTPPCl to form charge-transfer complex. The chapter first begins with the optical, morphological and structural properties of the TCNQ films deposited on weakly-interacting substrates, and the influence of the TCNQ deposition rate on the film coverage and texture. Then, the effect of the nature of substrate on the growth of TCNQ is investigated by inserting a 20 nm thick PTCDA layer, which induces apparent changes to the

film morphology and structure adopted by TCNQ. On PTCDA, the island shape of TCNQ changes from a more croissant-like to rectangular. The molecular orientation adopted by TCNQ reduces from (022), (021) and (020) on weakly interacting substrates, to (020) as the only molecular orientation observed when deposited on PTCDA. The chapter provides a discussion to rationalize the effect of the underlying PTCDA on the structure of the templated TCNQ.

Before the studies on the co-deposited [MnTPPCl][TCNQ] films are presented, Chapter 4 first starts with the film properties of MnTPPCl grown by OMBD. The optical properties of the as-deposited MnTPPCl are characterized by UV/Visible spectroscopy, which reveals presence of both Mn(II) and Mn(III) contained in the film. The composition of the as-deposited MnTPPCl film is compared to the MnTPPCl powder by using XPS, suggesting dissociation of the axial Cl ligand takes place in the film deposition. The as-deposited film exhibits a very smooth and featureless morphology, with an amorphous structure determined by XRD. Owing to the Mn(II) present in the as-deposited MnTPPCl film, the optical properties of the MnTPPCl film are studied as a function of time.

Then, the properties of the co-deposited [MnTPPCl][TCNQ] are presented, and compared to those observed in the pure TCNQ and MnTPPCl films. While the optical spectrum displays absorption features predominately belonging to MnTPPCl, the peak for Mn(II) is not observed, and the absorption bands at at $\lambda = 785$ and 885 nm become present when co-deposited with TCNQ, attributed to the reduction TCNQ $\longrightarrow$ $TCNQ^{\bullet -}$. The charge transfer between the donor and acceptor molecules is verified by the shift in the CN stretching by using IR spectroscopy. The composition of the co-deposited [MnTPPCl][TCNQ] film is determined by XPS, and the magnetic measurement on the co-deposited film indicates presence of antiferromagnetic interactions due to the charge transfer dimer formed by the two different molecules.

In contrast to charge transfer interactions that form the donor-acceptor dimer in [MnTPPCl][TCNQ] films, Chapter 5 begins with a different strategy towards controllable coercivities in the molecule-based systems for spintronic applications. We investigate a diluted ferromagnetic system consisting of two different phthalocyanine molecules. It is expected that partial substitution of H_2Pc in the FePc film would lead to the molecular columns of FePc with a wide distribution of lengths for the spin chains in comparison to the neat FePc film. The properties of the mixed H_2Pc:FePc films are studied as a function of the

concentration of H_2Pc, which is identified as a parameter to tune the coercivity of FePc.

Finally, the film properties of FePc when utilized as spin injector/detector are studied, with an emphasis on the effect of the Al substrate on the structural and magnetic properties exhibited by the FePc film. The magnetic behaviour of FePc is relatively unaffected, though the texture and crystallinity of the film is clearly suppressed when deposited on the Al substrate. Inserting a thin layer of H_2Pc prior to growth of FePc on the Al substrate leads to increased coercivity and magnetic anisotropy, attributed to the improved crystallinity and organic-organic interface for deposition onto H_2Pc.

2. Experimental methods

2.1 Sample preparation

The morphology and structure of the molecular thin films are obtained by deposition onto single crystal (100) silicon and glass. Commercially available glass substrates are purchased from VWR as microscopic glass slides, whereas silicon substrates were used without removing its native oxide. For low-temperature magnetic studies, kapton (25 μm) was used as substrates, consisting of polyimide. Kapton is a light-weight and flexible substrate with an excellent thermal stability for a wide temperature range. Owing to broad optical transparency (500–4000 cm^{-1}), the vibrational spectra were obtained from films deposited on single crystal (100) potassium bromide (KBr), and the pellets were made by cleaving along [100]. Except for KBr pellets, grease and contaminants on glass, silicon and kapton substrates were cleaned by immersion in an ultrasonic bath in acetone and isopropanol for 10-15 min each, followed by air dried prior to loading them into the Organic Molecular Beam Deposition (OMBD) growth chamber.

2.2 OMBD growth

All the molecular thin films studied were fabricated by using Organic Molecular Beam Deposition (OMBD) (Figure 2.1), a technique stemming from Molecular Beam Epitaxy (MBE), allowing for accurate control over thin film deposition as well as minimal contamination, thanks to the high vacuum growth environment. *In-situ* monitoring of the film deposition is accessible by the equipped a quartz crystal microbalance (QCM). The multiple Knudsen cells included in the OMBD enable doping, co-deposition, and deposition of electrodes, and subsequently highly complex film architectures are readily attained.

The specific OMBD used here is a commercial unit, Kurt J. Lesker SPECTROS system, in which high vacuum (10^{-6} to 10^{-7} mbar) is achieved using a cryo-pump backed up by a rotary pump. The OMBD growth chamber is accommodated with a three shelves-cassette on which

substrates holders together with substrates are loaded, and therefore multiple film depositions can be achieved without breaking vacuum.

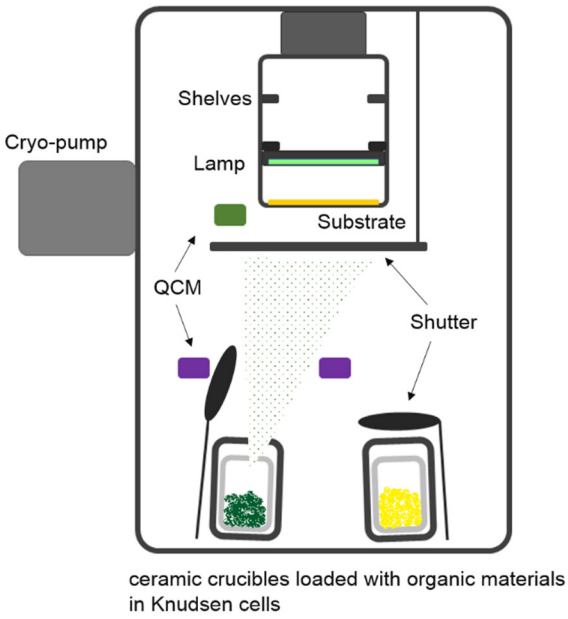


Figure 2.1 Schematic showing the OMBD growth chamber. The three-shelve cassette allows for multiple depositions and using a mask without breaking the vacuum, and the substrate temperature during the growth is controlled by the lamp. The distance between the substrate and the source is approximately 70 cm. The film homogeneity is optimized by rotating the substrate holder (cassette) during the deposition.

OMBD provides a substrate holder with 10 cm x 10 cm in size which allows for films with large area or deposition onto multiple substrates to be obtained; a mask can be used to define the area for the electrode/contacts if needed, while an aluminium mask that limits the film area to be deposited used for magnetic characterization is described in (2.4.7). The deposition procedure begins with pumping down the pressure of the OMBD growth chamber, and it is essential to obtain a satisfactory base pressure fulfilling the condition under which the molecular beam (flux) can be formed. Once the ideal base pressure is reached, the organic materials loaded in the ceramic crucibles need to be degassed by increasing the temperature stepwise with the source and substrate shutters closed (see Figure 2.1), gradually from room temperature to slightly lower than the sublimation temperature of the organic material. The purpose of degassing is to remove contaminants and/or residuals contained in the source

material so as to minimize inclusion of impurities into deposition. The rate for the source material is monitored by QCM placed close to the source shutter, and the deposition rate is achieved by heating for the source crucible, which is automatically adjusted by a feedback controlled loop provided by the particular OMBD system; as the deposition rate has reached the desired value and stabilized, the substrate shutter is opened to start the film deposition. During the deposition, the deposition rate, source temperature, substrate temperature and the thickness of the film that is deposited onto the substrate are recorded. After reaching the desired film thickness, the film deposition is stopped and the substrate shutter is closed.

2.3 Thickness calibration

In-situ

In-situ thickness calibration can be achieved by a quartz crystal microbalance (QCM), placed in the Organic Molecular Beam Deposition (OMBD) system close to the position of the source and substrate holder. QCM consists of a small piece of quartz crystal, which is very sensitive to the change of mass, and varies its vibrational frequency accordingly when molecules or other materials are adsorbed onto it. This allows us to monitor the deposition rate and film thickness during film deposition.

Ex-situ

In addition to QCM, a correction, tooling factor (TF), is needed and used in the growth recipe to correct the film thickness. While the measurement is extremely sensitive, the value read by the QCM cannot directly represent the actual film thickness. This is because the QCM cannot be too close to the substrate, or it would interfere with the deposition, and the geometrical errors results from the spatial arrangement of the QCM with respect to the substrate can be adjusted if TF is taken into consideration.

The TF of an unknown molecule X, TF(X) is calculated by comparing the thickness of a film grown with a TF that has already been calibrated, which is a reference, *e.g.* CuPc. To determine tooling factor for MnTPPCl, TF(MnTPPCl), the known tooling factor for CuPc, TF(CuPc) = 32, was employed to deposit MnTPPCl of two different nominal thicknesses,

which were found to be 100 nm and 50 nm, as shown by the QCM reading. TF(MnTPPCl) can then be related to the measured thickness, TF(CuPc) and the thickness read by the QCM and subsequently expressed as,

$$\mathrm{TF(MnTPPCl)} = \frac{\text{measured thickness} \times \mathrm{TF\ (reference)}}{\text{thickness read by QCM}}. \qquad (2.1)$$

The thicknesses of the MnTPPCl films measured using AFM were found to be 79.8 nm and 39.5 nm, respectively, and TF(MnTPPCl) can be derived. The relevant values are summarized in Table 2.1. The fact that two independent experiments lead to the same value of TF(MnTPPCl) indicates the experiments were consistent and reproducible, and therefore TF(MnTPPCl) = 25.4 was being used for all the MnTPPCl depositions.

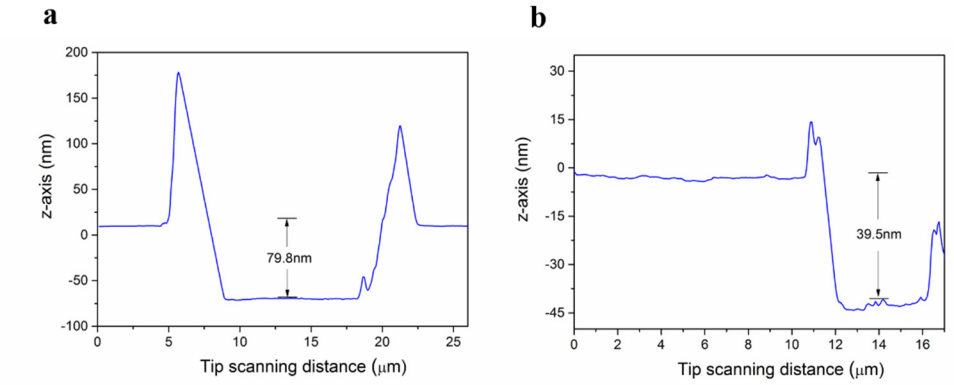


Figure 2.2 Profiles of cross-sections made on two MnTPPCl thin films on silicon, with their thicknesses measured by AFM, corresponding to (a) 79.8 nm and (b) 39.5 nm, respectively.

Table 2.1 Relevant values of the MnTPPCl films obtained from two film depositions.

AFM thickness(nm)	TF(CuPc)	QCM thickness (nm)	TF(MnTPPCl)
79.8	32	100	25.5
39.5	32	50	25.3

Calculating the deposition rates for MnTPPCl and TCNQ

In order to achieve a stoichiometry of 1:1 for the donor and acceptor molecules, MnTPPCl and TCNQ, during the co-evaporation process, the growth rates for MnTPPCl and TCNQ

were not 1:1. Instead, the rates were calculated to obtain equal amounts of molecules arriving at the substrate surface. The growth rates for MnTPPCl and TCNQ were derived in the following way:

Assuming the surface area is x^2 cm^2, the volume of the TCNQ thin film at the rate of 1 Å/s will be $10^{-8}x^2$ cm^3 per second. Therefore, the number of TCNQ molecules present in the film within this time frame will be,

$$\frac{1.315x^2 10^{-8}}{204.19} \cdot 6.02 \times 10^{23} \tag{2.2}$$

Similarly, the number of MnTPPCl molecules included in the thin film will be,

$$\frac{1.308x^2 10^{-8}}{703.11} \cdot 6.02 \times 10^{23} \tag{2.3}$$

Ratio between the TCNQ and MnTPPCl can obtained by dividing (2.2) by (2.3),

$$\frac{1.315x^2 10^{-8}}{204.19} \cdot 6.02 \times 10^{23} \div \frac{1.308x^2 10^{-8}}{703.11} \cdot 6.02 \times 10^{23} \tag{2.4}$$

The ratio between the number of TCNQ molecules to that of MnTPPCl is calculated to be 3.462:1, when the growth rate of 1 Å/s is used for both molecules on a substrate surface with an area of x^2 cm^2. Therefore, to obtain a 1:1 stoichiometry for co-deposited MnTPPCl and TCNQ thin films, MnTPPCl and TCNQ were grown at a rate of 0.9 Å /s and 0.26 Å/s, respectively.

Table 2.2 The deposition rates calculated for co-evaporation of MnTPPCl and TCNQ used in this work.

Molecules	Molecular Weight (g/mole)	Density (g/cm^3)	Tooling Factor	Growth rates (Å/s)
TCNQ	204.19	1.315(*obs.*); 1.329(*calc.*)	32	0.26, 0.13, 0.09
MnTPPCl	703.11	1.308	25.6	0.9, 0.45, 0.1

2.4 Ex-situ Characterizations

A variety of *ex-situ* techniques were applied to study the spectroscopic, morphological and structural properties of the molecular thin films. The optical absorption of the MnTPPCl films was characterized by using UV/Visible spectroscopy. The vibrational properties and the core-level electronic structure of the MnTPPCl, and the co-deposited [MnTPPCl][TCNQ] films were investigated by Infrared spectroscopy (IR) and X-ray Photoelectron Spectroscopy (XPS).

The morphologies of the films are obtained by scanning electron (SEM) and atomic force microscopies (AFM); the former provides quick morphological characterization on a relatively large surface, whereas the latter can access rich morphological details such as the grain height and surface roughness of the film. Structural characterization of the single layers and multi-layered structures, including TCNQ deposited on substrates pre-coated with PTCDA and FePc/Al, was performed by using X-ray diffraction (XRD). Finally, the magnetic properties of the co-deposited [MnTPPCl][TCNQ] film and FePc layers in the multi-layered structures were characterized by Superconducting Quantum Interference Device (SQUID) magnetometry.

2.4.1 UV/Visible Absorption Spectroscopy

Electromagnetic waves interact with matter in many ways. When irradiated by incoming light with a wavelength, λ, a molecule can be promoted from its ground state, S_0, to an excited state, S_1, which is known as an excitation (transition). There are several possible pathways for the excited molecule to return to its original ground state, and in general can be referred to radiative or non-radiative relaxations. In radiative relaxation, light can be re-emitted by the excited molecule as fluorescence if the relaxation first proceeds with internal conversion between the different excited states, *e.g.* the excited molecule undergoes transition from S_2 to S_1 (singlet), before eventually returning to S_0. The excited molecule can emit phosphorescence if it undergoes intersystem crossing to T_1 (triplet). On the other hand, in non-radiative relaxation the molecule decays to its original ground state, with the energy between the excited and ground state released in the form of heat, through dissipation or thermal exchange with the environment. These processes can be summarized in a simplified

version of a Jablonski diagram. An excitation can occur only when the energy of the incoming light corresponds to the difference between different energy levels (*e.g.* the ground and excited states), but in reality the likelihood to observe a particular transition is governed by the selection rules [138].

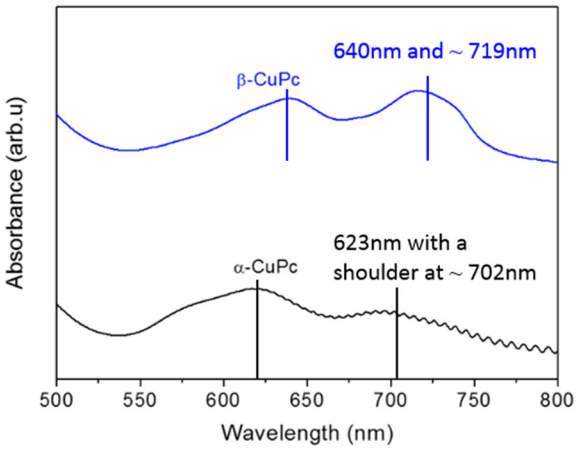


Figure 2.3 Optical absorption spectra of α- and β-CuPc on kapton substrate. Note that the high frequency oscillations on the α-CuPc are due to the substrate.

Beer-Lambert Law

A large number of organic molecules can absorb electromagnetic radiation in wavelengths between 190 and 800 nm, and the optical spectrum that observes transitions arising from absorption of radiation in this range are mostly related to electronic transitions, most probably due to chromophore being excited from the highest occupied molecular orbital (HOMO) to the lowest unoccupied molecular orbital (LUMO). The absorption intensity can be expressed empirically known as Beer-Lambert Law, as below,

$$A = log\left(\frac{I_0}{I}\right) = \varepsilon cl \quad \text{for a given wavelength} \tag{2.5}$$

, where A is absorbance, I_0 and I represent the intensities of the light irradiated on the sample and leaving the sample, respectively. ε stands for the molar absorptivity, c is the concentration of the sample in molarity [M], and l is the sample cell length [138]. Thus, at a given wavelength the absorbance is proportional to the molar concentration in ideal solutions (*i.e* dilute solution so as to reduce the interactions between the molecules).

The Beer-Lambert law given in (2.5) can be expressed as (2.6), which is a more general form and can be applied to thin films,

$$A = \alpha l \tag{2.6}$$

where the absorbance is related to the absorptivity of the film (α) and the film thickness (l). Due to the broadening and splitting in the absorption peaks in the solid state, as discussed below, it is more accurate to use integral of an absorption band.

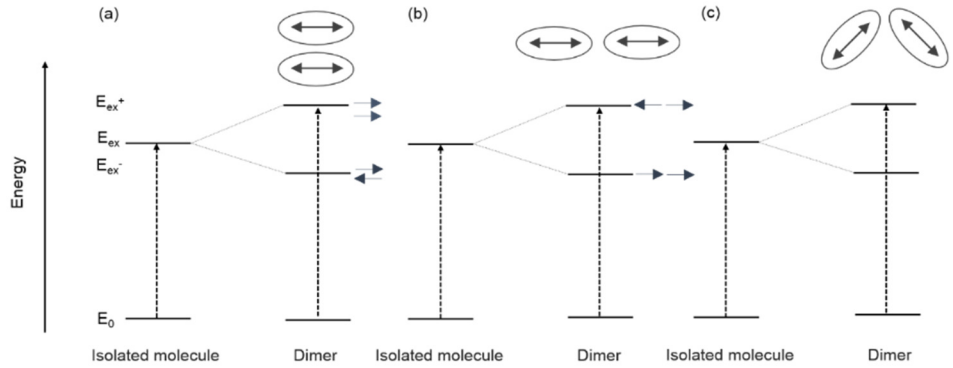


Figure 2.4 Davydov splitting, adapted from [139].

Solid state spectroscopy

Molecules with chromophores in solid state can display absorption spectra slightly different from those obtained from the solutions. Shifts or splitting of a specific absorption band, are mostly attributed to a different environment the molecules experience in contrast to that in the gaseous or liquid phase. In the gaseous phase, the average intermolecular distance between the molecules is rather large, and often the corresponding optical spectrum of a single molecule is observed. In the solid state, the short intermolecular distance between the molecules can lead to two excited molecules forming a dimer, resulting in splitting of the excited states, known as Davydov splitting [139]. This effect largely depends on the geometrical orientation of the transition dipoles associated with the excited molecules, as depicted in Figure 2.4, where three different orientations are possible, corresponding to (a) edge-to-edge, (b) head-to-tail and (c) an oblique orientation, subsequently leading to a blue, red-shift and splitting in the absorption band.

Practical details

The optical spectrum of the films are recorded from Perkin Elmer Lambda 25 UV-Vis spectrometer in the wavelength of 300 to 1000 nm and the step size is 4 nm.

2.4.2 Infrared Spectroscopy

For wavelengths between 2.5 and 15 μm the electromagnetic radiation are referred as infrared, and absorption of radiation in this range correspond to the vibrational frequencies, such as stretching or bending of molecules. Radiation in the absorption spectrum in the infrared range is commonly expressed in terms of wavenumber (cm^{-1}).

Absorption of infrared radiation can only occur for molecules with bonds that have dipole moments which change as a function of time. If the frequency of an incoming radiation matches with the natural vibrational frequency of a specific bond within the molecule, then the radiation can be absorbed and increases the amplitude of the vibration.

Common vibrational modes exhibited by molecules include stretching and bending, which are IR-active. The normal modes of a molecules, consisting of N atoms, can be calculated by,

$$3\mathrm{N}-5,\ \text{linear molecules, and}\ 3\mathrm{N}-6,\ \text{non linear molecules} \qquad (2.7)$$

In addition to the fundamental vibrational frequencies discussed above, overtones can arise from combinations of multiple or integral numbers of vibrations. Since the vibrations are associated with bonds, absorption of radiation can be related to the bond strength, and the natural frequency of a vibration, $\tilde{\nu}$, can be expressed as following,

$$\tilde{\nu} = \frac{1}{2\pi c}\sqrt{\frac{K}{\mu}},$$

$$\mu = \frac{m_1 m_2}{m_1 + m_2} \qquad (2.8)$$

, where the stiffness of the bond is represented by K (force constant), and μ corresponds to the reduced mass of the two bonded atoms (m_1 and m_2).

Attenuated Total Reflectance (ATR)

Attenuated Total Reflectance (ATR) is a non-destructive technique to obtained infrared spectra, and as opposed to transmission infrared spectroscopy, no modifications to the samples are required, which are ideal for molecular thin films.

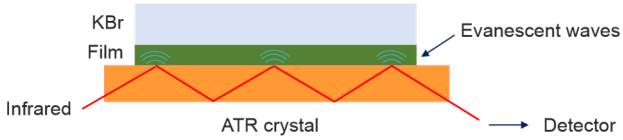


Figure 2.5 Schematics for ATR-IR.

This technique is based on total internal reflection, and when the condition for total internal reflection is satisfied an evanescent wave is generated, which penetrates to the sample (the films) and the infrared radiation with appropriate frequencies can be absorbed.

$$\theta_c = sin^{-1}\ \frac{n_2}{n_1} \tag{2.9}$$

, where θ_c is the critical angle, n_1 and n_2 are the refractive index of the total internal reflection element and that of the sample, respectively. As the evanescent wave penetrates the interface, the amplitude of the electric field decays and the penetration depth, d_p , is given as below,

$$d_p = \frac{\lambda_1}{2\pi(sin^2\theta - n_{21}^2)^{1/2}} \tag{2.10}$$

In ATR-Infrared spectroscopy the total internal reflection element is made with crystals with a high refractive index, and the sample is brought in close contact to the crystal.

Practical details

The IR spectrum of the films are recorded from Nicolet™ iS™10 FT (Fourier Transform)-IR spectrometer, which consists of an IR source (Electronically Temperature Controlled (ETC), EverGlo* IR, white light), beam splitter (KBr) and photodetector (DTGS KBr). A reference spectrum is required to obtain the spectrum of the sample, since in FT-IR the

interferogram contains the spectrum of the sample minus the source. Prior to the experiment, the interferogram recorded from the background (air and moisture) was collected, and the reproducibility of the spectrum was confirmed by using a reference sample, polyethylene, with its known spectrum. The spectrum of the molecular films were collected in the wavenumber of 500 to 3000 cm^{-1} with a step size of 4 cm^{-1}, while the number of scans was set to 64 in each measurement so as to improve the signal to noise ratio.

2.4.3 X-ray photoelectron Spectroscopy

X-ray photoelectron spectroscopy (XPS) is a spectroscopic technique widely used for studying the elemental compositions of solid samples. Irradiation of photoelectrons onto solid samples can penetrate several μms in depth, yet only electrons close to the surface of the sample will not be re-absorbed. The absorption of the incident X-ray by the medium is determined by the Beer-Lambert's law (2.11),

$$I_s = I_0 \, e^{-d/\lambda} \tag{2.11}$$

where I_0 corresponds to the electrons produced per unit time, whereas I_s is the electrons that reach the surface per unit time. d and λ are the sampling depth and the mean free path of the electron, which follows the universal curve (the plot of escape depth of the electron as a function its kinetic energy) and is thus element-specific [140]. Approximately 95% of the photoelectrons are absorbed by the medium when d is close to 3 λ. As a consequence, XPS is a surface sensitive technique which examines materials up to ~10 nm in depth.

The principle of XPS is based on the photoelectric effect, where the incoming photoelectrons with energy hv eject the electrons in the bound state of the elements constituting the sample, leaving the surface with kinetic energy KE. The work function of the spectrometer φ is around 4-5 eV, and the binding energy, E_B, of the ejected electron can be related to Koopman's theory, as below,

$$KE = hv - E_B - \varphi \quad . \tag{2.12}$$

Since the binding energy is element-specific, XPS allows for identification of the elemental composition of the sample, and the chemical state of a particular element is revealed from the chemical shift in the binding energy. The peak shape depends on the angular quantum

number, *l*, of the electrons that are emitted, and exhibits multiplets due to spin-orbit splitting. Finally, the peak ratios between different elements present in the XPS spectrum enables quantitative analysis. While in principle the absorption of irradiation resulting in electrons emitted with *K.E* should follow the Koopman's theory, in reality the process is extremely rapid, which can give rise to additional shake-up features in the XPS spectrum [140].

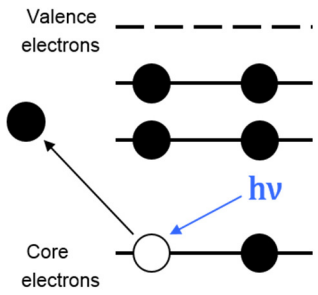


Figure 2.6 Schematic depicting the photoelectric process in XPS.

XPS requires an ultrahigh vacuum environment so as to minimize surface contamination, and the specific model used in this work is a Thermo Scientific k-Alpha XPS, with a typical base pressure of ~ $2x10^{-9}$ mbar. The incident X-ray of Al corresponding to a photo energy of 1486.6 eV was irradiated onto the samples, with a spot size of 400 μm^2.

2.4.4 Scanning electron microscopy

Scanning electron microscopy (SEM) (JEOL LEO 1521) was used to assess the surface morphology of the MnTPPCl and TCNQ layers (plane-view) and evaluate the film structure as well as thickness of the single layer (cross-section). SEM is a very useful tool to study the topography of a wide range of samples, ranging from metals to biological materials. In SEM, the morphological information of a sample is obtained by the way the sample interacts with electrons.

A high energy electron gun ranging between 1 keV to 40 keV is used to irradiate the sample, and subsequently various scenarios are possible, including X-rays, Auger electrons, primary backscattered electrons, secondary electrons and cathodoluminescence, and amongst all, the backscattered electrons as well as secondary electrons contain useful information

about the surface morphology of the sample.

Since the images generated by SEM are caused by the interaction between electrons and the sample, insulators will not be appropriate for SEM imaging, and the sample will be severely damaged by charging from the electron beam. This problem can in principle be by-passed by pre-coating a thin layer of metal to improve the interaction between the electrons and the sample. Due to the considerably low electrical conductivity of the molecular thin films, a thin layer of chromium was coated on the thin films using a sputtering coater prior to SEM imaging to reduce charging in the sample and improve the image quality. In addition, during the imaging, 5 kV was set for the electron gun to avoid damaging the molecular film.

2.4.5 Atomic force microscopy

The atomic force microscopy (AFM) allows us to obtain morphological details with a resolution down to a few tens of nanometers. The fundamental principle of the operation of AFM is that as the length-scale approaches the atomic level, the interaction between substances such as the attractive and repulsive forces become more apparent within a very small distance. In AFM attractive or repulsive forces induced by interaction between the tip and the sample can be used so that information on the surface appearance (height, amplitude and phase) can be collected. Thus, AFM is a non-destructive technique and suitable for probing a wide range of materials, including insulators, biomaterials, such as DNA, and liquid. Additionally, operation of AFM at ambient conditions and no sample preparation is required prior to scanning processes.

Several atomic forces can occur in between the AFM tip and substrate, and whether it is attractive or repulsive depends on the distance between the two. When the distance between the tip and substrate is long, the resulting forces tend to be attractive, *e.g.* Van der Waals and capillary, whereas repulsive forces are dominant for short distances. In AFM, a tip mounted onto a cantilever spring is used to probe by scanning across the substrate surface, in which the cantilever spring controlled by the reflection of a laser beam from the mirror can detect the deflection. During the scan, the probing tip is kept at a fixed height along the *z*-axis away from the substrate surface and horizontal movement of the tip along the surface is in the *xy*-plane. When the attractive (or repulsive) force between the probing tip and substrate surface is too large, the tip will be attracted to (repelled from) the surface and cause the cantilever to

bend, resulting in a deflection in the *z*-axis. Then, a decrease or increase in the deflection along the *z*-axis would be collected and transferred to a photo diode detector, which can be processed by the computer to image the substrate topography.

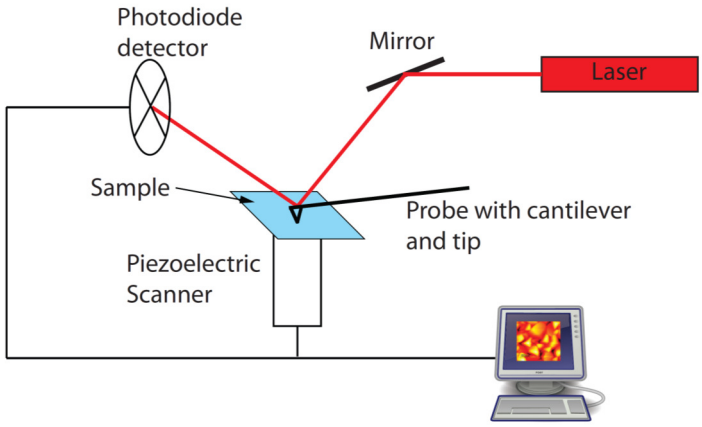


Figure 2.7 Schematics of atomic force microscopy.

The changes in the force detected during an AFM scan can be expressed by the force constant of the cantilever spring, as below,

$$\Delta z = \frac{\Delta F}{c} \tag{2.13}$$

, where the deflection Δz is determined by the acting force ΔF and the spring constant c.

Different modes are available in AFM, including contact, non-contact and tapping mode. Operation of contact mode is in the repulsive regime, and during the scanning process the surface may be damaged or changed, owing to the forces applied by the tip towards the substrate. On the other hand, oscillations of non-contact is operated in the attractive regime, and as a consequence the tip would not be in contact with the surface. The operation of the tapping mode is somewhat in between the contact and non-contact mode. During the scanning contact between the tip and surface is only for a short time periodically then removed from the surface, and the cantilever oscillates slightly below its resonance frequency, defined as,

$$\omega = \omega_0 \sqrt{1 + \frac{1}{k}\frac{dF}{dx}} \tag{2.14}$$

where *k* is the spring constant and x for cantilever deflection. ω and ω_0 correspond to the oscillation frequencies at the resonance and during the scan. Tapping mode becomes popular for AFM uses, because the vertical movement (tapping) by the tip significantly reduces the lateral forces the tip experiences when scanning across the surface, with improved stability in comparison to non-contact mode.

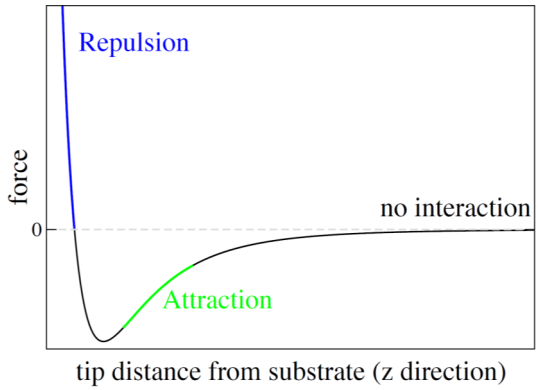


Figure 2.8 Typical behaviour of the force an AFM tip experiences as a function of distance to the substrate.

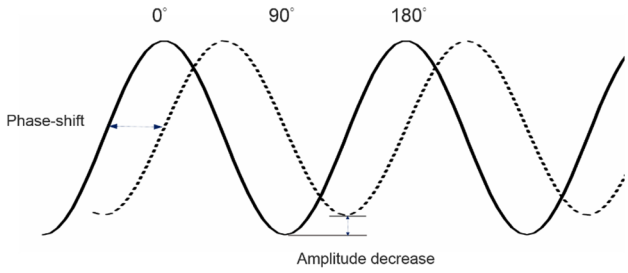


Figure 2.9 The effects of free oscillations (black solid curve) and oscillations on surface (black dashed curve) experienced by the tip, adopted from [141].

The resolution that AFM can attain is 0.1 nm [141] but the absolute resolution is directly determined by the sharpness of a tip. Based on the height data collected by AFM, with the software analysis the height, volume, size and roughness of a feature can be easily measured from the generated AFM image by using software analysis. In addition to height data, amplitude and phase data are simultaneously obtained (see Figure 2.9). During the scanning process, the tapping mode AFM records the phase shift signal between the oscillations. It was

thought the phase images could reflect viscoelastic properties and adhesion forces of the materials, but other factors, such as differences in slope, can lead to phase contrast, which is actually related to energy dissipation between the tip and surface [141].

Practical details

For the molecular films studied in this work Veeco (Dimension 3100, tapping mode) was used to collect images of the surface morphology, with the cantilevers/tips coated with Al (resonance frequency, 320 Hz), and the image is typically obtained at a scan rate between 0.3 to 0.9 Hz.

2.4.6 X-ray diffraction

The structures of the molecular thin films were determined by using powder X-ray diffraction (XRD) using Ni filtered Cu Kα radiation at 40 kV/40 mA. Crystals are solids with sets of points that form repetitive patterns, which are called crystal lattices. Owing to the periodicity, it is possible to reduce the crystal structure to an irreducible unit cell: in this way, any crystal structure can be represented by its unit cell. To define a unit cell, three vectors and three angles are assigned. These six parameters are crucial for crystallography, of which a crystal structure can be represented systematically. In crystallography, a plane that contains non-collinear lattice points is called a lattice plane, and as the lattice plane intersects with the axes of the unit cell, the corresponding reciprocals of the intercepts between *a*, *b* and *c*-axes are therefore 1/*a*, 1/*b* and 1/*c*, defined as Miller indices, *h*, *k* and *l*, accordingly.

Bragg Diffraction

Constructive interference occurs as the incident beam of the X-ray with respect to the lattice plane satisfies Bragg's law,

$$n\lambda = 2d_{hkl}\, sin\, \theta \tag{2.15}$$

where n is an integer, λ is the wavelength of the incident light, θ is the angle between the incident light and d_{hkl} is the interplanar spacing.

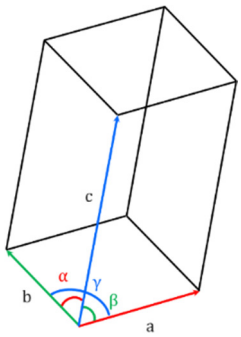


Figure 2.10 Schematics of a 3D unit cell structure with the crystal axes.

Powder X-Ray Diffraction

Powders consist of mostly randomly oriented crystallites, and when irradiated with an incident beam of X-ray each of the crystallites diffract independently, and, inside the crystallites planes that satisfy Bragg's law are unlikely to reflect at the same time. This explains why sometimes more diffractions peaks can be observed for the powder sample in contrast to single crystals.

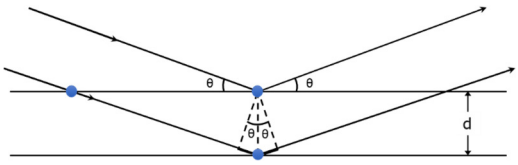


Figure 2.11 Illustrating Bragg's law for reflections from the planes in a crystal.

Thus, for powder samples, any possible lattice planes inside crystallites that meet Bragg's law can give rise to the same reflection of a certain wavelength of X-ray, resulting in a diffraction pattern of a cone of 90°-θ. The total diffraction pattern produced by a set of planes inside crystallites will be a set of cones. The diffraction pattern is recorded by a cylindrical camera with a film strip, where each of the reflected cones appears as a pair of arcs. The arcs provide information on the crystal structure and allow us to calculate approximate Bragg's angles. The diffraction lines on the film indicate the inter-planar spacings, known as the *d*-spacing. Lattice planes with the same *d*-spacing diffract at the same Bragg angle. As a

consequence, the line corresponding to each lattice plane can be resolved so that the indices of the planes can be determined.

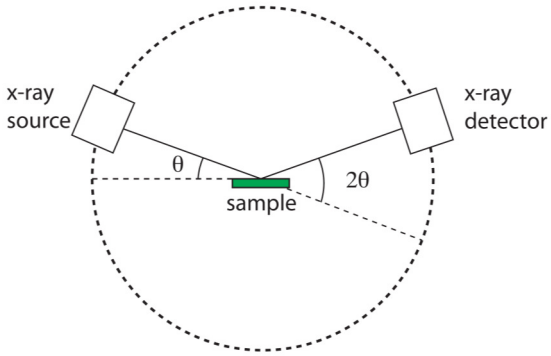


Figure 2.12 Schematics of an X-ray diffractometer with Bragg-Brentano geometry.

The structure of the molecular films were determined by using Philips X'Pert PRO PANalytical diffractometers, with filtered Cu K_α radiation, operated in the $\theta - 2\theta$ mode. Typical scans were recorded between 2θ = 5-30° (films on glass substrates) and 5-35° (films on silicon and kapton substrates) with a step size of 0.033° and 50 second per step or 120 second per step for films with a thickness below 50 nm.

Determination of crystallite sizes

Diffraction patterns from powder samples are subject to broadening effects, including widths and heights of the slit for the incident radiation, the wavelength and so on. Broadening of the peak can result from temperature during the measurement, strain, inhomogeneous composition, and the size of the diffracting crystallites along the direction normal to the diffracting plane, known as particle-size broadening. This applies to crystallites with size between 300 to 2000 Å [142], beyond which the size effect is negligible. Therefore, analysis of the XRD results allowed us to estimate the crystallite sizes in the molecular thin films, as other factors are negligible or can be corrected (instrumental broadening).

The size of the crystallites can be deduced by using the Scherrer equation,

$$\mathrm{D} = \frac{\mathrm{K}\lambda}{\mathrm{W}_{2\theta}\cos\theta} \tag{2.16}$$

, where D is the crystallite size, θ is the Bragg angle at a given wavelength, λ. K is a constant, with a value that depends on the shape of the diffracting crystallites. For spherical shaped crystallites, K is equal to 0.9, and for approximate determination a series of crystallites K can be assumed to be 1, which is used in this work. The width, $W_{2\theta}$, which is in units of radians, should take into account the effects from instrumental broadenings, W_{inst}, whose values are determined from measurements of single crystals and corresponds to 0.08 and 0.13 for the range of $5 < 2\theta < 10$ and $25 < 2\theta < 30$ resepctivley. The peak width W_{obs} is estimated from the FWHM extracted by fitting the peak profile with a Gaussian function, and to account for the uncertainty in the grain size deduced by using the Scherrer equation both (2.17) and (2.18) were used, with K = 1

$$W_{2\theta} = W_{obs} - W_{inst} \tag{2.17}$$

$$W_{2\theta}{}^2 = W_{obs}{}^2 - W_{inst}{}^2 \tag{2.18}$$

Texture Coefficients

In addition to the diffracting planes and crystallite sizes, the XRD θ-2θ scans provide another quantitative measure of the film texture and orientation, the texture coefficients (TC), which can be calculated as the following expression [142],

$$TC_{hkl} = \frac{\frac{I\,(hkl)}{I_0\,(hkl)}}{\frac{1}{n}\sum_i^n \frac{I\,(hkl)_i}{I_0\,(hkl)_i}} \tag{2.19}$$

, where $I(hkl)$ is the intensity from the (hkl) plane observed in the XRD spectrum of the molecular film, I_0 (hkl) corresponds to that diffracted intensity from the (hkl) plane in a fully randomly oriented powder samples, and n is the number of reflections considered. The (hkl) plane would be a preferential molecular orientation if TC(hkl) is calculated to be greater than unity.

Texture analysis

While the XRD diffraction obtained by using Bragg-Brentano geometry (θ-2θ) reveals the presence of diffracting planes parallel with respect to the substrate, the signal is in fact

diffraction arising from a spread of planes slightly deviated away from the horizon up to ± 10°. A more accurate determination on the preferential orientation of the molecular films can be achieved by performing the texture mode, which is known as Schulz reflection technique [142]. Diffraction of the sample is obtained at a fixed 2θ (Bragg angle, which can be determined by Bragg-Brentano geometry (θ-2θ), as discussed above), placed in parallel with respect to the plane normal to the pathway formed by the incoming and outgoing X-ray beams, as shown in Figure 2.13. The diffraction pattern recorded by tilting the sample in out of the plane fashion by ψ gives rise to a ψ-curve, whose full width half maximum (FWHM) can be considered as a quantitative measure for the average tilting of the diffracting planes at 2θ. The Schulz reflection technique also allows for pole figure measurements.

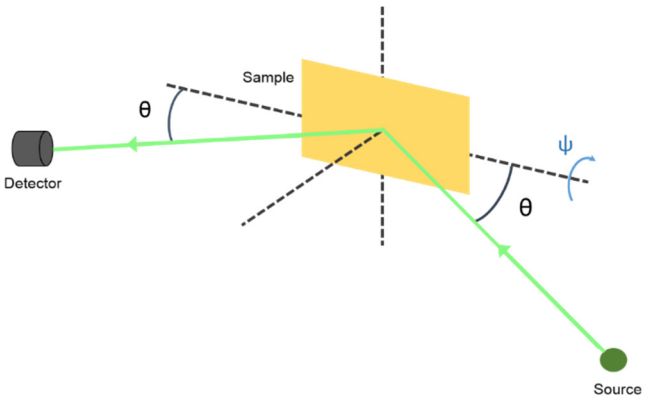


Figure 2.13 Schematics depicting the texture mode provided by XRD with Schulz geometry.

A Philips X'Pert MRD PANalytical diffractometer, with filtered Cu K_α radiation, and the texture mode (40 kV, 40 mA) was used in this work, and the step size is 0.5° and 100 second per step.

2.4.7 Superconducting quantum interference device (SQUID) magnetometry

In this work the magnetic properties of the molecular films are investigated by using Superconducting Quantum Interference Device (SQUID) magnetometery, Quantum Design MPMS-7. Most of the magnetometers nowadays are based on induction techniques, and

detection of magnetization is through the induced current caused by changes in the magnetic flux, based on Faraday's law. The magnetization of the sample is detected by a series of pickup coils, known as gradiometers (see Figure 2.14). The generated current induced by the moving sample that flows through the coils processed as induced voltage, and with the fitting software, MPMS MultiVu, the voltage can be related to the magnetic moment of the sample.

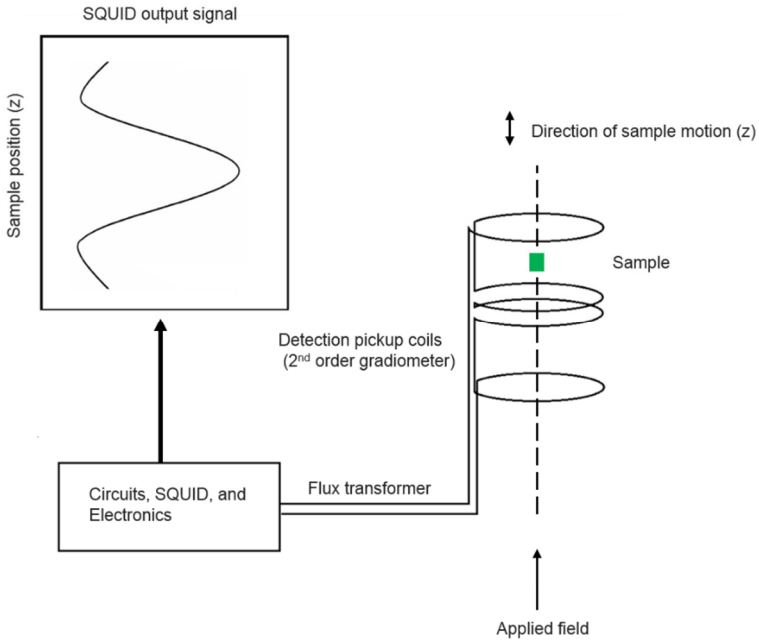


Figure 2.14 Schematics showing the SQUID magnetometry.

MPMS-7 utilizes a second-order gradiometer, consisting of N set of loops and 2N set of loops in the center (as shown in Figure 2.14) wound in the opposite direction to that of N set, sensing the gradient change in the magnetic flux generated by the sample. SQUID enables accurate and sensitive magnetic measurements, with sensitivity down to 10^{-8} emu [143]. Temperature control in SQUID allows for measurements to be performed in the range of 1.8 to 400 K, and the magnetic fields that can be applied in the range between ± 7 Tesla. The superconducting components, magnets are in the cryogenic part of SQUID, where the low temperature regime is attained by a helium bath inside the system. The helium consumption is preserved by the combination of nitrogen and vacuum shield.

The sample is attached to a sample rod that is inserted inside the sample chamber between the pickup coils as well as the magnets. During the measurements the sample is oscillated by

a linear motor along the direction of the applied field, in between the first and middle set of coils (see Figure 2.14). The sample geometry plays a crucial role and can affect the magnetization that is measured by SQUID, which assumes the sample as a point dipole, and to avoid magnetic artefacts an ideal sample size should not be larger than 5 mm. In MPMS-7 induced voltages can be obtained by two different modes, corresponding to DC, direct measurement, and Reciprocating sample option (RSO), in which the obtained signal is averaged over measurements of the sample oscillated along several centimeters, typically 1 Hz; in this way the RSO mode eliminates the noises and provides better sensitivity and was used for the magnetic measurements used in this work.

Sample Preparation and Mounting

A SQUID magnetometer can measure samples from powder to films, which however require different sample preparation and mounting procedures. For the powder sample, MnTPPCl is weighed and placed carefully into a gelatine capsule packed with glass wools to secure the powder from displacement during the measurement, as shown in Figure 2.15. The capsule then is loaded into a clean plastic straw, and held by two additional straws cut of the same length (approximately half length of the straw) from both side. This way of sample mounting is to fix the position of the capsule and minimize the diamagnetic background signal from the plastic straw.

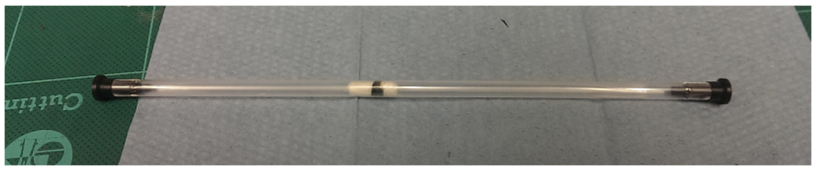


Figure 2.15 powder sample for SQUID measurement.

The films of co-deposited [MnTPPCl][TCNQ] and FePc are deposited onto kapton substrate with a thickness of 25 μm, cut with a size approximately 14 cm in length and 9 cm in width, respectively, as shown in Figure 2.16. The size and shape of the film needs to fulfil the geometry requirement by SQUID, and subsequently the film area can be defined by using an aluminium mask during film deposition, resulting in a strip of a size approximately 3 mm in width and 9 cm in length. This method ensures signals arising from kapton substrate, which

is diamagnetic, uncovered by the film, can be minimized. The film deposited on kapton is then rolled and inserted into a plastic straw, and placed carefully in the center. This way of sample mounting should produce magnetic signals primarily due to the molecular film during the SQUID measurements, only introducing very minimal background signals, assuming a homogeneous composition in the plastic sample straw as well as that of kapton [132].

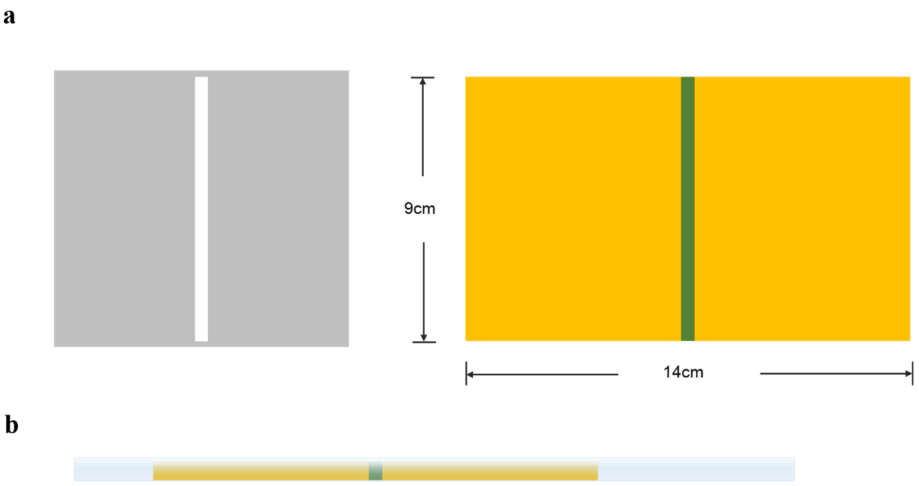


Figure 2.16 SQUID sample preparation (a) left: a mask to delimit the area where film is deposited; right: the film (green) deposited on the kapton substrate (yellow), and (b) the film on kapton rolled and inserted into the sample straw.

Magnetic measurements

Magnetic characterization of the molecular films consists of two types of experiments; magnetization as a function of the applied field, $M(H)$, and as a function of temperature $M(T)$, respectively. The former reveals magnetic signatures such as saturation moment, remanence and coercivity if the film exhibits a hysteretic behaviour. For each measurement, the sample is warmed up to 150 K which is above the ordering temperature for MPcs then cooled down to a desired temperature with the magnetic field applied; before each scan, the magnet is reset to minimize the effects of the remanent magnetic field. Calibration for the SQUID magnetometer is routinely performed by measuring a palladium (Pd) pellet with its known magnetic characteristics so as to be used as a reference sample. Whilst a geometrical difference between the Pd reference sample and the films in this study, it appears that the geometry factor has no observable and/or detectable magnetic signals, since our previous

studies following the same calibration procedure prior to the magnetic measurements have shown that the magnetic properties of CoPc observed in the powder form are retained in films [66]. Two protocols were used to measure temperature dependent magnetization, $M(T)$, corresponding to Zero-field cooled (ZFC) and Field Cooled (FC). For the former, the sample placed inside the SQUID is cooled down from 150 to 2 K in the absence of the applied field and the magnetization as a function of temperature is measured under a specific applied field. In the case of FC, the sample is cooled down at a constant field. Results of $M(T)$ allow one to calculate magnetic susceptibilities, and reveals history-dependent magnetic behaviours present in the sample, as difference in the ZFC and FC measurements can indicate presence of canted antiferromagnetic/ferromagnetic systems, dipolar (inter-chain) interactions, slow relaxation processes and spin-glass behaviours [144]. In order to calculate the magnetic susceptibility a choice of the applied field for $M(T)$ measurements is made by inspecting the linear regime of the $M(H)$ curve, described by the expression in (2.18)

$$\chi(T) = \frac{\partial M}{\partial B} \cong \frac{1}{\mu_0}\frac{\partial M}{\partial H} \cong \frac{1}{\mu_0}\frac{M_{H_1}(T) - M_{H_2}(T)}{H_1 - H_2} \tag{2.20}$$

, where M and B are the magnetization and magnetic flux density, respectively, μ_0 is the magnetic permeability in vacuum and dimensionless in SI units. For this work the magnetic flux density is approximated to the applied field, ($B \cong \mu_0 H$), and often the field found for $M(T)$ measurements is reasonably weak yet large enough to give rise to reliable signal detected by SQUID.

All the magnetic data presented in the thesis here are expressed in units of μ_B; the molar magnetization M is divided by a mole Bohr magneton ($N_A\mu_B$ = 5584.9 emu/mole) and the magnetic susceptibility can therefore be represented in unit of μ_B. The diamagnetic corrections for the co-deposited [MnTPPCl][TCNQ] films [145, 146] and FePc films [129] were used prior to data analysis.

3. TCNQ thin films

This chapter presents the strongly negative electron acceptor, TCNQ, selected to form the charge transfer salt [MnTPP][TCNQ]. Compared to MnTPPCl, the much lighter molecular weight of TCNQ requires a lower sublimation temperature, and in turn influences the way molecules are adsorbed and deposited onto substrates, giving rise to the growth behaviours significantly different from what characterize planar polyaromatic macrocyclic compounds (e.g. transition metal phthalocyanines). Substrate-adsorbate interaction plays a dominant role in determining the preferential orientation in the molecular films, as already seen as in PTCDA/Pcs. Such an influence is expected to be stronger in the case of TCNQ, whose growth is characterized and the effects of the nature of the underlying substrate on the film properties are investigated. Deposition of TCNQ on weakly-interacting substrates results in inhomogeneous coverage of spiral-shaped islands, with three preferential orientations (022), (021), and (020). Inserting a PTCDA first layer is shown to switch the island shape and molecular orientations adopted by TCNQ, changing from the spiral contour to rectangle, with only the (020) orientation observed in the templated film.

3.1 TCNQ on the weakly interacting substrates

3.1.1 UV/Visible spectroscopy of the films

The optical spectrum of the 80 nm thick TCNQ film grown at the rate of 0.37 Å/s, shown in Figure 3.1, consists of absorbance across the entire range wavelengths of visible lights, and a broad peak between 450 and 500 nm, very similar to what is reported for the films obtained by vacuum evaporation [147]. Presence of the former in the absorption spectrum is caused by the effect of interference with scattering, suggesting the surface contains clusters or particles with a size small and/or large relative to the wavelength used in the UV/Visible spectroscopic measurement [148]. The broad peak at ~ 450 to 500 nm is assigned to the single

transition of TCNQ, slightly red-shifted from the peak~ 400 nm exhibited by the solution spectrum, [83, 86].

While very little change on the peak position and shape can be observed when increasing the deposition rate of TCNQ from 0.37 Å/s to 1.0 Å/s, the slight increased absorbance between 300 nm to 500 nm is obtained for the film with the same thickness deposited at a higher rate, suggesting the influence of the rate on the film homogeneity and the absorption maximum when depositing on glass substrate.

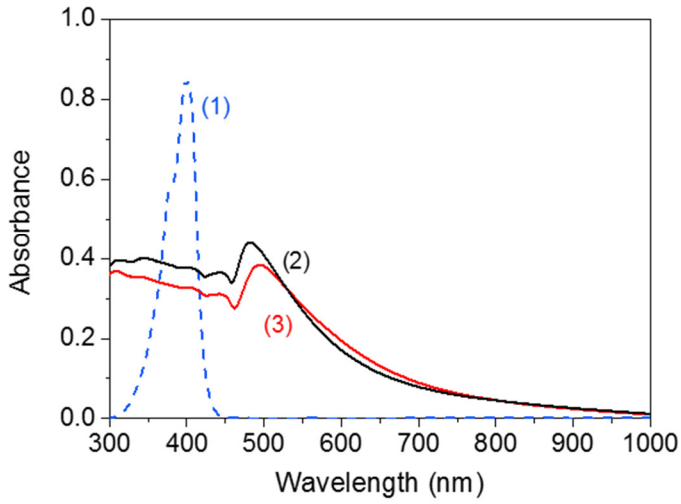


Figure 3.1 Optical spectra of (1) TCNQ solution in dicholoromethane (DCM) with a concentration of .5x10^{-3} M, 80 nm thick TCNQ films deposited on glass at the rate of (2) 1.0 Å/s, and (3) 0.37 Å/s, respectively.

3.1.2 Morphology and structure of the films

The appearance of the TCNQ films deposited at the rate of 0.37 Å/s and 1.0 Å/s is obtained by optical microscopy. At the rate of 0.37 Å/s, randomly oriented micro-sized islands in a rice-like shaped can be observed, and form an inhomogeneous and irregular coverage across the surface, as indicated by the colour variation Figure 3.2 (a). The birefringence of the TCNQ film is revealed by introduction of a cross polariser, and the contrast in the light intensity reflects presence of crystalline structure and grain boundaries in different orientations in the micro-sized islands (see Figure 3.2 (b)).

In order to improve the film homogeneity, the deposition rate was subsequently increased to 1.0 Å/s. While similar micro-sized islands can be obtained, using a higher rate has apparent effects on the island density and size. The increased island density and reduced island size induced by the deposition rate can be observed by inspecting the change in the intensity contrast in the birefringence of the film (see Figure 3.2 (d)).

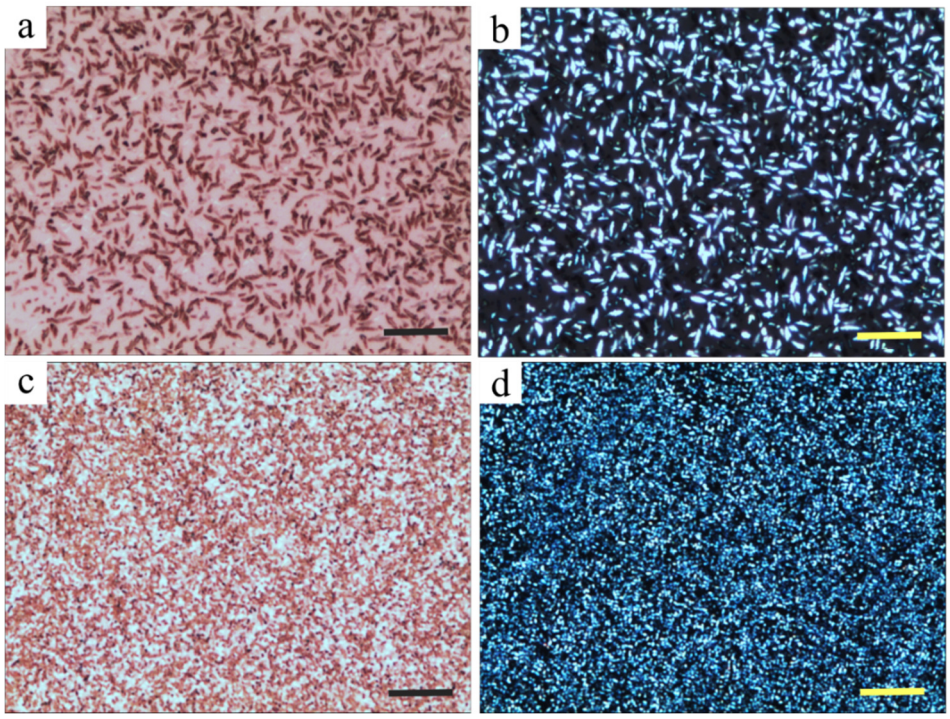


Figure 3.2 Optical micrographs of the 80 nm thick TCNQ films grown at the rate of (a) 0.37 Å/s, and (b) the same area observed with a cross polariser, and at the rate of (c) 1.0 Å/s and (d) (d) the same area observed with a cross polariser. The scale bars in (a), (b), (c) and (d) are 20 μm.

The morphological details of the 80 nm thick TCNQ films deposited at the rate of 0.37 Å/s and 1.0 Å/s are observed by SEM. For the deposition at the rate of 0.37 Å/s, TCNQ displays croissant-like shaped islands in a length up to 10 μm with random orientation across the surface. The shape and size of the islands are comparatively similar to that of C_{60}-TCNQ [75, 149, 150] and pure TCNQ [151] grown by ionized-cluster beam and vacuum thermal sublimation.

Increasing the deposition rate to 1.0 Å/s leads to the increased island density and reduced island size with a slightly different shape, in consistent with what is observed by optical

microscopy. Although using a higher rate has apparently leads to an improved coverage of the TCNQ islands, a considerable fraction of the substrate is still not covered.

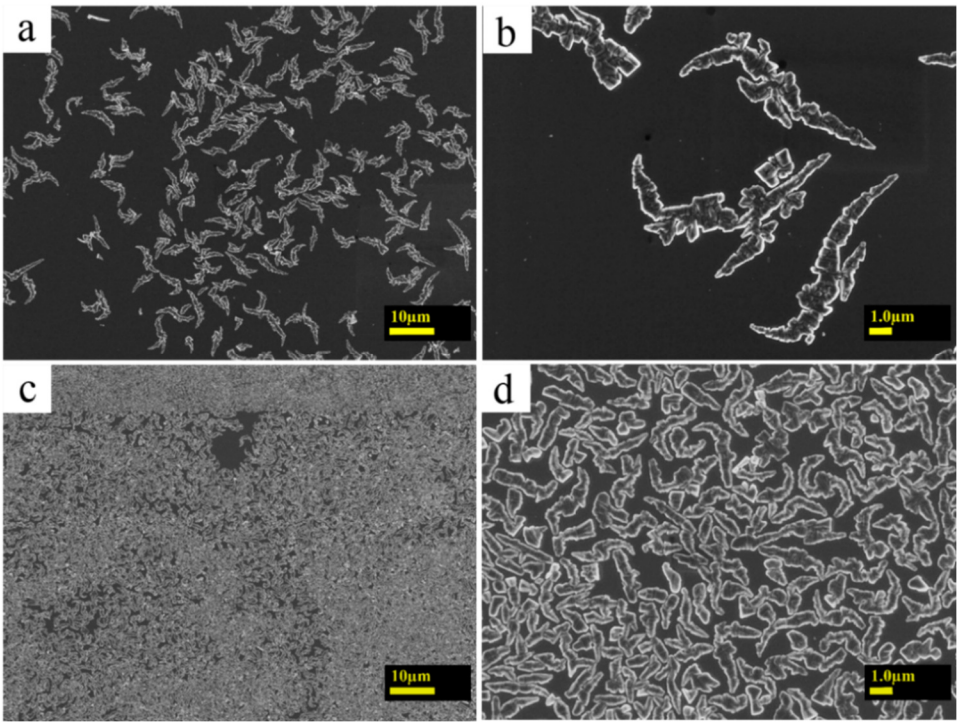


Figure 3.3 SEM micrographs of the 80 nm thick TCNQ films deposited at the rate of (a) and (b) 0.37 Å/s, and (c) and (d) 1.0 Å/s on bare silicon substrates.

More information on the morphological properties of the TCNQ films deposited at the two rates is provided by AFM (see Figure 3.4). Similar to what was observed by SEM, randomly oriented islands with several μms in length can be identified, as shown in Figure 3.4 (a). Based on the purple profile in Figure 3.4 (a), it can be seen that the surface covered by the islands are up to 180 nm in height, and the area not covered by the island appears to be relatively flat, overall giving rise to a very large RMS = 56 nm. While the coverage of the TCNQ islands appears to be inhomogeneous, the area between the islands actually contains TCNQ deposit, as suggested by the contrast in the corresponding phase image (see the inner panel in Figure 3.4 (a)). The film area not covered by the islands is further examined, and as shown in Figure 3.4 (c), except for few particles can be found, the area appears to be relatively smooth, characterized by RMS = 1.2 nm.

A similar morphology can be observed for deposition at the rate of 1.0 Å/s, with a height and shape of the islands almost indistinguishable to those obtained at the rate of 0.37 Å/s, as indicated by the height profile in Figure 3.4. The morphology of the area between the islands is alike, corresponding to a low roughness of RMS = 1.3 nm.

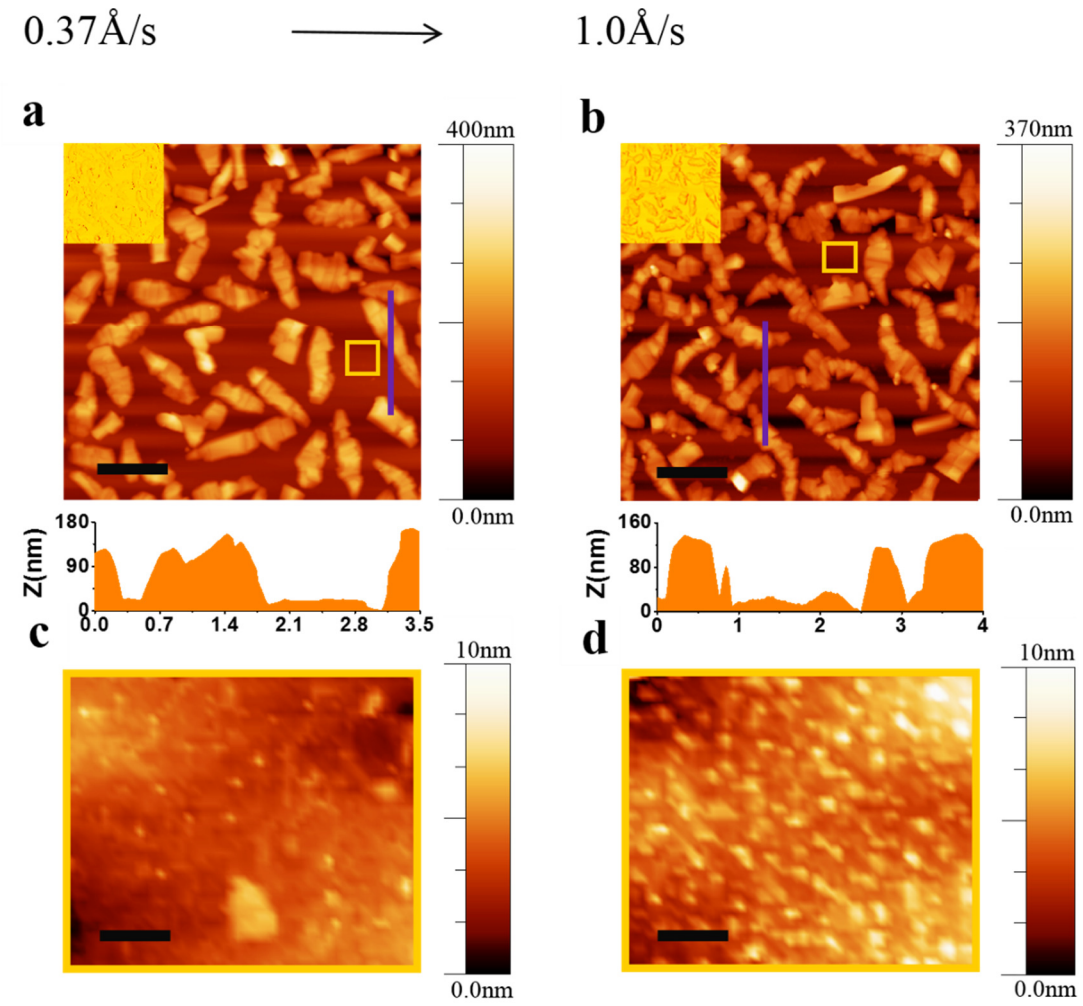


Figure 3.4 AFM micrographs of the 80 nm thick TCNQ films deposited on glass at the rate of 0.37 Å/s (a) and (c), and 1.0 Å/s (b) and (d) on bare glass (substrates). The inner panels in (a) and (c) show the corresponding phase images. The height profile along the purple line in (a) and (c) reveals the TCNQ grain height, plotted below the figures. The area between the TCNQ islands highlighted by the yellow boxes in (a) and (b) are shown in (c) and (d). The scale bars are 2 µm in (a) and (b), and 200 nm in (c) and (d), respectively.

The shape of TCNQ islands revealed by the AFM micrographs appears to be less affected by the deposition rate, in contrast to what is observed by SEM. This discrepancy in the results observed by two different techniques is possibly because the film is not entirely uniform, due to the irregular island coverage formed by TCNQ, particularly at a very low deposition rate, and a quick morphological assessment for a reasonably large surface is more often obtained by SEM.

Structure

The structure of the 80 nm thick TCNQ films deposited at the two rates is determined by using X-ray diffraction (XRD), and compared to the TCNQ powder used as received from the supplier, shown in Figure 3.5. In the range of 2θ = 5-30°, TCNQ exhibits diffraction peaks expected from the literature values obtained on single crystals [98]. Differences in the relative intensity and absence of other peaks indicate the powder sample is textured.

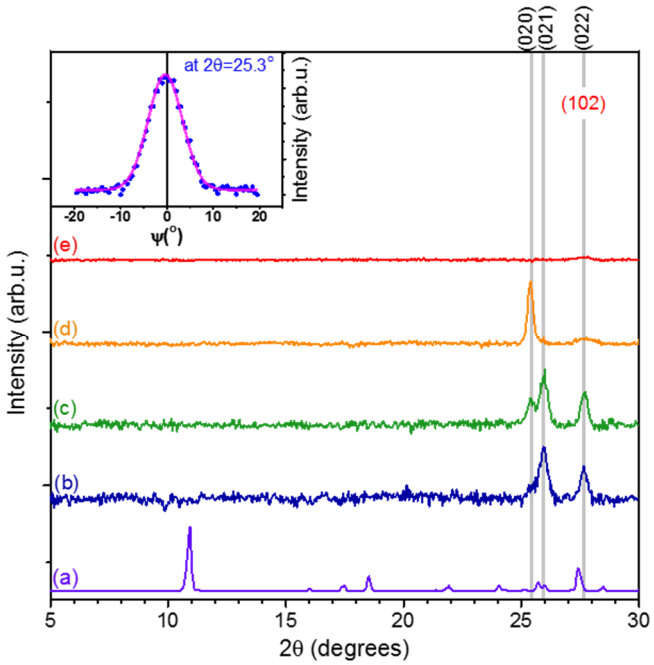


Figure 3.5 X-ray diffraction (XRD) patterns of (a) TCNQ powder, 80 nm thick TCNQ films deposited on glass at the rate of (b) 1.0 Å/s, (c) 0.37 Å/s, and on a 20 nm thick PTCDA film, (d) 0.37 Å/s, with the diffraction pattern of a 20 nm thick PTCDA film shown in (e). Inset: the ψ curve at 2θ = 25.3° obtained on the TCNQ film deposited onto PTCDA shown in blue circles, plotted with the Gaussian fit (magenta) with FWHM = 8.8°.

For the TCNQ films, three peaks at 2θ = 25.3, 25.9 and 27.6° can be observed for the rate of 0.37 Å/s and 1.0 Å/s, owing to the (020), (021) and (022) diffracting planes parallel to the substrate. Compared to the powder sample, presence of fewer diffraction peaks and the lack of the dominant diffraction at 2θ = 11° suggests the TCNQ films deposited on bare substrate are highly textured.

The molecular orientations adopted by TCNQ when deposited on bare glass substrate are relatively unaffected by the deposition rate. To visualize the preferential orientations deduced from the diffraction results, the schematics in Figure 3.10 depict the TCNQ unit cell, and the observed (020), (021) and (022) diffraction planes. The (020) plane is shown parallel to the substrate, though the same orientation is needed for the (021) and (022) planes to account for the other observed peaks. As can be seen, the (022), (021) and (020) planes are very close, each intersected by an angle of ~ 12°.

Table 3.1 Texture coefficients of the 80 nm thick TCNQ films deposited onto bare substrates and PTCDA.

2θ /Plane	TCNQ - substrate angle	TC for TCNQ on glass (0.37 Å/s)	TC for TCNQ on glass (1.0 Å/s)	TC for TCNQ on PTCDA (0.37 Å/s)
27.6°/(022)	2.6° (50%); 44.9°(50%)	0.13	0.22	0
25.9°/(021)	9.2° (50%); 33.7°(50%)	0.75	1.22	0
25.3°/(020)	21.4° (100%)	2.12	1.56	3

The effect of the deposition rate on the film texture is investigated. The texture coefficients (TC) for the (020), (021) and (022) diffraction planes observed for the films obtained at the two different rates are calculated and summarized in Table 3.1. For the film deposited at the rate of 0.37 Å/s, the most possible orientation is predicted to be (020), as indicated by TC = 2.12, whereas both the (020) and (021) orientations (corresponding to TC = 1.56 and 1.22, respectively) are suggested to be likely for the film obtained at the rate of 1.0 Å/s, indicating the influence of the growth rate on the film texture.

3.2 TCNQ on PTCDA

While increasing the deposition rate has a significant influence on the island density and size, using bare substrates leads to a considerable fraction of the substrate not covered by the islands. In order to improve the film coverage and texture, a thin layer of perylene-3,4,9,10-tetracarboxylic dianhydride (PTCDA) with a thickness of 20 nm is used to pre-coat the substrate prior to the TCNQ growth. PTCDA is known to adopt a face-on orientation with its (102) plane parallel to the substrate [152]. The types of intermolecular interactions involved in the packing of PTCDA include in-plane C = O…H-C hydrogen bonding, and the π-π interactions along the stacking axis of the molecular columns (out-of-plane) [153, 154]. PTCDA has been successfully demonstrated as a structural template for Pcs, which adopt a face-on orientation with respect to the (102) plane of PTCDA, as opposed to the edge on orientation that characterizes the film grown on weakly-interacting substrates [155].

3.2.1 UV/Visible spectroscopy of the films

The optical spectrum of the 80 nm thick TCNQ film deposited at the rate of 0.37 Å/s on glass pre-coated with a 20 nm thick PTCDA layer is shown in Figure 3.6 with the optical spectra recorded separately from a 20 nm thick PTCDA film, and a 80 nm thick TCNQ film grown on glass substrate as a comparison.

The 20 nm thick PTCDA film exhibits a broad absorption band between ~ 400 to 540 nm, and an isolated peak at 555 nm (Figure 3.6 (1)), in good agreement with the values expected from the literature [152]. For the TCNQ film on PTCDA, except for the broad absorbance across the entire spectrum, due to interference with scattering as seen for those on bare substrates, a peak at ~ 500 nm and the two shoulders at~ 450 and 550 nm, respectively, can be found. The former corresponds to the absorption peak exhibited in the TCNQ film, whereas the two shoulders can be attributed to the absorbance from the underlying PTCDA layer. The peak assignments can be confirmed by a reasonably good match with the simulated spectrum based on the sum of the individual films of TCNQ and PTCDA, with the thicknesses of 80 nm and 20 nm, respectively, identical to those used in the PTCDA/TCNQ double-layer. The absorbance between 300 nm to 600 nm for the PTCDA/TCNQ double-layer is more intense than that for the simulated spectrum, suggesting the effect of using PTCDA as the

underlying substrate on the film coverage.

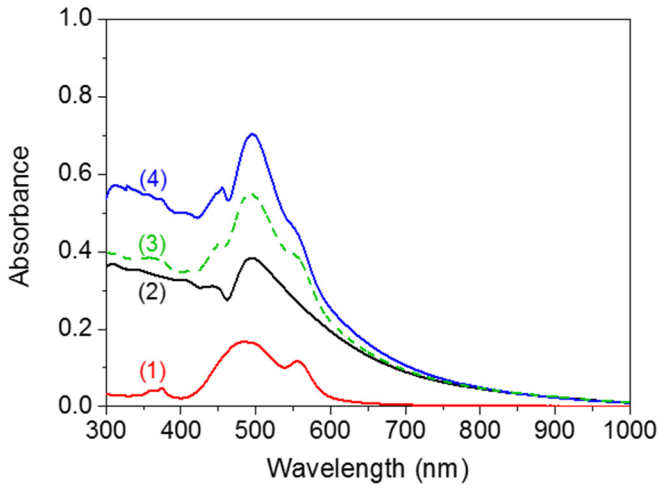


Figure 3.6 The optical spectra of (1) a 20 nm thick PTCDA film, (2) a 80 nm thick TCNQ film, (3) a simulated spectrum based on the sum of optical absorption recorded from a 20 nm thick PTCDA film, and that of a 80 nm thick TCNQ film, and (4) the 80 nm thick TCNQ film deposited onto 20 nm thick PTCDA film. All the samples are grown on glass substrate.

3.2.2 Morphology and structure of the films

The appearance of the TCNQ film on glass substrate pre-coated with a 20 nm thick layer of PTCDA is shown in Figure 3.7.

Micro-sized tubular-shaped features can be found across the entire sample, suggesting a more uniform and homogeneous coverage of TCNQ can be obtained when depositing onto PTCDA, in contrast to those obtained on bare substrate. Similar to the film on bare substrates, crystalline domains and grain-boundaries in the TCNQ film on PTCDA are reflected by the birefringence.

The morphology of the TCNQ film deposited on PTCDA observed by SEM is shown in Figure 3.8 (a) and (b). TCNQ exhibits islands with a size comparable to those obtained on bare substrates, yet, on PTCDA the shape of the islands appears to be more rectangular, very similar to that is observed after deposition on KCl(100) [156].

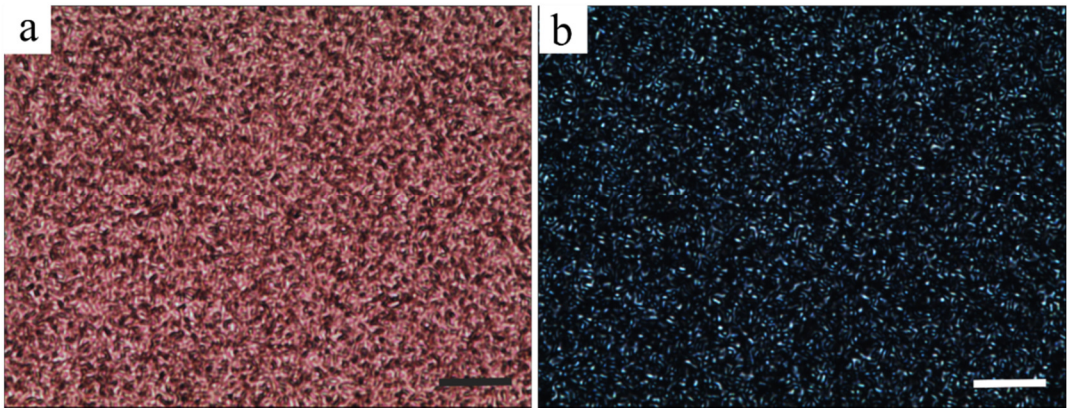


Figure 3.7 Optical micrographs of (a) the 80 nm thick TCNQ film grown at the rate of 0.37 Å/s on glass substrate pre-coated with a 20 nm thick PTCDA film (which is deposited at the rate of 0.2 Å/s), and (b) the same area observed with a cross polariser. The scare bars in (a) and (b) are 20 µm, respectively.

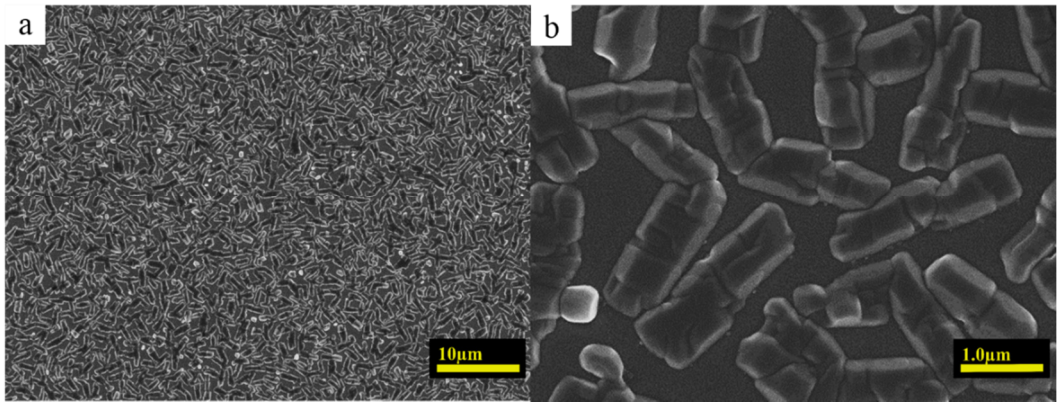


Figure 3.8 SEM micrographs on the 80 nm thick TCNQ film deposited at the rate of 0.37 Å/s on the 20 nm thick PTCDA layer on silicon substrate. The scare bars are 10 µm in (a) and 1.0 µm in (b), respectively.

More morphological details are deduced by AFM (see Figure 3.9). The 20 nm thick PTCDA film displays small spherical islands with a diameter between 40-60 nm and a RMS = 1.6 nm, in good agreement with the literature [152], thus giving rise to a smooth and homogenous film coverage (as the height profile along the purple line and the phase image given in the inner panel in Figure 3.9 (a)). When deposited onto PTCDA, TCNQ forms micro-sized rectangular shaped islands up to 200 nm in height, as indicated by the height profile, resulting in a large roughness (RMS = 58 nm), in consistent with what is observed by SEM.

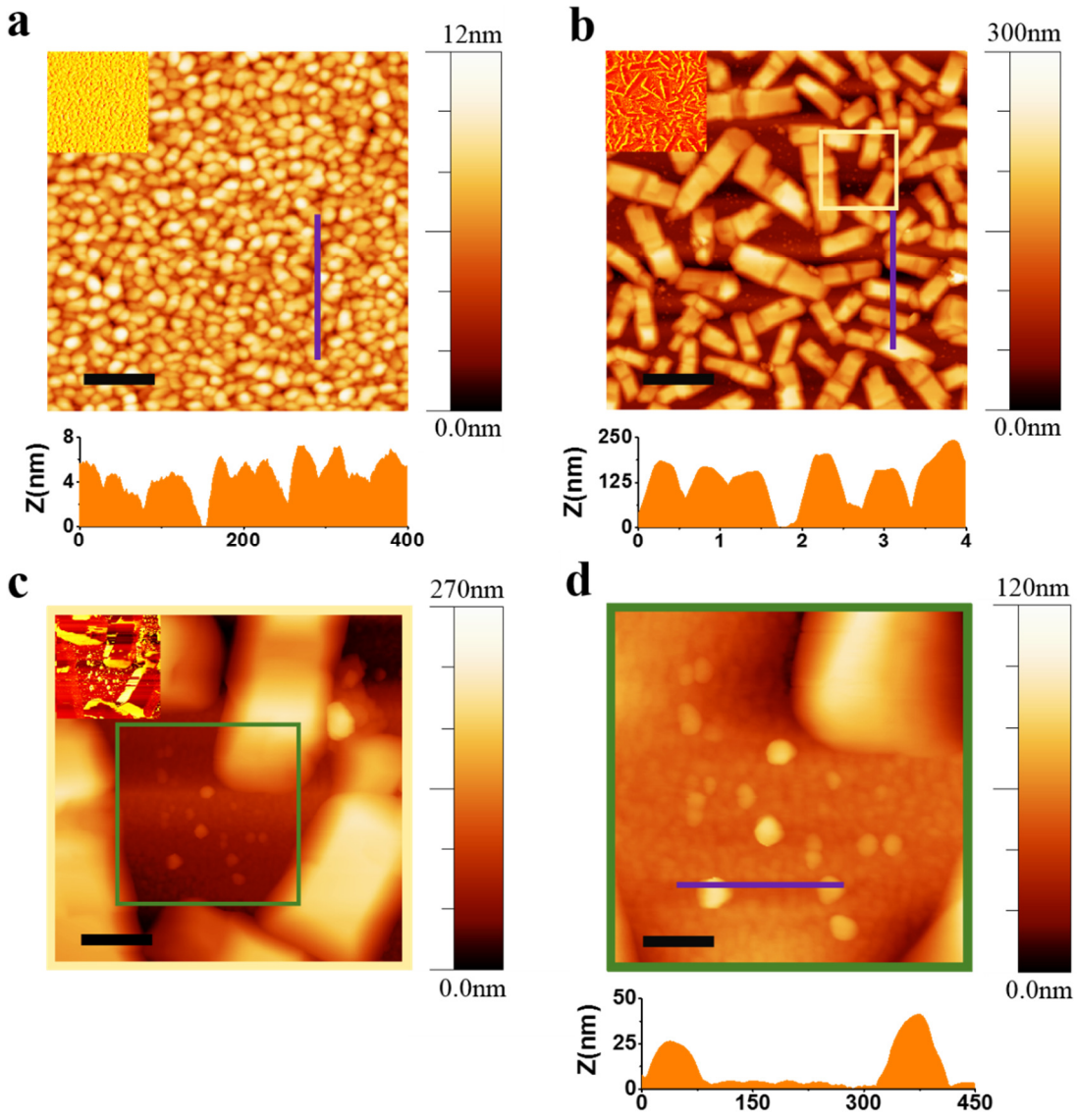


Figure 3.9 AFM micrographs of (a) a 20 nm thick PTCDA film deposited on glass substrate, (b), (c) and (d): the 80 nm thick TCNQ deposited at the rate of 0.37 Å/s on glass pre-coated with a 20 nm thick PTCDA film. The inner panel in (a), (b) and (c) represent the corresponding phase images, and the height profiles in (a), (b) and (d) are depicted by the purple line, plotted below the figures. The area uncovered by the rectangular-shaped islands highlighted by the yellow and green boxes are show in (c) and (d). The scale bars are 200 nm in (a) and (d), 400 nm in (c) and 2 µm in (b).

The film composition appears to be inhomogeneous, especially on the area not covered by the islands, as suggested by the contrast in the corresponding phase image in the inner panel of Figure 3.9 (b). Further examination on the area between the protruding islands (shown on Figure 3.9 (d)) reveals the area adopts a morphology indistinguishable from that of the PTCDA film, characterized by a low RMS ~ 2.5 nm.

Deposition of TCNQ onto PTCDA is more likely to proceed without wetting, as suggested by AFM, in contrast to what is previously seen for the films on bare substrates, and pre-coating with PTCDA clearly induces several morphological changes to the subsequent TCNQ layer.

Structure

The effects from the underlying PTCDA film on the structure of the TCNQ film are investigated by using XRD (given in Figure 3.5(e)). The XRD scan of the 20 nm thick PTCDA film shows a diffraction peak at $2\theta = 27.6°$ corresponding to the (102) plane, indicating the face-on orientation adopted by the PTCDA film [152]. As for the TCNQ film deposited onto PTCDA, two diffractions at $2\theta = 25.3$ and $27.6°$ can be observed in the corresponding XRD pattern.

Based on the peak intensity and width, the peak at $2\theta = 25.3°$corresponds to the diffraction expected from TCNQ crystals, and the latter is attributed to the underlying PTCDA film. The diffraction peaks at $2\theta = 25.9°$ and $27.6°$ that can be found when using bare substrates are now absent, indicating deposition of TCNQ onto PTCDA leads to only one preferential orientation, with the (020) plane parallel to the substrate.

The effect of the underlying PTCDA film on the film texture is further examined by obtaining a ψ curve at $2\theta = 25.3°$ (shown in Figure 3.5 the inner panel), corresponding to a full-width half maximum (FWHM) of 8.8°, indicating spatial deviation from the (020) plane observed by the XRD is expected to be in the range of ± 8.8°. Thus, on PTCDA the TCNQ film is highly textured along the (020) orientation.

Using substrates pre-coated with PTCDA is shown to induce several morphological changes, but more profound effects are observed on the structure of the TCNQ film. To interpret the effect on the structure of the TCNQ film from the underlying PTCDA, the types of

intermolecular interactions and intermolecular contacts in both molecules need to be considered. In PTCDA/Pcs, the structural/orientational templating is mainly driven by the π-π interactions, which force the Pc molecules to adopt the face-on orientation parallel to the substrate to maximize the interaction with the PTCDA ring [155].

For PTCDA and TCNQ, intermolecular interactions in addition to van der Waals interactions can arise, owing to the strongly electronegative CN groups in TCNQ, and the anhydride group in PTCDA. The presence of strongly electronegative anhydride groups also polarizes the charge distribution along the long molecular axis of PTCDA [157]. The electronegative functional groups consist of oxygen and nitrogen atoms, which are able to hydrogen bond to the hydrogen atoms, giving rise to attractive interactions, via intermolecular contacts between the CN(TCNQ) and HC(PTCDA) and/or CH(TCNQ) and O = C(PTCDA), respectively. Therefore, in PTCDA/TCNQ, strong intermolecular interactions, such as repulsive, electrostatic, and attractive, hydrogen bonding, are more likely to dominate over the van der Waals interactions. Balance amongst the various attractive and repulsive intermolecular interactions, and in particular hydrogen bond [158, 159] is expected to play a decisive role on the resulting molecular alignment/orientation in the PTCDA/TCNQ heterostructure.

The information on the spatial relationship for the TCNQ and PTCDA planes parallel to the substrate deduced from the XRD results is shown in Figure 3.10 (c) and (d). It can be immediately seen that the (020) plane of TCNQ is quite nitrogen-rich, with two out-of-plane arrays of CN groups separated by ~ 16 Å. The (102) plane of PTCDA is shown in the wireframe style except for the oxygen atoms (the bottom panel in Figure 3.10 (c)). The (102) plane is oxygen-rich, and the location of the oxygen atoms essentially follows the periodicity predetermined by the herringbone structure of PTCDA, giving rise to ~ 16 Å, as depicted by the red box in Figure 3.10 (c). The same distance is found between the repetitive H-atoms in the perylene core on parallel PTCDA molecules.

The distance separating the two out-of-plane arrays of CN groups exhibited by the TCNQ (020) plane appears to match up with that between the perylene H-atoms (hydrogen bond donor) located on the (102) plane of PTCDA (shown in Figure 3.10 (d), the molecular arrangements for TCNQ and PTCDA are generated by combing the upper and lower panel in (c)). The compatibility between the hydrogen bond donors/acceptors in the bottom and top molecular layers account for the only observed (020) orientation, which could be further stabilized by additional hydrogen bonds that could be obtained along the edge of PTCDA

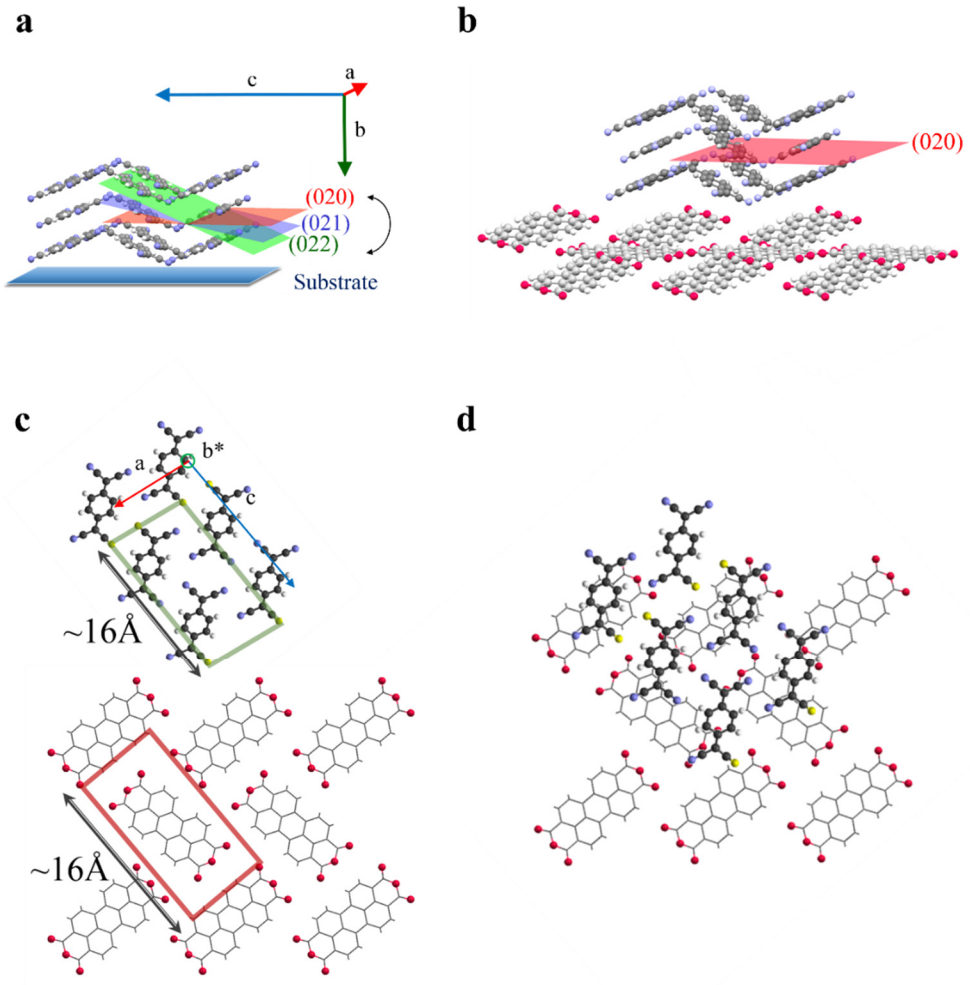


Figure 3.10 The schematics of (a) the TCNQ crystal structure obtained from [98] with its (020), (021) and (022) diffracting planes, and the corresponding unit cell axes given in the upper-right, (b) the (020) plane of TCNQ parallel to the (102) plane of PTCDA, which is characterized by the face-on orientation when grown at room temperature, (c) upper panel: the lattice of TCNQ on its (020) plane highlighted by the green box; lower panel: the (102) plane of PTCDA shown in the wireframe style except for the oxygen atom represented by the red spheres, and a similar lattice highlighted in the red box to depict the displacement of the perylene H atoms on parallel PTCDA molecules; (d) **top-view:** possible molecular arrangement of the TCNQ unit cell along its (020) direction projected onto the PTCDA layer adopting (102) orientation, using the same scale as in (c). Grey, red and white spheres represent carbon, oxygen and hydrogen atoms. Both purple and yellow are used to represent nitrogen atoms, and the latter is used to mark those are the out-of-plane and thus close to the (102) plane of PTCDA.

grain (owing to the similarities in the inter-planar distances in PTCDA and TCNQ, corresponding to 3.4 [160] and 3.5 Å [98], respectively).

On the contrary, fewer intermolecular contacts (CN groups and HC(PTCDA) and/or CH(TCNQ) and O = C(PTCDA)) can be obtained in PTCDA and TCNQ in other orientations, such as the (022) and (021), which are not observed by XRD. The oxygen-rich (102) PTCDA provides an adequate environment to interact with the (020) TCNQ via hydrogen bond and electro-static interactions, with the match in the distance that separates the perylene H atoms given in (102) PTCDA and the spacing between the CN groups in (020) TCNQ, allowing for maximized interactions. These results show the underlying substrate has a very profound impact on the resultant morphological and structural properties of molecular films. Deposition of one type of molecular layer onto another barely suffers from strains and/or lattice-mismatch, both of which are key to achieve inorganic heterostructures through expitaxy [161]. Molecular heterostructures benefit from the flexibility of the molecular layer itself, and ease of fabrication. The former is a consequence of the nature of molecular crystals, self-assembled by the weaker van der Waals forces, and other types of intermolecular (supramolecular) interactions [139]. In the present case, it is shown that the CN group in TCNQ interacts very differently from weakly-interacting substrates to (102) PTCDA, with stronger intermolecular interactions induced by the particular functional groups and more intermolecular contacts available when combined with the respective crystal lattice of each molecular layer. This approach to obtaining controlled molecular orientation in the molecular heterostructure is therefore significantly different from what is observed in PTCDA/Pcs, where the face-on orientation adopted by the templated Pcs is predominantly driven by the π-π interactions.

4. MnTPPCl thin films

Previous chapter has shown one of the key components, TCNQ, needed to form the charge-transfer salt [MnTPP][TCNQ] can be sublimed and deposited as thin films. The second component that acts as the electron donor, MnTPPCl, is presented in this chapter. This particular dye molecule on its own has attracted significant research interest for its role in numerous biological and photochemical reactions, owing to easy accessibility to the various oxidation states exhibited by the central Mn ion in the porphyrin complex. The materials properties of MnTPPCl when deposited as thin films also show the same type of chemical reactions that have been previously observed in its solutions and vapour phase, respectively, suggesting that the rich chemistries characteristic of MnTPPCl can be largely retained. Through the film processing, the oxidation state for the Mn ion is shown to self-reduce from +3 to +2, an intrinsic property that is only seen for the vapour phase MnTPPCl, leading to both MnTPP and MnTPPCl contained in the as-deposited film.

4.1 As-deposited films

4.1.1 UV/Visible spectroscopy of the films

The as-deposited 100 nm thick MnTPPCl film exhibits optical absorption from 300 to 700 nm, as shown in Figure 4.1. In the near UV range, the optical spectrum is dominated by two sharp and intense absorption peaks at 447 nm and 484 nm, followed by a shoulder at 379 nm. Two other absorption bands with relatively weak intensities are found at λ = 581 nm and 624 nm, with a shoulder at λ = 535 nm. Except for the peak at λ = 447 nm, the absorption features are found to be consistent with those observed for the MnTPPCl solution spectrum (the green curve shown in Figure 4.1), in good agreement with the literature [101, 102, 105], suggesting that the main properties of MnTPPCl are retained.

The sharp and intense peak at λ = 484 nm can be assigned to the Band V (Soret band), arising

from the charge-transfer transitions (a_{1u}, $a_{2u} \rightarrow e_{g2\pi}$) [102, 105]. As for the shoulder at λ = 379 nm, a counterpart with a similar absorption intensity can be found at λ ~ 375 nm in the MnTPPCl solution spectrum, originating from charge-transfer transitions and known as the B-band (or Band VI), characteristics of MnTPPCl absorption [102, 105]. The shoulder at λ = 379 nm in the thin film spectrum is subsequently ascribed to the B-band.

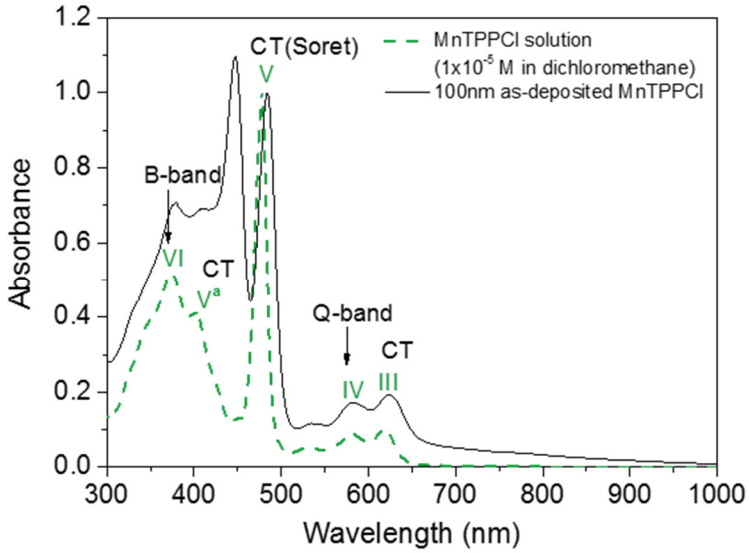


Figure 4.1 Optical spectra of a 100 nm thick MnTPPCl film deposited at the rate of 0.9 Å/s on glass that is recorded immediately after the film deposition (black solid line), and the MnTPPCl solution (green dotted line) in dichloromethane, with the concentration of 10^{-5} M, B-band, VI, V_a, V, IV (Q-band) and III used to label the absorption band following the notations from Boucher [104] as previously summarized in Table 1.2 in section (1.3.2).

In the range between 500 nm and 700 nm, the two absorption bands at λ = 581 nm and 624 nm correspond to the Q-band of MnTPPCl, whereas the origin for the latter is additionally attributed to the charge-transfer transitions ($b_{2u} \rightarrow d_{\pi}$) between the Mn ion and porphyrin ligand, assigned as the Band III. The radical differences between the UV-bands and visible bands can be explained by Gouterman's four orbital model [101]. Thus, the solution spectrum of MnTPPCl shows no absorption bands with a shape and oscillator strength comparable to the peak at λ = 447 nm observed for the as-deposited MnTPPCl film. The peak at λ = 447 nm is therefore a distinctive feature to the as-deposited MnTPPCl film.

The distinctive B- and Q-bands that characterize MnTPPCl can be found and its absorption approximately is proportional to the film thickness, shown in inset of Figure 4.2, consistent with the Beer-Lambert's law. The absorption in the B-band appears to increase linearly with

the thickness, as seen for the 100 nm and 50 nm thick as-deposited films, in contrast to the Q-band and Band III region. This difference is likely because the transitions responsible for the B- and Soret band are sharp and intense charge transfer transitions (porphyrin ligand – Mn). In addition, the absorption peak at λ = 447 nm previously seen in the 100 nm thick as-deposited MnTPPCl film is present in other thicknesses, and can still be observed in the 25 nm thick film. Thus, the presence of the absorption peak at λ = 447 nm is an intrinsic feature for the as-deposited MnTPPCl film.

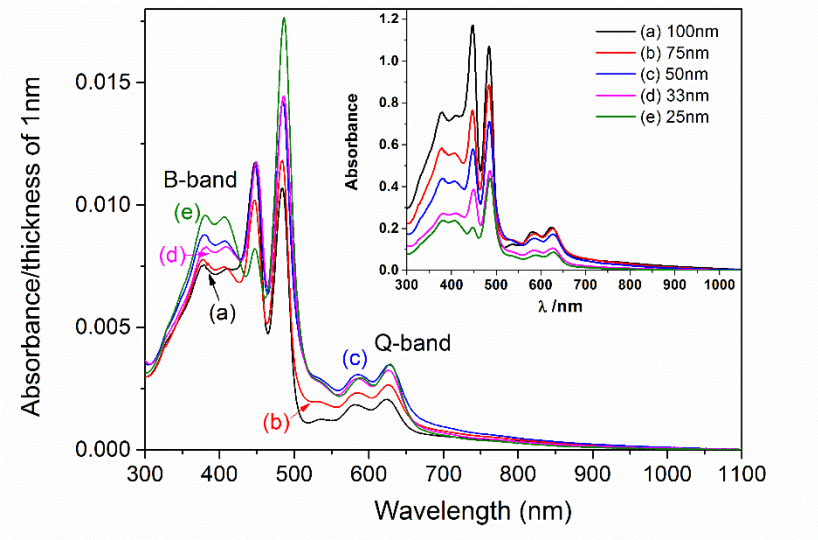


Figure 4.2 Optical spectra recorded from the as-deposited MnTPPCl films deposited at the rate of 0.9 Å/s on glass substrates, with the thickness of (a) 100 nm, (b) 75 nm, (c) 50 nm, (d) 33 nm, and (e) 25 nm, respectively, with the absorption intensity normalized to 1 nm thick for comparison. Inset: the optical spectra of the MnTPPCl films of 100 nm, 75 nm, 50 nm, 33 nm and 25 nm without normalization to the absorption intensity.

While the overall appearance of the optical spectra obtained from all the film thicknesses are alike, its intensity relative to the Soret band (λ = 484 nm) appears to vary with the film thickness. The effects of the thickness on the absorption intensity in the Soret band (λ = 484 nm) is shown in Figure 4.2, with the optical spectra of the as-deposited films with various thicknesses normalized to 1 nm for comparison. The absorbance in the Soret band (λ = 484 nm) roughly increases with decreasing film thickness, whereas the opposite trend is found for the peak at λ = 447 nm. The same behaviour can be observed in the ratio between the peaks at λ = 447 nm and 484 nm as a function of film thickness, which are summarized in Table 4.1. Again, the ratio between the two peaks increases with the film thickness, only exceeding 1 for the 100 nm thick film. These observations reveal the absorption intensity in

the peak at λ = 447 nm is thickness-dependent, and its presence only seen in the as-deposited films in turn suggests change to the Mn oxidation state has occurred during film processing.

Table 4.1 Ratios of the absorption peaks at λ = 447 nm to 484 nm, calculated by using the respective peak heights obtained from the optical spectra recorded from the as-deposited MnTPPCl films with a thickness of 100, 75, 50, 33 and 25 nm.

Thickness (nm)	Normalized Absorbance (arb.u.)	
	λ = 447nm	λ = 484nm
100	1.1	1
75	0.86	1
50	0.82	1
33	0.81	1
25	0.45	1

A similar behaviour has been observed for the vapour phase MnTPPCl, whose absorption spectrum first displays the typical absorption of Mn(III), followed by the Soret peak characteristic of Mn(II), attributed to self-reduction of Mn(III) to Mn(II), although the details remain unclear [105]. The spectroelectrochemical studies on the MnTPPCl solution show a gradual shift from λ = 476 nm (2.61 eV) to λ = 444 nm (2.79 eV) in the Soret region, as Mn(III)TPPCl is reduced to Mn(II)TPPCl$^-$ [106]. The position of the Soret feature exhibited by Mn(II) porphyrins that are four-coordinate or axially ligated by neutral solvent appears to be higher in energy, giving rise to an absorption maximum at λ = 437 nm [106]. The peak at 447 nm is a sharp and isolated feature, which is in good agreement with those observed for Mn(II) porphyrins [107, 162]. As a consequence, the peak at λ = 447 nm seen in the as-deposited films can be assigned to Mn(II) species contained in the as-deposited MnTPPCl films, and the fraction of Mn(III)TPPCl that undergo reduction Mn(III) → Mn(II) during the film deposition appears to increase with decreasing film thickness.

To gain more insight in the origin of the band at λ = 447 nm, the optical spectrum recorded from the 100 nm thick as-deposited MnTPPCl film can be deconvoluted by eight Gaussian components (Figure 4.3), whose positions, heights, full-width half maximums (FWHM) and areas are summarized in Table 4.2. The Peak4 and Peak5 correspond to the absorption bands at λ = 484 nm and λ = 447 nm seen in the as-deposited MnTPPCl film. The difference

between the Peak4 and Peak5 observed in the as-deposited MnTPPCl film is calculated to be 0.20 eV, in an excellent agreement with the values of 0.18 eV and 0.25 eV reported for solutions of Mn(III)TPPCl/Mn(II)TPPCl$^-$ and Mn(III)TPP(CH_3OH)/MnTPP(CH_3OH_2)$^-$ respectively [106].

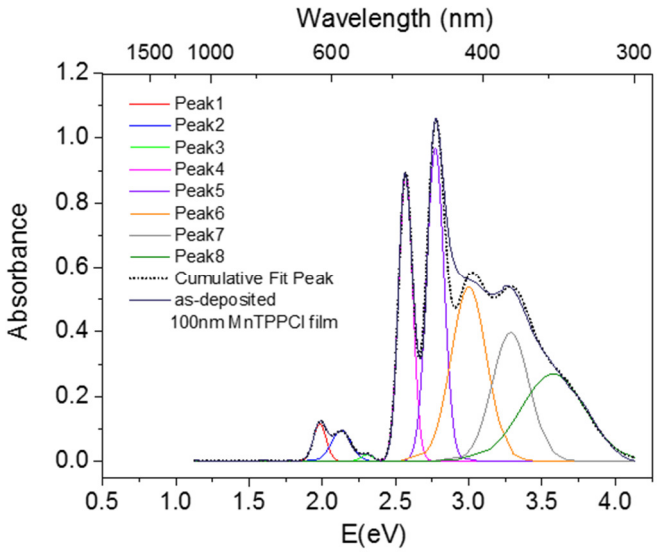


Figure 4.3 The optical spectrum of the100 nm thick as-deposited MnTPPCl film deposited at the rate of 0.9 Å/s (black solid line) plotted in the scale of energy (eV), presented with the eight Gaussian functions used for deconvolution, with the cumulative fit shown in black dotted line.

The ratios (listed in Table 4.1) between the bands at $\lambda = 447$ nm and $\lambda = 484$ nm, corresponding to Peak 4 and Peak 5 extracted from the fitting, are found to increase with the thicknesses. The peak at $\lambda = 447$ nm can still be identified for the 25 nm thick film, despite the low intensity, suggesting the film deposition process in the OMBD to some extent provides an adequate environment that is favourable for Mn(III) to self-reduce to Mn(II).

Since the optical absorption in this region appears to observe the Beer Lambert's law, the peak ratios in turn indicate the relative amounts of Mn(II) and Mn(III) contained in the as-deposited MnTPPCl film. As a consequence, the amount of Mn(II) in the 25 nm MnTPPCl film appears to be slightly lower in comparison to the 100 nm thick film, giving rise to Mn(II)/Mn(III) ratio of ~0.33 and 0.57 for the 25 nm and 100 nm thick film, respectively (Table 4.3, the details for the calculations are given in section 4.2). The influence of the thickness on the peak ratio is possibly because the time needed for depositing a 25 nm

Table 4.2 The extracted peak positions, heights, FWHMs and areas by fitting the optical spectrum with Gaussian functions as shown in Figure 4.3. Peak4 (the Soret band for Mn(III)) corresponds to the absorption at λ = 484 nm (2.57 eV), whereas Peak5 (λ = 447 nm, 2.77 eV) is absent in the MnTPPCl solution spectrum and only observed for the as-deposited MnTPPCl film.

As-deposited 100 nm thick film		E(eV)	λ(nm)	Height(arb.u)	FWHM(arb.u)	Area(arb.u)
	Peak1	1.98	625	0.1136	0.1027	0.0124
	Peak2	2.13	583	0.0933	0.1583	0.0157
	Peak3	2.31	538	0.0200	0.0915	0.0019
Mn(III)	Peak4	2.57	483	0.8904	0.1124	0.1065
Mn(II)	Peak5	2.77	448	0.9680	0.1389	0.1432
	Peak6	3.00	413	0.5375	0.2826	0.1617
	Peak7	3.29	377	0.396	0.2967	0.1251
	Peak8	3.58	347	0.2688	0.5112	0.1463

Table 4.3 The relative amounts calculated for the Mn(III) and Mn(II) species in the as-deposited MnTPPCl films.

	Mn(III) relative amount (%) and error (%)		Mn(II) relative amount (%) and error (%)	
100nm	42.7	0.8	57.3	1.8
75nm	49.5	0.6	50.5	1.1
50nm	55.6	0.6	44.4	1.1
33nm	54.1	0.7	45.9	1.4
25nm	67.3	0.7	32.6	1.0

MnTPPCl film is relatively short, compared to that for a 100 nm thick film. Thus, a small amount of Mn(II) relative to that in the thicker film could be obtained once the onset of Mn(III) self-reaction had been activated. Dissociation of the Cl ligand from the adsorbed MnTPPCl molecules on Ag(111) at ~ 423 K has been reported to proceed at a slow rate, attributed to the thermal liability of MnTPPCl. A similar phenomenon has also been observed for the vapour-phase MnTPPCl [70], where the absorption spectrum consisting largely of Mn(II) only appears around 10 min after evaporating Mn(III)TPPCl [70]. Additionally, the larger surface/volume ratio for the thinner film causes the Mn(II) ion to oxidize to Mn(III) more

readily than that in a thicker film, and thus a relatively smaller fraction for Mn(II) could be detected by UV/Visible spectroscopy.

4.1.2 Morphology and structure of the films

The morphology of the 100 nm thick MnTPPCl film deposited on a bare silicon substrate is observed by SEM, shown in Figure 4.4. Except for few spherical particles, the MnTPPCl film appears to be smooth and flat, giving rise to a featureless morphology. The cross-sectional image (Figure 4.4 (b)) reveals that a uniform and continuous film coverage is formed by MnTPPCl, consisting of small oval-shaped particles in irregular sizes, corresponding to the vertical diameter less than 100 nm.

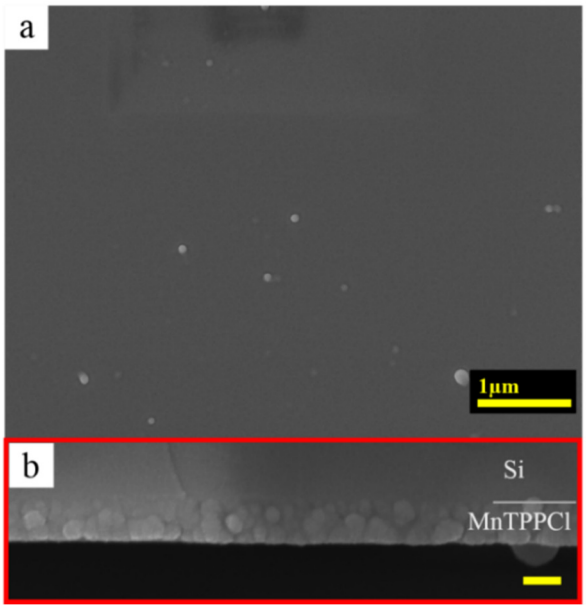


Figure 4.4 SEM micrographs of (a) the 100 nm MnTPPCl film deposited at the rate of 0.9 Å/s onto silicon, and (b) a cross-section of the same film (with the scale bar of 100 nm). The black area at the bottom corresponds to vacuum.

Further morphological information on the MnTPPCl film is obtained by AFM (see Figure 4.5 (a) and (b)). The surface of the MnTPPCl film is very smooth and flat, corresponding to a considerably low RMS = 0.4-0.7 nm, close to the values expected for amorphous substances. In contrast to what was observed by SEM, no spherical particles can be found on

the film surface, characterized by a featureless morphology. The difference in the results of two techniques is likely due to the irregular and sporadic displacement for these particles on a relatively large film surface, and these morphological features are more easily to be accessed by SEM during a quick morphological examination, as previously discussed in section (3.1.2).

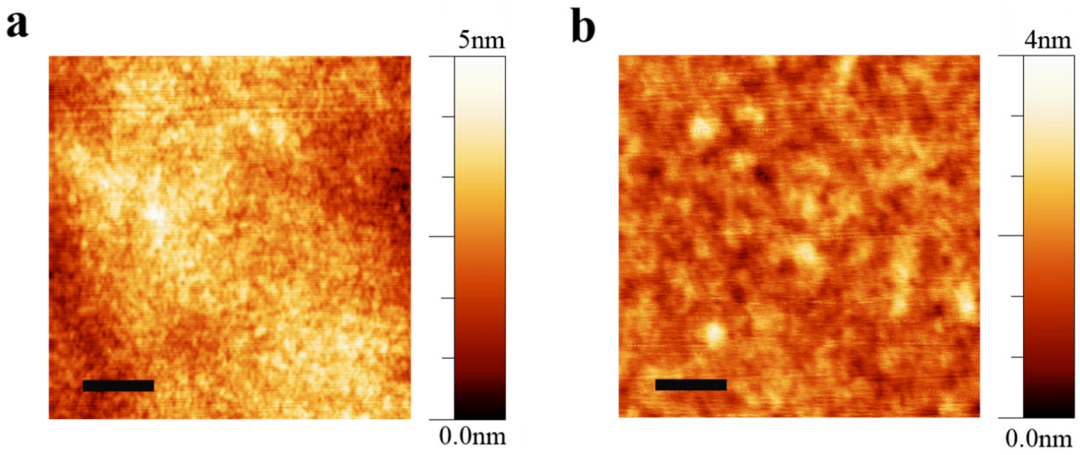


Figure 4.5 AFM micrographs of a 100 nm thick MnTPPCl film deposited at the rate of 0.9 Å/s on glass substrate with the scale bars of 400 nm in (a) and 200 nm in (b), respectively.

The structure of the MnTPPCl films is studied by XRD. For the MnTPPCl film deposited on glass in the range of 2θ = 5-30°, the XRD scan (Figure 4.6 (a)) displays a very broad background, attributed to the underlying glass substrate. Absence of diffractions expected from MnTPPCl single crystal [119] suggests an amorphous structure adopted by MnTPPCl when depositing on glass substrate, though the film could exhibit orientations that are not parallel to the substrate surface or form nanocrystallites.

Deposition onto the glass substrate pre-coated with a 20 nm thick PTCDA layer (Figure 4.6 (2)) has no influence on the structure of the MnTPPCl film, and only displays a diffraction peak at 2θ = 27.6°, attributed to the underlying PTCDA layer adopting the (102) orientation based on its peak intensity and width. Thus, the MnTPPCl films deposited on glass and kapton substrates by using OMBD are found to be amorphous, with absence of crystallites and texture. This is in sharp contrast to what was observed for TCNQ in section (3.1.2) and (3.2.2), where micro-sized islands can be found for deposition on both bare (weakly-interacting) substrates and PTCDA.

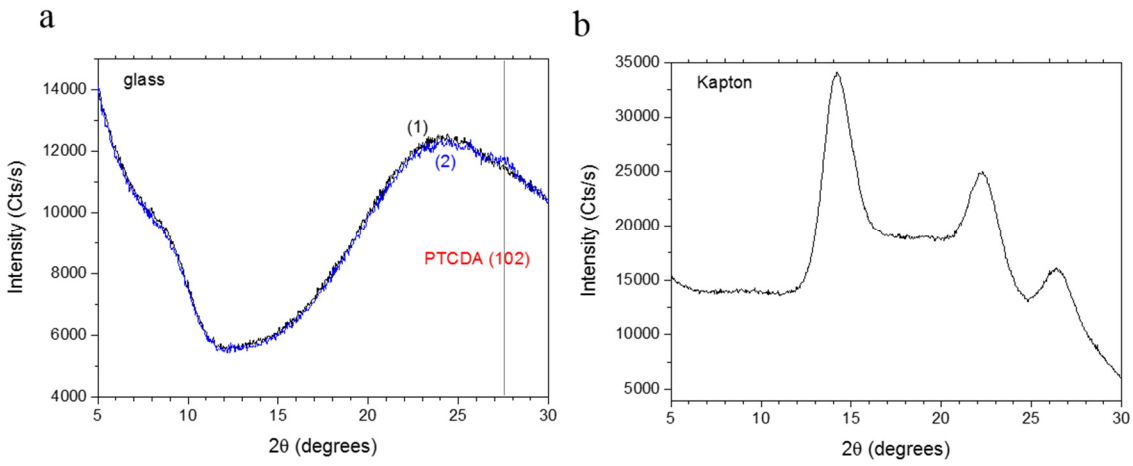


Figure 4.6 XRD scans of (a) a 100 nm thick MnTPPCl films deposited at the rate of 0.9 Å/s on (1) glass substrate, (2) on glass substrate pre-coated with a 20 nm thick PTCDA layer, and (b) on kapton. A. The solid grey line plotted to index the diffraction peak at $2\theta = 27.6°$ due to (102) plane of PTCDA.

4.1.3 X-ray Photoelectron Spectroscopy

The electronic structure of MnTPPCl in the form of powder and as-deposited film is investigated by using XPS. First of all, the survey scans of the MnTPPCl powder and a 125 nm MnTPPCl film are presented in Figure 4.7.

As can be seen, the MnTPPCl powder displays a series of XPS peaks corresponding to the characteristic binding energies of C1s, Mn2p, N1s, Cl2p and O1s. Except for the O1s peak, the chemical composition identified by the XPS survey scan on the MnTPPCl powder is in good agreement with the molecular formula of MnTPPCl.

For the 125 nm MnTPPCl film, the same peaks at binding energies of C1s, Mn2p, N1s, Cl2p and O1s, respectively, can be observed in the corresponding survey scan. Similar to the MnTPPCl powder, the elements, except for the oxygen, observed by XPS suggest the chemical composition found in the as-deposited MnTPPCl film agrees with what is expected from MnTPPCl.

The presence of the O1s peak for both the MnTPPCl powder and the film is attributed to the oxygen introduced to the sample, while handling in ambient conditions prior to loading into the XPS UHV chamber.

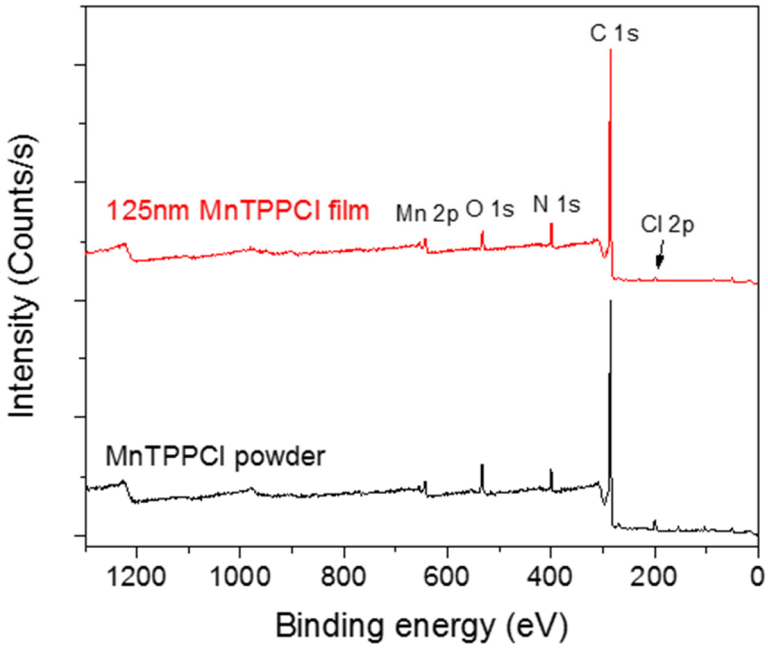


Figure 4.7 XPS survey scans of the MnTPPCl powder (black), and the 125 nm thick as-deposited MnTPPCl film grown at the rate of 0.9 Å/s on silicon substrate (red).

The XPS peaks enable further analysis on the MnTPPCl powder and 125 nm MnTPPCl film samples, whose chemical compositions can be deduced by integrating the area underneath the photoemission line of C1s, N1s, Mn2p and Cl2p, accordingly. The integrated areas underneath the respective XPS peaks are corrected by the element-specific sensitivity factor to account for the different photoemission cross-section and spin-orbit coupling effects. The results of the chemical compositions obtained by the XPS peaks for the MnTPPCl powder and the MnTPPCl film samples are represented in the element to manganese ratios.

The ratio C, N, Mn, and Cl are calculated to be 66.7, 5.6, 1 and 1.3, respectively, for the MnTPPCl powder, in agreement with the values expected from the molecular formula of MnTPPCl ($C_{44}H_{28}ClMnN_4$), corresponding to C, N, Mn and Cl ratio of 44, 4, 1 and 1 respectively. It can be confirmed that the chemical composition of the powder used for this work is roughly as expected, though a slightly higher Cl:Mn ratio could be because the powder (purity *c.a* 98 %) is used as received, and may contain traces of chlorine residual in the synthesis of MnTPPCl [163]. A similar ratio for C, N and Mn can be found for the 125 nm MnTPPCl film, giving rise to 59.6, 5.0 and 1, respectively. Yet, the ratio of Cl to Mn appears

to deviate from the 1 to 1 (theoretical) and 1.3:1 (powder), resulting in a reduction of Cl up to ~ 60 %, in comparison to that observed for the MnTPPCl powder sample.

Table 4.4 The elements to manganese (Mn) ratios calculated for MnTPPCl (theoretical values), the MnTPPCl powder, and the 125 nm MnTPPCl film grown at the rate of 0.9 Å/s on silicon substrate after correcting for the empirical sensitivity factors. The photoemission lines of the XPS C1s, N1s, Cl2p and Mn2p peaks are fitted with the Voigt function (see Figure 4.8).

Species	Sensitivity Factor[164]	Element to Mn Ratio		
		MnTPPCl (Theoretical)	MnTPPCl powder	125 nm MnTPPCl film
C (1s)	0.25	44	66.6	59.6
N (1s)	0.42	4	5.6	5.0
Mn ($2p_{3/2}$)	1.7	1	1	1
Cl (2p)	0.73	1	1.3	0.5

Thus, the decrease in the Cl:Mn ratio reveals a substantial Cl loss for the MnTPPCl film, suggesting partial dissociation of the axial Cl ligands from MnTPPCl during the film deposition, due to Cl-Mn bond cleavage, giving rise to MnTPP and MnTPPCl, respectively. Removal of the axial Cl ligand has been reported for MnTPPCl on Ag(111), where thermally induced dissociation of the Cl ligand is shown to result in unsaturated four-coordinate Mn(III)TPP^+ with the porphyrin ring still structurally intact [110]. On the contrary, dissociation of the axial Cl ligand leads to MnTPP in the as-deposited MnTPPCl film, with the oxidation state for the Mn ion in +2 oxidation state as suggested by UV/Visible spectroscopy.

The high resolution Cl2p XPS spectra of the MnTPPCl powder and 125 nm MnTPPCl film, shown in Figure 4.8 (a) and (b) respectively, exhibit the distinctive doublet structure arising from spin-orbit splitting to $2p_{3/2}$ and $2p_{1/2}$ [110, 140]. The doublet feature and the relative positions of the Cl2p photoemission lines seen in the MnTPPCl powder and film are alike, with the binding energies of $2p_{3/2}$, and $2p_{1/2}$ corresponding to 198.1 and 199.7 eV, and 197.9 and 199.5 eV respectively with spin-orbit spitting of 1.6 eV, consistent with the value of 197.6 eV reported for Mn(III)TPPCl [165], suggesting the Cl ligand is in the axial coordination in MnTPPCl for both powder and film.

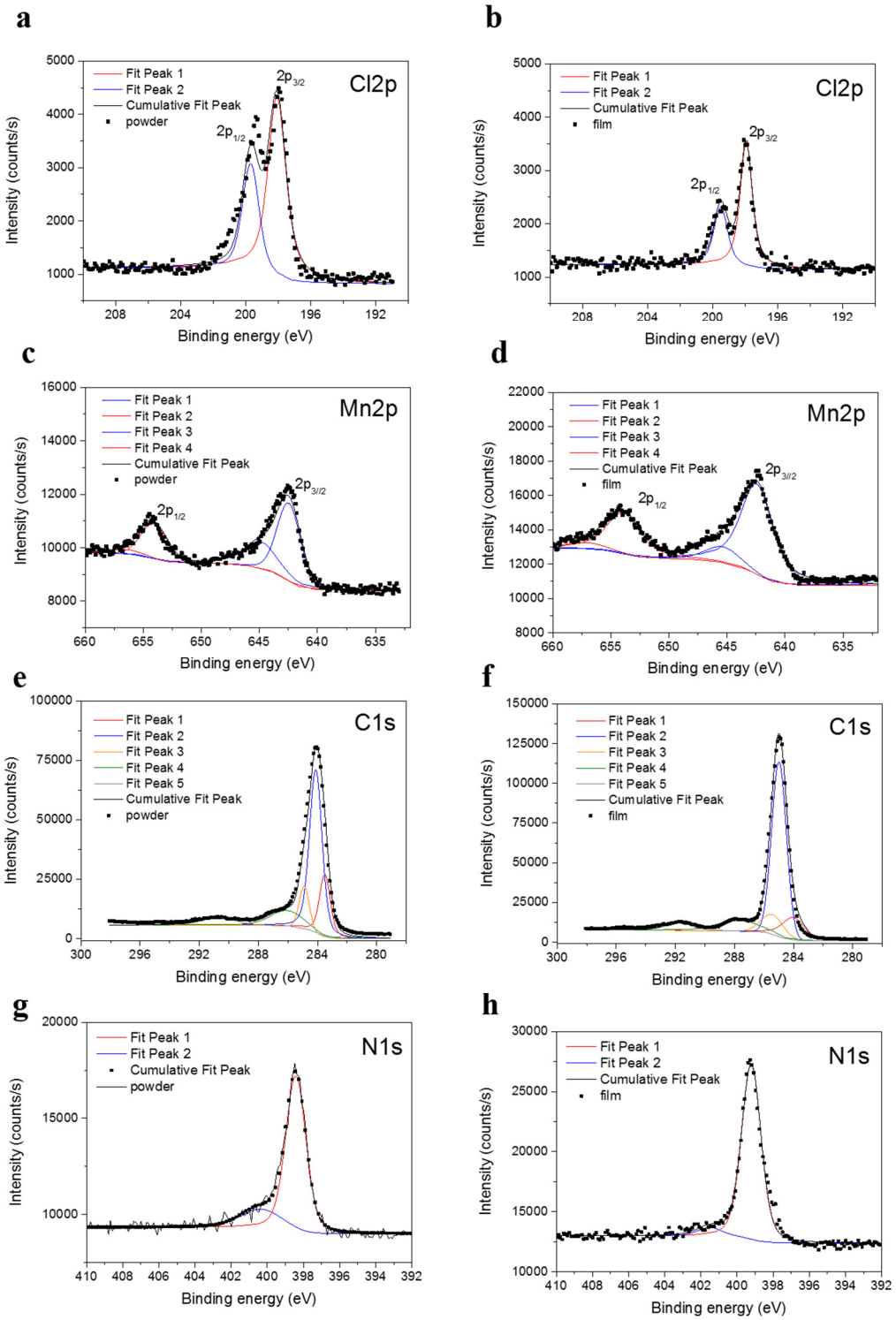


Figure 4.8 High resolution of XPS core-level spectra of (a), (c), (e) and (g) the MnTPPCl powder and (b), (d), (f) and (h) MnTPPCl film. The photoemission lines are deconvoluted with the Voigt peak shape and the background is subtracted with the Shirley algorithm.

Table 4.5 Summary of the peak centers and areas extracted by using the Voigt function to deconvolute the C1s, N1s, Cl2p and Mn2p spectra recorded from the MnTPPCl powder and 125 nm thick MnTPPCl film. The relative quantities for the different chemically inequivalent C atoms listed in bracket are calculated without contribution from the π-π shake-up.

		MnTPPCl powder		125 nm MnTPPCl film	
		B.E. (eV)	%	B.E. (eV)	%
C1s	$C_{N\beta}$	284.4	17.8 (19)	284.0	12.8 (13.6)
	C_{phen}	285.0	53.0 (56.2)	285.0	59.5 (63.0)
	$C_{meso\text{-}bridged}$	285.7	9.7 (9.6)	285.4	10.0 (10.6)
	$C_{N\alpha}$	287.0	13.1 (14.6)	287.7	12.2 (12.9)
	π-π shake-up	291.6	6.4 (-)	291.8	5.6 (-)
N1s		399.3	81.1	399.2	92.9
	π-π shake-up	401.3	19.0	401.5	7.1
Mn2p	$2p_{3/2}$	642.5	66.8	642.4	67.3
	$2p_{1/2}$	654.1	33.2	653.9	32.7
Cl2p	$2p_{3/2}$	198.1	67.1	197.9	66.5
	$2p_{1/2}$	199.7	32.9	199.5	33.5

Whilst a significant reduction in the Cl:Mn ratio is found in the MnTPPCl film, the observed binding energies suggest that the Cl ligands that contribute to the photoelectron signal should adopt the same chemical state as that in the MnTPPCl powder. Therefore, the Cl ligands that are undissociated are in the axial coordination to the Mn ion, maintaining as a five-coordinate Mn (III) porphyrin complex.

Thus, except for ~ 60 % of the Cl ligands originally in the axial coordination to the Mn ions in MnTPPCl that become dissociated, the environment of the Cl ligands in the MnTPPCl film appears to be relatively unaffected by the film deposition. To investigate the effect of the dissociation of the axial Cl ligands on the Mn ion, the corresponding high resolution Mn2p spectra of the MnTPPCl powder and film are shown Figure 4.8 (c) and (d).

The high resolution Mn2p spectrum obtained from the MnTPPCl film is compared to the powder, as shown in Figure 4.8 (d) and (c). The spectrum of the MnTPPCl powder exhibits $Mn2p_{1/2}$ and $Mn2p_{3/2}$ peaks owing to spin-orbit splitting (11.6 eV), corresponding to two peaks observed at the binding energies of 654.1 and 642.5 eV, along with low intensity satellites [166], close to the reported values of 653.8 and 642.2 eV for Mn $2p_{1/2}$ and $2p_{3/2}$

peaks [159] in the five-coordinate Mn(III)TPPCl. Therefore, the oxidation state for the Mn ion present in the MnTPPCl powder is attributed to +3 as expected.

As for the as-deposited MnTPPCl film, similar spin-orbit splitting features can be found, with very little change to the line-shape and peak positions corresponding to Mn $2p_{1/2}$ (653.9 eV) and Mn $2p_{3/2}$ (642.4 eV) peaks, suggesting that the oxidation state adopted by the Mn ion contained in the film to be the same as that in the powder. Although these observed values appear to be more consistent with those reported for Mn(III)TPPCl rather than Mn(II) in the four-coordinate environment, Mn(II)TPP, with expected binding energies for the Mn $2p_{1/2}$ and Mn $2p_{3/2}$ peaks corresponding to 653.1 and 641.1 eV [159] respectively, it is difficult to unambiguously attribute the Mn oxidation state based on the Mn2p photoemission lines, since the difference in Mn2p peaks only ranges in 0.5 eV when the oxidation state changes from Mn(II) to Mn(IV) [167]. Presence of both Mn(II) and Mn(III) in the as-deposited MnTPPCl film previously observed by UV/Visible spectroscopy is due to different sampling depths/schemes used in the two different techniques. XPS is comparatively local, and surface-sensitive technique, primarily collecting chemical information limited to 10 nm in-depth in the sample. Moreover, the respective Mn(II)/Mn(III) ratio might vary accordingly from inside the film to its surface, where spontaneous oxidation of Mn(II) $\longrightarrow$ Mn(III) under ambient conditions is more likely to proceed at an even faster rate.

The line-shape of the high resolution of C1s spectra is very similar in the MnTPPCl powder and MnTPPCl film (Figure 4.8 (e) and (f)), suggesting that the structure of the porphyrin ring is relatively unaffected upon dissociation of the Cl ligand. The MnTPPCl powder displays a main peak at 285.0 eV with a shoulder at higher binding energy, with presence of a small and broad peak at 291.6 eV, in agreement with the value expected for the metal-free TPP [168].

The broadened peak base observed for the C1s profiles in both the MnTPPCl powder and MnTPPCl film can be interpreted by the multiple components of chemically distinct C atoms (see Figure 4.9). In a recent report by Beggan *et al.* [110], the C1s line-shape obtained from MnTPPCl on Ag(111) can be deconvoluted into five different spectral components in accordance with the chemical environment present in MnTPPCl, in which 20 C atoms in the benzene ring are attached to the main porphyrin ligand via the four meso-bridged C atoms connected to the imidazoyl nitrogen, and the two different C atoms at the α, and β positions composed in the pyrole groups, respectively.

Following the analysis as in [110], the fit for the C1s profile obtained from the MnTPPCl powder reveals a main peak at the binding energy of 285.0 eV, which corresponds to the C atoms in the benzene ring, accounting for the 56 .2 % of contribution to the C1s signal, and two peaks at 287.0 and 284.4 eV with contributions of nearly 1 to 1 ratio (14.6 % and 19.0 %, respectively) are ascribed to the spectral emission by the C atoms in the α and β positions. Lastly, the smallest area corresponding to ~ 9.6 % can be attributed to photoemission from the C atoms in the meso-bridged position. For the MnTPPCl film, the analysis on the C1s spectrum shows a peak at 285.0 eV (59.5 %), and areas with almost the same ratio underneath the 284.4 and 287.8 eV peaks, followed by the smallest area at the peak at 285.4 eV, giving rise to a 6.0:1.3:1.2:1.0 ratio, consistent with the ratio of 5.7:2.0:1.5:1.0 found for the MnTPPCl powder and the theoretical ratio of 5:2:2:1. Therefore, the structure of the porphyrin macrocycle is intact upon the Cl dissociation. This is possibly due to the molecular orbitals being very localized on the porphyrin ligand, largely unmixed with molecular orbitals originating from the Cl ligand [110].

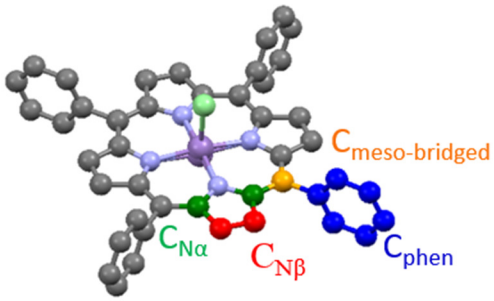


Figure 4.9 Colour scheme for the molecular structure of MnTPPCl and the chemically distinctive carbon atoms, adapted from [119].

As with what is observed for the C atoms in the porphyrin ring, no observable differences on the chemical environment for the N atoms can be found between the MnTPPCl powder and MnTPPCl film, as shown in Figure 4.8 (g) and (h). The N1 photoemission line seen in the MnTPPCl powder displays a main peak at 399.3 eV and a very weak band at 401.3 eV, with a difference in binding energy ~ + 2.0 eV away from the N1s main peak, attributed to π-π shake-up. Again, a similar spectrum is obtained from the MnTPPCl film, where the N1s main peaks can be found at the binding energy of 399.2 eV, followed by a π-π shake-up present at 401.5 eV. The N1s binding energies observed for the MnTPPCl powder and film are comparable to the value of 398.9 eV reported for N1s seen in Mn(III)TPPCl [165],

confirming that the porphyrin macrocycle is uninfluenced by the dissociation of the axial Cl ligand.

In conclusion, the composition of the MnTPPCl film grown by OMBD shows a substantial loss of the axial Cl ligand from MnTPPCl, possibly triggered by the thermal sublimation during the film deposition. The observed Cl:Mn ratio shows ~ 60 % of the Cl ligands previously bound to the Mn ions have dissociated from MnTPPCl, resulting in four-coordinate and five-coordinate Mn porphyrin complexes both contained in the as-deposited MnTPPCl film, corresponding to Mn(II)TPP and Mn(III)TPPCl, respectively. The Mn oxidation state for the MnTPPCl film is tentatively assigned to be in +3, due to the oxidation on the MnTPPCl film surface.

4.1.4 Magnetic characterization of the films

The magnetic properties of MnTPPCl were measured by SQUID, using powder instead of an as-deposited MnTPPCl film to ensure a system only containing Mn(III)TPPCl.

The isothermal magnetization curves of the MnTPPCl powder measured between 2 and 10 K are shown in Figure 4.10 (a). As can be seen, no hysteresis is observed for the MnTPPCl powder when the applied field is swept between ± 7 Tesla for all the temperatures studied. At the temperature of 2 K, the net magnetic moment per Mn ion is found to increase at a reasonably fast rate, reaching 2.0 μ_B at H = 2 Tesla. Between the applied field (H) of 2 to 7 Tesla, the magnetic moment increases gradually and finally saturates at (μ_{sat}) ~ 4.4 μ_B as the field is swept to 7 Tesla, in good agreement with the expected saturated moment reported for Mn(III)TPPCl [104], suggesting the Mn ion in MnTPPCl adopts a high-spin d^4 Mn(III) with spin state S = 2.

The net magnetic moment per Mn atom is found to reduce with increasing temperature, and the shape of the $M(H)$ curves only becomes more linear as the temperature is increased to 10 K. Figure 4.10 (a) shows that at 2 K the magnetization per Mn as a function of the applied field can be described by a Brillouin function based on an uncoupled spin system with S = 2, g = 2. This finding therefore confirms MnTPPCl in the powder sample exhibits paramagnetic behaviour.

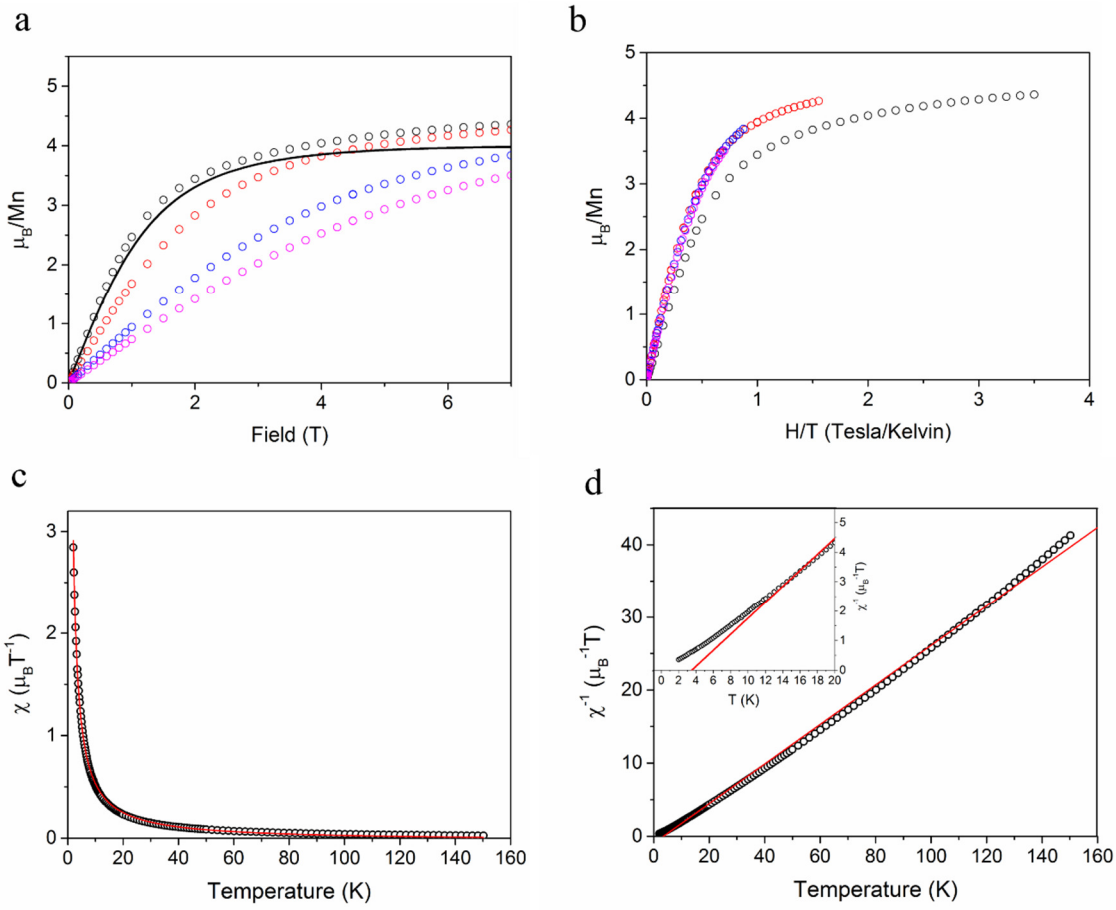


Figure 4.10 (a) Field dependent magnetization curves, M(H), at 2 K (black), 4.2 K (red), 8 K (blue) and 10 K (magenta) of the MnTPPCl powder, the solid line representing a paramagnetic spin $S = 2$, $g = 2$, $T = 2$ K (black), (b) the net moment as a as a function of the ratio of field over temperature (H/T) of the MnTPPCl powder, at 2 K (black), 4.2 K (red), 8 K (blue) and 10 K (magenta), (c) magnetic susceptibility as a function of temperature $\chi(T)$ of the MnTPPCl powder (open black circle) with the Curie-Weiss expression (red), and (d) inverse magnetic susceptibility as a function of temperature $1/\chi$ (open black circle) fitted with the Curie-Weiss fit (red) applied between 14 and 120 K.

The saturation moment (μ_{sat}) ~ 4.4 μ_B in the MnTPPCl powder is slightly larger than the saturation moment (μ_{sat}) of 4 μ_B expected from a fully uncoupled spin system $S = 2$, possibly due to very small amount of ferromagnetic impurities in the sample, since the MnTPPCl powder was used as received. The paramagnetic behaviour of MnTPPCl is reflected by the scaling law H/T, (Figure 4.10 (b)), where the H/T scaling behaviour can be observed for all the temperatures, except for a very slight suppression seen in the 2 K magnetization curve. This might suggest presence of weak antiferromagnetic correlations.

The temperature dependent magnetic susceptibility $\chi(T)$ of the MnTPPCl powder is shown in Figure 4.10 (c). For the temperature between 14 and 120 K, the magnetic susceptibility of the powder is fitted with the Curie-Weiss expression (shown in red in Figure 4.10 (d)), extracting a slightly positive Weiss temperature of + 3.5 K and Curie constant (C) of $5.5\,\mu_B K T^{-1}$, corresponding to a spin state of $S = 2$ with $g = 2$.

Therefore, both the $M(H)$ and $M(T)$ measurements indicate that the MnTPPCl powder to be a paramagnetic material, and the magnetization per Mn ion as a function of the applied field (H) can be described by Brillouin $S = 2$, $g = 2$, confirming the high-spin d^4 Mn(III) with the spin state $S = 2$.

4.2 Degradation of the films

Significant changes in the intensities for the optical absorbance in Peak5 (λ = 447 nm) and Peak4 (λ = 484 nm) (see Table 4.2), corresponding to the Soret features due to Mn(II) and Mn(III), respectively, can be observed for the spectra of the 100 nm MnTPPCl film recorded at different time intervals, as shown in Figure 4.11. The spectral changes are therefore attributed to the degradation of the MnTPPCl film.

The most apparent change can be found for the Peak5 (2.77 eV), which is the absorption maximum in the optical spectrum recorded from the 100 nm thick MnTPPCl film after film deposition (Figure 4.11 (1)), but drastically decreases its absorption intensity within 28 days after growth (Figure 4.11 (2)), and becomes almost not observable approximately two years later (Figure 4.11 (3)). On the contrary, a gradual increase in the absorbance can be observed for the Peak4 (2.57 eV), corresponding to the absorption maximum in the optical spectrum obtained 2 years after growth, in comparison to the those recorded 28 days and immediately after film deposition.

Differences in both the shape and intensity for the B-band region can also be noticed, and the B-band seen in the optical spectra recorded 28 days and around 2 years after the growth has become very similar to that in the solution, due to the sharp decrease in the neighbouring absorption at 2.77 eV (corresponding to the Soret band of Mn(II)).

By contrast, no apparent spectral changes can be found in the Q-band and Band III, indicating the absorption at a wavelength between 500 to 700 nm is less affected by degradation. This

contradiction is most likely due to the different origins for the Q-band and Band III with considerably low absorption intensities. The transitions occur within the porphyrin macrocycle that are relatively inert towards the change for the oxidation state of the metal ion, while both the B-band and Soret band arise from the charge-transfer transitions (Mn(III) - porphyrin ring), thus more sensitive to perturbation on the electron density of the metal ion and more diagnostic for the Mn oxidation state.

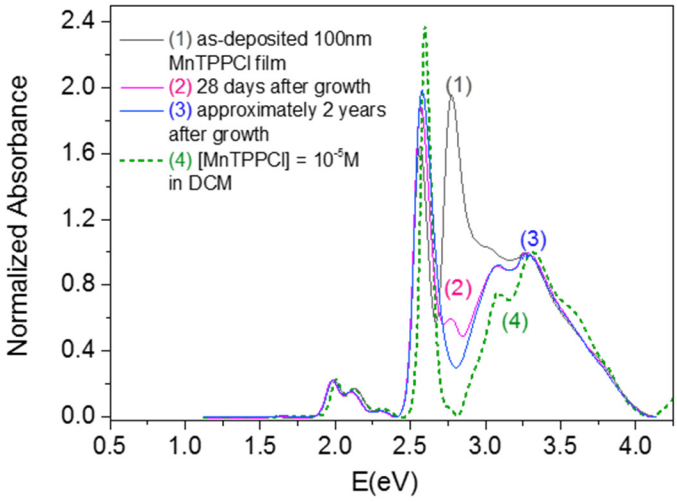


Figure 4.11 Optical spectra of the 100 nm thick MnTPPCl film deposited at the rate of 0.9 Å/s on glass, recorded under different times and conditions, (1) as-deposited, (2) 28 days, (3) nearly 2 years after the film deposition, and (4) the MnTPPCl solution in dichloromethane (DCM), with the concentration of 10^{-5} M. All the spectra are normalized to the absorption intensity of the B-band, λ = 375 nm.

These time-dependent spectral responses seen for the Peak4 (Mn(III)), Peak5 (Mn(II)) as well as the B-band in the 100 nm thick MnTPPCl film subsequently suggest the Mn(II) present in the as-deposited MnTPPCl film gradually oxidizes to Mn(III) with time when stored under ambient conditions in the absence of light, giving rise to an absorption spectrum almost indistinguishable from that recorded from the MnTPPCl solution (Figure 4.11 (4)). By contrast, it appears that the rate of degradation can be significantly reduced if stored under an anaerobic environment, as seen for the MnTPPCl film kept under the dark in the glovebox in which the oxygen level had been maintained to be ~ 20 ppm, as shown in Figure 4.12. This subsequently confirms the role oxygen plays in the degradation observed for the MnTPPCl films.

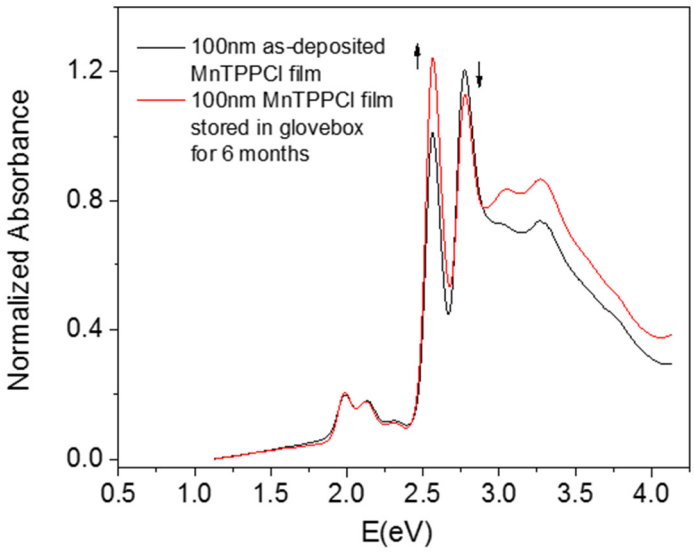


Figure 4.12 Optical spectra of the 100 nm MnTPPCl film obtained right after the growth (black) and stored in the glovebox for 6 months (red).

In MnTPPCl solutions, Mn adopts high-spin d^4 Mn(III), which is the most stable oxidation state for Mn ions under the aerobic environment [104]. The stability of Mn(III) towards other oxidation state such as +2 and/or +4 in ambient conditions can be verified after removing oxygen by bubbling inert gas, for instance, Ar into the sealed MnTPPCl solution continuously for at least 20 min, with no observable changes in both the shape or intensity for the Soret band for Mn(III), as shown in Figure 4.13.

In order to investigate the effect of the thickness on the film degradation, the absorption spectra of the MnTPPCl films with thicknesses of 100 nm, 75 nm, 50 nm, 33 nm and 25 nm, respectively, were recorded at periodic time intervals and shown in Figure 4.14. As can be seen, a similar trend in the changes to the relative absorption intensities in Peak4/Peak5 previously observed for the 100 nm MnTPPCl film can also be found, and the absorption maximums are seen to shift from Peak5 to Peak4 due to the gradual increase/decrease in the absorption intensities for the respective bands with time. This finding suggests that the degradation is typical for the as-deposited MnTPPCl film, and occurs for all the thicknesses studied.

Film thickness does however slightly influence the rate at which degradation proceeds. For example, Figure 4.14 shows that for the thinnest film studied, 25 nm, the band at λ = 447 nm

is almost unobservable when stored under ambient conditions for one week after the film was deposited, suggesting that most of the Mn(II) ions formed during the deposition were oxidized within seven days, leaving predominately Mn(III) in the 25 nm MnTPPCl film. By contrast, the peak at λ = 474 nm can still be identified for the 100 nm thick MnTPPCl film after storage under the same conditions for 28 days after deposition, indicating the time needed to obtain a fully oxidized MnTPPCl film is thickness dependent.

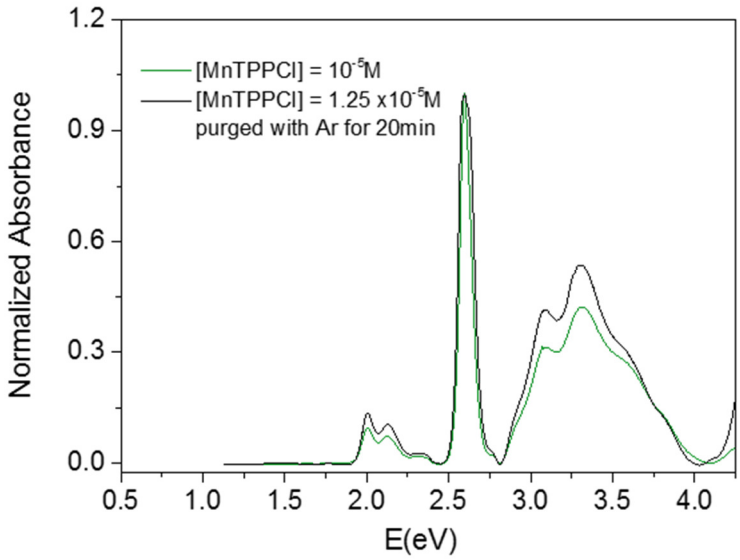


Figure 4.13 Optical spectra of the MnTPPCl solutions under ambient conditions (green), with a concentration of 10^{-5} M in dichloromethane, and in a sealed cuvette purged with Ar for 20 mins with a concentration of 1.25×10^{-5} M in dicholoromethane (black). All the spectra are normalized to the absorbance in the respective Soret band, λ = 478 nm. The position for the same band in the as-deposited MnTPPCl film is λ = 484 nm.

The different degradation rates seen for the various film thicknesses should be correlated to the ratio of Mn(II) and Mn(III) ions contained in the as-deposited MnTPPCl film, as reflected by the band ratios and/or peak areas in the absorption intensity at λ = 447 nm and λ = 484 nm, which indicates the largest ratio Mn(II)/Mn(III) ratio found in the as-deposited 100 nm MnTPPCl film. In addition, the surface area for all the film thicknesses studied is similar in size, and thus, degradation is expected to proceed faster with decreasing film thickness, since the initial amount of Mn(II) in the 25 nm film is relatively lower than that observed for the 100 nm film (see Table 4.3).

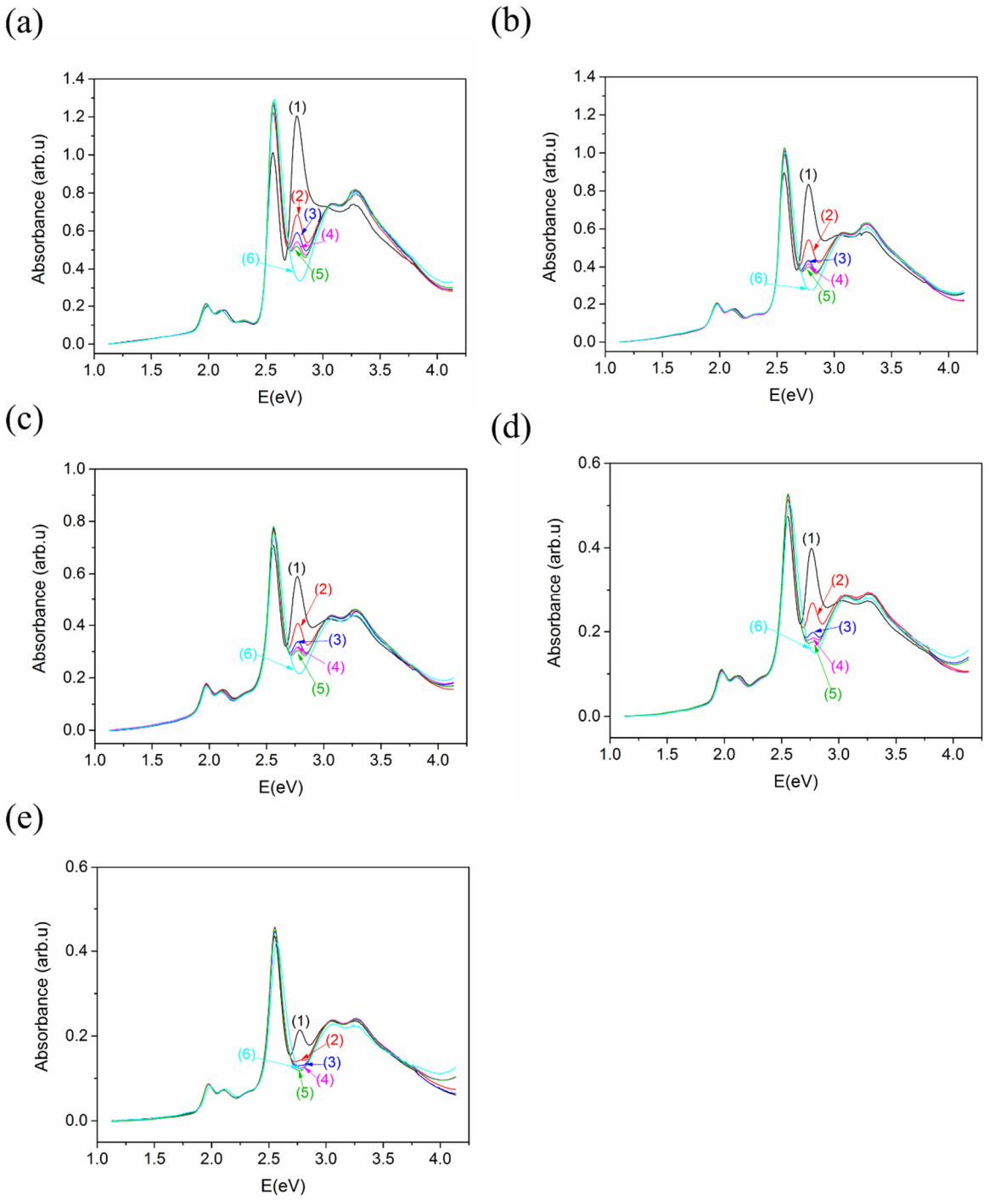


Figure 4.14 Electronic absorption spectra of the MnTPPCl films deposited at the rate of 0.9 Å/s on glass, with the thickness of (a) 100 nm (b) 75 nm (c) 50 nm (d) 33 nm, and (e) 25 nm, recorded at different time intervals shown in black, red, blue, magenta, olive and cyan curves with labels, (1) as-deposited, (2) 7 days, (3) 14 days (4) 21 days (5) 28 days, and (6) approximately after two years after film deposition. The films were stored under ambient conditions in the absence of light during the course of this study.

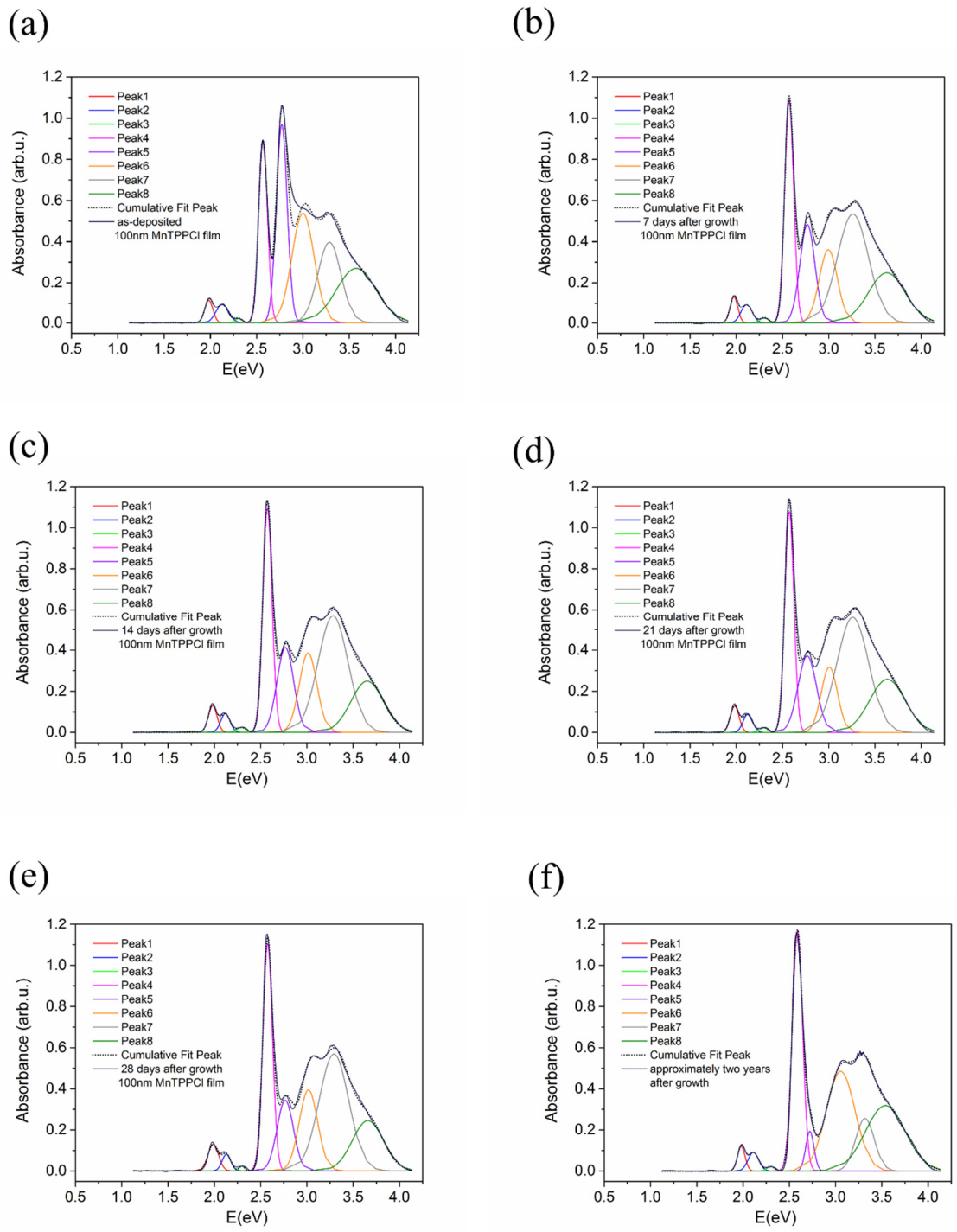


Figure 4.15 Optical spectra of a 100 nm thick MnTPPCl film recorded at different time intervals, corresponding to (a) as-deposited, (b) 7 days, (c) 14 days, (d) 21 days, (e) 28 days, and (f) approximately 2 years after film deposition stored under dark and ambient conditions, plotted in the scale of eV and shown with the individual Gaussian functions that are to deconvolute the spectra. Peak4 and Peak5 correspond to the Soret features for Mn(III)- and Mn(II)-porphyrins, respectively.

Table 4.6 The parameters extracted for the absorption bands at λ = 447 nm (2.77 eV) and λ = 484 nm (2.57 eV) in the optical spectra for a 100 nm thick MnTPPCl film recorded at different time intervals (see text).

	Peak4/Mn(III)				Peak5/Mn(II)			
	Center (eV)	Height (arb.u)	FWHM (eV)	Area (arb.u)	Center (eV)	Height (arb.u)	FWHM (eV)	Area (arb.u)
As-deposited	2.57	0.8904	0.1124	0.1066	2.77	0.9680	0.1389	0.1432
7 days	2.57	1.0811	0.1151	0.1325	2.77	0.4833	0.1910	0.0983
14 days	2.57	1.0926	0.1174	0.1365	2.77	0.4121	0.2117	0.0929
21 days	2.57	1.0800	0.1150	0.1323	2.77	0.4121	0.2355	0.0933
28 days	2.58	1.1032	0.1214	0.1426	2.77	0.4121	0.2072	0.0756
~ 2 years later	2.59	1.1659	0.1312	0.1628	2.72	0.1930	0.1048	0.0215

The absorption spectra of the 100 nm MnTPPCl film recorded at different time intervals were deconvoluted into Gaussian components (see Figure 4.15 for the 100 nm thick film), extracting the peak positions, heights, FWHMs and areas for the Peak4 (λ = 484 nm) and Peak5 (λ = 447 nm), summarized in Table 4.6. It can be immediately seen that both the peak height and area for Peak4 gradually increase with time, whereas an opposite trend can be observed for the Peak5.

Thus, the kinetic aspects of the degradation can be obtained by plotting the respective areas for the Peak4 at λ = 484 nm (2.57 eV, Mn(III)) and Peak5 at λ = 447 nm (2.77 eV, Mn(II)) as a function of time, as shown in Figure 4.16. Again, the area for the Peak4 at λ = 447 nm (Mn(II), 2.77 eV) appears to gradually decrease, whereas the opposite is seen for the Peak5 at λ = 447 nm (Mn(III), 2.57 eV) over the entire duration. It appears that the most apparent changes in the areas for both the absorption peaks occur in the first seven days, and then proceed by a gradual increase/decrease, in a good agreement with the optical spectra recorded from the 100 nm film, as shown in Figure 4.14. The peak parameters extracted for the Peak5 from the optical spectrum recorded 2 years afterwards are however more likely to include larger errors, due to its very low absorption intensity.

The trend in the increase and decrease observed for the absorption intensities in the Peak4 and Peak5 is analogous to the oscillatory behaviour reported for the MnTPPCl solutions, where a shift in the absorption maxima is accompanied by the one electron reduction [106,

169], with the Peak5 corresponding to the Soret band for the Mn(II) porphyrins [105, 106, 169]. The changes to the absorption intensities in turn reflect the increase and decrease in the quantities for the Mn(III) and Mn(III) ions with time. As a consequence, the sum of the amounts of Mn(II) and Mn(III) contained in the MnTPPCl film is expected to be a constant at any time during the course of study.

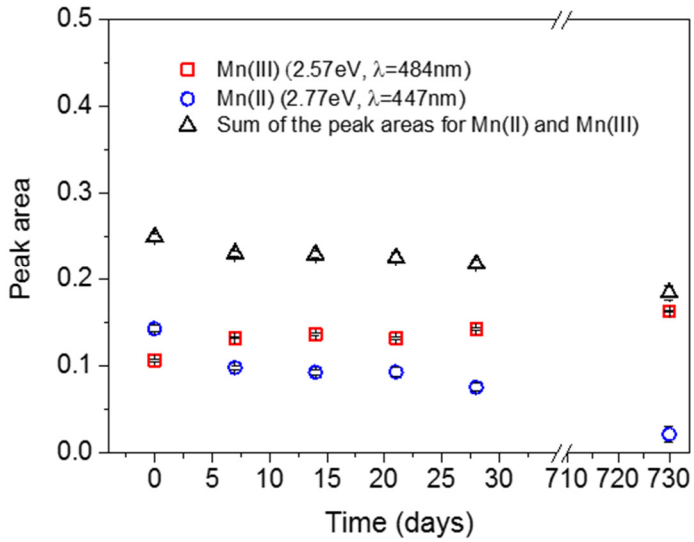


Figure 4.16 The areas for Peak4 (λ = 484 nm, Mn(III), shown in red rectangle) and Peak5 (λ = 447 nm, Mn(II), shown in blue circle) extracted from the optical spectra recorded from the 100 nm thick MnTPPCl film by deconvolution with the Gaussian components (see text), plotted as a function of time, and the sum (shown in black triangle) obtained by adding the peak areas for Peak4 and Peak5, plotted as a function of time.

Thus, the Peak5 and Peak4 are actually the Soret features for Mn(II)- and Mn(III)-porphyrins, indicating the origins for the two absorption bands should correspond to a similar type of transitions. Guided by the optical spectrum recorded from the 100 nm thick as-deposited MnTPPCl film, shown in Figure 4.14, the oscillator strengths for the two bands must be very similar, or at least on the same order of magnitude. The absorption peaks for Mn(II)TPP and Mn(III)TPP^+ in DMSO solution were reported to exhibit strong absorption intensity at λ_{max} = 437 nm (extinction coefficient (ε), $\varepsilon = 2.5\text{x}10^5$) and λ_{max} = 463 nm ($\varepsilon = 1.4\text{x}10^5$), respectively [169]. Given the optical behaviour observed for the MnTPPCl film is remarkably similar to isolated MnTPPCl, as represented by the solution spectrum, it is possible that other optical characteristics of both Mn(II) and Mn(III), such as their respective extinction coefficients, despite determined based on the solutions, are also alike for the thin film form.

If the oscillator strength for the respective Soret peaks seen for the as-deposited MnTPPCl film is truly similar, the corresponding peak areas would allow one to deduce the amount or concentration for the Mn species present in the film. Thus, the sums of the areas extracted for the Peak4 at λ = 447 nm (Mn(II), 2.77 eV) and Peak5 at λ = 484 nm (Mn(III), 2.57 eV) are plotted as a function of time, shown in Figure 4.16. The result of this analysis shows the total amount of Mn(II) and Mn(III) species obtained in the MnTPPCl film at any time during this study is almost unchanged, and validates the our assumption for the oscillator strengths of the Soret bands corresponding to the two Mn species obtained from the as-deposited 100 nm film.

Since Mn(II) observed in the as-deposited film gradually oxidizes to Mn(III) over time, the decrease in Mn(II) species is expected to be equivalent to the increase for the Mn(III) ions. The relative amounts of the Mn(II) and Mn(III) species contained in the as-deposited MnTPPCl film can be calculated from the areas extracted for the Peak4 and Peak5 (Table 4.6) by using the Beer-Lambert's law (see section 2.4.1), which quantitatively relates the observed absorption intensity to concentration of the analyte.

As a consequence, the ratio between Mn(II) and Mn(III) species contained in the as-deposited 100 nm thick MnTPPCl film is 0.57:0.43, respectively. It is likely that the ratio somewhat underrepresents the actual quantity in the MnTPPCl film, owing to larger errors in the low intensity recorded two years after the growth. The calculations have not considered the difference between the oscillator strengths for the two Soret bands, due to the lack of absolute values for the MnTPPCl film. This analysis nevertheless confirms degradation observed for the as-deposited MnTPPCl films proceeds as the Mn(II) species contained in the as-deposited MnTPPCl film gradually oxidize to Mn(III), as reflected by the increasing peak intensity (Peak4) with time, and confirms the origin of Peak5 to be Mn(II). Using the same approach, information on the rate at which Mn(II) contained in the as-deposited MnTPPCl films oxidizes can be obtained, and oxidation appears to proceed faster with decreasing thicknesses, as shown in Figure 4.17, consistent with the spectral evolution as a function of time, seen in Figure 4.14.

In summary, when deposited as thin films, the oxidation state for the Mn ion in MnTPPCl first changes from +3 to +2, via self-reduction Mn(III) → Mn(II), during the film processing provided by the OMBD. The self-reduction of Mn(III) that occurs in the vapour phase of Mn(III)TPPCl is accompanied by the partial dissociation of the Cl ligands in the axial ligation

to the Mn ion. As a consequence, both Mn(II)TPP and Mn(III)TPPCl are contained in the as-deposited MnTPPCl film, since the Soret peaks corresponding to both Mn(II) and Mn(III) porphyrins can be observed by the UV/Visible spectroscopy. The absorption intensity in the Soret peak for Mn(III) is found to increase with time, and meanwhile, the opposite trend is seen for the Soret peak for Mn(II). These spectral changes are considered as film degradation, which shows both time and thickness dependence, for the as-deposited MnTPPCl films that were stored under ambient conditions in absence of light.

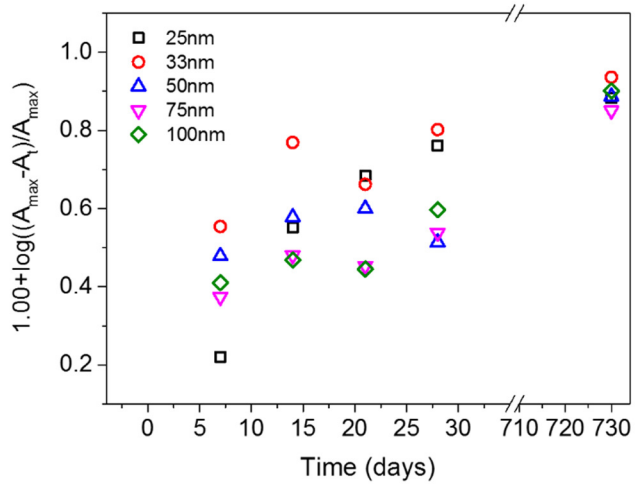


Figure 4.17 The decease of % Mn(II) contained in the MnTPPCl films with the thickness of 25 nm (black rectangle), 33 nm (red circle), 50 nm (blue triangle), 75 nm (magenta triangle) and 100 nm (green diamond) plotted in logarithm as a function of time.

Table 4.7 The relative amounts calculated for the Mn(III) and Mn(II) species.

	Mn(III) relative amount (%) and error (%)		Mn(II) relative amount (%) and error (%)	
As-deposited	42.7	0.8	57.3	1.8
7 days	57.4	0.8	42.6	1.3
14 days	60.0	1.0	40.5	1.6
21 days	58.6	1.8	41.4	2.8
28 days	65.4	1.5	34.6	2.1
~ 2 years later	88.3	4.2	11.7	4.8

Presence of oxygen is a key factor in degradation for MnTPPCl films, and the oxygen concertation dominates the rate at which the degradation proceeds, as the study was conducted in the absence of light. While the same type of degradation could still be found in the MnTPPCl film stored under the nitrogen environment in the glovebox, the Soret peak for Mn(II) porphyrin could still be observed around six months after the film deposition, giving rise to ~ 51.1 % Mn(II). This observation reveals the degradation for the MnTPPCl film is linked to oxygen, which diffuses through the amorphous film structure and slowly oxidizes Mn(II)TPP that is introduced through the film processing. Degradation seen in the MnTPPCl film is expected to occur and proceed with presence of light, which is likely to further influence the rate at which Mn(II) oxidizes.

The changes in the respective Soret peaks for the Mn(II) and Mn(III) porphyrins studied as a function of time reflect the increase and decrease are a consequence of Mn(II) oxidation, whose relative quantities contained in the MnTPPCl film can be deduced from their respective absorbance, based on the Beer-Lambert's law. Given the degradation is both time and thickness dependent, it is more likely that oxidation of Mn(II) begins from the first few monolayers in close proximity of the MnTPPCl film surface, on which the adsorbed oxygen can start to diffuse through and reach further with time. As shown in Figure 4.17, the film thickness influences the rate at which Mn(II) oxidizes, in addition to the time it needs to convert all the Mn ions to Mn(III). As the thickness is increased to 50 nm, the rate for Mn(II) to oxidize is considerably slower than those seen for the films with a thickness below 50 nm, and appears to be independent of thickness as observed for the 75 nm and 100 nm film. This suggests diffusion from the film surface through the molecular layer is relatively easier and faster with the thickness of 50 nm, and the upper molecular layers that are already oxidized might have passivated the film surface, giving rise to a slower rate for Mn(II) to oxidize seen in the thicker films.

These results show it is relatively easy to access various oxidation states of Mn ion in the five-coordinate porphyrin complex, and the redox reactions can occur under mild conditions, and in absence of sources of strong electron donors that would have been required to reduce Mn(III)TPPCl to Mn(II)TPPCl in solutions [24, 170]. In this respect, sublimation of Mn(III)TPPCl is the only pre-requisite for Mn(II)TPP to form, since the self-reduction of Mn(III) to Mn(II) has so far been reported for the vapour phase, suggesting the conditions for film processing, *i.e.* the temperature for the knuden cell during deposition and/or post-growth annealing, might be useful for controlling the oxidation state for Mn porphyrins.

Although the details and mechanism are not clear, it is very likely that the onset of growth proceeds with sublimation of Mn(III)TPPCl, which self-reduces to Mn(II)TPP through a pathway generated in the growth conditions provided by the OMBD. Thus, co-evaporation with MnTPPCl and TCNQ by using OMBD to form the charge transfer salt [MnTPP][TCNQ] can be particularly advantageous, since around 50% of Mn(III)TPPCl molecules used to deposit a film have already converted to the precursor Mn(II)TPP, as suggested by UV/Visible spectroscopy and XPS.

5. Co-deposited [MnTPPCl][TCNQ]

Previous chapters have shown that MnTPPCl and TCNQ can be deposited controllably, even though MnTPPCl is partially reduced upon growth and oxidized with time. These materials are building blocks for molecular magnets in powder form. Here we investigate how they behave as their films. The effects of blending electron donor and acceptor via co-deposition on the resultant film properties are investigate. The co-deposited [MnTPPCl][TCNQ] films represent an interesting charge transfer system, which shows distinctive properties that do not belong to those seen for isolated MnTPPCl or TCNQ, but attributed to the charge transfer donor-acceptor dimer [MnTPP][TCNQ] contained in the film. SQUID measurements reveal presence of antiferromagnetic coupling arising from the interactions between the unpaired spins on the Mn center and $TCNQ^{\bullet -}$ for the charge-transfer dimer [MnTPP][TCNQ] in the co-deposited film, giving rise to an overall magnetic moment consistent with the expectation from a net spin S = 3/2 system.

5.1 UV/Visible spectroscopy of the films

The [MnTPPCl][TCNQ] films are fabricated by co-deposition of MnTPPCl and TCNQ. The MnTPPCl and TCNQ powders are loaded in separate Knudsen cells in the OMBD chamber. The composition for films based on a mixture of two different molecules can be directly adjusted through the deposition rate, and the details to calculate the deposition rate for the two molecules are discussed in section (2.3). A 1 to 1 stoichiometry is obtained by using the deposition rates of 0.9 Å/s and 0.1 Å/s, and 0.26 Å/s and 0.03 Å/s for MnTPPCl and TCNQ, respectively, and the co-deposited films used in this study are all grown at room temperature.

The optical spectrum of the co-deposited [MnTPPCl][TCNQ] film exhibits several differences compared to those obtained from the as-deposited MnTPPCl film (see Figure 5.1). While the Soret peak for Mn(III) at $\lambda = 484$ nm and the distinctive B- and Q- bands characteristics of MnTPPCl can still be identified in the co-deposited [MnTPPCl][TCNQ]

film, the Soret peak for Mn(II) (λ = 447 nm) previously observed for the as-deposited MnTPPCl film is absent. Instead, two new absorption bands in a rather broad shape, at λ = 785 and 885 nm, can be found, accompanied by a marginal increase in the absorbance close to the UV range.

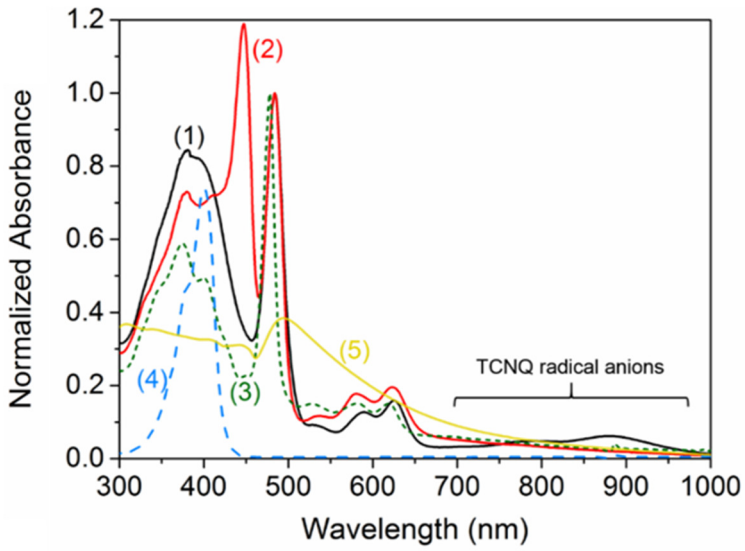


Figure 5.1 Optical spectra of (1) the co-deposited [MnTPPCl][TCNQ] film on glass substrate (an equivalent thickness of 100 nm for MnTPPCl, by using the deposition rates of 0.9 Å/s and 0.26Å/s for MnTPPCl and TCNQ, respectively), (2) the 100 nm thick as-deposited MnTPPCl film grown at the rate of 0.9Å/s on glass substrate, (3) the MnTPPCl solution dissolved in dichloromethane (DCM), with a concentration of 10^{-5} M,(4) the TCNQ solution dissolved in dichloromethane (DCM), with a concentration of $2.5x10^{-3}$M and (5) the 80 nm thick TCNQ film deposited at the rate of 0.37 Å/s on glass.

By contrast, the optical spectrum of the co-deposited [MnTPPCl][TCNQ] film shows no similar absorption features to those obtained from the TCNQ thin film, whose absorption spectrum was largely obscured by scattering effects, as shown in section (3.1.1) and (3.2.1). The increased absorbance for the B-band range seen in the co-deposited [MnTPPCl][TCNQ] film with respect to that in the as-deposited MnTPPCl film may be related to the presence of TCNQ, due to the single transition ~ 400 nm observed for isolated TCNQ [83, 86]. Thus, the spectrum of the co-deposited [MnTPPCl][TCNQ] film can be differentiated from that of the as-deposited MnTPPCl film, an effect from the co-deposited TCNQ.

The appearance of the optical spectrum of the co-deposited [MnTPPCl][TCNQ] film is dominated by the absorption features characteristics of the as-deposited MnTPPCl film,

except for the absence of the Soret peak for Mn(II)-porphyrin (at λ = 447 nm), suggesting in the co-deposited [MnTPPCl][TCNQ] film the Mn species predominately adopt +3 oxidation state. More interestingly, co-deposition with TCNQ leads to two new absorption bands in the near IR range that cannot be directly related to the optical spectrum of either isolated MnTPPCl or TCNQ.

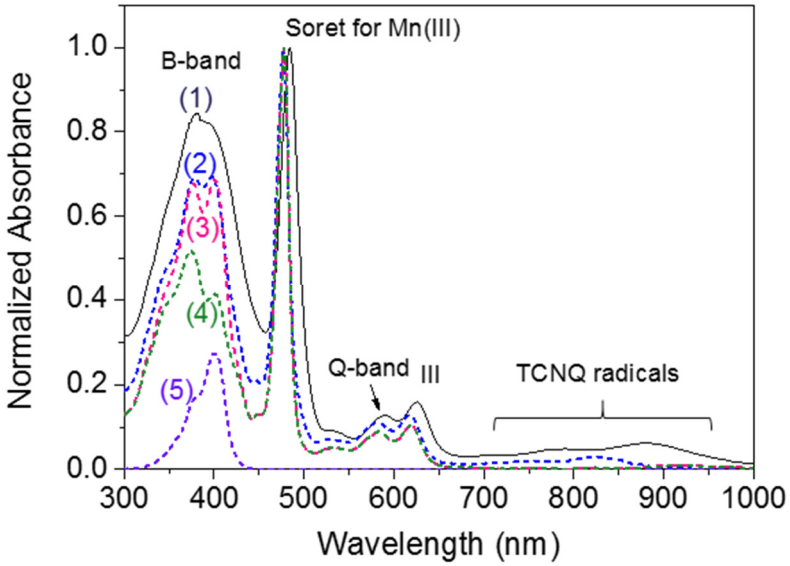


Figure 5.2 (1) Optical spectra of the co-deposited [MnTPPCl][TCNQ] film on glass substrate (an equivalent thickness of 100 nm for MnTPPCl, with a 1 to 1 ratio between MnTPPCl and TCNQ obtained by using the deposition rates of 0.9 Å/s and 0.26 Å/s for MnTPPCl and TCNQ, respectively), (2) the solution spectrum of a co-deposited [MnTPPCl][TCNQ] film grown on glass with the same deposition parameters used as in (1) fully dissolved in dichloromethane (DCM), (3) the sum of the optical spectra recorded from the MnTPPCl and TCNQ solution by combining (4): normalized solution spectrum of MnTPPCl with a concentration of 10^{-5} M in DCM and (5): the normalized solution spectrum of TCNQ with a concentration of 6.25×10^{-4} M in DCM.

To resolve the origin for the near IR bands, the optical spectrum of the co-deposited [MnTPPCl][TCNQ] film is compared to a simulated absorption spectrum that combines the absorption features of isolated MnTPPCl and TCNQ, based on superposition of the optical spectra recorded from the corresponding solutions (normalized with respect to the highest absorption intensity, shown in Figure 5.2). While the simulated spectrum seems to match with the Soret band for Mn(III), the Q-band and Band III, it cannot produce the two absorption bands at λ = 785 and 885 nm seen in the co-deposited [MnTPPCl][TCNQ] film.

Moreover, as the co-deposited [MnTPPCl][TCNQ] film is dissolved in dichloromethane, the characteristic Mn(III) peak, B- and Q-band and Band III can be seen in the absorption spectrum, the same as those observed for the MnTPPCl solution. What is more interesting to see is that the additional absorption bands at λ = 785 and 885 nm can still be found, even after the co-deposited [MnTPPCl][TCNQ] film has been fully dissolved. The additional bands in the near IR range are therefore considered as a unique optical characteristics for the co-deposited [MnTPPCl][TCNQ] film, able to survive in the dichloromethane solution for at least 10 min through the UV/Visible measurement.

Similar behaviours have been observed for other charge-transfer systems, where the appearance of additional bands that do not belong to absorption features exhibited by the individual component are a consequence of the charge-transfer between the donor and acceptor molecule. For example, CuTCNQ thin films fabricated by co-deposition of Cu and TCNQ under vacuum are reported to exhibit absorption bands in the range of 600 to 1200 nm that were otherwise absent in the neat TCNQ thin film, subsequently attributed to the charge-transfer complex [171]. In the case of molecular thin films based on MnPc/F_{16}CoPc system, the charge transfer between MnPc and the electronegative F_{16}CoPc gives rise to formation of $MnPc^{\delta+}/F_{16}CoPc^{\delta-}$ in the heterojunction, in which the transferred charge is found to be largely confined between the metal ions, as suggested by XPS [172]. The effects of charge transfer are also reported for the mixed MnPc/F_{16}CoPc films, characterized by a new spectral feature at 0.6 eV that cannot be related to either the respective spectrum of MnPc or F_{16}CoPc, in turn attributed to the hybrid states arising from the $MnPc^{\delta+}/F_{16}CoPc^{\delta-}$ dimer, consistent with the DFT calculations [173].

While no analogous absorptions can be seen in the TCNQ solution spectrum, the absorption bands at λ = 785 and 885 nm in the co-deposited [MnTPPCl][TCNQ] film actually match with what has been reported for $TCNQ^{\bullet-}$ [87, 174-177]. Neutral TCNQ is characterized by λ_{max} = 395 nm, whereas λ_{max} = 395 nm and 842 nm are reported for $TCNQ^{\bullet-}$ in a 1:1 simple salt [(Et_3NH)(TCNQ)] [177]. The ratio between the intensities for the two absorptions can indicate the relative content of TCNQ [177], though deviations can be caused by absorptions from the cation. In addition to λ = 842 nm, shoulders at λ = 760 and 743 nm are also observed for $TCNQ^{\bullet-}$ [178]. The absorption bands at λ = 785 and 885 nm present in the co-deposited [MnTPPCl][TCNQ] film are subsequently attributed to $TCNQ^{\bullet-}$, with a broader shape compared to what is seen in the corresponding solution spectrum [174, 178]. Thus, the

absorption bands at λ = 785 and 885 nm are a result of reduction of the neutral TCNQ, indicating charge-transfer has occurred between the two different molecules in the co-deposited [MnTPPCl][TCNQ] film, and conserved in solution.

To conclude, the absorption maximum at λ = 484 nm, and absence of the absorption band λ = 447 nm owing to the Mn(II) species indicate that the oxidation state for the Mn species in the co-deposited [MnTPPCl][TCNQ] film is predominately +3. This suggests that Mn(II) previously observed for the as-deposited MnTPPCl film is unable to form in the co-deposited [MnTPPCl][TCNQ] film, due to the presence of strongly electronegative TCNQ.

The oxidation of MnTPP is accompanied by reduction of TCNQ, as shown by the appearance of the radical anion $TCNQ^{\bullet -}$ in the co-deposited [MnTPPCl][TCNQ] film, characterized by the absorption bands at λ = 785 and 885 nm. As the changes in the oxidation state are found to be bound to the Mn ion and TCNQ, it therefore suggests that charge-transfer between MnTPPCl and TCNQ in the co-deposited [MnTPPCl][TCNQ] film is largely confined to the Mn ion and TCNQ, accompanied by the oxidation for Mn ion: Mn(II) ⟶ Mn(III) and reduction for TCNQ: TCNQ ⟶ $TCNQ^{\bullet -}$, concurrently.

5.2 Infrared Spectroscopy of the films

The effect of charge-transfer in the co-deposited [MnTPPCl][TCNQ] film is further investigated by IR spectroscopy. As can be seen, the neat TCNQ film displays two main peaks at 2226 cm^{-1} and 863 cm^{-1}, respectively (black curve in Figure 5.3 (a)). The former corresponds to the characteristic of ν(C≡N) stretching, with the latter arising from the σ(C-H) in the benzene ring, in good agreement with the signature vibration frequencies expected from the neutral TCNQ [91, 93]. These values subsequently indicate the molecular structure as well as the oxidation state of TCNQ are unaffected by thermal sublimation during the film deposition.

As for MnTPPCl (red curve in Figure 5.3), the complex absorption spectrum between 900 and 1600 cm^{-1} results from the various C-C vibration modes and aromatic C-H stretching frequencies around 3000 - 3200 cm^{-1}, consistent with the typical finger-print features reported for TPP [179].

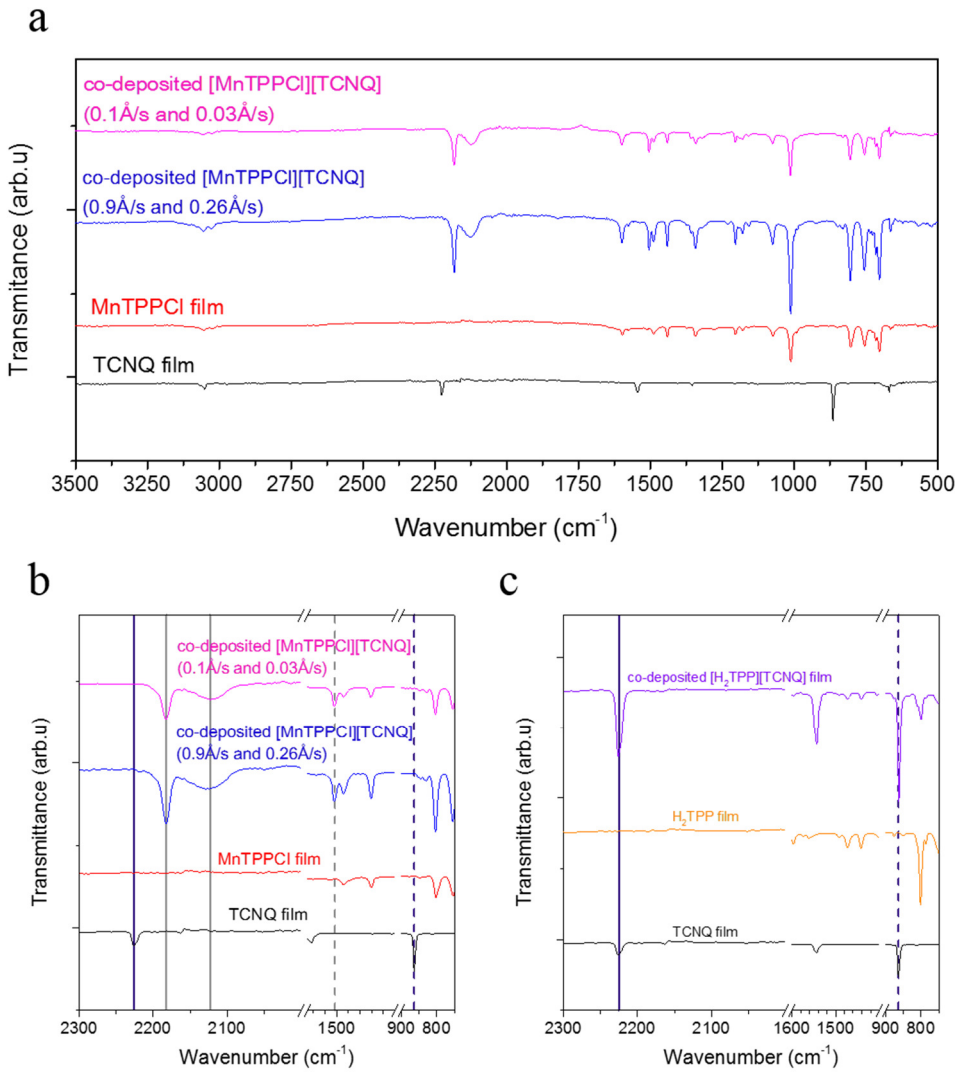


Figure 5.3 (a) IR spectra of the 80 nm TCNQ film grown at the rate of 0.37 Å/s (black), the 100 nm MnTPPCl film grown at the rate of 0.9 Å/s (red), the co-deposited [MnTPPCl][TCNQ] films with 1:1 ratio obtained two sets of deposition rates, corresponding to MnTPPCl = 0.9 Å/s, TCNQ = 0.26 Å/s (blue), MnTPPCl = 0.1 Å/s and TCNQ = 0.03 Å/s (magenta), where an equivalent thickness of 100 nm for MnTPPCl was used in the two depositions. (b) is a zoom on the key region for the finger-printing, and (c) the IR spectra of the 100 nm H_2TPP film (orange), and the co-deposited [H_2TPP][TCNQ] film (an equivalent thickness of 100 nm for H_2TPP) (purple) with 1:1 ratio between H_2TPP and TCNQ obtained at the deposition rates of H_2TPP =0.9 Å/s and TCNQ = 0.29 Å/s, respectively. All the films are deposited onto KBr (100), shown the vertical lines to label the ν(C≡N) stretching in the nitrile group in neutral (purple solid) and ionized bound state (grey solid), and ν(C-C) stretching (grey dotted) and σ(C-H) deformation (bending) (purple dotted) in benzene.

When TCNQ is co-deposited with MnTPPCl, the corresponding IR spectrum shows significantly different vibrational features in comparison to the neat TCNQ film. The single sharp and intense absorption distinctive for the ν(C≡N) stretching peak at 2226 cm^{-1} now appears at low wavenumber, splitting into two bands at 2182 and 2125 cm^{-1}, respectively. The band at 863 cm^{-1} owing to the deformation C-H (bending) of the benzene previously seen in the neat TCNQ film is replaced by the σ(C-H) bending~ 830 cm^{-1}, and the ν(C-C) stretching at 1504 cm^{-1} can be observed for the co-deposited [MnTPPCl][TCNQ] film. The former is the characteristic C-H bending reported for $TCNQ^{\bullet-}$ [82], whereas the latter is due to the π-delocalization within the $TCNQ^{\bullet-}$ ring [82, 180]. Thus, the vibrational properties exhibited by TCNQ in the co-deposited [MnTPPCl][TCNQ] films can be distinguished from those found in the neat TCNQ film, with the splitting in the ν(C≡N) stretching mode, and the presence of vibrations at ~ 830 cm^{-1} and 1504 cm^{-1}, indicating the changes to the molecular structure of TCNQ after co-deposition with MnTPPCl. The influence of MnTPPCl on the ν(C≡N) stretching, the σ(C-H) bending and ν(C-C) stretching for TCNQ indicates presence of $TCNQ^{\bullet-}$ in the co-deposited [MnTPPCl][TCNQ] film as a consequence of charge transfer from MnTPPCl to TCNQ, which can be observed for films co-deposited at two sets of deposition rates (see Figure 5.3 (a) and (b)), with the stoichiometry between MnTPPCl and TCNQ maintained as 1:1.

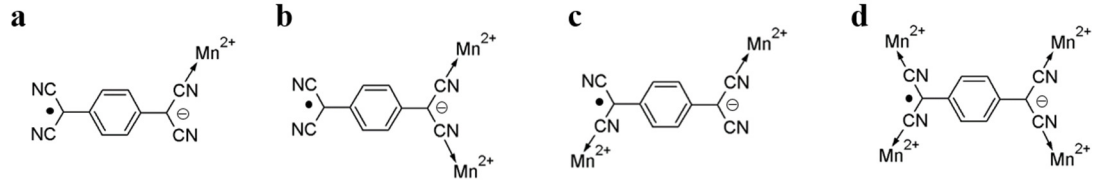


Figure 5.4 Transition metal complex upon reaction with TCNQ, or similar polynitriles resulting in single coordination (a) σ- or as a bridging ligand to bond to metal via (b) $\mu_{1,1}$, TCNQ *cis*-bonding, (c) $\mu_{1,2}$, TCNQ *trans*-bonding, and (d) μ_4 TCNQ bonding, respectively.

The absence of the characteristic ν(C≡N) stretching and σ(C-H) bending seen in the neutral TCNQ, in conjunction with the signature σ(C-H) and the ν(C-C) modes present at ~ 830 cm^{-1} and 1504 cm^{-1} respectively are consistent with the literature values reported for $TCNQ^{\bullet-}$ [82, 92, 96], suggesting that the TCNQ contained in the co-deposited [MnTPPCl][TCNQ] is reduced. This observation is in good agreement with what is observed by UV/Visible

spectroscopy. $TCNQ^{\bullet -}$ can dimerize to form stable and long-lived σ-$[TCNQ\text{-}TCNQ]^2$ in both crystals and solutions [82, 97, 181], with the σ(C-H) bending frequency characterized to be at 803 cm^{-1}.

However, the out-of-plane porphyrin deformation mode of MnTPPCl is observed to occur at a very similar frequency, identified as one of the oxidation sensitive bands for FeTPPCl, MnTPPCl and CoTPPCl [100]. The band at 804 cm^{-1} present in the co-deposited [MnTPPCl][TCNQ] film is therefore attributed to MnTPPCl, though it is possible the co-deposited film might have contained trace of σ-$[TCNQ\text{-}TCNQ]^2$ formed after ionization of TCNQ after film deposition.

The shift in the ν(C≡N) stretching mode in the co-deposited [MnTPPCl][TCNQ] film is actually observed to be at a wavenumber lower than what has been characterized for $TCNQ^{\bullet -}$ [24]. While the frequencies for the ν(C≡H) stretching mode reported for the unbound $TCNQ^{\bullet -}$ [80, 82] are consistently 2184 and 2144 cm^{-1}, deviation in the ν(C≡N) stretching modes to higher or lower energy frequently suggest coordination to the metal [80, 82]. In addition, the number of peaks for the ν(C≡N) stretching modes can reflect the coordination environment in TCNQ/TCNE-based complexes. When used as a σ-donor ligand, interaction of TCNQ/TCNE towards the metal ion via the nitrogen lone pair on the CN groups leads TCNQ/TCNE to bind as a single coordination (σ-bond), Figure 5.4 (a), or bridge several metal centers (μ-bond), as shown in Figure 5.4 (b), (c) and (d) [81]. Due to the low symmetry for the σ-bonding, in principle more ν(C≡H) stretching modes can be observed [80], in comparison to the μ-bonding [80].

The trend in the ν(C≡N) stretching shift from 2226 to 2182 and 2125 cm^{-1} observed for the co-deposited [MnTPPCl][TCNQ] film is actually very similar to those reported for the charge-transfer salts based on [MnTPP][TCNE][24], where the ν(C≡N) stretching mode splits into two peaks at 2192 and 2147 cm^{-1}, respectively, attributed to the dissimilar coordination of C≡N of $TCNE^{\bullet -}$, *trans*-*μ*-N-*σ*- bound to Mn ion in MnTPP (see section 1) [14, 24]. The number of the ν(C≡H) stretching modes for the co-deposited [MnTPPCl][TCNQ] film obtained by using two sets of deposition rates in this study are consistently observed to be two, in contrast to the three modes that are more often seen in the σ-bonded TCNQ/TCNE complexes [80], in turn suggesting in the co-deposited [MnTPPCl][TCNQ] film $TCNQ^{\bullet -}$ is bound to the Mn ion, giving rise to a charge transfer donor-acceptor pair, reminiscent to the charge transfer complex based on [MnTPP][TCNE]

[14, 24]. Thus, co-deposition the structural analogues of MnTPP and TCNE by using OMBD leads to molecular films based on a mixture of MnTPPCl and TCNQ, characterized by the charge transfer complex formed by coordination of nitrile CN(TCNQ) to the Mn center.

The determination of the oxidation state and the coordination of TCNQ based on IR spectroscopy [82, 96] reveals presence of $TCNQ^{\bullet-}$ in the co-deposited [MnTPPCl][TCNQ] film, indicating that during the co-deposition with MnTPPCl, TCNQ undergoes reduction: $TCNQ \longrightarrow TCNQ^{\bullet-}$, in turn suggesting an oxidative reaction takes place in parallel to counter the TCNQ reduction.

Table 5.1 Summary of the CN vibration frequencies (in the unit of cm^{-1}), of TCNE radical anion (isolated and bound state), TCNQ in its neutral form and radical anion (isolated and bound state), and the observed frequencies for the co-deposited [MnTPPCl][TCNQ] films obtained by two sets of deposition rates.

TCNE			TCNQ		Co-deposited [MnTPPCl][TCNQ]	
Neutral [80]	Isolated $TCNE^{\bullet-}$ [80]	Bound state $TCNE^{\bullet-}$ with MnTPP [13]	Neutral [92]	Isolated $TCNQ^{\bullet-}$ [24]	Bound state $TCNQ^{\bullet-}$ (this work) 0.9 Å/s, 0.26 Å/s	0.1 Å/s, 0.03 Å/s
2228	2144	2147	2226	2144	2125	2125
	2183	2192		2184	2182	2183

While it is expected the Mn ion in the co-deposited [MnTPPCl][TCNQ] film to be a redox-active center with potentials that can couple to the TCNQ reduction, as suggested by UV/Visible spectroscopy, no information on the oxidation state for the Mn ion in the as-deposited MnTPPCl film and co-deposited [MnTPPCl][TCNQ] film can be obtained by IR spectroscopy. This is because the wavelength at which the Mn-Cl bond stretching vibration occurs is between 200 and 400 cm^{-1} in the far-IR range [100], which is not accessible by the particular IR instrument used in this work.

The effect of the Mn ion on the oxidation state of TCNQ is subsequently investigated by replacing MnTPPCl with metal-free TPP (H_2TPP), which is used as the donor to co-deposit with TCNQ. Figure 5.3 (c) shows the IR spectrum of the co-deposited [H_2TPP][TCNQ] film, where the vibrational peaks at 2226 cm^{-1} and 863 cm^{-1}, and absence of the vibration band at 1504 cm^{-1} indicate TCNQ remains to be neutral in the co-deposited [H_2TPP][TCNQ] film, in

sharp contrast to what is seen for the co-deposited [MnTPPCl][TCNQ] film. Absence of $TCNQ^{\bullet-}$ in the co-deposited [H_2TPP][TCNQ] film subsequently suggests that the TCNQ reduction: TCNQ ⟶ $TCNQ^{\bullet-}$ does not take place when co-deposited with H_2TPP, attributed to the lack of the metal ion. As for H_2TPP, the vibrational structures in the co-deposited [H_2TPP][TCNQ] film related to those seen in the neat H_2TPP film can still be observed, and it can therefore be concluded that no apparent changes to the porphyrin ligands are introduced by the co-deposited TCNQ.

This result highlights the presence of donor with a sufficient reducing ability is essential to form charge-transfer systems, and the accessibility of various oxidation states makes Mn porphryins (+2, +3, +4 and +5) [182, 183] more capable of catalyzing electron transfer process so as to reduce TCNQ. This is not the case for the co-deposited [H_2TPP][TCNQ] film, where absence of $TCNQ^{\bullet-}$ suggests co-deposition with H_2TPP does not lead to reduction of TCNQ. Indeed, studies on the charge-transfer systems based on reaction of transition metal porphyrins with a strong electron acceptor, such as TCNE and TCNQ in solutions, have shown that if the metal center is Mg(II) instead of Mn(II) (For MnTPP, Mn(II)/Mn(III) $E°_{1/2}$ = -0.37 *V* in MeCN *vs* saturated calomel electrode (SCE)), a strong oxidizing agent is required, as the first oxidation on the porphyrin ring ($E°_{1/2}$ = 0.57 *V*, por ⟶ $por^{\bullet+}$) is greater than the reduction potentials of TCNE ($E°_{1/2}$ = 0.15 *V* in MeCN *vs* SCE) and TCNQ ($E°_{1/2}$ = 0.17 *V* in MeCN *vs* SCE) [19]. The porphyrin ligand is not easily oxidizeable in reaction with TCNQ, and as a consequence, co-deposition results in neutral TCNQ observed for the co-deposited [H_2TPP][TCNQ] film. Thus, the relevance of the Mn ion to the reduction of TCNQ can be confirmed, and charge transfer between MnTPPCl and TCNQ is found to be predominately limited to the Mn ion and C≡N of TCNQ upon coordination through concurrent redox reactions, in turn giving rise to a charge transfer donor-acceptor pair formed by the two different molecules in the co-deposited [MnTPPCl][TCNQ] film.

5.3 X-ray Photoelectron Spectroscopy

The electronic structure of the co-deposited [MnTPPC][TCNQ] film (with an equivalent thickness of 200 nm for MnTPPCl) investigated by using XPS, with a 1 to 1 ratio obtained by using the deposition rates of 0.45 Å/s and 0.13 Å/s for MnTPPCl and TCNQ, respectively.

The survey scan of the co-deposited [MnTPPCl][TCNQ] film shows XPS peaks with binding energies corresponding to Mn2p, N1s, C1s and Cl2p, in agreement with the elements present in MnTPPCl and TCNQ. The presence of O1s peak (close to 530 eV) is attributed to the exposure to air prior to sample loading.

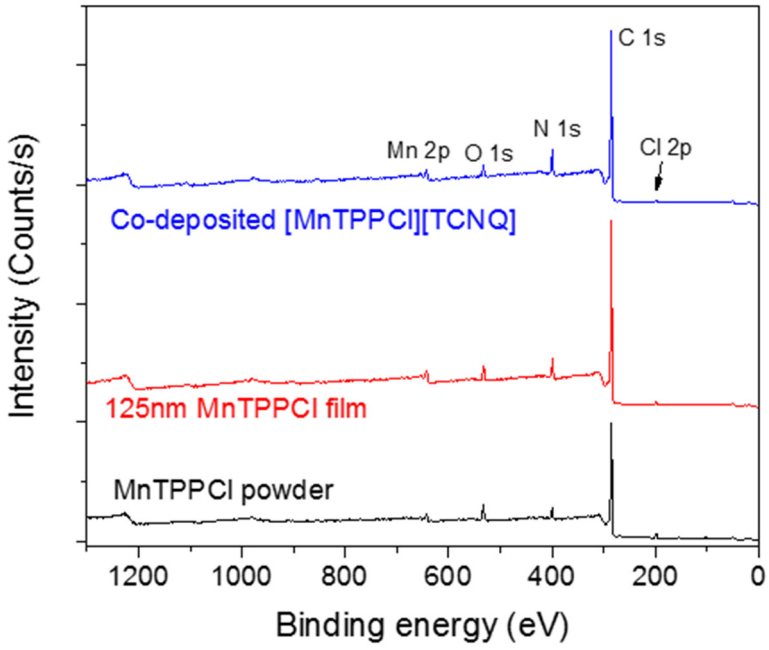


Figure 5.5 XPS survey scans of the MnTPPCl powder (black), the 125 nm thick as-deposited MnTPPCl film grown at the rate of 0.9 Å/s on silicon substrate (red), and the co-deposited [MnTPPCl][TCNQ] film on silicon substrate, (an equivalent thickness of 200 nm for MnTPPCl, with a 1 to 1 ratio obtained by using MnTPPCl = 0.45 Å/s, TCNQ = 0.13 Å/s, respectively) (blue).

The composition of the co-deposited [MnTPPCl][TCNQ] film can be deduced by using the same method previously applied to the MnTPPCl powder and MnTPPCl film in section (4.1.3). The resultant element to manganese ratios in the co-deposited [MnTPPCl][TCNQ] film are summarized in Table 5.2, with the ratios observed for the MnTPPCl powder and MnTPPCl film included.

The C: N: Mn of 66.0: 7.2: 1 in the co-deposited [MnTPPCl][TCNQ] film is larger than what is seen for the MnTPPCl powder and MnTPPCl film, but agrees with the theoretical C: N: Mn ratio of 56: 8: 1, with the assumption of 1 to 1 ratio between MnTPPCl and TCNQ. Thus,

the composition in terms of C, N and Mn contained in the co-deposited [MnTPPC][TCNQ] film is consistent with that in the MnTPPCl powder and MnTPPCl film, whereas the increases in both the C and N contents can confirm co-deposited TCNQ is incorporated in the film.

Table 5.2 Summary of the element to manganese (Mn) ratios, of MnTPPCl powder, 125 nm thick as-deposited MnTPPCl film grown at the rate of 0.9 Å/s on silicon substrate, and the co-deposited [MnTPPCl][TCNQ] film on silicon substrate, (an equivalent thickness of 200 nm for MnTPPCl, with a 1 to 1 ratio between MnTPPCl and TCNQ obtained by using the deposition rates of MnTPPCl = 0.45 Å/s and TCNQ = 0.13 Å/s, respectively). The photoemission lines of the XPS C1s, N1s, Cl2p and Mn2p peaks are fitted with Voigt function (see Figure 5.6).

Species	Sensitivity Factor[164]	Element to Mn Ratio				
		MnTPPCl			Co-deposited [MnTPPCl][TCNQ]	
		Theoretical	powder	film	Theoretical	film
C (1s)	0.25	44	66.6	59.6	56	66.0
N (1s)	0.42	4	5.6	5.0	8	7.2
Mn ($2p_{3/2}$)	1.7	1	1	1	1	1
Cl (2p)	0.73	1	1.3	0.5	1-0	0.5

As for Cl, the co-deposited [MnTPPCl][TCNQ] film displays a Cl:Mn ratio of 0.5 to 1, significantly lower than the theoretical value of 1:1 for MnTPPCl, giving rise to a decrease up to 60 % in comparison to what is found for the MnTPPCl powder, indicating a substantial loss in the axial Cl ligands in the co-deposited [MnTPPCl][TCNQ] film. The Cl:Mn ratio (0.5:1) in the co-deposited [MnTPPCl][TCNQ] film is found to be identical to the ratio of 0.5:1 seen in the neat MnTPPCl film, despite different deposition rates of MnTPPCl used to obtain the neat and co-deposited films, corresponding to 0.9 Å/s and 0.45 Å/s, respectively. Thus, dissociation from the axial Cl ligand from MnTPPCl also occurs during the co-deposition, leading to the four-coordinate Mn(II)TPP. The same has been previously seen for the neat MnTPPCl film, where the Cl ligands that remain undissociated are found to be in the axial coordination to the Mn ion, which maintains as a five-coordinate Mn(III) porphyrin complex.

Consequently, when Mn(III)TPPCl is co-deposited with TCNQ, partial dissociation of the axial Cl ligand leads to Mn(III)TPPCl and Mn(II)TPP, and both can act as an electron donor

with respect to TCNQ. Mn(II) is considerably more reducing than Mn(III), with a redox potential sufficient to reduce TCNQ [104] to form the donor-acceptor charge transfer pair. It is therefore expected that formation of [MnTPP][TCNQ] should be energetically more favorable than [MnTPPCl][TCNQ], though both are likely to be found in the co-deposited [MnTPPCl][TCNQ] films.

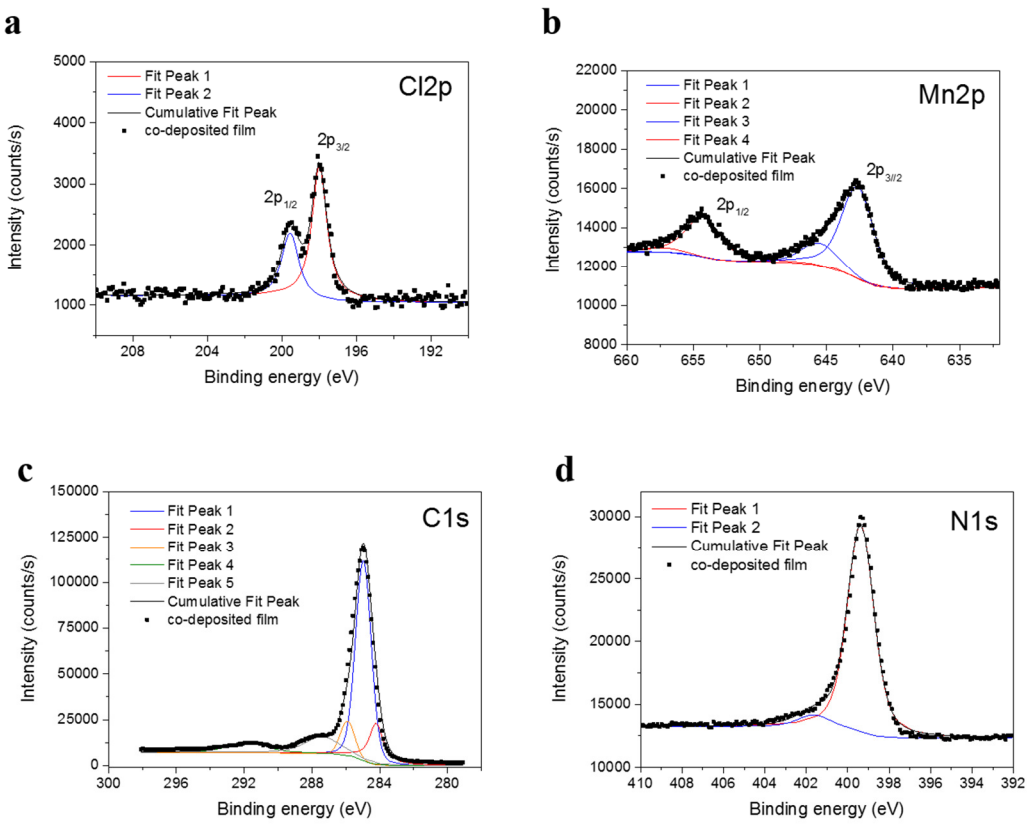


Figure 5.6 High resolution of XPS core-level (a) Cl2p (b) Mn2p (c) C1s and (d) N1s spectra of the co-deposited [MnTPPCl][TCNQ] film. The photoemission lines are deconvoluted with the Voigt peak shape and the background is subtracted with the Shirley algorithm.

Co-deposition with TCNQ leading to a Cl:Mn ratio almost the same as seen in the neat MnTPPCl film seems to indicate that addition of TCNQ to MnTPPCl has no influence on the Cl ligand, suggesting reactions similar to displacement of the axial ligand observed for Mn(III) porphyrins solutions [104] do not occur during the co-deposition. Thus, TCNQ is possibly not involved in the pathway in which the axial Cl ligand dissociates from MnTPPCl, and the loss of the axial (Cl) ligands is an intrinsic property to the vapor phase MnTPPCl, in agreement with the thermal lability reported in the literature [110].

Table 5.3 The observed binding energies of C1s, N1s, Mn2p and Cl2p XPS profiles for the MnTPPCl powder, MnTPPCl film, and co-deposited [MnTPPCl][TCNQ] film. The XPS line-shape is fitted with the Voigt functions for the MnTPPCl powder, the 125 nm thick as-deposited MnTPPCl film grown at the rate of 0.9 Å/s, and the co-deposited [MnTPPCl][TCNQ] film (an equivalent thickness of 200 nm for MnTPPCl, with a 1 to 1 ratio between MnTPPCl and TCNQ obtained by using the deposition rates of MnTPPCl = 0.45 Å/s, TCNQ = 0.13 Å/s, respectively). Both the neat MnTPPCl film and the co-deposited [MnTPPCl][TCNQ] films were deposited on silicon substrate. The relative quantities for the different chemically inequivalent C atoms listed in bracket are calculated without contribution from the π-π shake-up.

		MnTPPCl powder		125 nm MnTPPCl film		Co-deposited [MnTPPCl][TCNQ]	
		B.E. (eV)	%	B.E. (eV)	%	B.E. (eV)	%
C1s	$C_{N\beta}$	284.4	17.8 (19)	284.0	12.8 (13.6)	284.6	13.9 (14.6)
	C_{phen}	285.0	53.0 (56.6)	285.0	59.5 (63.0)	285.0	50.3 (52.7)
	$C_{meso\text{-}bridged}$	285.7	9.7 (10.4)	285.4	10.0 (10.6)	285.7	10.4 (10.9)
	$C_{N\alpha}$	287.0	13.1 (14.0)	287.7	12.2 (12.9)	286.9	20.8 (21.8)
	π-π shake-up	291.6	6.4 (-)	291.8	5.6 (-)	292.0	4.5 (-)
N1s		399.3	81.1	399.2	92.9	399.4	92.9
	π-π shake-up	401.3	19.0	401.5	7.1	401.6	7.1
Mn2p	$2p_{3/2}$	642.5	66.8	642.4	67.3	642.7	66.7
	$2p_{1/2}$	654.1	33.2	653.9	32.7	654.3	33.3
Cl2p	$2p_{3/2}$	198.1	67.1	197.9	66.5	198.0	66.6
	$2p_{1/2}$	199.7	32.9	199.5	33.5	199.6	33.4

The high resolution Cl2p XPS spectrum of the co-deposited [MnTPPCl][TCNQ] film is presented in Figure 5.6 (a). Similar to the MnTPPCl powder and MnTPPCl film (see Figure 4.8 (a) and (b)), the Cl2p spectrum of the co-deposited [MnTPPCl][TCNQ]] film exhibits the Cl2p spin-orbit splitting to $2p_{3/2}$ and $2p_{1/2}$, with peaks at binding energies of 198.0 and 198.6 eV, respectively. The shape and the positions of the binding energies for the Cl2p doublet peaks for the co-deposited [MnTPPCl][TCNQ] film resemble to those seen in the MnTPPCl powder and MnTPPCl film, in a good agreement with the value of 197.6 eV reported for Mn(III)TPPCl [165], indicating the chemical state of the Cl ligands in the co-deposited [MnTPPCl][TCNQ] film to be the same as what was found in the MnTPPCl

powder and MnTPPCl film, respectively. Thus, after dissociation of ~ 60 % of the Cl ligands, those that are undissociated remain to be in the axial coordination to the Mn ion in the co-deposited [MnTPPCl][TCNQ] film, confirming co-deposition with TCNQ has no observable effect on the ligation of the Cl ligands for MnTPPCl.

To investigate the influence of the co-deposited TCNQ on the Mn ion, the high resolution Mn 2p spectrum of the co-deposited [MnTPPCl][TCNQ] film is shown in Figure 5.6 (b). The spectrum of the co-deposited [MnTPPCl][TCNQ] film exhibits multiplet splitting into Mn $2p_{1/2}$ and $2p_{3/2}$ with peaks at the binding energies of 654.3 and 642.7 eV, and their low intensity satellites [166]. Again, the Mn2p line-shape and positions of the binding energies are found to resemble those previously seen for the MnTPPCl powder and MnTPPCl film (as summarized in Table 5.3), consistent with the literature values reported for Mn(III)TPPCl [165], suggesting the oxidation state (+3) for the Mn ion present in the MnTPPCl powder is relatively unaffected after co-depositing with TCNQ.

While the difference in the values for the Mn2p peaks is less than 0.5 eV and incomparable to those seen as a consequence of change in the Mn oxidation [167], the positions of the peaks are observed to shift slightly to higher binding energies, going from 654.1 (Mn $2p_{1/2}$) and 642.5 eV (Mn $2p_{3/2}$) for the MnTPPCl powder, to 654.3 (Mn $2p_{1/2}$) and 642.7 eV (Mn $2p_{3/2}$) for the co-deposited [MnTPPCl][TCNQ] film. The subtle chemical shifts with respect to those found in the MnTPPCl powder are attributed to TCNQ present in the co-deposited film, which changes the coordinate number if bound to the Mn ion in the axial ligation. For example, Sugiura *et al.* showed that increasing the Mn coordination number leads to a slight shift to higher binding energy (~ 0.4 eV) for the Mn2p peaks, as observed for the five coordinate MnTPPCl and six coordinate [Mn(III)TPP][TCNE]·2PhMe [165]. Consequently, no significant changes found in the Mn2p binding energies is possibly because the chemical shift induced by increasing coordination number for the Mn ion in the five-coordinate porphyrin is considerably small, and further obscured by a mixture of [MnTPPCl][TCNQ] and [MnTPP][TCNQ] contained in the co-deposited [MnTPPCl][TCNQ] film. In this case higher resolution XPS measurements may resolve shifts related to changes in the local coordination environment for the charge transfer donor-acceptor dimer [MnTPP][TCNQ].

It appears the carbon environment is relatively unaffected by the co-deposited TCNQ. The high resolution C1s spectrum of the co-deposited [MnTPPCl][TCNQ] film exhibits a main peak at 285.0 eV with a shoulder at higher binding energy, and small and broad satellite peak

at 292.0 eV, very similar to those seen in the MnTPPCl powder and MnTPPCl film, in good agreement with the characteristic C1s spectrum observed for metal-free TPP [168].

Table 5.4 Binding energies for Mn 2p in similar compounds reported in the literature.

Mn 2p XPS	Mn $2p_{1/2}$ (eV)	Mn $2p_{3/2}$ (eV)
Mn(II)TPP [165]	653.1	641.1
Mn(III)TPPCl [165]	653.8	642.2
[Mn(III)TPP][TCNE]·2PhMe [165]	654.2	642.6

Analysis on the C1s XPS signal of the co-deposited [MnTPPCl][TCNQ] film follows the same approach previously used for the MnTPPCl powder and MnTPPCl film in section (4.1.3). Addition of TCNQ is expected to introduce three other types of chemically distinct C atoms (see Figure 5.7), corresponding to phenyl, tertiary (bonded to the phenyl ring and cyano groups) and ones directly involved in the cyano groups, respectively. Yet, both TCNQ and MnTPPCl actually exhibit similar functional groups and linkages as shown in (Figure 5.7), and the C atoms in the benzene rings in TCNQ and MnTPPCl are therefore spectrally indistinguishable. The same is with the tertiary C and those in the cyano groups, which are expected to be similar to C atoms in the meso-bridged and the β-position composed in the pyrole that are previously identified in MnTPPCl. Consequently, the C atoms present in TCNQ and MnTPPCl are categorized into four chemically inequivalent carbon species.

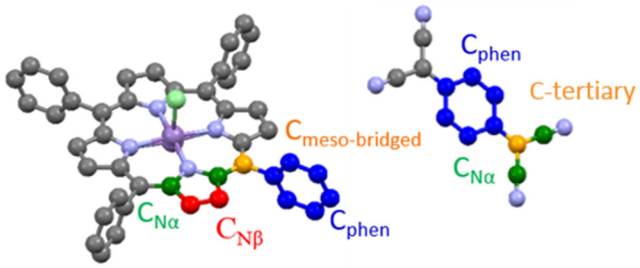


Figure 5.7 Colour scheme used for MnTPPCl (adapted from [119]) and the chemically distinctive carbon atoms (left). The blue, orange, red and green spheres represent the carbons in the phenyl group, meso-bridged, and the two nitrogen-bonded, namely N_α and N_β; (right) the molecular structure of TCNQ (adapted from [98]), where the carbon atoms in different chemical environments are labelled in blue, orange and green, accordingly.

The result of the fit for the co-deposited [MnTPPCl][TCNQ] film is summarized in Table 5.3, and the largest spectral component giving rise to 52.7 % of C1s emission with a peak in binding energy of 285 eV is assigned to C atoms in the benzene ring. Two peaks at 286.9 eV and 284.6 eV show similar contributions to the C1s signal (14.6 % and 21.8 %), attributed to the C atoms located in the α-and β-position, respectively, followed by a smallest peak (10.7 %) at 285.7 eV, due to the meso-bridged C atom. These values are in agreement with the theoretical ratio of 14.3 %, 53.6 %, 10.7 % and 21.4 % (1.3:5.0:1.0:2.0) respectively, with 1:1 ratio between MnTPPCl and TCNQ, and consequently, the structure of the porphyrin ligand is relatively unaffected by dissociation of the axial Cl ligands, similar to what was seen for the neat MnTPPCl film.

Inclusion of TCNQ has no observable effects on the N1s profile. High resolution N1s spectrum of the co-deposited [MnTPPCl][TCNQ] film shows a main peak at 399.4 eV, followed by a π-π shake-up feature present in binding energy of 401.6 eV. These values are found to be close to those in the MnTPPCl powder and MnTPPCl film, and comparable with the value of 398.6 eV reported for N1s XPS on Mn(III)TPPCl [165]. The observed N1s binding energies are also comparable to the literature values expected from TCNQ powder, corresponding to a main peak at 399.6 eV accompanied by a shake-up feature at 401.9 eV [184]. Deconvolution of the N1s signal obtained from the co-deposited [MnTPPCl][TCNQ] film gives rise to a single main peak centering at 399.4 eV, suggesting the relative positions in binding energies for the pyrole-N and cyano-N present in the co-deposited [MnTPPCl][TCNQ] film are close and therefore spectroscopically indistinguishable.

To conclude, the co-deposited [MnTPPCl][TCNQ] film shows a significantly low Cl:Mn ratio compared to the MnTPPCl powder, corresponding to ~ 60 % loss in the Cl content. The same behavior has been previously observed for the neat MnTPPCl film grown by using OMBD, and co-deposition with TCNQ resulting in an almost identical Cl:Mn ratio suggests TCNQ is not involved in the pathway for dissociation of the axial Cl ligand. Removal of the axial Cl ligands leads to Mn(III)TPPCl and Mn(II)TPPCl, with a ratio of around 1 to 1, and both act as electron donors for TCNQ to interact during co-evaporation, giving rise to charge transfer donor-acceptor dimer [MnTPP][TCNQ]. Since +3 is the only observable Mn oxidation state for the co-deposited [MnTPPCl][TCNQ] film, it is suggested TCNQ selectively reacts with Mn(II)TPP, leading to Mn(II) → Mn(III), while unreacted Mn(III)TPPCl remain as isolated molecules. This finding is in good agreement with what is observed by UV/Visible spectroscopy.

5.4 Morphology and structure of the films

The morphology of the co-deposited [MnTPPCl][TCNQ] film is observed by SEM. Except for the few spherical particles found from the top view, as shown in Figure 5.8.

Overall, the film surface is flat and smooth, very similar to what is seen for the neat MnTPPCl film in section (4.1.2). The same morphology can also be found from the cross-sectional image, and inside the smooth layer is found to consist of closely-packed oval-shaped clusters with a vertical diameter less than 100 nm (Figure 5.8 (b)).

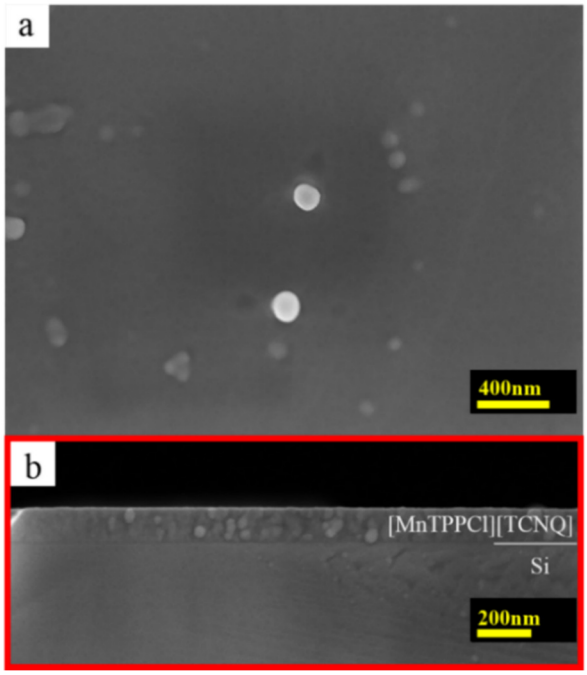


Figure 5.8 SEM micrographs of (a) the co-deposited [MnTPPCl][TCNQ] film on silicon substrate, (an equivalent thickness of 100 nm for MnTPPCl, with a 1 to 1 ratio between MnTPPCl and TCNQ obtained by using the deposition rates of MnTPPCl = 0.9 Å/s and TCNQ = 0.26 Å/s, respectively), and (b) a cross-section of the film (with the scale bar of 200 nm). The black area on the top of (b) corresponds to vacuum.

Further morphological details on the co-deposited [MnTPPCl][TCNQ] films are shown in Figure 5.9. Two sets of depositions rates were used while the stoichiometry between MnTPPCl and TCNQ are maintained to be 1 to 1.

The surface of the co-deposited [MnTPPCl][TCNQ] film deposited at the rate of 0.9 Å/s for

MnTPPCl (Figure 5.9 (a)) appears to be very smooth, giving rise to a very low RMS = 0.4 nm. No particles previously observed by SEM is found in the AFM micrographs. The discrepancy between the results obtained by two different imaging techniques is possibly because SEM can provide a quick morphological characterization across a large surface, similar to what was observed for MnTPPCl films and TCNQ films in section (4.1.2) and (3.1.2).

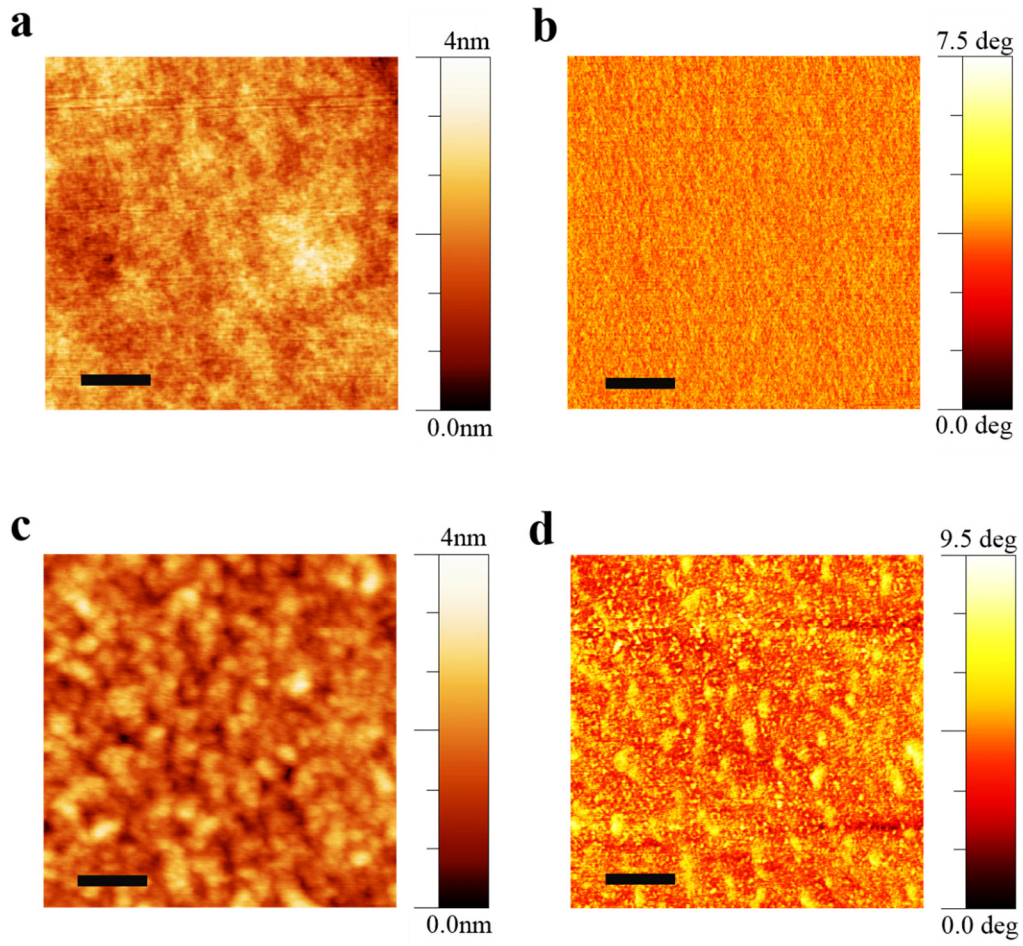


Figure 5.9 AFM micrographs of the co-deposited [MnTPPCl][TCNQ] films on glass substrate, with an equivalent thickness of 100 nm for MnTPPCl used for the two depositions. (a) corresponds to a film with 1 to 1 ratio obtained by using the deposition rates of MnTPPCl = 0.9 Å/s and TCNQ = 0.26 Å/s, respectively, with the corresponding phase image in (b), whereas (c) represents a 1 to 1 ratio between MnTPPCl and TCNQ for the film obtained at a lower set of deposition rates, using MnTPPCl = 0.1 Å/s, TCNQ = 0.03 Å/s, respectively, and the corresponding phase image in (d). The scale bars are 400 nm in (a) and (b), and 200 nm in (c) and (d), respectively.

The roughness observed for the co-deposited [MnTPPCl][TCNQ] film is close to the values expected for amorphous substances, and very similar to what is seen for the neat MnTPPCl film (RMS = 0.4-0.7 nm). Therefore, the morphology exhibited by the co-deposited [MnTPPCl][TCNQ] film and the neat MnTPPCl film are alike, and the absence of micro-sized islands previously characterized for the TCNQ films indicates no visible phase segregation by co-deposition with TCNQ, in turn suggesting the two different molecules are well mixed in the co-deposited [MnTPPCl][TCNQ] film. Furthermore, the film composition appears to be homogeneous, as suggested by the corresponding phase image, confirming co-deposition of MnTPPCl and TCNQ by using OMBD leads to [MnTPPCl][TCNQ] films consisting of a homogeneous blend, although inhomogeneities at the molecular level cannot be excluded.

The surface roughness of the co-deposited [MnTPPCl][TCNQ] film is found to increase, as the deposition rates for MnTPPCl and TCNQ are reduced to 0.1 Å/s and 0.03 Å/s, as suggested by RMS = 1.1 nm, marginally larger than what is obtained from the higher rate. More profound impact from the deposition rate can be seen for the film homogeneity, and the colour contrast in the corresponding phase image (see Figure 5.9 (d)) indicates presence of clusters with a size up to ~100 nm. This observation therefore suggests during the film deposition, the deposition rate can be a key to determine the degree of mixing between MnTPPCl and TCNQ in the co-deposited [MnTPPCl][TCNQ] film. The influence of the deposition rate on the roughness and homogeneity for the co-deposited [MnTPPCl][TCNQ] films may be related to the difference in the growth behaviours seen for the two different molecules. The film morphology and texture adopted by TCNQ are sensitive to the TCNQ growth rate, and in particular lowering the TCNQ rate results in increased island size and reduced island density (*i.e.* nucleation), as discussed in section (3.1.1).

The structure of the co-deposited [MnTPPCl][TCNQ] films obtained at two different rates is determined by using XRD. Using the rates of 0.9 Å/s and 0.26 Å/s for MnTPPCl and TCNQ, the corresponding XRD scan, between 2θ = 5-30°, displays a very broad band, characteristic of amorphous substances, attributed to the underlying glass substrate. Absence of diffraction peaks expected for either MnTPPCl [119] or TCNQ [98] therefore indicates the structure of the co-deposited film to be amorphous, suggesting the co-deposited TCNQ is blended with MnTPPCl, and that no ordered arrangements can be detected.

It appears that the deposition rate has no observable effect on the structure of the co-deposited

[MnTPPCl][TCNQ] film, and absence of diffraction peaks between 2θ = 5-30° reveals the film adopts amorphous structure when obtained at the lower rate. The less homogeneous composition previously observed by AFM could be because lowering the deposition rate leads to clustering in localized region at the molecular level and is below the detection limit for XRD, typically ~ 10 nm [185].

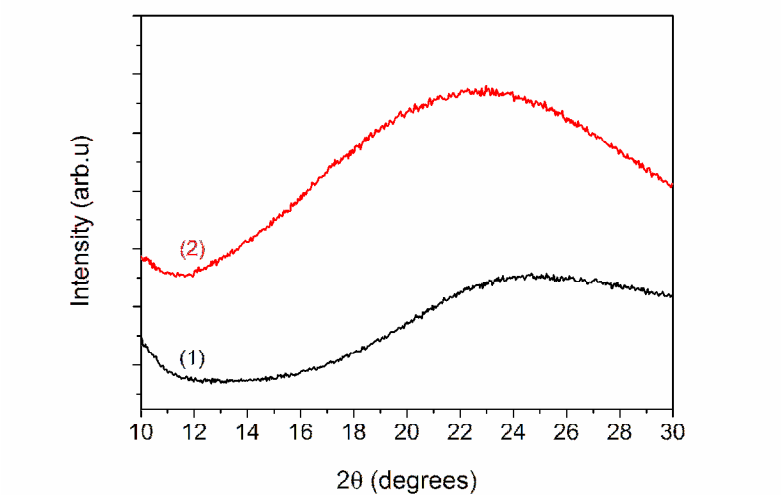


Figure 5.10 XRD scans of (1) the co-deposited [MnTPPCl][TCNQ] film (with an equivalent thickness of 200 nm for MnTPPCl, and a 1 to 1 ratio between MnTPPCl and TCNQ is obtained by using the deposition rates of MnTPPCl = 0.9Å/s and TCNQ = 0.26Å/s), and (2) the co-deposited [MnTPPCl][TCNQ] film (an equivalent thickness of 100 nm for MnTPPCl, with a 1 to 1 ratio between MnTPPCl and TCNQ obtained by using the deposition rates of MnTPPCl = 0.1 Å/s, TCNQ = 0.03 Å/s, respectively). Both films are deposited on glass substrate.

5.5 Magnetic characterization of the films

The magnetic properties of the co-deposited [MnTPPCl][TCNQ] film grown on kapton are studied by SQUID magnetometry, with an equivalent thickness of 200 nm for MnTPPCl to obtain a stronger signal. The isothermal magnetization curves were measured from 2 to 10 K, Figure 5.11 (a), and expressed in the unit of μ_B per Mn atom, equivalent to the net magnetic moment (μ_B) per pair of MnTPPCl and TCNQ with a 1 to 1 ratio.

The magnetic moment per Mn atom reduces with increasing temperature from 2 to 10 K. When expressed as a function of the ratio of the field over temperature (*H/T*), shown in Figure 5.11 (b), the 2 K and 4.2 K magnetization curves appear to be suppressed, while the *H/T*

scaling behaviour is only observed for higher temperatures. These observations indicate the co-deposited [MnTPPCl][TCNQ] film does not behave like a paramagnet.

The slope of the $M(H)$ curve measured at 2 K is rather different from what is obtained from the MnTPPCl powder, giving rise to a somewhat suppressed magnetic moment as the field increases up to 7 Tesla, only approaching ~ 3.4 μ_B, lower than what is reported for Mn(III)TPPCl [104]. The paramagnetic behaviour previously seen for the MnTPPCl powder is absent, attributed to the co-deposited TCNQ. While lack of coercivity and metamagnetic-like behaviours that are seen for [MnTPP][TCNE] obtained in polycrystalline form [46, 56], the magnetic properties exhibited by the co-deposited [MnTPPCl][TCNQ] film differ from those of neat MnTPPCl, indicating changes to the magnetic ground state are induced through co-evaporation of MnTPPCl and TCNQ.

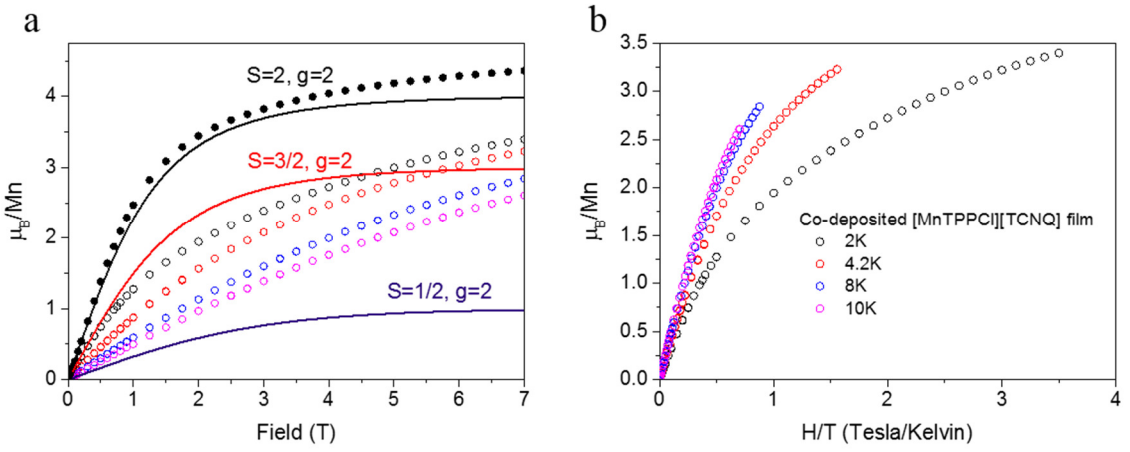


Figure 5.11 (a) Isothermal magnetization curves as a function of the applied field, $M(H)$, at 2 K (black open circle), 4.2 K (red open circle), 8 K (blue open circle) and 10 K (magenta open circle) of the co-deposited [MnTPPCl][TCNQ] film (an equivalent thickness of 200 nm for MnTPPCl, with a 1 to 1 ratio between MnTPPCl and TCNQ obtained by using the deposition rates of MnTPPCl = 0.45 Å/s and TCNQ = 0.13 Å/s, respectively), and magnetization at 2 K (black circle) obtained from MnTPPCl powder, shown with the Brillouin fit with $S = 2$, $S = 3/2$, and 1/2 with $g = 2$ at 2 K (black, red and purple solid line), and (b) the net moment as a as a function of the ratio of field over temperature (H/T) of the co-deposited [MnTPPCl][TCNQ] film,

The magnetic moment observed for the co-deposited [MnTPPCl][TCNQ] film appears to be slightly larger than the expected value from a uncoupled spin $S = 3/2$ with $g = 2$ yet lower than $S = 2$ with $g = 2$, indicating the unpaired spin ($s = 1/2$) on $TCNQ^{\bullet -}$, is active and involved in the spin coupling with Mn(III), leading to a net spin $S = 3/2$ system. This

behaviour appears to be very similar to what has been observed in cyanide-bridged Fe(III)-Mn(III) dinuclear complexes, where the spins carriers of Fe(III), $s = 1/2$ and Mn(III), $S = 2$, are antiferromagnetically coupled, giving rise to an overall magnetic ground state equivalent to $S = 3/2$ [186].

Thus, co-evaporation of MnTPPCl and TCNQ leads to formation of donor-acceptor dimer induced by charge transfer between the two different molecules, giving rise to a magnetic ground state more comparable to those seen for Fe(III)-Mn(III) dinuclear complexes ($S_{total} = 3/2$, antiferromagnetic coupling between $s = 1/2$ and $S = 2$), subsequently attributed to the co-deposited TCNQ. Yet, the saturation moment appears to be slightly larger than the expectation for an uncoupled spin $S = 3/2$ with $g = 2$ ($\mu_{eff} \simeq gS = 3\,\mu_B$), suggesting presence of isolated spins in the co-deposited [MnTPPCl][TCNQ] film. It is likely that reaction of MnTPPCl with TCNQ by co-deposition leads to a fraction of charge transfer donor-acceptor dimers, as suggested by XPS, leaving unreacted MnTPPCl and TCNQ molecules as either paramagnetic or diamagnetic impurities to contribute to the magnetic signal. The former, if present as unreacted and isolated, could lead to considerable paramagnetic signal in the $M(H)$ curve, due to the high-spin d^4 configuration.

These observations are consistent with the results obtained by UV/Visible spectroscopy and XPS, which suggest reaction of Mn(II)TPP with TCNQ should be more favourable than Mn(III)TPPCl, leading to charge transfer donor-acceptor dimer [MnTPP][TCNQ], in which charge transfer between Mn(II)TPP and TCNQ involves electron transfer processes through the concurrent redox reactions, Mn(II) ⟶ Mn(III) and TCNQ ⟶ $TCNQ^{\bullet -}$, respectively.

The temperature dependent differential susceptibility $\chi(T)$ of the co-deposited [MnTPPCl][TCNQ] film is shown in Figure 5.12 (a). Between 2 and 150 K, the magnetic susceptibility of the co-deposited film can be fitted with the standard Curie-Weiss law (shown in red), and the resulting fit extracts a negative Weiss temperature of ~ -1.7 K and a Curie constant (C) of 3.3 $\mu_B K T^{-1}$, corresponding to $g = 1.81$ with a spin state, $S = 3/2$. This finding reveals the magnetic ground state of the co-deposited film corresponds to the total spin state $S = 3/2$ instead of $S = 2$ seen in the MnTPPCl powder, suggesting presence of antiferromagnetic coupling between the spin centers Mn(III), $S = 2$ and $TCNQ^{\bullet -}$, $s = 1/2$ in the donor-acceptor dimer [MnTPP][TCNQ], arising from charge transfer between the two different molecules by co-depositing MnTPPCl with TCNQ. The value smaller than $g = 2.00$

has been reported for a dinuclear Mn(III)-Cu(II) single-molecule magnet, due to Mn(III) in the d^4 configuration [187].

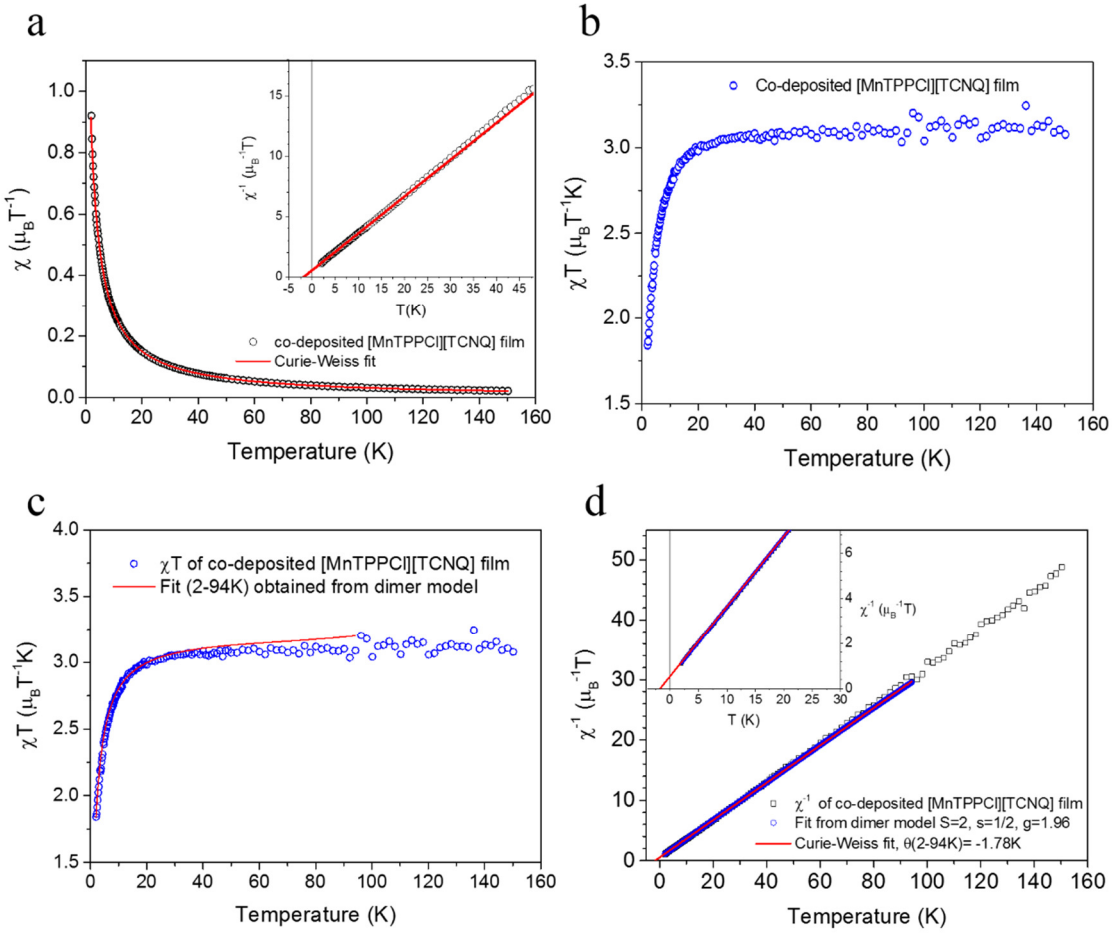


Figure 5.12 (a) Differential susceptibility as a function of temperature $\chi(T)$ of the co-deposited [MnTPPCl][TCNQ] film (with an equivalent thickness of 200 nm for MnTPPCl and a 1 to 1 ratio by using the deposition rates of MnTPPCl = 0.45 Å/s, TCNQ = 0.13 Å/s, respectively) (open black circle) with the Curie-Weiss fit (red), inset: inverse differential susceptibility as a function of temperature $1/\chi$ (open black circle) fitted with the Curie-Weiss law (red), (b) $\chi T(T)$ product as a function of temperature of the co-deposited [MnTPPCl][TCNQ] film, (c) $\chi T(T)$ product as a function of temperature of the co-deposited [MnTPPCl][TNCQ] film shown with χT (T = 2 - 94 K) simulated by the isotropic Heisenberg dimer model ($S = 2$ and $s = 1/2$, $g = 1.96$, intra-dimer coupling constant $(J/k_B) \sim -100$ K and $zJ'/k_B \sim -5$ K for inter-dimeric interactions) (red), and (d) inverse differential susceptibility as a function of temperature $\chi^{-1}(T)$ of the co-deposited [MnTPPCl][TCNQ] film (black open square), shown with $\chi^{-1}(T)$ simulated by the isotropic Heisenberg dimer model ($S = 2$ and $s = 1/2$, $g = 1.96$) (see text).

Figure 5.12 (b) shows that the χT product of the co-deposited [MnTPPCl][TCNQ] film at 150 K saturates ~ 3.1 μ_B, corresponding to C = ~ 3.1 $\mu_B K T^{-1}$, in good agreement with the Curie constant (C) of 3.3 $\mu_B K T^{-1}$ obtained from the Curie-Weiss fit. The χT product maintains ~ 3.0 μ_B with the temperature decreasing to ~ 40 K, slowly reducing (~ 2.9 μ_B) as the temperature is further decreased to 20 K, and drastically drops to ~ 1.8 μ_B at 2 K, indicating presence of antiferromagnetic interactions in the co-deposited [MnTPPCl][TCNQ] film, consistent with the negative Weiss constant (- 1.7 K).

These observations also indicate presence of Mn(II)TPP formed by-self-reduction of Mn(III)TPPCl found in the as-deposited MnTPPCl film can be excluded, consistent with the UV/Visible spectroscopy and XPS results, since unreacted Mn(II)TPP would have resulted in a larger magnetic moment (~6.2 μ_B) [170], giving rise to a magnetic ground state different from what is seen for the co-deposited [MnTPPCl][TCNQ] film. The co-deposited [MnTPPCl][TCNQ] lacks an ordered film structure, and a broad maximum in $\chi(T)$ that indicates presence of a typical 1D uniform ferrimagnetic chains of alternating spins [*S, s*] is not observed [27-29, 188, 189]. Thus, instead of the Seiden expression (see section 1), the $\chi T(T)$ data is fitted with the isotropic Heisenberg dimer model, which has the spin Hamiltonian as following [28],

$$\mathcal{H} = -JS_{Mn} \cdot S_{TCNQ} \tag{5.1}$$

while the inter-dimer interactions have been considered under the mean field approximation [186, 190, 191]. The magnetic susceptibility deduced from (5.1) has the following expression [186],

$$\chi \mathrm{T}_{MnTCNQ} = \frac{N_A g^2 {\mu_B}^2}{k_B} \frac{\left(10 + 35exp(5J/K_BT)\right)}{4\left(\left(2 + 3xp(5J/K_BT)\right)\right)} \tag{5.2}$$

, where J represents the magnetic exchange coupling between the unpaired spins on the Mn center and TCNQ, and N_A, g, k_B and T are the Avogadro constant, g-factor, Boltzmann constant and temperature, respectively.

Using this model, a simulation of χT versus T in the temperature range of 2-94 K, with g = 1.96, J/k_B~ -100 K and zJ'/k_B ~-5 K corresponding to the respective intra- and inter-dimeric interactions, can be obtained and compared with the $\chi T(T)$ data of the co-deposited [MnTPPCl][TCNQ] film, as shown in Figure 5.12 (c). The obtained values are consistent

with what have been reported for the magnetic charge transfer salts composed of similar donor and/or acceptor. For instance, the values of intra-chain coupling constants (J_{intra}) between Mn-porphyrin (donor) and TCNE/TCNQ (acceptor) deduced by the 1D ferrimagnetic Seiden model typically range between -70 and -100 K, as seen respectively for [MnT(X)PP][TCNE] (X = F, Br and I) [188] and $MnT(MeO)_3PP][TCNQF_4]$ (MeO = methoxy group) [192].

The inverse magnetic susceptibility (χ^{-1}) as a function of temperature simulated by the dimer model is fitted by the Curie-Weiss expression, extracting a Weiss constant of ~- 1.78 K (see Figure 5.12 (d)), in good agreement with what is obtained (~-1.7 K) from the co-deposited [MnTPPCl][TCNQ] film. This analysis therefore confirms that the spin centers Mn(III), $S = 2$ and $TCNQ^{\bullet -}$, $s = 1/2$ are antiferromagnetically coupled, with the intra-dimeric coupling constant (J/k_B) of ~ 100 K along with inter-dimeric interactions ($z'J/k_B$~ - 5 K) between the donor-acceptor dimer [MnTPP][TCNQ], though the co-deposited [MnTPPCl][TCNQ] film appears to be weakly antiferromagnetic, and almost paramagnetic-like. While the inter-dimeric interactions might be over-estimated due to the effects from the magnetic anisotropy of the Mn center at low temperature ($T < 2\ K$), as reported for Fe(III)-Mn(III) dinuclear complexes [186], the negative sign and strength of the coupling between the charge transfer donor-acceptor dimer are consistent with the suppression observed in the scaling law $H/T(T)$ curves (Figure 5.11 (b)).

Using the structural analogues of MnTPP and TCNE by co-evaporation is shown to result in charge transfer donor-acceptor dimer [MnTPP][TCNQ], characterized by antiferromagnetic, almost paramagnetic-like behaviors. Absence of a broad minimum in the $\chi T(T)$ data indicates co-evaporation of MnTPPCl and TCNQ did not form the typical quasi-1D coordination polymers of [MnTPP][TCNE], as seen in its polycrystalline form, where the linear ferrimagnetic alignment arises from 1D uniform chains of alternating spins, Mn(III), $S = 2$ and TCNE, $s = 1/2$, respectively.

This finding nevertheless highlights the particular type of chemistry applied to synthesize the charge transfer salt, in the case of [MnTPP][TCNE], is not limited to solution approaches, since the same reactions ($Mn(II) \rightarrow Mn(III)$, and $TCNQ \rightarrow TCNQ^{\bullet -}$) also occur when sublimed into the vapour phase. Charge transfer between Mn(II)TPP and TCNQ is driven by the way the two different molecules interact to find each other during co-deposition, such that electron transfer processes are predominately confined to the Mn ion and the CN groups

of TCNQ, respectively, leading to formation of donor acceptor dimer [MnTPP][TCNQ]. Accompanied by the charge transfer through MnTPP to TCNQ is the change to the spin state for the co-deposited [MnTPPCl][TCNQ] film, which reduces from $S = 2$ to $S = 3/2$, compared to the neat MnTPPCl film. Indeed, it has been observed that the magnetic moment or spin is connected to the transition metal charge state ($MnPc^{\delta+}/F_{16}CoPc^{\delta-}$), as a consequence of charge transfer from MnPc to F_{16}CoPc [172, 173].

Since the difference in the electronegativity for MnTPP/TCNQ [19] is greater than MnPc/F_{16}CoPc [172], change in the magnetic ground state and effective moment may suggest the strength of the coupling between the unpaired spins on Mn(III) ($S = 2$) and $TCNQ^{\bullet-}$($s = 1/2$), and within the [MnTPP][TCNQ] dimer, the antiferromagnetic interaction between the nearest-neighboring spins can be described by the Heisenberg dimer model, $S = 2$ and $s = 1/2$. This finding is consistent with what is observed in [MnTPP][TCNE] [13, 193], cyanide-bridged Fe(III)-Mn(III) bimetallic complexes [194, 195], and nitronyl nitroxide biradicals (with Cu(II) adduct) [196]. Furthermore, both the sign and strength of the intra-dimeric (J/k_B) coupling constant extracted by the simulated χT are found to be very comparable to those obtained from the polycrystalline form of [MnT(X)PP][TCNE] (X = F, Br and I) [188] and $MnT(MeO)_3PP][TCNQF_4]$ (MeO = methoxy group) [192], in turn suggesting the spin centers Mn(III), $S = 2$ and $TCNQ^{\bullet-}$, $s = 1/2$ in the charge transfer donor-acceptor dimer are antiferromagnetically coupled via direct exchange through the singly occupied molecular orbitals (SOMO), where spin coupling strongly depends on the nature and magnitude of the interaction between the metal ion and organic bridging ligands [197].

In this respect, co-deposition under high vacuum conditions is shown to be an effective and simple approach for obtaining films of charge transfer salts, where the parent molecules are combined in absence of solvent molecules, with a ratio determined by the respective deposition rates. What is more interesting is that formation of charge transfer donor-acceptor [MnTPP][TCNQ] dimer appears to proceed via an intermediate Mn(II)TPP in reaction with TCNQ. Whilst the absorption peak for Mn(II) porphyrin is not observed for the co-deposited [MnTPPCl][TCNQ] film, Mn(II)TPP is spectroscopically characterized and contained in the as-deposited MnTPPCl film, determined as a product of self-reduction of the vapor phase Mn(III)TPPCl accompanied by partial dissociation of the axial Cl ligands. Due to the ease of oxidation for Mn(II), it is more likely that TCNQ selectively reacts with Mn(II)TPP, whereas unreacted Mn(III)TPPCl remain as isolated molecules. Although co-evaporation leads to the concurrent redox reactions as expected for MnTPP and TCNQ, it is possible that in the

deposition chamber different kinetics operate in the process of condensation into film, and formation of dinuclear molecular compound of [MnTPP][TCNQ] becomes more favorable. By contrast, slow crystallization processes in the solution allow the two different molecules to form a uniform linear chain (1D) of coordination-polymeric structures [32, 198].

6. FePc in mixed films and spin-valve structures

Previous chapter shows that films of the charge transfer system [MnTPP][TCNQ] can be fabricated by co-evaporation, and the interactions between the unpaired spins giving rise to antiferromagnetic couplings, rather than the ferromagnetic type that is needed for spintronic devices. Now we focus on FePc which is a molecular ferromagnet. We show that the ferromagnetic behaviours can still be observed as a thin film deposited onto flexible substrates, with thickness down to 25 nm. Furthermore, the effects of insertion of electrodes prior to FePc deposition are investigated, and it is shown that the magnitude of the coercivities (H_{cr}) is uninfluenced compared to growth on to kapton substrate. However, an H_2Pc spacer layer significantly improves the crystallinity and coercivity (H_{cr}) for FePc. We further show that coercivity can be tuned by dilution with H_2Pc. Both the magnetization and coercivity are suppressed in the diluted films compared to what is observed for neat FePc, indicating inclusion of such a non-magnetic substituent has a strong influence on the correlation lengths of the Fe chains required for the long range ferromagnetic ordering.

Co-deposition of MnTPPCl and TCNQ with a 1 to 1 ratio has been shown to lead to films containing the charge transfer donor-acceptor dimer [MnTPP][TCNQ], characterized by the charge transfer bands and weak antiferromagnetic interactions attributed to the magnetic coupling between the unpaired spins on the Mn ion and CN groups of TCNQ. In the charge transfer system based on a mixture of manganese phthalocyanine (MnPc) and copper hexadecafluorophthalocyanine ($F_{16}CoPc$), the transferred charge causes the change in the transition metal charge state ($MnPc^{\delta+}/F_{16}CoPc^{\delta-}$), and charge transfer interaction between the organic-organic interfaces is intimately connected to the transfer of magnetic moment or spin [140]. These studies suggest the exotic properties can be created through rational design of the film composition, with the expectation of magnetic couplings directly tuned by the

functional molecules incorporated in the film. However, those systems so far did not deliver ferromagnetism and we therefore explore the molecular semiconductor FePc, which has been shown to be ferromagnetic [3, 199].

Based on the concepts developed in the previous chapters, we investigate a diluted ferromagnetic system based on a mixture of FePc and H_2Pc towards molecular films with controllable coercivities. Transition metal phthalocyanines crystallize in a wide range of polymorphs, and different types of magnetic properties are a consequence of structural dependent exchange pathway operated in these planar π conjugated molecular systems [30, 159]. Spin interactions responsible for the magnetic correlation and susceptibility mainly arise from the magnetic ions stacked within the columns, while the weaker dipolar interactions between the parallel columns can influence the ordering temperature, as seen in some of the ferrimagnetic chain systems [27, 188, 200]. The intra-chain interaction can be rationalized by the coupling between molecular orbitals of the transition metal ions, whose symmetry can play a key role on the degree of couplings [23]. In the case of FePc, the Fe ions stacked within the columns can be modelled with a 1D Ising ferromagnetic chain [27], and the length for such chains is inherently limited by the grain size, and defects within the grains. The effect of the grain size on the Fe chains has been proposed by Gredig *et al.*, where the increased coercivity and the magnetic anisotropy are obtained from larger crystallites in the FePc film grown at the elevated substrate temperature [160].

The chapter begins with the film properties of a diluted ferromagnetic system formed by mixing H_2Pc with FePc. It is anticipated that the bulk magnetic properties, for instance, the coercivity of FePc, may be modified by co-deposition with a non-magnetic substituent, H_2Pc. H_2Pc is isomorphous to FePc, and co-deposition of FePc and H_2Pc is expected to give rise to molecular columns heterogeneously occupied by two different phthalocyanine molecules, giving rise to a wide distribution of Fe chain lengths, determined by the concentration of H_2Pc. Blending H_2Pc with C_{60} has been shown to result in a homogeneous mixture, with the improved efficiency primarily due to the increased interfacial area between the two different molecules that form nanoclusters with a size below the detection limit of XRD [152]; homogeneous blends are obtained when CuPc is co-evaporated with H_2Pc, highly textured as in the single component films [152]. It is therefore expected phase separation between H_2Pc and FePc should not occur during the co-evaporation, and the degree of mixing for the two phthalocyanine molecules will be demonstrated by magnetism.

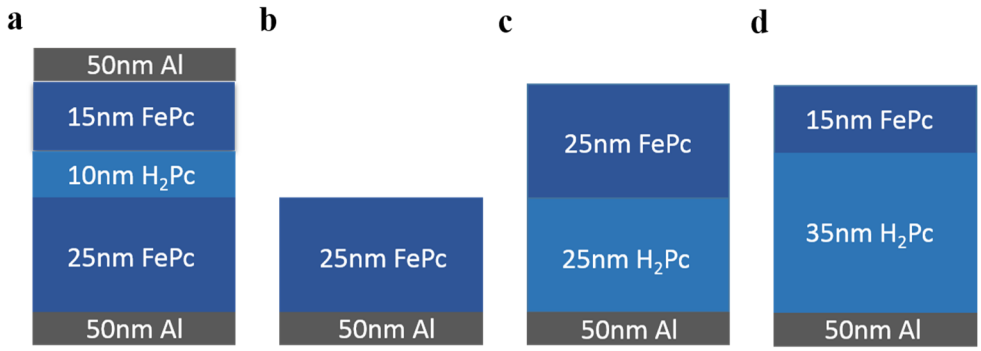


Figure 6.1 Schematics depicting (a) an all organic spin valve, or all phthalocyanine spin valve, consisting of Al/FePc/H_2Pc/FePc/Al. The molecular ferromagnet, FePc, can be utilized as a spin injector and detector with different coercivities, decoupled by a thin layer of H_2Pc as the non-magnetic spacer. (b), (c) and (d); three multi-layers similar to the device structure given in (a), but fabricated with only one layer of FePc, (b) 25 nm FePc on 50 nm Al, (c) 25 nm FePc/25 nm H_2Pc/50 nm Al, and (d) 15 nm FePc/35 nm H_2Pc/50 nm Al. All the multi-layered structures for magnetic characterizations are grown on kapton substrate.

The ferromagnetism makes FePc a particularly promising candidate as a magnetic component for spintronic applications, and thus the studies on FePc are extended into spintronic devices. For the simplest all-organic spin valve, the device architecture would at least consist of two ferromagnetic layers, as a spin injector and detector, decoupled by a thin layer of non-magnetic spacer, finished with non-magnetic metal bottom and top contacts. Figure 6.1 (a) represents a possible structure for a novel all-organic spin valve concept, consisting of two ferromagnetic layers of FePc with the thickness of 25 nm and 15 nm, respectively, separated by a 10 nm thick layer of H_2Pc as the non-magnetic spacer. While the choice of thickness for the spin injector/detector and non-magnetic spacer predominately depends on the conductivity of phthalocyanines, deposition of phthalocyanine with a thickness of 10 to 25 nm leads to crystallites with a correlation length still detectable by XRD, allowing for a systematic study on the coercivity and film structure of FePc. Knowledge of the organic/metal heterostructure is crucial for understanding and optimization of devices. In this context, the film properties of FePc grown on substrates coated with metal contacts, *i.e.* a heterostructure based on FePc/Al need to be explored. Al is extensively used as bottom/top contact in thin film devices for its excellent conductivity (at 20 °C, the electrical resistance ~ 26.5 nΩ m) [161], stability and non-magnetic properties [162]. Fabrication of Al contacts by thermal evaporation in the OMBD chamber allows growth of the subsequent molecular layers without breaking vacuum so as to minimize Al oxidation, with the rate of 0.2 Å/s at room temperature in order to obtain a smooth organic/metal interface. The morphological and

structural properties of the Al films on commercially available substrates (glass, silicon and kapton) fabricated by thermal evaporation in the OMBD are characterized, and an overall thickness of 50 nm for the subsequent phthalocyanine layer is used to investigate the effects of the underlying substrate on the resultant film morphology and structure, allowing us to understand and improve the device performance.

Finally, the film properties of FePc when used as an injector and detector are revealed by investigating three types of device architectures based on multi-layers of FePc, H_2Pc and Al, which are designed to simulate the typical device configurations implemented in an all organic spin valve, and three types of multi-layered structures based on FePc and H_2Pc are fabricated based on the device geometry identical to what we envisage for a spin valve. The structures (b), (c) and (d) are not functional devices, yet they allow us to isolate the film properties of FePc as a spin injector and detector in the all-organic spin valve. All the multi-layered structures are deposited onto kapton substrate for magnetic measurements.

6.1 Mixed H_2Pc:FePc films

6.1.1 Morphology of the films

The mixed H_2Pc:FePc films, are fabricated by co-deposition of the respective powders placed in separate Knudsen cells in the OMBD chamber, and the stoichiometry is adjusted by the deposition rate, similar to the co-deposition of MnTPPCl and TCNQ.

The morphology of 100 nm thick films of mixed H_2Pc:FePc containing 10% and 50% of H_2Pc, respectively, is observed by AFM. Figure 6.2 (a) and (b), inclusion of 10% of H_2Pc has no apparent effects on the morphological properties exhibited by FePc, where the spherical islands characteristic of α-phthalocyanine films, with different island sizes of 33 nm and 40 nm (see Figure 6.2 (c) and (f)) can be found for the 10% H_2Pc films on silicon and kapton substrates, corresponding to a roughness (RMS) of ~ 3.4 nm and ~ 4.7 nm, respectively. Co-depositing H_2Pc with CuPc also results in a typical morphology adopted by phthalocyanines, confirming the structural conformity of the different phthalocyanine molecules, independent of the H_2Pc concentration [163].

Similar spherical islands can be observed when the concentration of H_2Pc is increased from 10 % to 50 %, and again, the film on silicon substrate forms a homogeneous and smooth

coverage, corresponding to a relatively low RMS ~3.5 nm, with an averaged island size of 37 nm. On kapton, the islands appear to be larger and more elongated than those obtained on silicon substrate, giving rise to an averaged grain size of 43 nm. The film surface appears to be rather smooth, as suggested by RMS~ 3.6 nm. The differences in the island size and shape are attributed to the substrate effects.

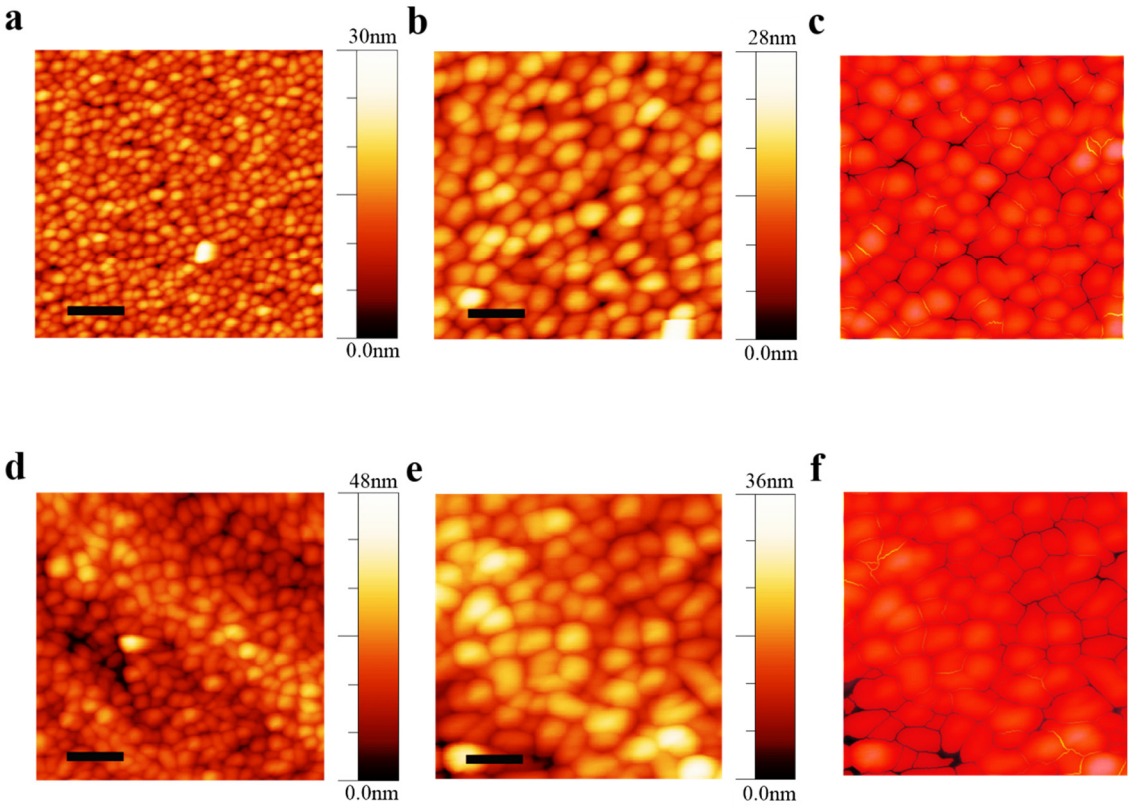


Figure 6.2 AFM micrographs of 100 nm thick films of mixed H_2Pc:FePc (H_2Pc = 10%) on (a) and (b) silicon substrate, (d) and (e) on kapton. The scale bars in (a) and (d) are 200 nm, and 100 nm for (b) and (e), respectively; (c) and (f) corresponding to the watershed mark used for (b) and (e) to extract the average lateral grain size of the mixed H_2Pc:FePc films.

Overall, the morphology exhibited by the mixed H_2Pc:FePc film (10 %) resembles that seen for the neat phthalocyanine films, characterized by homogeneous small spherical islands [132]. The size of the islands appears to be somewhat affected by the H_2Pc concentration, and are found to be slightly smaller compared to those observed for the mixed film with 50 % H_2Pc. The change in the island shape under different H_2Pc concentrations becomes more apparent for deposition onto kapton substrate. Although both silicon (covered by its native oxide) and kapton are weakly interacting substrates, the surface roughness found for the

kapton and silicon corresponding to RMS = 1.9 nm and 0.5 nm respectively may account for the marginally different island sizes obtained from the two films.

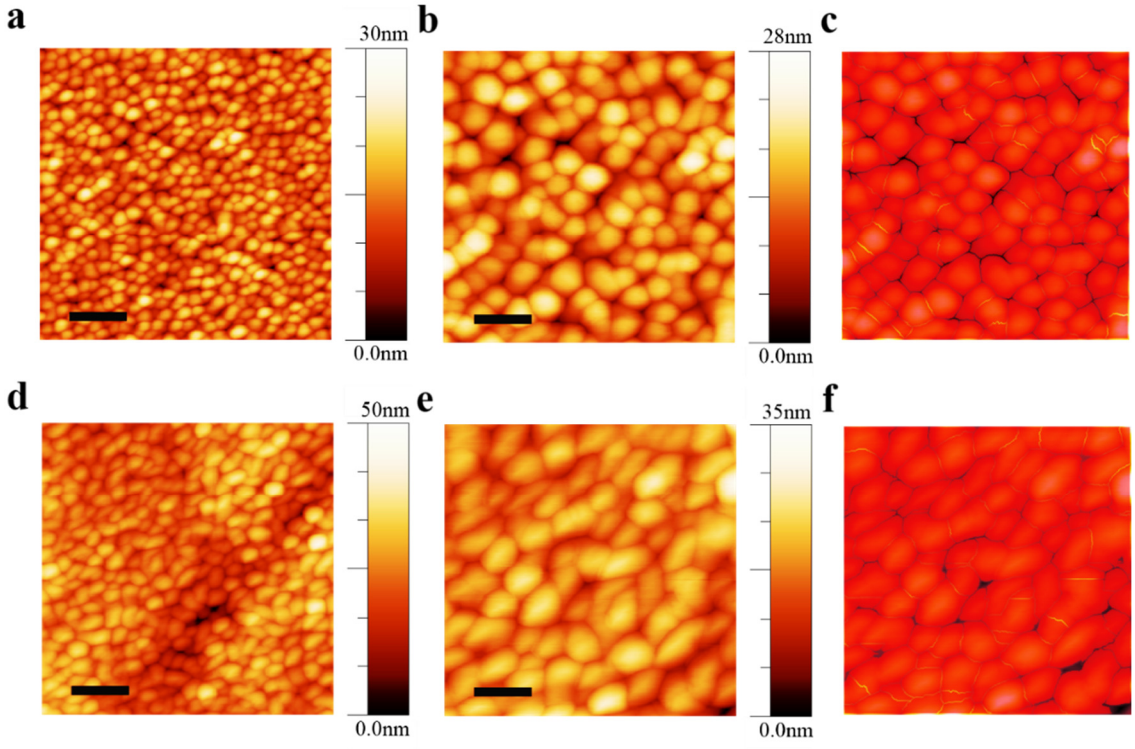


Figure 6.3 AFM micrograph of 100 nm thick films of mixed H_2Pc:FePc films (H_2Pc = 50 %) on (a) and (b) silicon substrate, (d) and (e) on kapton. The scale bars in (a) and (d) are 200 nm, whereas those for (b) and (e) are 100 nm, respectively; (c) and (f) corresponding to the watershed mark used for (b) and (e) to extract the average lateral grain size of the H_2Pc:FePc films.

6.1.2 Structure of the films

The structure of the mixed H_2Pc:FePc films with 10 % and 50 % of H_2Pc deposited on silicon substrate is determined by XRD, with a 50 nm thick neat FePc film on silicon included for comparison, in Figure 6.4.

In the range of 2θ = 5-35°, the FePc film exhibits a diffraction peak at 2θ = 6.9°, whereas a sharp diffraction at 2θ = 33° corresponds to the underlying silicon substrate (100). Presence of the diffraction peak at 2θ = 6.9° suggests the FePc film on silicon is preferentially textured

along the (100) plane parallel to the substrate plane. The molecular columns stack along the *b*-axis, and the molecular orientation relative to (100) is 82°.

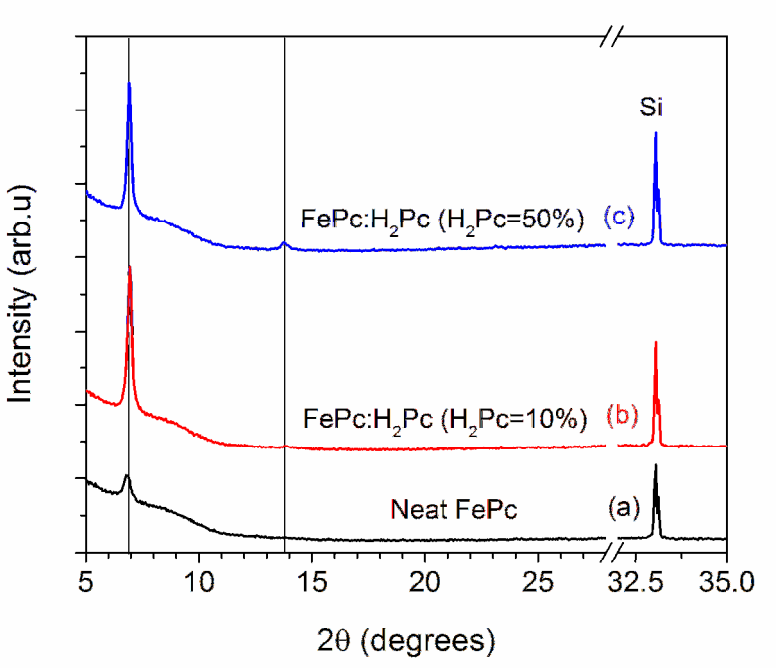


Figure 6.4 XRD scans of (a) a 50 nm thick FePc film, and 100 nm thick films of mixed H_2Pc:FePc containing (b) 10 % of H_2Pc, and (c) 50 % of H_2Pc. All the films are deposited on silicon substrate, and the data are offset for clarity. The light grey lines plotted to index the (100) diffraction peak at $2\theta = 6.9°$ and the 2nd order diffraction at $2\theta = 13.8°$.

For the film with 10 % H_2Pc, the same peak at $2\theta = 6.9°$corresponding to the (100) orientation expected from FePc can be observed, accompanied by a very weak peak at $2\theta = 13.8°$ ascribed to the 2nd order diffraction from the (200) plane. The peak at $2\theta = 33°$ again corresponds to the silicon substrate (100). It can therefore be concluded that diluting FePc with H_2Pc results in the mixed films highly textured in (100), adopting the edge on orientation that characterizes the growth of phthalocyanine on weakly-interacting substrates [104]. Note that the H_2Pc film has a similar crystal structure for FePc [155], although the structure factor differences lead to enhanced 2nd order diffraction on the (100) peak for H_2Pc.

Increasing the concentration of H_2Pc to 50 % leads to a very similar diffraction pattern, as shown in Figure 6.4. The same sharp and intense peak at $2\theta = 6.9°$due to the (100) plane parallel to the substrate can be found, yet the peak at $2\theta = 13.8°$ corresponding to the 2nd order diffraction is more intense than that seen for the film with 10 % H_2Pc.

Table 6.1 Summary of the XRD patterns obtained from 100 nm thick films of mixed H_2Pc:FePc with a concentrations of 10 % and 50 % of H_2Pc deposited on silicon substrate, and the respective grain sizes calculated by the Sherrer analysis, $2\theta(°)$ represents the peak center, whereas $w_{2\theta}(°)$ corresponds to the peak width obtained from the full width half maximum (FWHM) of the Gaussian fit, expressed in the unit of degree.

H_2Pc:FePc films	$2\theta(°)$	$w_{2\theta}(°)$	Scherrer size (nm)
H_2Pc = 10 %	6.95	0.25	31.8-46.8
H_2Pc = 50 %	6.93	0.22	36.2-58.6

The intensity of the 2nd order peak becomes more prominent as the H_2Pc concentration increases. Similar behaviour has been observed for a 200 nm thick film of mixed CuPc:H_2Pc (CuPc = 5 %), which exhibits the 2nd order peak that is otherwise absent in the neat CuPc film with the same thickness, due to the difference between the structure factors between the two phthalocyanine molecules [163].

The size of the crystalline domains in the mixed H_2Pc:FePc films can be quantified, by applying the Scherrer analysis to the XRD results. The crystallite sizes for the films with 10 % and 50 % of H_2Pc are calculated and summarized in Table 6.1, corresponding to 31.8-46.8 nm and 36.2-58.6 nm, respectively. The resulting values are consistent with what was observed by AFM, therefore suggesting the influence of the concentration of H_2Pc on the grain sizes and film crystallinity.

Inclusion of H_2Pc leads to the mixed H_2Pc:FePc films preferentially textured with the (100) plane, and during co-deposition both FePc and H_2Pc stack into columns, the typical stacking seen for the neat phthalocyanines, with the lattice constant in the *a*-axis corresponding to ~ 12.9 Å [104], confirming the two different phthalocyanines can co-crystalize in the same crystal structure. XRD does not allow us to deduce the actual film configuration, *e.g.* a homogeneous ordered mixture or phase segregation at the molecular level in the mixed film. However, previous studies on the molecular blends based on the mixture of H_2Pc and CuPc indicate phase segregation at large scale is unlikely [152], which can give rise to different magnetic behaviour for the mixed H_2Pc:FePc films, as discussed in the following section.

6.1.3 Magnetic characterization of the films

The 2 K isothermal magnetization M(H) curves of the 100 nm thick H_2Pc:FePc films with 10 % and 50 % of H_2Pc are presented in Figure 6.5, with the neat 25 nm thick FePc film included for comparison. The magnetization as a function of the applied field is normalized to Fe atom for both the neat FePc, and the mixed H_2Pc:FePc films.

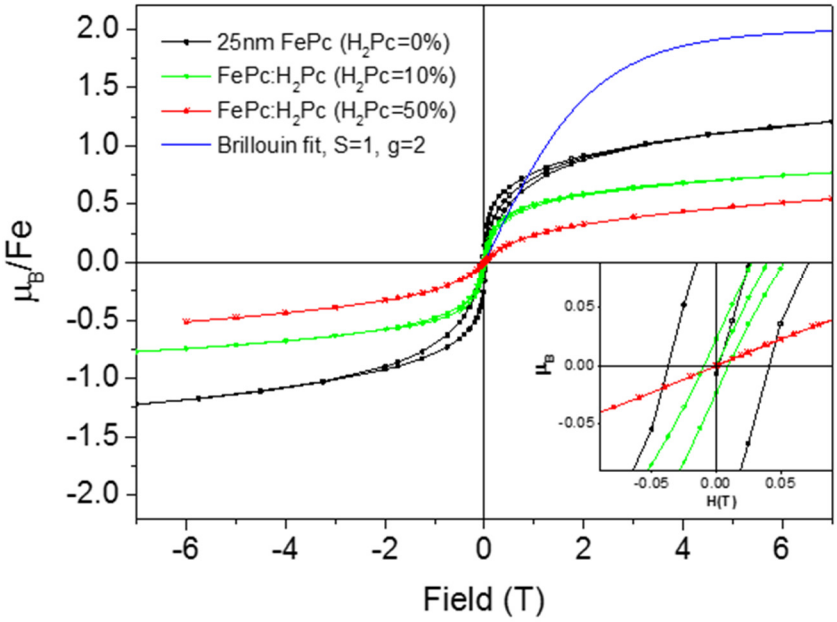


Figure 6.5 Isothermal magnetization curves as a function of the applied field, $M(H)$, measured at the temperature of 2 K for the neat 25 nm FePc film (black solid curve), 100 nm thick films of mixed H_2Pc:FePc, with ratios of 10 % (red solid curve) and 50 % of H_2Pc (blue solid curve), respectively, shown with the Brillouin fit for a spin $S = 1$ with $g = 2$. The magnetic moment is expressed in the unit of μ_B per Fe atom. Inner panel: no hysteresis loop can be observed for the mixed film consisting of 50 % of H_2Pc.

The field dependent isothermal magnetization $M(H)$ measured at 2 K (black curve) of the neat FePc film displays a hysteretic behaviour, with the coercivity of ~ 400 Oe observed at 2 K, indicating FePc to be a ferromagnetic material. The moment per Fe atom first increases sharply to 0.61 μ_B as sweeping the applied field (H) from 0-0.4 T, then steadily increases up to 1 μ_B under a field of 3.25 T, slowly reaching a value of 1.21 μ_B, comparable to the expected value for a $S = 1$ system ($g = 2$). The coercivity found for the 25 nm film appears to be lower than that seen for a 100 nm film (~ 850 Oe, 2 K) [111], but overall consistent with the range

of values between 100 to 2000 Oe (2 K) reported for films with a thickness of 200 nm obtained by using different substrate temperatures [112]. This discrepancy possibly arises from the different growth conditions that often lead to variations to the film structure, without considerations of the field sweeping rate a direct comparison between the literature values for coercivities can be misleading, due to the slow relaxation processes of FePc. For this reason, the same sequence is used to measure the field dependent magnetization for all the FePc films in this work.

The hysteresis loop is still open when H_2Pc concentration is increased to 10 %, as shown in the red curve in Figure 6.5, and the magnetization as a function of applied field (H) indicates the mixed H_2Pc:FePc film exhibits a remanence of ~ 0.02 μ_B and coercivity (H_{cr}) of ~ 100 Oe (0.01 T), considerably smaller than is seen for the neat 25 nm FePc film. The shape of the magnetization curve similar to that of the neat FePc suggests the ferromagnetic behaviour is not overly suppressed by substitution of 10 % H_2Pc. The moment per Fe atom is observed to increase at a reasonably faster rate for the film consisting of 10 % H_2Pc, with magnetization corresponding to ~ 0.34 μ_B under the applied field H = 0.3 T and ~ 0.77 μ_B when the field is swept to 7 T. As a result, the film reaches a value relatively lower than that seen in the neat FePc film under the applied field of 7 Tesla, where at 2 K the moment is observed to be ~ 1.2 μ_B at H = 7 T [111]. Substitution of 10 % of diamagnetic H_2Pc into the FePc film appears to reduce the overall magnetization as a function of the applied field, however does not entirely disrupt the ferromagnetic interactions and long range ordering in FePc.

Increasing the concentration of H_2Pc from 10 % to 50 % leads to apparent changes in the slope of the 2 K isothermal $M(H)$ curve (the green curve in Figure 6.5) for both the low and high field regime, and the magnetic behaviour previously seen in the neat FePc film becomes absent. Moreover, the moment per Fe atom is considerably suppressed in comparison to what is found for the neat FePc film. The magnetization gradually increases with the applied field H, and approaches ~ 0.55 μ_B at 7 T, which is significantly lower than the expected moment for Fe(II) with spin state S = 1 and g = 2. The inclusion of 50 % H_2Pc has drastically changed the magnetic properties exhibited by FePc, and the lack of a coercivity indicates absence of long range ferromagnetic orderings for the mixed H_2Pc:FePc film, attributed to a large occupation of the non-magnetic substituent.

In order to interpret the magnetic behaviour observed for the mixed H_2Pc:FePc films, the effects of dilution with H_2Pc on the film composition at the molecular level has to be considered. Incorporation of H_2Pc is expected to lead to at least three possible film

configurations, including molecular columns consisting of 1) solely H_2Pc, 2) solely FePc, and/or 3) both H_2Pc and FePc (see Figure 6.6). In the latter case, the presence of H_2Pc molecules can form a homogeneous mixture leading to shorter segments of continuous FePc chains. The fact that the magnetism changes progressively with H_2Pc concentration suggests that H_2Pc and FePc molecules both crystallize into the same crystal structure and that the third possibility is the most likely, in turn giving rise to co-crystals of the two different phthalocyanines.

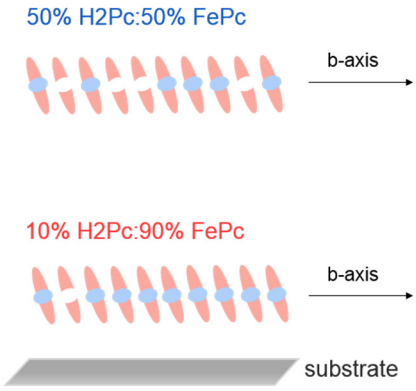


Figure 6.6 Schematics show possible film configuration for the H_2Pc:FePc films, based on the number of FePc molecules that are likely to be found in the molecular column at the given concentration of H_2Pc; top panel: mixed H_2Pc:FePc film containing 50 % FePc, and lower panel: 90 % FePc. The blue, and white spheres represent FePc and metal-free H_2Pc, respectively.

The inclusion of H_2Pc as a non-magnetic defect reduces the length of the Fe continuous chains, in addition to the structural defects within the crystalline grain, or at the grain boundary that can produce cut-chains as identified for neat α-phthalocyanines [66]. The bulk magnetic properties of FePc are largely determined by the magnetic interaction along the Fe chains within the column, suggesting a lower limit for the chain length required for the long range ferromagnetic orderings to be observed for the mixed of H_2Pc:FePc film. The film with 10 % H_2Pc shows a drastic decrease in the coercivity compared to that obtained in the neat 25 nm thick FePc film, suggesting mixing H_2Pc with FePc by co-deposition leads to a considerably uniform molecular blend formed by the two phthalocyanine molecules; the correlation lengths needed for the ferromagnetic couplings would have been more similar to those in the neat FePc film, if phase separation had occurred and resulted in homogeneous columns formed by H_2Pc and/or FePc. This is in agreement with what is observed for the

mixed H_2Pc:CuPc films [185], indicating co-deposition with H_2Pc is an effective approach to modulate the magnetic couplings and correlations within the columns of Pcs through controlling the correlation lengths at the molecular level. This observation is consistent with a recent report by Gredig *et al.* on the variable coercivities of FePc obtained from the larger grain sizes, due to the longer correlation length for the Fe ion chains [199].

Thus, the strategies for controlling magnetic properties of FePc are not limited to those obtained by using different growth substrates and higher substrate temperature. Mixing with H_2Pc results in similar but different magnetic behaviours from those seen in FePc, with the coercivities and magnetization as a function of the applied field directly modified by the relative composition of the two different phthalocyanine molecules contained in the film, by means of simple co-deposition. Mixed phthalocyanines are therefore a very attractive strategy towards controllable magnetic properties, and mixing two molecular materials at any ratio is particularly straightforward, since issues such as strain and incongruent melting are rare for such systems. While diluting with H_2Pc has shown to drastically reduce both the magnetization and coercivity, this result confirms the intra-columnar interactions along the Fe chains are crucial to the magnetic coupling responsible for the ferromagnetic behaviours observed in both crystals and films of FePc.

6.2 Substrate effects on FePc films

6.2.1 Morphology of Al

Prior to fabrication of the multilayers, the Al films obtained by using OMBD were characterized. The typical morphology of the Al films fabricated by thermal sublimation in the OMBD chamber observed by AFM is given in Figure 6.7.

Figure 6.7 (a) and (b) show two different Al films deposited onto glass substrates, with thicknesses of 100 nm and 50 nm, respectively, and for both films, randomly oriented spherical particles between ~ 20-50 nm in diameter can be observed to cover the surface. The particle size appears to increase with the film thickness, as suggested by the height profile along the green line in Figure 6.7 (a) and (b). A smaller roughness of RMS ~ 2.4 nm is found for the 50 nm thick film, in comparison to 4.4 nm for the 100 nm thick films, suggesting the roughness of the Al film is slightly decreased by reducing the film thickness.

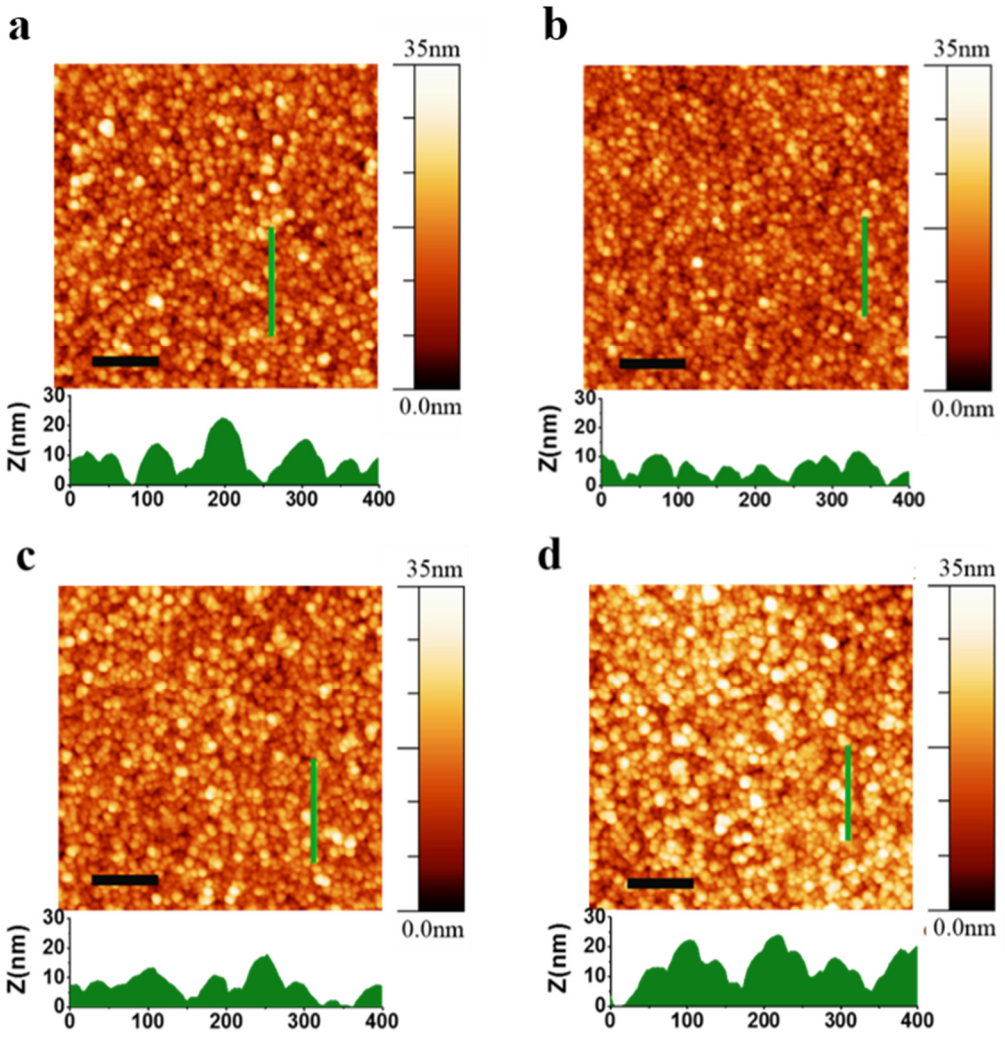


Figure 6.7 AFM micrographs of Al films deposited at the rate of 0.2 Å/s by using OMBD on glass with a thickness of 100 nm (a) and 50 nm (b), and 100 nm thick films on (c) silicon and (d) kapton substrates, and the height profile along the green line in (a), (b), (c) and (d) reveals the Al grain height, plotted below the figures. The respective RMS measured for each sample corresponds to 4.6, 2.4, 4.4 and 5.5 nm for (a), (b), (c) and (d), respectively, and the scale bars in all figures are 300 nm.

Deposition of Al at the same rate with a thickness of 100 nm onto silicon and kapton substrates results in a morphology very close to that obtained on glass substrates, with a similar size distribution ranging from ~ 10 to 50 nm in diameter, although the roughness is higher on kapton (RMS = 4-5 nm, see Figure 6.7).

The roughness and the grain size (see the height profiles) for the Al films somewhat increase with the roughness of the underlying substrate used for growth, similar to what was

previously seen for the mixed FePc: H_2Pc films. As a consequence, the thickness for the Al contact is maintained to be 50 nm as the studies continue, as indicated by AFM, since a relatively smooth and continuous Al layer can be obtained at a lower film thickness for molecular spintronic devices.

6.2.2 Structure of Al

The Al film deposited on silicon substrate by using OMBD (see Figure 6.8) shows very intense and sharp diffraction at $2\theta = 69°$ and $2\theta = 33°$, followed by relatively weak diffraction observed at $2\theta = 61.8°$.

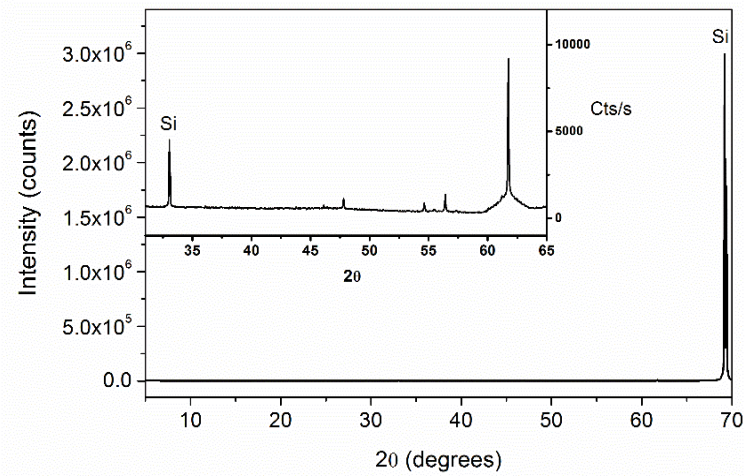


Figure 6.8 the XRD scan of a 50 nm thick Al film deposited at the rate of 0.2 Å/s at room temperature on silicon covered by its native oxide.

The former two diffractions peaks are assigned to the underlying silicon substrate, and correspond to the (100) plane [201] and the 2nd order diffraction arising from the (200) plane, while the diffraction peak at $2\theta = 61.8°$ does not correspond to any expected values for Al (see Table 6.2) [202] or silicon. Films obtained under similar growth conditions by using the thermal evaporation in OMBD are suggested to be poly-crystalline [203].

Table 6.2 Diffraction peaks, intensities and the corresponding crystallographic planes observed for the Al crystal structure, adapted from [202].

2θ (°)	Intensity (%)	(*h*,*k*,*l*)
38.50	100.00	1 1 1
44.76	47.49	2 0 0
65.16	28.01	2 2 0
78.30	30.71	3 1 1
82.52	8.74	2 2 2

6.2.3 Morphological and structural properties of FePc on Al

The morphology of a 50 nm thick (thickness chosen because it corresponds to the total thickness of our proposed spintronic device as seen in Figure 6.1) FePc films deposited on substrates (glass and silicon covered by its native oxide) pre-coated with 50 nm thick Al films are shown in Figure 6.9.

For Al first layers, a similar morphology previously seen for the thicker film can also be found for the 50 nm Al film. The roughness of the films deposited on glass and silicon substrate is rather similar, corresponding to 3.5 and 4.3 nm, respectively, as observed by AFM. The slightly raised roughness observed here could be due to larger protruding particles scattered sporadically, as seen for the film on silicon substrate (in Figure 6.9 (a)).

As for the 50 nm thick FePc films, small spherical islands characteristic of the α-phthalocyanine films [155, 204] can be observed on both glass and silicon substrate (see Figure 6.9 (b), (e) and (h)). The height and size of the islands are smaller than those seen in the 100 nm film [136], as indicated in the height profile, with the averaged island size of 32 nm found in the film on glass, with RMS ~ 1.6-1.7 nm.

When deposited onto the Al substrate (Figure 6.9 (c) and (f)), very similar islands can be observed for the 50 nm FePc. Yet, compared to those obtained on bare glass and silicon substrate, it seems both the size and surface roughness have increased (Figure 6.9 (e) and (f)), as indicated by the height profiles (along the purple line given in (h) and (i)), in turn giving rise to an average lateral size of 38 nm.

The roughness of the FePc film is found to increase when grown on the Al substrate, RMS ~

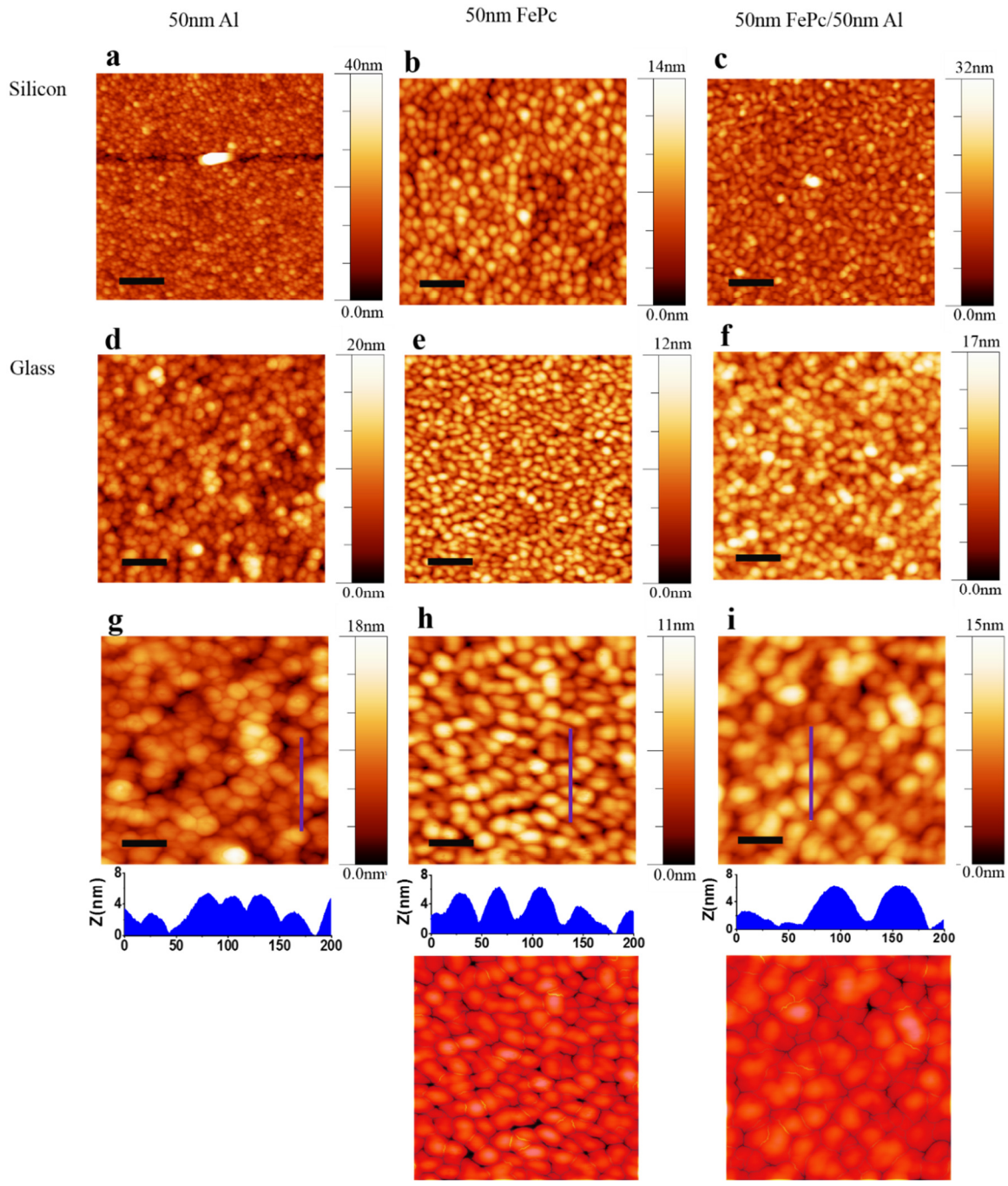


Figure 6.9 AFM micrographs of the 50 nm thick Al films deposited at the rate of 0.2 Å/s (a) on silicon substrate, (d) and (g) on glass substrates, 50 nm thick FePc films on (b) silicon and (e) and (h) on glass substrates, and 50 nm thick FePc films on substrates coated with 50 nm thick Al films deposited at the rate of 0.2 Å/s (c) on silicon substrate and (f) and (i) on glass substrates. The height profile along the purple line in (g), (h) and (i) reveals the grain height, plotted below the figures, and the watershed mark used to estimate the average grain size of 50 nm FePc films (h) on glass, and (i) on 50 nm thick Al deposited on glass, respectively. The scale bars in (g), (h) and (i) are 100 nm, whereas a scale bar of 200 nm is used in the rest of the images.

2-3 nm (see Table 6.3), in comparison to deposition on bare substrates. The observed value however appears to be lower than the roughness found in the Al films (with RMS = 3.5-4.3 nm), as FePc forms a smoother and homogenous layer on top of the metallic film.

Thus, using the Al coated substrate does not cause major changes to the morphological features displayed in the FePc films, and in particular increases the height, size, and roughness of the FePc islands, compared to those obtained on the bare substrates.

Table 6.3 Summary of the RMS values measured from the 50 nm FePc films deposited on glass, silicon and 50 nm Al films.

	RMS (nm) obtained from AFM		
	50 nm Al	50 nm FePc	50 nm FePc/50 nm Al
Glass	3.5	1.6	2.2
Silicon	4.3	1.7	3.0

Structure

The structure of the FePc films on Al is determined by XRD, as shown in Figure 6.10, with the XRD scans of the Al and films deposited onto bare silicon and glass substrates included for comparison.

The structure of the 50 nm thick Al deposited onto glass and silicon substrate is found to be amorphous, except for the peak at $2\theta = 33°$ due to the silicon substrate, as no other diffraction can be observed, different from the very weak diffraction peaks previously seen in the range of $2\theta = 50\text{-}60°$ for a different film. The purpose of this study is to obtain Al layers with reduced roughness so as to form a smooth organic/metal interface ideal for device applications. The growth protocol, *i.e.* the deposition rate, film thickness and substrate temperature used to fabricate the Al contacts here is not designed for growing metallic films with well-defined structural properties, which often require different types of growth parameters and substrates [205].

Between $2\theta = 5\text{-}30°$, the 50 nm thick FePc film deposited on both glass and silicon substrate displays a sharp and intense diffraction peak at $2\theta = 6.9°$, due to the (100) plane, confirming the film is textured with the (100) plane parallel to the substrate. The correspondingly grain

sizes deduced by the Scherrer analysis, summarized in Table 6.3 are found to be 20.4-25.7 nm and 24.9-33.2 nm, respectively, consistent with what is observed by AFM.

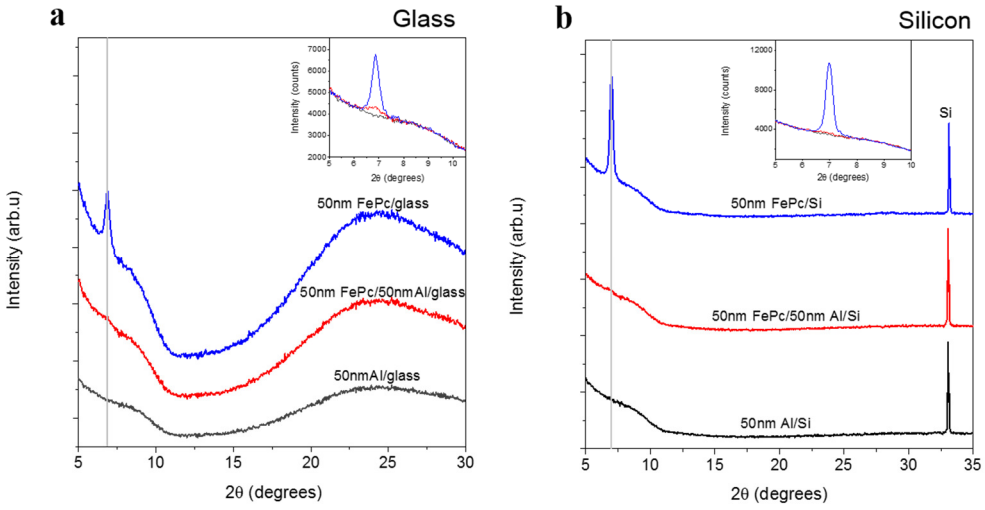


Figure 6.10 XRD scans of the 50 nm thick FePc films deposited on 50 nm thick Al films (red solid curves), the 50 nm Al film (black solid curves), and the 50 nm FePc films (blue solid curves) on (a) glass, and (b) silicon substrate, with the light grey line plotted to index the (100) diffraction peak at $2\theta = 6.9°$. The deposition rates for FePc and Al are 0.5 Å/s and 0.2 Å/s, respectively. No background subtraction is applied and the data are offset for clarity. The step size and time per step used for the XRD measurements are 0.033° and 50 second, respectively.

When deposited onto glass pre-deposited with 50 nm Al film, the peak at $2\theta = 6.9°$ is present, but with a significantly low intensity (Figure 6.10 (a) and (b) inner panel shows the scan between $2\theta = 5$-12), and for deposition on silicon substrate the same diffraction becomes almost invisible. This suggests the crystallinity for the FePc film is disrupted due to the roughness of the underlying Al layer, or perturbing interactions between the growth of FePc.

Growth of FePc onto the Al substrate induces several changes to the film morphology and structure. The islands are slightly larger in diameter and height, giving rise to a relatively rough film surface, in comparison to those on bare substrates, but more profound impact is observed for the FePc film structure.

The preferential molecular orientation of the FePc film on Al remains to be (100), indicating the film adopts a same orientation as seen for those obtained from bare substrate. Yet, the diffraction intensity for this peak has become very weak, suggesting a drastic decrease in the

texture, giving rise to a more disordered film structure, due to the relatively large surface roughness of the Al substrate. It can therefore be expected modifications to the film morphology and structure are induced by the underlying Al substrate when FePc is used as spin injector.

Table 6.4 Summary of the XRD patterns obtained from the 50 nm FePc films on glass and silicon substrate, and the respective grain sizes calculated by the Sherrer analysis, $2\theta(°)$ represents the peak center, whereas $w_{2\theta}(°)$ corresponds to the peak width obtained from the full width half maximum (FWHM) of the Gaussian fit, expressed in the unit of degree.

50nm FePc	$2\theta(°)$	$w_{2\theta}(°)$	Scherrer size (nm)
Glass	6.88	0.39	20.4-25.7
Silicon	6.98	0.32	24.9-33.2

6.3 FePc in spin-valve structures

6.3.1 Morphology of the films

AFM micrographs (Figure 6.11) show the morphology of a 25 nm thick FePc film deposited onto glass, and again, the FePc film is covered by randomly oriented small spherical islands, similar to those previously seen in the 50 nm FePc films and 100 nm thick films of mixed H_2Pc:FePc films on both glass and silicon substrates.

At the thickness of 25 nm, the film appears very smooth, and the averaged size of the islands corresponds to 26 nm, with a roughness RMS = 2.3 nm obtained by AFM. Therefore, between 25 to 50 nm the morphology adopted by the FePc films is independent of the thickness, but on average the islands obtained for the thinner film are slightly smaller. This behaviour is similar to the trend reported for the CuPc films, where the grain size is observed to increase as a function of film thickness [206].

The morphological properties of the 25 nm FePc film (structure (b) as shown in Figure 6.1) deposited onto substrates coated with a 50 nm thick Al film are presented in Figure 6.12 (a), (d) and (g), corresponding to films deposited on glass and kapton substrates, respectively.

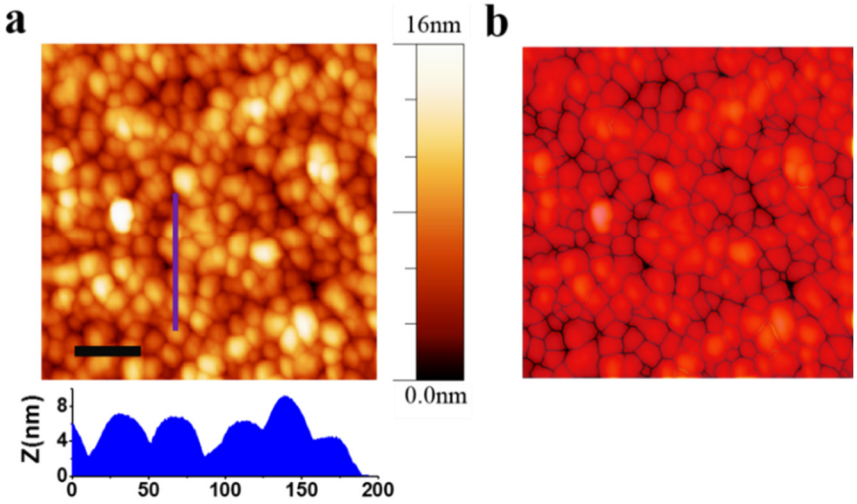


Figure 6.11 AFM micrograph of (a) the 25 nm thick FePc film deposited at the rate of 0.5 Å/s on glass, and the height profile along the purple line in (a) reveals the FePc grain height, plotted below the figure, with the scale bar of 100 nm included. (b)The watershed mark for (a) used to extract the average lateral grain size of the 25 nm FePc film.

Similar to the 50 nm FePc film on Al and 25 nm FePc film on glass, small spherical islands with random orientation can be observed, and the islands appear to be larger than those obtained for deposition on glass substrate, (shown in the height profile along the purple line in Figure 6.12 (g)), with averaged lateral size in 27 nm and 24 nm on glass and kapton, respectively, in turn giving rise to a relatively large roughness RMS = 4.9 nm.

Thus, the 25 nm FePc film on Al is considerably rougher than that on glass (RMS ~ 2.3 nm), and the roughening for the FePc film is attributed to the surface morphology, *e.g.* large RMS of 3.5-4.3 nm, of the Al substrate, as previously seen for the 50 nm FePc films on Al. The roughness of the 50 nm FePc film on Al (RMS ~ 3.5 nm) is slightly lower than what is found in the 25 nm thick film, indicating the roughening from the underlying Al substrate becomes more apparent as the film thickness decreases.

Figure 6.12 (b), (e) and (h) shows similar islands can be observed when the same thickness of FePc is deposited onto the Al substrate pre-coated with a 25 nm H_2Pc film (corresponding to the structure (c) in Figure 6.12). When using a glass substrate, see Figure 6.12 (a) and (b), FePc forms even large islands on H_2Pc than those seen in the 25 nm FePc film on Al, with an increase in grain size from 27 nm to 31 nm.

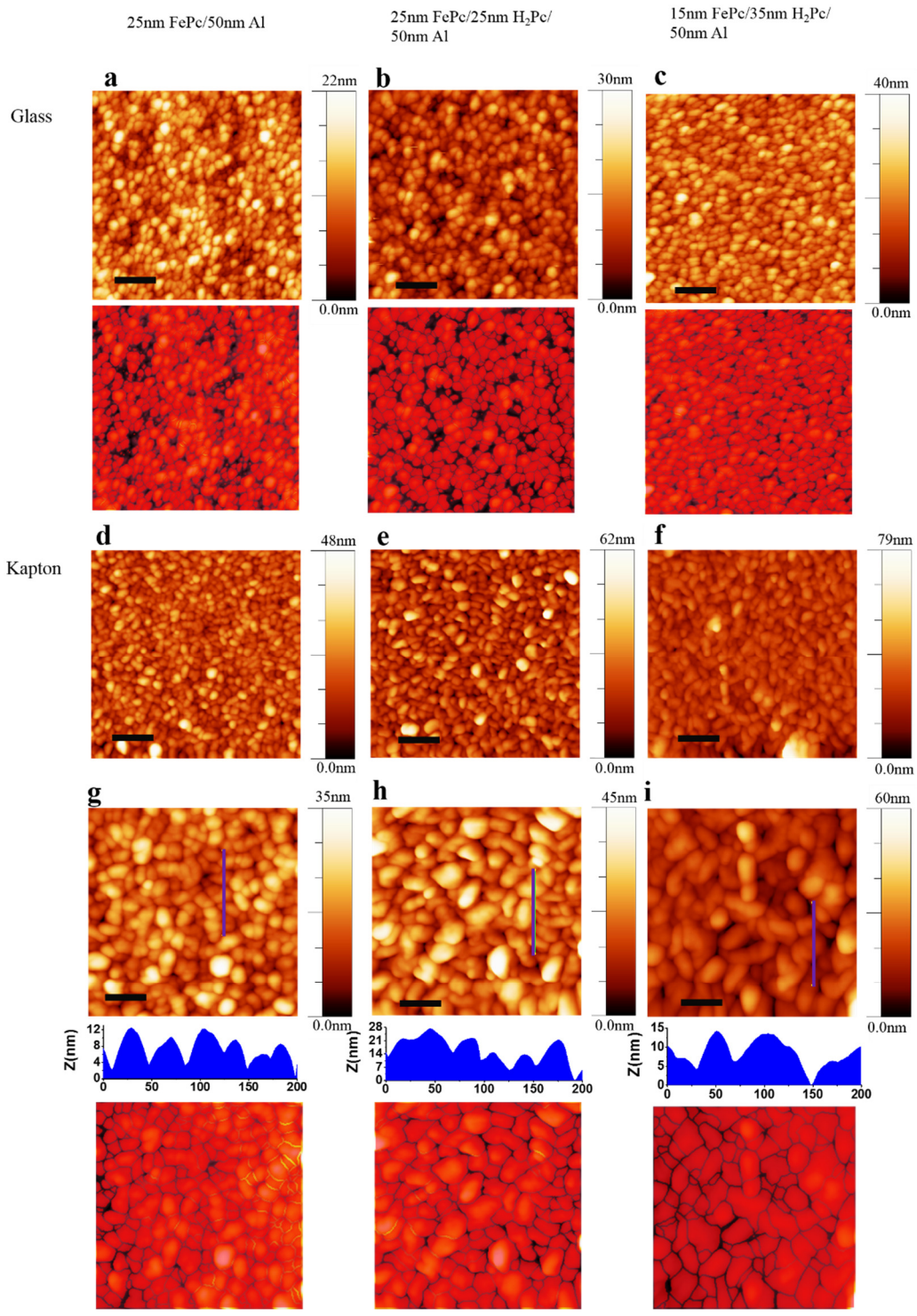


Figure 6.12 AFM micrographs of multi-layered structures, 25 nm FePc on 50 nm Al on (a) glass, (d) and (g) kapton substrate, 25 nm FePc/25 nm H_2Pc on 50 nm Al on (b) glass, (e) and and (h) on kapton substrate, and 15 nm FePc/35 nm H_2Pc on 50 nm Al on (e) glass substrate, (f) and (i) on kapton substrate. The deposition rates for FePc, H_2Pc and Al are 0.5 Å/s, 0.5 Å/s and 0.2 Å/s, respectively. The figures shown with the watershed mark below (a), (b), (c), (g), (h) and (i) are used to extract the average lateral grain size of the corresponding films. Except for (g), (h) and (i) where the scale bars of 100 nm is used, the scale bars given in the rest are 200 nm.

This effect becomes more apparent for the film on kapton substrate, and the island shape becomes relatively irregular and distorted, in comparison to those found in the 25 nm FePc film on glass and Al substrate, respectively, with the lateral grain size of ~ 35 nm, similar to those obtained from 100 nm thick films of mixed H_2Pc:FePc and 50 nm FePc films. The increase in the grain height is indicated by the height profile along the purple line, leading to a relatively large RMS = 7.3 nm.

Changes to the island size and shape can still be observed as the thickness of the FePc film is reduced to 15 nm (corresponding to structure shown in Figure 6.12 (c)), but the overall thickness of the phthalocyanine layer is still 50 nm. As can be seen, the 15 nm FePc/35 nm H_2Pc/Al on kapton substrate (Figure 6.12 (f) and (i)) is covered by the elongated shaped islands in an averaged size of 35 nm, which is similar to the grain size found for the 50 nm FePc film on Al. The film therefore is characterized by a considerably rough surface, as suggested by the height profile along the purple line and the large RMS~ 6.3 nm.

Table 6.5 Average lateral grain sizes (d) and roughness of multilayers based on FePc, H_2Pc and Al and 25 nm FePc observed by AFM (see text).

Substrate	Al	25 nm FePc		25 nm FePc/Al		25 nm FePc/ 25 nm H_2Pc/Al		15 nm FePc/ 35 nm H_2Pc/Al	
	RMS (nm)	d (nm)	RMS (nm)	d (nm)	RMS (nm)	d (nm)	RMS (nm)	d (nm)	RMS (nm)
Glass	2.4-3.5	26	2.3	27	2.3	31	3.6	30	4.5
Kapton	5.5	N/A	N/A	24	4.9	35	7.3	35	6.3

On a glass substrate, the 15 nm FePc film deposited onto H_2Pc exhibits a morphology similar to those seen for 25 nm FePc film on glass and Al, with an average lateral size of 30 nm, consistent with the spherical islands exhibited by phthalocyanines [204].

Therefore, the shape of the islands exhibited in the 15 nm and 25 nm FePc films changes from spherical to more distorted and elongated when deposited onto the Al substrate pre-coated with H_2Pc, resulting in relatively large island size and height, in comparison to the 25 nm FePc film on glass.

With a total thickness of 50 nm, the island shape and height found in the FePc/H_2Pc double layers on Al on glass substrate are considerably more irregular and larger than those found in the 50 nm FePc film directly deposited onto Al. As a result, the film surfaces of 25 nm

FePc/25 nm H_2Pc/Al, and 15 nmFePc/35 nm H_2Pc/Al on glass substrate, with RMS corresponding to 3.6 and 4.5 nm, respectively, are relatively rougher than what is observed for the 50 nm FePc/Al on glass substrate (RMS ~ 2.3 nm). The changes in the shape and size of the islands observed for the FePc films are therefore attributed to the underlying H_2Pc film, as substrate effects. Although H_2Pc and FePc are considered isomorphous, the fact that the growth has been interrupted (albeit *in-situ*) between both layers has introduced an interface between both that influences the overall morphology. This might be advantageous for spin valves.

6.3.2 Structure of the films

The structure of the multi-layered FePc/H_2Pc/Al is determined by XRD, and compared with the films on bare substrates (glass and kapton, respectively), as summarized in Figure 6.13.

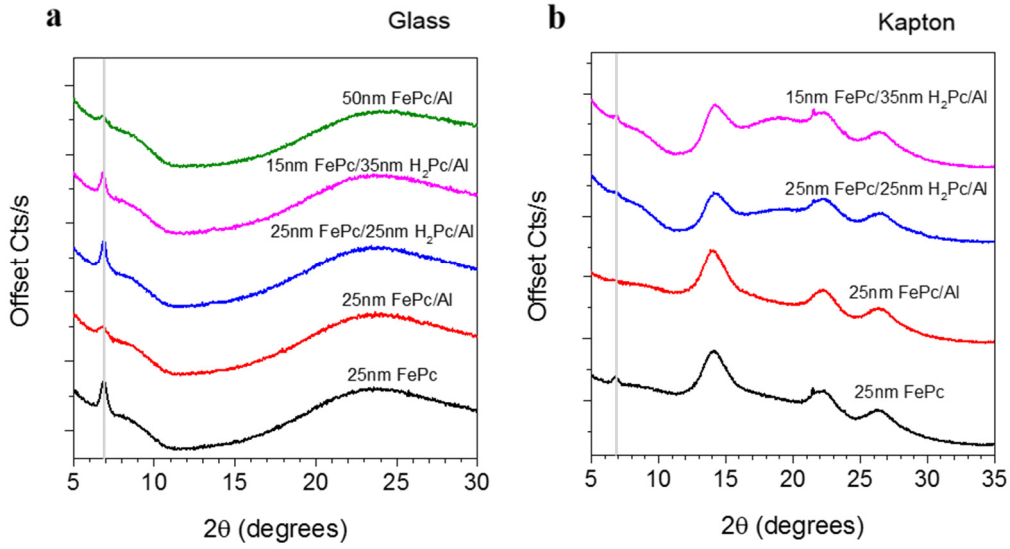


Figure 6.13 XRD scans of the 25 nm FePc (black solid curves), 25 nm FePc/50 nm Al (red solid curves), 25 nm FePc/25 nm H_2Pc/50 nm Al (blue solid curves), and 15 nm FePc/35 nm H_2Pc/50 nm Al (magenta solid curves) on (a) glass and (b) kapton substrates, and a 50 nm FePc film on glass coated with a 50 nm thick Al (green solid curve), with the light grey line plotted to index the (100) diffraction peak at $2\theta = 6.9°$. The deposition rates for FePc, H_2Pc and Al are 0.5 Å/s, 0.5 Å/s and 0.2 Å/s, respectively. No background subtraction is applied and the data are offset for clarity. The step size is identical to what is used for other XRD measurements but the time per step is increased to 120 second to improve the diffraction signal.

Similar to the 50 nm FePc film on Al, the change in the intensity and shape of diffraction from the (100) preferential orientation can be observed for the 25 nm FePc film deposited on Al (shown in Figure 6.13), indicating the film on Al is less textured, compared to the 25 nm FePc film deposited on glass. The Scherrer analysis on the XRD results suggests the size for the (100) grains in the FePc films to be 18.1-22.1 nm, in agreement with what is observed by AFM. The decrease in the crystallinity appears to be more severe on kapton, as the (100) diffraction peak becomes unobservable, due to the different roughness between the glass and kapton substrate.

Again, the diffraction peak at $2\theta = 6.9°$ corresponding to the (100) orientation can be observed for the 25 and 15 nm FePc films deposited onto Al pre-coated by H_2Pc by using both glass and kapton substrate, therefore indicating no significant changes to the texture can be found for different thickness of FePc/H_2Pc contained in the double-layers. Presence of the (100) peak as the only observed orientation in the two FePc/H_2Pc double-layers suggests individual films of FePc and H_2Pc adopt the same molecular orientation, though it is not possible to quantify the crystalline materials contained in the individual FePc/H_2Pc layer.

Table 6.6 Summary of the XRD pattern obtained from 25 nm and 50 nm FePc films, and multilayers based FePc, H_2Pc and Al. The grain size are calculated by the Sherrer analysis. $2\theta(°)$ is the peak center, whereas $w_{2\theta}(°)$ corresponds to the peak width extracted by full width maximum (FWHM) of the Gaussian fit, expressed in the unit of degree.

	$2\theta(°)$	$w_{2\theta}(°)$	Scherrer size (nm)
25 nm FePc /glass	6.88	0.44	18.1-22.1
50 nm FePc/glass	6.88	0.39	20.4-25.7
50 nm FePc/silicon	6.98	0.32	18.1-22.1
25 nm FePc/25 nm H_2Pc/Al/glass	6.87	0.39	20.4-25.7
15 nm FePc/35 nm H_2Pc/Al/glass	6.81	0.36	22.1-28.4

To see the effect from the underlying H_2Pc, the FePc/H_2Pc double-layers deposited onto Al are compared with a neat FePc film. Figure 6.13 shows a 50 nm thick FePc film directly deposited onto a 50 nm Al film on glass substrate. While the peak at $2\theta = 6.9°$ indicating the (100) molecular orientation is present for the 50 nm FePc on Al, 25 nm FePc/25 nm H_2Pc on Al, and 15 nm FePc/35 nm H_2Pc on Al (corresponding to blue and magenta curve, respectively, in the Figure 6.13), the (100) diffraction is found to be more intense in the

double-layers, whereas the same peak for the 50 nm FePc on Al appears to be considerably broad, with significantly low diffraction intensity. For the same film thickness, the FePc/H_2Pc double-layer on Al appears to be more crystalline than the neat FePc/Al, as indicated by XRD, therefore suggesting the improved crystallinity is induced by the underlying H_2Pc layer. On the other hand, the diffraction intensity and width for the (100) peak appear to be similar for both the 25 nm and 50 nm thick FePc layers when directly deposited onto Al. This seems to indicate crystal growth along (100) and the film crystallinity can be enhanced by inserting a layer of H_2Pc, possibly due to the interface between the two different phthalocyanine layers, or higher ability of H_2Pc to crystallize and form a seed layer for FePc growth.

6.3.3 Magnetic characterization of the films

While the ferromagnetic behaviour of neat FePc has been previously presented with the mixed films in section 6.1.3, a more detailed analysis on the field and temperature dependent magnetization measured for the FePc film is given here to compare those obtained for the device structures.

The isothermal field dependent magnetization curves $M(H)$ of the 25 nm FePc film (deposited onto kapton) are shown in Figure 6.14 (a), and as the field is swept between ±7 Tesla, the hysteresis loop is observed to open up at 2 K, corresponding to a coercivity ~ 400 Oe and remanence ~ 0.15 μ_B, indicative of ferromagnetic interactions present in the sample. At 2 K, the magnetic moment is found to reach ~ 1.21 μ_B, somewhat lower than what can be expected for Fe(II), $S = 1$ with $g = 2$, and it can be seen that the magnetization increases at a reasonably fast rate, reaching 0.61 μ_B under $H = 0.4$ Tesla. At 4.2 K the hysteresis loop appears to be closed, similar to what was previously observed for thicker FePc layers [3, 136, 199].

The temperature dependent magnetization $M(T)$ of the FePc film (see Figure 6.14 (c)) measured with ZFC and FC modes displays a bifurcation (T_B) at ~ 3 K. The magnetization $M(T)$ obtained with ZFC protocol is found to first increase with decreasing temperature but starts to decrease at ~ 4 K, suggesting presence of inter-chain dipolar interactions. The irreversibility has been observed for α-FePc crystals, which display the long relaxation times similar to what is expected for spin glasses [3] and/or superparamagnetic-like systems [3]. In the range of $T = 15$-42 K, the magnetic susceptibility $\chi(T)$ can be fitted with the Curie-Weiss

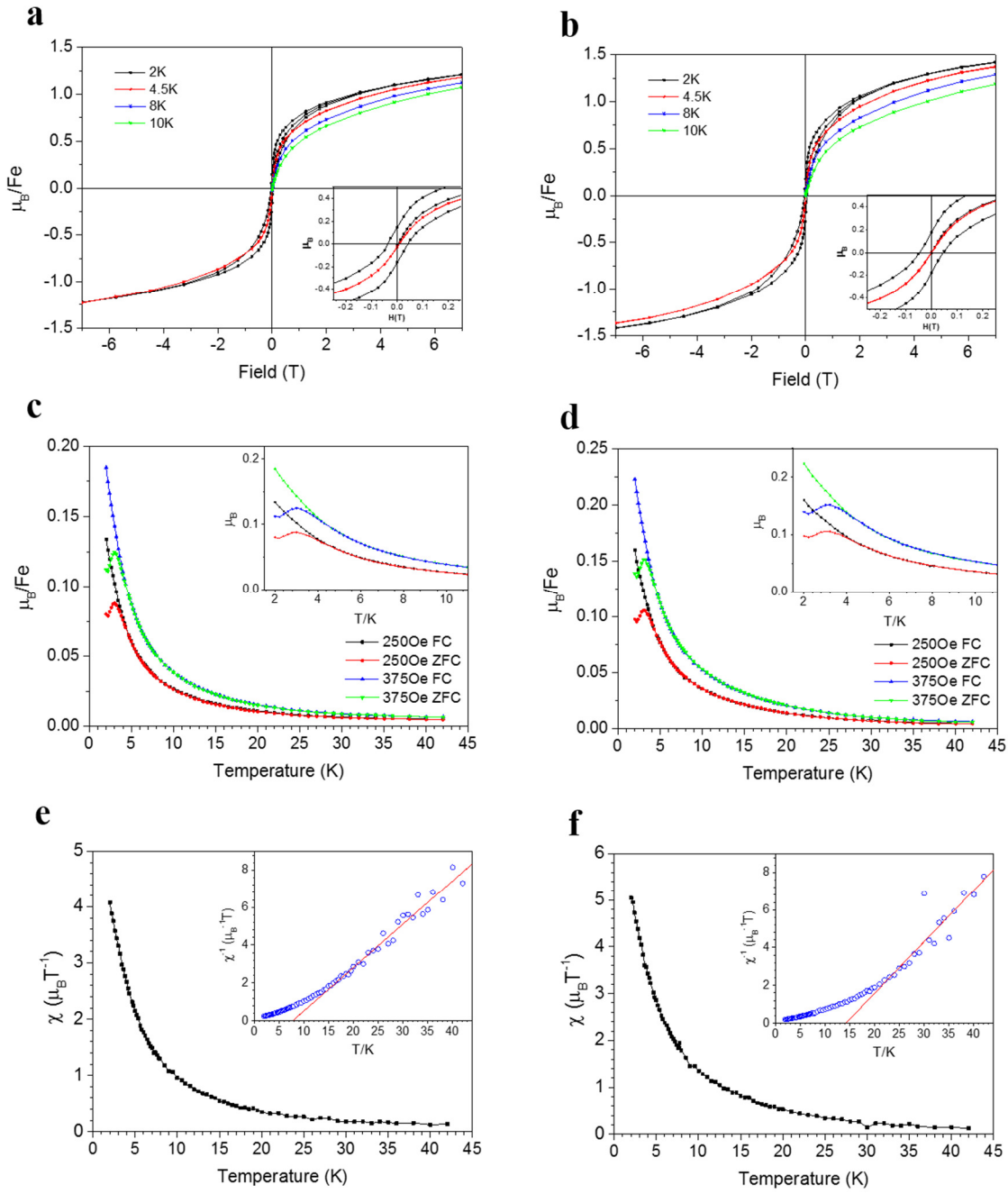


Figure 6.14 The magnetization as a function of the applied field and temperature $M(H)$ and $M(T)$ curves for the 25 nm FePc films deposited onto (a), (c) and (e) bare kapton substrate, and (b), (d) and (f) on kapton coated with a first Al layer with a thickness of 50 nm. (c) and (d) temperature dependent magnetization $M(T)$ curves measured with zero-field cooled (ZFC) and field-cooled (FC) protocols under the applied field H = 250 Oe and 375 Oe, and (e) and (f) the differential susceptibility as a function of temperature; inner panel in (e) and (f): the inverse differential susceptibility ($1/\chi$) as a function of temperature fitted by the Curie-Weiss expression (solid red line).

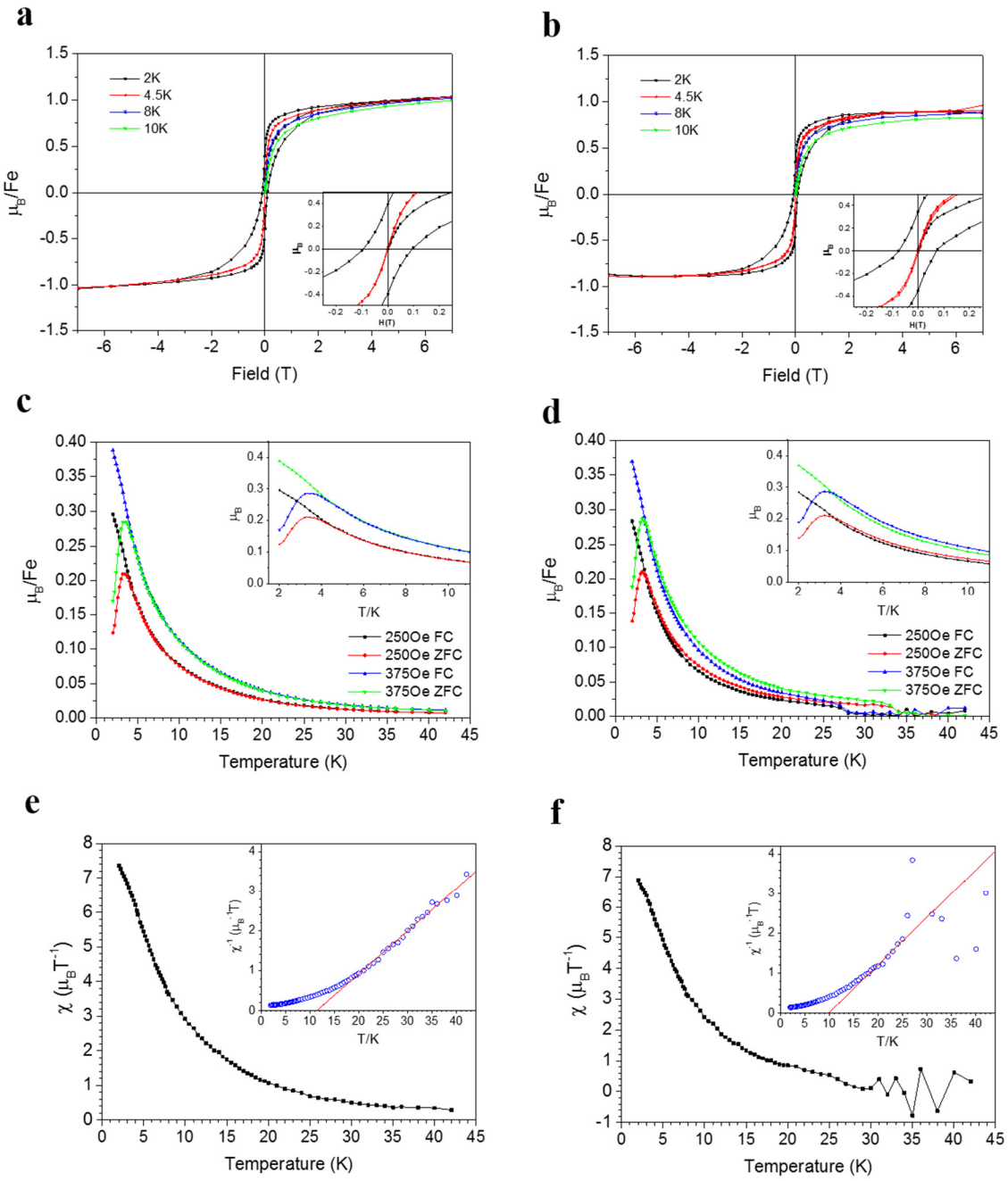


Figure 6.15 The magnetization as a function of applied field and temperature $M(H)$ and $M(T)$ curves for (a), (c) and (e) for the 25 nm FePc/25 nm H_2Pc/50 nm Al, and (b), (d) and (f) for 15 nm FePc/35 nm H_2Pc/50 nm Al. (c) and (d) temperature dependent magnetization $M(T)$ curves measured with zero-field cooled (ZFC) and field-cooled (FC) protocols under the applied field $H = 250$ Oe and 375 Oe, and (e) and (f) the differential susceptibility as a function of temperature; inner panel in (e) and (f): the inverse differential susceptibility ($1/\chi$) as a function of temperature fitted by the Curie-Weiss expression (solid red line).

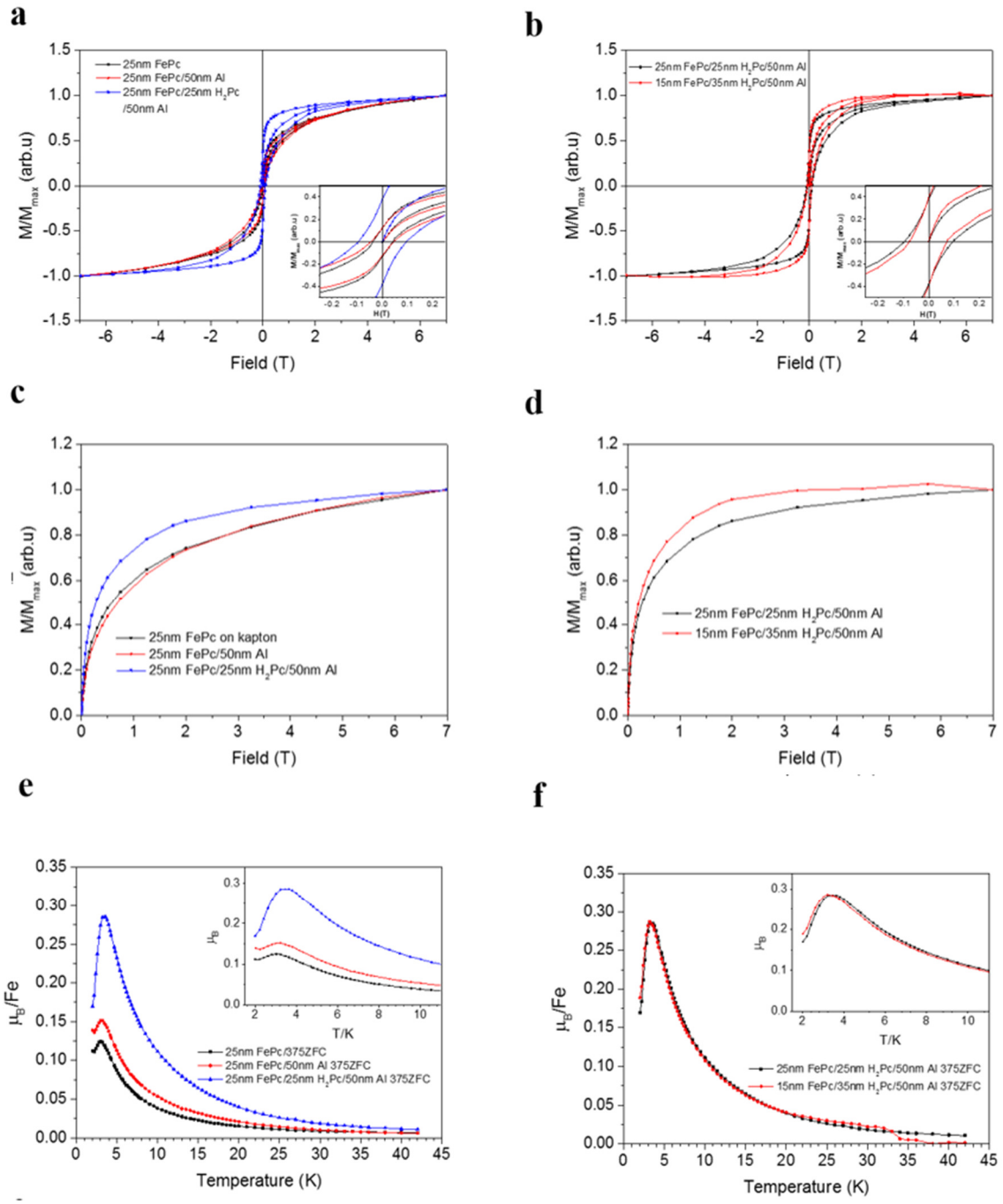


Figure 6.16 (a) and (b) $M(H)$ curves of the 25 nm FePc/kapton, 25 nm FePc/Al, 25 nm FePc/25 nm H_2Pc/Al and 15 nm FePc/35 nm H_2Pc/Al measured at 2 K, (c) and (d) the virgin curves measured from the 25 nm FePc/25 nm H_2Pc/Al and 15 nm FePc/35 nm H_2Pc/Al at 2 K, normalized to the respective moments at $H = 7$ T, and (e) and (f) the $M(T)$ curves measured with zero-field cooled (ZFC) protocols under the applied field $H = 375$ Oe obtained from the 25 nm FePc/kapton, 25 nm FePc/Al and 25 nm FePc/25 nm H_2Pc/Al and 15 nm FePc/35 nm H_2Pc/Al; inner panel in (e) and (f), the bifurcation points observed for 25 nm FePc/kapton, 25 nm FePc/Al, 25 nm FePc/25 nm H_2Pc/Al and 15 nm FePc/35 nm H_2Pc/Al, with approximately 3.5 K seen for the 25 nm and 15 nm FePc films grown on Al pre-coated with H_2Pc.

expression, extracting the positive T_c ~ 7.8 K, indicating ferromagnetic exchange interactions present in the film.

The magnetic behaviour of FePc appears to be relatively unaffected when the film is directly deposited onto the Al substrate. Figure 6.14 (b) shows the temperature dependent magnetization $M(H)$ at 2, 4.5, 8 and 10 K obtained from 25 nm FePc, and it can be seen that at 2 K the film exhibits a hysteretic behaviour as the field is swept from +7 to -7 Tesla, giving rise to a coercivity H_{cr} ~ 450 Oe, remanence ~ 0.2 μ_B, reaching the moment of ~ 1.42 μ_B at 7 T at 2 K, still very comparable to those previously observed for the film deposited onto kapton. Beyond 2 K the hysteresis is not observed, and the shape of the $M(H)$ curves and those obtained from kapton substrate are alike.

Temperature dependent magnetization $M(T)$ of the 25 nm FePc/Al displays similar features as seen for the film on kapton substrate, exhibiting a bifurcation in the $M(T)$ curves obtained by ZFC and FC modes, at which the moment per Fe atom is observed to increase with decreasing temperature followed by a suppression at ~ 3 K. The magnetic susceptibility $\chi(T)$ between 18-42 K fitted by the Curie-Weiss expression extracts a T_c ~ 14.2 K, suggesting presence of ferromagnetic couplings.

However, insertion of a 25 nm H_2Pc film between Al and FePc results in apparent changes to the $M(H)$ curves of the 25 nm FePc film, (see Figure 6.15 (a)) whose the S-shape appears to be more squared than that in the film on Al and bare substrate, respectively. Between 0 to 0.4 Tesla, the 2 K magnetic moment per Fe atom increases with a considerably fast rate, then steadily approaches ~ 1.0 μ_B at 7 Tesla. The hysteresis loop is observed at 2 K, giving rise to a coercivity (H_{cr}) ~ 950 Oe and remanence ~ 0.2 μ_B, larger than the values obtained for the films on Al and kapton substrate. Since the values in the coercivities may vary somewhat by the sweeping rate, owing to the slow relaxation behaviours observed for FePc [3], the sweep rate of 200 Oe/s between the measurement points under the applied field H = 0-7 Tesla was used for the three different multi-layered structures studied, allowing for a comparison on the effects of the underlying substrate and influence of the FePc thickness.

The magnetization as a function of temperature (Figure 6.15 (c)) exhibits a bifurcation at ~ 3.5 K between the moments obtained from ZFC and FC modes. Thus, the irreversibility characteristics of FePc can be observed when deposited on H_2Pc, with T_c ~ 11.4 K extracted from the Curie-Weiss fit for the magnetic susceptibility, confirming the ferromagnetic orderings in the FePc/H_2Pc double-layer.

Table 6.7 Coercivities (H_{cr}), Curie-Weiss constants (T_c), the birfucation temperature (T_B) and the magnetization (M_s) under the applied field (H) = 7 T observed for the three multi-layered structures consisting of FePc, H_2Pc and Al grown on kapton substrate at 2 K (see text).

	H_{cr} (Oe)	T_c (K)	T_B (K)	M_s (μ_B)
25 nm FePc	~ 400	7.8	~ 3	~ 1.21
25 nm FePc/50 nm Al	~ 450	14.2	~ 3.2	~ 1.42
25 nm FePc/25 nm H_2Pc/50 nm Al	~ 950	11.4	~ 3.6	~ 1.0
15 nm FePc/35 nm H_2Pc/50 nm Al	~ 650	9.9	~ 3.2	~ 0.88

Similar magnetic behaviour can be observed as the film thickness of FePc is reduced to 15 nm, as shown in Figure 6.15 (b). Again, the hysteretic behaviour is only present at 2 K, corresponding to a coercivity of ~ 650 Oe, consistent with what has been observed for FePc [136], and the magnetic moment increases sharply at low field (H = 0-0.5 Tesla), slowly approaching ~ 0.88 μ_B at H = 7 Tesla. The temperature dependent magnetization $M(T)$ reveals a bifurcation at ~ 3.5 K, which has been observed for all the FePc samples deposited on various substrates (including Al, kapton and PTCDA), with the presence of ferromagnetic interactions suggested by T_c ~ 9.9 K, derived by the Curie-Weiss fit (over the range 20-42 K) for the corresponding magnetic susceptibility (shown in Figure 6.15 (e)).

Figure 6.16 (a) presents the 2 K field dependent magnetization curves obtained from the 25 nm FePc films deposited onto different substrates, *i.e.* kapton, Al and H_2Pc-coated Al. The shape of the 2 K magnetization curves of the films on kapton and Al substrate is nearly identical, and the observed initial magnetization curves are almost overlapped, corresponding to a coercivity (H_{cr}) of ~ 400 and 450 Oe, respectively.

While the crystallinity of the FePc film on Al or kapton is poor, it seems that the ferromagnetic behaviour of FePc is not suppressed by the lack of texture in the (100) orientation. The resultant values of coercivity and T_c are very consistent, indicating the long-range ordering for ferromagnetic interactions can still be maintained. It appears that the magnetic structure in the FePc film is actually unaffected by the underlying Al substrate compared to the growth on kapton, indicating the Fe chains in FePc/Al are still ferromagnetically coupled, in turn suggesting a similar stacking adopted by the FePc columns when deposited onto Al. Instead, the coercivities observed for the neat FePc film and the multilayers strongly depend on the grain size, with nearly identical values in the magnetization under H = 7 T at T = 2 K, due to similar film thicknesses, as shown in Figure 6.17 (a) and (b). No diffraction peaks observed in the XRD pattern are likely because crystal

growth in the (100) direction is not favourable, due to the large surface roughness of Al. Alternatively, the ferromagnetic coupling could only require short chain lengths, which are below the correlation length for diffraction. However, this is at odds with the observation of the reduced coercivity in the mixed H_2Pc:FePc film consisting of 10 % H_2Pc whose film structure is highly textured, with the coercivity found to be only ~ 100 Oe. Inclusion of the non-magnetic substituent has a stronger influence on the magnetic structure, *i.e.* the correlation lengths for the Fe chains that maintain the magnetic long range ordering for FePc.

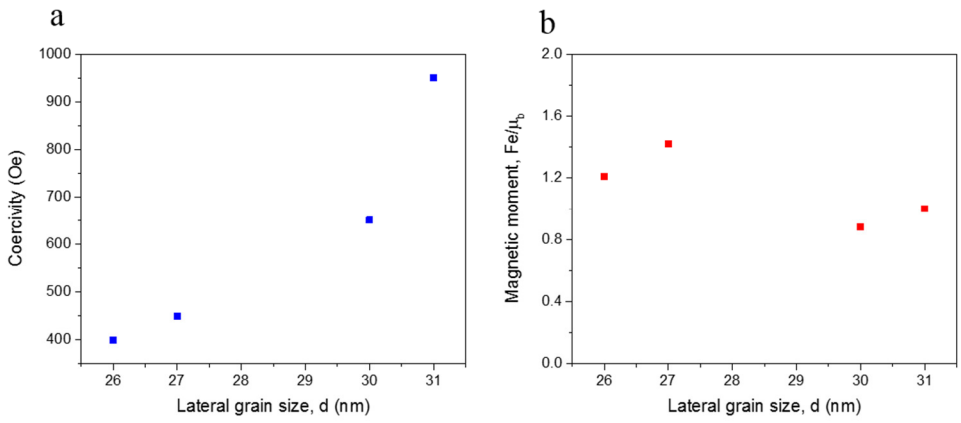


Figure 6.17 The observed coercivities (a) and the magnetization obtained under the applied field of 7 Tesla at 2 K (b) for the FePc multilayers as a function of lateral grain sizes determined by AFM.

Inserting a thin H_2Pc layer gives rise to a change of slope in the magnetization curve exhibited in the 25 nm and 15 nm FePc films, shown in Figure 6.16 (a) and (b), characteristics of ferromagnetic materials, indicating a significantly faster magnetization process at the low field in comparison to the films on kapton and Al substrate. Figure 6.16 (c) shows the initial magnetization curves of the FePc films on H_2Pc increases rapidly and at the applied filed 1.25 T reaches 80 % of the magnetic moment obtained for $H = 7$ T, whereas under the same applied field the magnetization for the FePc films on kapton and the Al substrate corresponds to ~ 65 %. This discrepancy indicates different saturation fields [137] are required for deposition onto H_2Pc. The faster magnetization accompanied by change in the shape of magnetization curves has been observed for FePc deposited onto Au [135] and PTCDA [136], owing to the in-plane anisotropy (*xy*) and the orientation of the films being approximately normal to what is seen on bare substrates. However, the possibility of a change in texture does not correlate with the results from XRD. Furthermore, the increase observed for the

coercivity in the 25 nm thick FePc seems to suggest the lengths of the Fe chains responsible for the bulk magnetic properties vary in films obtained on bare kapton, Al to substrates coated with H_2Pc, with higher lengths in the latter, consistent with XRD.

The Curie-Weiss constants (T_c), found in the FePc and FePc/H_2Pc double-layers are ~ 10 K, consistent with the literature value reported for the bulk α-FePc [3], but are marginally lower than what is found for the 100 nm FePc film [136], possibly due to the size effect, as the film thickness is between 15 to 25 nm. Deposition onto H_2Pc also shows very minor effect on the temperature dependent magnetization, as seen for both the 15 nm and 25 nm FePc films, corresponding to a bifurcation point (T_B) slightly higher compared to those obtained for the films deposited onto kapton and Al substrate, respectively. The subtle difference in the bifurcation points is likely caused by higher crystallinity or texture when FePc is deposited on H_2Pc, as observed by XRD.

Moreover, the rate at which the magnetization increases seems to be somewhat affected by the FePc film thickness. As can be seen from Figure 6.16 (b), the magnetization for the 15 nm thick FePc film appears to increase slightly faster than that obtained from the corresponding 25 nm film, suggesting the influence of the underlying H_2Pc becomes stronger with decreasing film thickness, with the coercivity (~ 650 Oe) obtained from the 15 nm film still larger than those seen for the 25 nm films that are directly deposited onto kapton or Al. The increase in the coercivity and magnetic anisotropy observed for the FePc/H_2Pc double-layers can therefore be attributed to the underlying H_2Pc. Although deposition onto H_2Pc does not induce templating effects to the FePc layers, as observed for deposition on Au [135] and substrates coated with PTCDA [136], respectively, inserting a thin layer of H_2Pc nevertheless separates the FePc layer from the direct contact with the Al substrate, introducing a more structurally and chemically compatible surface for the subsequent growth.

Structurally, the FePc/H_2Pc double-layers with 50 nm total thickness are more crystalline than the 50 nm FePc film directly deposited onto the Al substrate, as indicated by XRD, in turn suggesting that when the Al substrate is pre-coated by a thin layer of H_2Pc, deposition of FePc leads to larger crystallites, therefore more likely to contain averaged longer spin chains than those in the film on bare and Al substrate. This observation is consistent with the increased island size and elongated shape for the FePc/H_2Pc double-layers observed by AFM (Figure 6.17 (a)).

In conclusion, ferromagnetic molecular films based on FePc with T_c ~10 K were obtained.

Three different factors were identified that control the coercivity, including dilution, thickness of FePc layers, and substrate type on which FePc is to be deposited, suggesting crystal engineering via film processing can be the key to manipulate the magnetic exchange and spin couplings in phthalocyanines.

Diluting FePc with H_2Pc leads to significant changes to the coercivity, compared to that in neat FePc. In addition to cut-chains caused by structural defects present in the grain and the grainboundaries seen for neat phthalocyanines, the Fe chain lengths required for the magnetic interactions and long range ordering can be pinned by non-magnetic defects by co-evaporating a structurally similar H_2Pc. Dilution is shown to be an effective and simple strategy for obtaining variable coercivities in ferromagnetic molecular films, a desired property for spintronic applications. The resultant film structure and texture resemble those seen in neat phthalocyanines, indicating the materials properties of the diluted films can be readily exploited, and benefited from minimum strains at the organic-organic interface, if integrated into devices based on stacks of other phthalocyanine layers. The variable coercivities in diluted films reflect the magnetic interactions that contribute to the long range orderings are linked to the correlation lengths for the Fe chains, corresponding to an upper bound defined by the grain size.

In the case of neat FePc films, coercivities are both thickness- and substrate-dependent, which can cause differences in the correlation lengths due to variations in the resultant grain size, and therefore the coercivity reduces with the FePc film thickness as expected. While deposition of FePc onto Al leads to poorly crystalline films, yet the magnetization is unaffected and still very comparable to those deposited on other substrates, giving rise to similar values in the coercivities. The ferromagnetic properties of FePc can be confirmed to be as expected when implemented as a spin injector. Deposition onto Al pre-coated with a thin layer of H_2Pc is shown to enhance the coercivity, indicating using H_2Pc as a non-magnetic spacer can be advantageous for all organic spin valve. This study shows the possibility of a functional all organic spin valve solely integrated by phthalocyanine materials.

7. Conclusions

The aim of this thesis is to investigate molecular thin films that display controllable coercivities for spintronic applications, and focuses on two types of molecular systems: the charge transfer salt, [MnTPP][TCNQ], and the ferromagnet, (H_2Pc:)FePc, respectively. The former in (poly)crystalline form belongs to the charge transfer salt [MnTPP][TCNE] family, which exhibits large remanence and high coercivity, whereas the magnetic behaviours seen for isolated FePc make the latter a unique ferromagnetic system with tuneable coercivities. Blending functional molecules through co-evaporation under high vacuum provided by OMBD has shown very interesting physical properties that cannot be observed in the isolated molecular species, pointing towards films based on molecular mixture as an alternative approach to create novel film properties, allowing the magnetic interactions to be directly tuned by the film composition.

The thin film properties of the individual donor and acceptor molecules needed for the charge transfer salt are presented first. The growth of TCNQ on weakly interacting substrates such as glass and silicon covered by its native oxide, and those pre-coated with a thin layer of PTCDA has been characterized. On weakly interacting substrates, TCNQ forms micro-sized islands with a curved contour, and overall forms rather inhomogeneous island coverage, characterized by a very large surface roughness (RMS ~ 55-60 nm). Increasing the deposition rate induces several morphological changes, and improves the film coverage. The increased island (nucleation) density and reduced island size obtained by using a higher TCNQ growth rate reflect the effect of the growth kinetics on morphology.

Inserting a thin layer of PTCDA is shown to induce significant changes to the film morphology. Deposition onto PTCDA results in a uniform coverage of rectangular shaped micro-sized islands formed by TCNQ, corresponding to a large surface roughness. The underlying PTCDA has a profound impact on the preferential molecular orientations adopted by TCNQ, reducing from (022), (021) and (020) on weakly-interacting substrates to only (020) when deposited on PTCDA. The predominance of (020) orientation is rationalized by the structural considerations of the TCNQ and PTCDA planes parallel to the substrate deduced from diffraction results. This study suggests an alternative approach towards

controlling the molecular orientation in organic heterostructures, by choices of particular functional (*i.e.* electronegative) groups and their respective crystallographic orientations. This is contrast to structural templating observed in PTCDA/Pcs, where the π-π interactions are predominately the driving forces to induce Pcs to lie flat so as to maximize the interaction with the PTCDA ring. This result highlights the importance of intermolecular interactions used for packing within molecular solids. Despite being weak compared to the strong ionic type in the conventional semiconductors, intermolecular forces that act in a cooperative manner are shown to sufficiently induce both morphological and structural modifications to TCNQ films, confirming the films and/or nanostructures based on these molecules can be easily manipulated.

The following chapter then investigates the film properties of the donor molecule, MnTPPCl, grown by using OMBD. While the properties of MnTPPCl are retained in the films, the Mn ion in MnTPPCl undergoes reduction during the film deposition, giving rise to both Soret peaks characteristic of Mn(II) and Mn(III) respectively observed for the as-deposited film. The reduction of Mn is accompanied by the cleavage of Mn-Cl bonds, giving rise to Mn(II)TPP as an electron donor to interact with TCNQ. The optical behaviour of the MnTPPCl film resemble those seen for the isolated system as represented by the solution spectrum. Since the oxidation of Mn(II) to Mn(III) is spontaneous under ambient conditions, subsequently the time dependent spectral changes are considered as degradation for the MnTPPCl film, in which the quantities for Mn(II) and Mn(III) contained in the MnTPPCl film can be deduced from the respective absorption intensities, by using Beer-Lambert's law.

The morphology and structure of the MnTPPCl films are significantly different from those seen in the TCNQ films. The radical difference between the growth behaviours of MnTPPCl and the structurally similar Pcs is likely due to presence of the substituted phenyl groups, which can rotate out-of-plane, preventing close packing (steric effects) during crystallization into film at room temperature. The magnetic properties of MnTPPCl are studied by using the powder sample, where the oxidation state for the Mn ions is +3. The magnetic ground state for MnTPPCl is determined to be high spin $d\,4$ Mn(III) $S = 2$, and the field dependent magnetization is as expected from a paramagnetic spin $S = 2$, confirming it behaves like a paramagnetic material.

The properties of the films prepared by co-depositing TCNQ and MnTPPCl with a 1 to 1 ratio by using OMBD show several differences compared to those seen for the neat MnTPPCl

and TCNQ films, as a consequence of charge transfer between the two different molecules. The Soret peak for the Mn(II) porphyrin is not observed, and new absorption peaks corresponding to $TCNQ^{\bullet -}$ suggest co-deposition of MnTPPCl and TCNQ leads to Mn(II) ⟶ Mn(III) and reduction TCNQ ⟶ $TCNQ^{\bullet -}$ concurrently, leading to electron transfer predominately limited to the Mn center and CN groups of TCNQ. Dissociation of the axial Cl ligands is intrinsic to the vapor phase MnTPPCl, accompanied by the self-reduction of Mn(III), giving rise to a more reducing Mn(II)TPP in reaction with TCNQ during the co-deposition, thus forming the charge transfer dimer [MnTPP][TCNQ] in the co-deposited film.

The influence of charge transfer on the magnetic properties of the co-deposited [MnTPPCl][TCNQ] film is investigated by SQUID magnetometry, suggesting presence of very weak antiferromagnetic interactions arising from the unpaired spins on the Mn center, $S = 2$, and $TCNQ^{\bullet -}$, $s = 1/2$, within the charge transfer dimer [MnTPP][TCNQ]. While the antiferromagnetic spin alignment induced by the interactions between the unpaired spins Mn(III) and $TCNQ^{\bullet -}$ after co-depositing the structural analogues of MnTPP and TCNE, the formation of the charge transfer dimer [MnTPP][TCNQ] is likely to be limited by the yield of Mn(II) formed by self-reduction.

Whilst the long range magnetic order leading to the ferrimagnetic behaviours is not observed for the co-deposited [MnTPPC][TCNQ] film, possibly because formation of the uniform linear (1D) coordination polymer seen for [MnTPP][TCNE] family is limited by the kinetics provided by the OMBD, co-evaporating the respective structural analogues, MnTPPCl and TCNQ, is an alternative approach to synthesize charge transfer salts, and the films of which can be fabricated under high vacuum conditions, through the concurrent redox reactions as expected from each molecule. This finding shows the materials properties of these molecules are easy to be manipulated, and the chemistries previously observed in their solution systems can still be translated to the vapour phase. The unpaired spin only appears after reduction of TCNQ in reaction with MnTPP proceeds also under high vacuum condition, and interaction between the unpaired spins on Mn(III) and $TCNQ^{\bullet -}$ is shown to induce an antiferromagnetic alignment, as seen in [MnTPP][TCNE] and V(TCNE) [12, 24]. Thus, other similar magnetic charge transfer complexes may also be obtained by co-evaporation, allows films to be fabricated without intercalation of any undesired solvent molecules that are otherwise encountered for the polycrystallites synthesized through chemistry approaches.

Charge transfer [MnTPPCl][TCNQ] system represents interesting physical phenomena that

deserve further investigations. For instance, the self-reduction of the vapor phase MnTPPCl that appears to occur during the film deposition. It is unclear whether this reaction is truly self-activated after the thermal evaporation, or assisted and/or catalyzed via other chemical elements present in the deposition chamber, and the answer should allow us to improve the yield for the donor-acceptor dimer [MnTPP][TCNQ] in the co-deposited film so as to optimize the magnetic properties. A possible experiment that could give us more insights on the self-reduction of MnTPPCl and co-evaporation of MnTPPCl and TCNQ molecules would be to monitor the chemical species in the deposition chamber during the film deposition using *e.g. in-situ* mass spectrometry.

Formation of the donor-acceptor dimer [MnTPP][TCNQ] is predominately limited by the amount of Mn(II) present in the co-deposited film. It is not certain whether the degree of the charge transfer between the two different molecules affects the dissociation of the axial Cl ligands during the co-evaporation. These experiments are expected to give us a deeper understanding in formation of charge-transfer pairs prepared by co-evaporation, allowing us to apply the same knowledge to explore films of other similar charge transfer systems such as [MnTPP][F_4TCNQ] and [TTF][TCNQ]. Furthermore, a precursor molecule containing Mn(II) centers could be a suitable alternative to MnTPPCl, although preliminary experiments with MnPc were non-conclusive. Although the magnetic properties seen in the co-deposited [MnTPP][TCNQ] film are dominated by the antiferromagnetic interactions, due to the charge transfer dimer [MnTPP][TCNQ], as suggested by UV/Visible spectroscopy and XPS, it is possible that the actual film composition consists of a distribution of cluster sizes and chain lengths for [MnTPP][TCNQ] that are unable to be detected by XRD, but may be resolved by using polarized neutron diffraction.

The diluted ferromagnetic system based on a molecular binary mixture of FePc and H_2Pc shows the ferromagnetic properties of FePc are not limited to its neat form, which allows the functional properties to be directly controlled by the film composition. Co-depositing H_2Pc and FePc leads to films with the morphology and structure that are characteristics of phthalocyanines, owing to their structural similarity, whilst drastic changes are seen for the coercivity and the field dependent magnetization compared to those obtained from the neat FePc film. The decrease in the coercivity indicates the long range ferromagnetic ordering is disrupted by the co-deposited H_2Pc. The mixed films of H_2Pc:FePc can be considered as an novel approach towards obtaining molecular films with controllable coercivities via simple co-deposition, where the magnetic interactions and thus the correlations within the columns

can be tuned by the concentration of H_2Pc. Such molecular binary blends are particularly advantageous compared to the conventional doped semiconductors, as issues like phase segregation, incongruent melting and strain are rare.

The variable coercivities observed in FePc and mixed films are particularly promising for all organic spin valves, and deserves more systematic studies on the mixing ratio between the non-magnetic substituent and FePc. While previous studies have suggested the increase in the coervities can be linked to the longer chain lengths owing to the larger grains obtained at elevated substrate temperatures, the results on the mixed H_2Pc:FePc films with different concentrations of H_2Pc shows mixing with H_2Pc has direct and significant impact on the values of coercivities, subsequently confirming the importance of intra-chain (column) interactions and the correlation lengths needed for magnetic orderings. The studies can be extended to using concentrations between 0-10 %, to systematically establish how the correlation lengths, the magnetization as well as the coercivity scale with respect to the concentration of non-magnetic substituent. The magnetization as a function of temperature for the mixed films should be studied, compared to those observed for neat FePc, which exhibits slow magnetization phenomena reminiscent of spin glass systems. In this respect, further studies on the neat and mixed H_2Pc:FePc films that focus on the slow relaxation process can possibly address the effects of H_2Pc on the crystalline size/domain formation in relation to the size of Fe chains formed via co-evaporation.

To exploit the magnetic properties of FePc for spintronic applications, three different types of multi-layers consisting of FePc, H_2Pc and Al are grown by using OMBD without breaking vacuum. Deposition of FePc on Al results in poorly crystalline films, .yet, the long range ferromagnetic orderings of FePc are relatively unaffected by the lack of film texture, and similar coercivities are obtained for the 25 nm FePc films on Al and kapton. The crystallinity of the FePc layer on both kapton and Al is severely disrupted, yet, the magnetic structure of FePc is virtually not interrupted. Whilst absence of diffractions peaks suggests crystallites in (100) orientation parallel to the substrate are small or in other directions that are not parallel to the substrate plane, the fashion in which FePc grows on bare and Al-coated substrates appears to be alike, *i.e.* crystallizes into 1D molecular columns, giving rise to the characteristic small spherical islands typically seen for the α-phthalocyanine films.

Inserting a thin layer of H_2Pc prior to FePc growth is shown to induce minor modifications to the film morphology, but more strongly affects the structural and magnetic properties for

FePc. On H_2Pc, FePc forms larger and more elongated shaped crystallites, with the increase seen for the magnetic anisotropy and coercivity compared to those obtained on kapton and Al-coated kapton. In this case, the increase magnetic anisotropy and coercivity is related to the underlying H_2Pc, which essentially passivates the metallic surface, introducing an organic interface owing to the fact that the growth is interrupted albeit *in-situ*.

These findings show that the functional properties of FePc when incorporated in a multilayer structure as need in a device (*e.g.* on an electrode) are very similar to those on bare substrates. Therefore, the ferromagnetic properties of FePc can be implemented in a spin valve, even if at present the operation temperature may be limited. The studies on the multilayers consisting of H_2Pc and FePc reveal that, for similar film thicknesses, using H_2Pc as the non-magnetic spacer leads to a higher coercivity for the second FePc layer than what is obtained for the first FePc layer directly deposited onto Al, indicating insertion of H_2Pc to decouple the ferromagnetic layers can be beneficial for all organic spin valves, particularly in the case of phthalocyanines.

Based on the results of this study, multilayers of H_2Pc and FePc should be a good starting point to study the magneto-resistive effects in phthalocyanine materials, and the proposed device structure should be measured by Physical Properties Measurement System (PPMS), complemented by the cross-section and structural analysis by Transmission Electron Microscopy (TEM) and structural characterizations by XRD. It is essential to characterize the electrical properties of the device, both as a function of the spacer thickness and temperature, so as to establish in which regime tunnelling through the 10 nm H_2Pc is operated, so that the spin injection from the FePc layer and the spin valve like behaviour to be observed is not obscured by other effects such as OMAR, if there are any. Since the values in the coercivities obtained for the thickness between 15 to 25 nm are observed to be relatively similar, the mixed H_2Pc:FePc films can be exploited if a larger difference in the coercivities of the first and second ferromagnetic layer is needed for further optimizing the device performance.

8. Bibliography

1. Woodruff DN, Winpenny REP, Layfield RA. Lanthanide Single-Molecule Magnets. Chemical Reviews. 2013;113(7):5110-48.
2. Dale BW, Williams RJP, Johnson CE, Thorp TL. S = 1 Spin State of Divalent Iron. I. Magnetic Properties of Phthalocyanine Iron (II). The Journal of Chemical Physics. 1968;49(8):3441-4.
3. Evangelisti M, Bartolomé J, de Jongh LJ, Filoti G. Magnetic properties of α-iron(II) phthalocyanine. Physical Review B. 2002;66(14):144410.
4. Miyoshi H, Ohya-Nishiguchi H, Deguchi Y. The Magnetic Properties of Manganese(II) Phthalocyanine. Bulletin of the Chemical Society of Japan. 1973;46(9):2724-8.
5. Awaga K, Maruyama Y. High-Pressure Effects on the Canted Ferromagnetism in Manganese(II) Phthalocyanine. Physical Review B. 1991;44(6):2589-94.
6. Yamada H, Shimada T, Koma A. Preparation and magnetic properties of manganese(II) phthalocyanine thin films. Journal of Chemical Physics. 1998;108(24):10256-61.
7. Miller JS. Organic- and molecule-based magnets. Pramana-Journal of Physics. 2006;67(1):1-16.
8. Miller JS, Epstein AJ. Molecule-Based Magnets—An Overview. MRS Bulletin. 2000;25(11):21-30.
9. Miller JS, Epstein AJ, Reiff WM. Molecular Crystals Liquid Crystals. 1985;120:27.
10. Chittipeddi S, Chromack KR, Miller JS, Epstein AJ. Physical Review Letters 1987;58.
11. Miller JS. Magnetically ordered molecule-based materials. Chemical Society Reviews. 2011;40(6):3266-96.
12. Haskel D, Islam Z, Lang J, Kmety C, Stajer G, Pokhodnya KI, et al. Local structural order in the disordered vanadium tetracyanoethylene room-temperature molecule-based magnet. Physical Review B. 2004;70:054422.
13. Miller JS, Calabrese JC, McLean RS, Epstein AJ. meso-(Tetraphenylporphinato)manganese(III)-tetracyanoethenide, [MnIIITPP]:: ⊕

[TCNE].⊖. A New Structure-Type Linear-Chain Magnet with a Tc of 18K. Advanced Materials. 1992;4(7-8):498-501.

14. Rittenberg DK, Sugiura K, Sakata Y, Mikami S, Epstein AJ, Miller JS. Large Coercivity and High Remanent Magnetization Organic-Based Magnets. Advanced Materials. 2000;12(2):126-30.
15. Kronmüller H, Long G, Grandjean F. Supermagnets, hard magnetic materials. Kluwer Academic Publishers, Dordrecht. 1991:461.
16. Rittenberg DK, Arif AM, Miller JS. Effect of thermal annealing on the ferrimagnetic behavior and ordering of the [MnTXPP]+[TCNE][radical dot]-[middle dot]solv (X = F, Cl, Br, I; solv = PhMe, CH2Cl2) family of magnets. Journal of the Chemical Society, Dalton Transactions. 2000(21):3939-48.
17. Sugiura K, Mikami S, Tanaka T, Sawada M, Manson JL, Miller JS, et al. ChemInform Abstract: Magnetic Ordering of 5,10,15,20-Tetrakis [4′-(trifluoromethyl)phenyl]porphyrinatomanganese(III) Tetracyanoethenide with a 6.0 K Tc. ChemInform. 1998;29(5):no-no.
18. Brandon EJ, Arif AM, Burkhart BM, Miller JS. Structure and magnetic properties of antiferromagnetic manganese(III) tetrakis(4-methoxyphenyl)porphyrin tetracyanoethenide, MnTOMePP TCNE center dot 2PhMe, and manganese(III) tetrakis(2-fluorophenyl)porphyrin tetracyanoethenide, MnTFPP TCNE center dot 2PhMe. Inorganic Chemistry. 1998;37(11):2792-8.
19. Hibbs W, Arif AM, Botoshansky M, Kaftory M, Miller JS. Structure and magnetic properties of tetraarylporphinatomagnesium(II) electron transfer salts of 2,3,5,6-tetrafluoro-7,7,8,8-tetracyanoquinodimethane, TCNQF(4). Inorganic Chemistry. 2003;42(7):2311-22.
20. Mikami S, Sugiura K-i, Maruta T, Maeda Y, Ohba M, Usuki N, et al. Structure, optical and magnetic behaviour of meso-tetraphenylporphyrinatoiron(III) tetracyanoethenide, [FeIII(TPP)]+[TCNE][radical dot]. Journal of the Chemical Society, Dalton Transactions. 2001(4):448-55.
21. Miller JS, Vazquez C, Calabrese JC, McLean RS, Epstein AJ. Cooperative magnetic behavior of α- and β-manganese(III) phthalocyanine tetracyanoethenide (1:1), [MnIIIPc]·⊕[TCNE]·⊖. Advanced Materials. 1994;6(3):217-21.
22. Miller JS, Vazquez C, Jones NL, McLean RS, Epstein AJ. Magnetic behaviour of octaethylporphyrinatomanganese(III) tetracyanoethenide, [MnOEP][TCNE], and

hexacyanobutadienide, [MnOEP][C4(CN)6]: the importance of a uniform chain for stabilizing strong effective ferromagnetic coupling. Journal of Materials Chemistry. 1995;5(5):707-11.

23. Rittenberg DK, Baars-Hibbe L, Bohm A, Miller JS. Manganese() octabutoxynaphthalocyanine and its ferrimagnetic electron-transfer salt with TCNE. Journal of Materials Chemistry. 2000;10(2):241-4.
24. Miller JS, Calabrese JC, McLean RS, Epstein AJ. Meso-(Tetraphenylporphinato)Manganese(III)-Tetracyanoethenide, MnIIITPP =circle-plus TCNE circle-minus - A New Structure-Type Linear-Chain Magnet withi a Tc of 18-K. Advanced Materials. 1992;4(7-8):498-501.
25. Böhm A, Vazquez C, McLean RS, Calabrese JC, Kalm SE, Manson JL, et al. Weak Effect on Tc with Increased Interchain Distances. Structure and Magnetic Properties of (meso-Tetrakis(3,5-di-tert-butyl-4-hydroxyphenyl)porphinato)manganese(III) Tetracyanoethenide, [MnIIITP‘P]+[TCNE]•- Inorganic Chemistry. 1996;35(11):3083-8.
26. Miller JS, Epstein AJ. Tetracyanoethylene-based organic magnets. Chemical Communications. 1998(13):1319-25.
27. Caneschi A, Gatteschi D, Renard JP, Rey P, Sessoli R. Magnetic coupling in zero- and one-dimensional magnetic systems formed by nickel(II) and nitronyl nitroxides. Magnetic phase transition of a ferrimagnetic chain. Inorganic Chemistry. 1989;28(15):2940-4.
28. Seiden J. Propriétés statiques d'une chaîne isotrope alternée de spins quantiques 1/2 et de spins classiques. J Physique Lett. 1983;44(23):947-52.
29. Drillon M, Coronado E, Beltran D, Georges R. Classical treatment of a heisenberg linear chain with spin alternation; application to the MnNi(EDTA)-6H2O complex. Chemical Physics. 1983;79(3):449-53.
30. Ise T, Ishida T, Hashizume D, Iwasaki F, Nogami T. Ferro- and Ferrimagnetic Chains of hin-Bridged Copper(II) and Manganese(II) and hnn-Bridged Manganese(II) Complexes (hin = 4,4,5,5-Tetramethylimidazolin-1-oxyl; hnn = 4,4,5,5-Tetramethylimidazolin-1-oxyl 3-Oxide). Inorganic Chemistry. 2003;42(19):6106-13.
31. Wynn CM, Girtu MA, Sugiura KI, Brandon EJ, Manson JL, Miller JS, et al. Long-range magnetic order in the quasi-1D metalloporphyrin family of molecule-based magnets. Synthetic Metals. 1997;85(1–3):1695-700.

32. Hibbs W, Rittenberg DK, Sugiura K-i, Burkhart BM, Morin BG, Arif AM, et al. Solvent Dependence of the Structure and Magnetic Ordering of Ferrimagnetic Manganese(III) meso-Tetraphenylporphyrin Tetracyanoethenide, [MnTPP]+[TCNE]•-·x(solvent). Evidence for Orientationally Disordered [TCNE]•. Inorganic Chemistry. 2001;40(8):1915-25.
33. Carboni RA. Tetracyanoethylene. Organic Syntheses, Collective Volume 1963;4:877.
34. Chappert C, Fert A, Van Dau FN. The emergence of spin electronics in data storage. Nat Mater. 2007;6(11):813-23.
35. Sanvito S. Molecular spintronics. Chemical Society Reviews. 2011;40(6):3336-55.
36. Forrest SR. The path to ubiquitous and low-cost organic electronic appliances on plastic. Nature. 2004;428(6986):911-8.
37. Peumans P, Yakimov A, Forrest SR. Small molecular weight organic thin-film photodetectors and solar cells. Journal of Applied Physics. 2003;93(7):3693-723.
38. O'Regan B, Gratzel M. A low-cost, high-efficiency solar cell based on dye-sensitized colloidal TiO2 films. Nature. 1991;353(6346):737-40.
39. Sun Y, Giebink NC, Kanno H, Ma B, Thompson ME, Forrest SR. Management of singlet and triplet excitons for efficient white organic light-emitting devices. Nature. 2006;440(7086):908-12.
40. Muller CD, Falcou A, Reckefuss N, Rojahn M, Wiederhirn V, Rudati P, et al. Multi-colour organic light-emitting displays by solution processing. Nature. 2003;421(6925):829-33.
41. Baldo MA, Thompson ME, Forrest SR. High-efficiency fluorescent organic light-emitting devices using a phosphorescent sensitizer. Nature. 2000;403(6771):750-3.
42. Jurchescu OD, Popinciuc M, van Wees BJ, Palstra T. Interface-controlled, high-mobility organic transistors. Advanced Materials-Deerfield Beach Then Weinheim-. 2007;19(5):688.
43. Katz HE, Lovinger AJ, Johnson J, Kloc C, Siegrist T, Li W, et al. A soluble and air-stable organic semiconductor with high electron mobility. Nature. 2000;404(6777):478-81.
44. Crone B, Dodabalapur A, Lin YY, Filas RW, Bao Z, LaDuca A, et al. Large-scale complementary integrated circuits based on organic transistors. Nature. 2000;403(6769):521-3.

45. Dediu V, Murgia M, Matacotta FC, Taliani C, Barbanera S. Room temperature spin polarized injection in organic semiconductor. Solid State Communications. 2002;122(3–4):181-4.
46. Xiong ZH, Wu D, Valy Vardeny Z, Shi J. Giant magnetoresistance in organic spin-valves. Nature. 2004;427(6977):821-4.
47. Mermer Ö, Veeraraghavan G, Francis TL, Sheng Y, Nguyen DT, Wohlgenannt M, et al. Large magnetoresistance in nonmagnetic $\ensuremath{\pi}$-conjugated semiconductor thin film devices. Physical Review B. 2005;72(20):205202.
48. Shim JH, Raman KV, Park YJ, Santos TS, Miao GX, Satpati B, et al. Large Spin Diffusion Length in an Amorphous Organic Semiconductor. Physical Review Letters. 2008;100(22):226603.
49. Kikkawa JM, Awschalom DD. Lateral drag of spin coherence in gallium arsenide. Nature. 1999;397(6715):139-41.
50. Xiao K, Li R, Tao J, Payzant EA, Ivanov IN, Puretzky AA, et al. Metastable Copper-Phthalocyanine Single-Crystal Nanowires and Their Use in Fabricating High-Performance Field-Effect Transistors. Advanced Functional Materials. 2009;19(23):3776-80.
51. Drew AJ, Hoppler J, Schulz L, Pratt FL, Desai P, Shakya P, et al. Direct measurement of the electronic spin diffusion length in a fully functional organic spin valve by low-energy muon spin rotation. Nat Mater. 2009;8(2):109-14.
52. Krinichnyi V. 2-mm Waveband electron paramagnetic resonance spectroscopy of conducting polymers. Synthetic Metals. 2000;108(3):173-222.
53. Droghetti A, Steil S, Grossmann N, Haag N, Zhang HT, Willis M, et al. Electronic and magnetic properties of the interface between metal-quinoline molecules and cobalt. Physical Review B. 2014;89(9):10.
54. Raman KV, Kamerbeek AM, Mukherjee A, Atodiresei N, Sen TK, Lazic P, et al. Interface-engineered templates for molecular spin memory devices. Nature. 2013;493(7433):509-13.
55. Barraud C, Seneor P, Mattana R, Fusil S, Bouzehouane K, Deranlot C, et al. Unravelling the role of the interface for spin injection into organic semiconductors. Nat Phys. 2010;6(8):615-20.
56. Sanvito S. Molecular spintronics: The rise of spinterface science. Nat Phys. 2010;6(8):562-4.

57. Yoo J-W, Chen C-Y, Jang HW, Bark CW, Prigodin VN, Eom CB, et al. Spin injection/detection using an organic-based magnetic semiconductor. Nature Materials. 2010;9(8):638.
58. Sun D, Yin L, Sun C, Guo H, Gai Z, Zhang XG, et al. Giant Magnetoresistance in Organic Spin Valves. Physical Review Letters. 2010;104(23):236602.
59. Dediu V, Hueso LE, Bergenti I, Riminucci A, Borgatti F, Graziosi P, et al. Room-temperature spintronic effects in Alq3-based hybrid devices. Physical Review B. 2008;78(11):6.
60. Dediu VA, Hueso LE, Bergenti I, Taliani C. Spin routes in organic semiconductors. Nature Materials. 2009;8(9):707-16.
61. Bowen M, Bibes M, Barthélémy A, Contour J-P, Anane A, Lemaıtre Y, et al. Nearly total spin polarization in La2/3Sr1/3MnO3 from tunneling experiments. Applied Physics Letters. 2003;82(2):233-5.
62. Schmidt G, Ferrand D, Molenkamp LW, Filip AT, van Wees BJ. Fundamental obstacle for electrical spin injection from a ferromagnetic metal into a diffusive semiconductor. Physical Review B. 2000;62(8):R4790-R3.
63. Li B, Kao C-Y, Yoo J-W, Prigodin VN, Epstein AJ. Magnetoresistance in an All-Organic-Based Spin Valve. Advanced Materials. 2011;23(30):3382-6.
64. Manriquez JM, Yee GT, McLean RS, Epstein AJ, Miller JS. A Room-Temperature Molecular Organic Based Magnet. Science. 1991;252(5011):1415-7.
65. Prigodin VN, Raju NP, Pokhodnya KI, Miller JS, Epstein AJ. Spin-Driven Resistance in Organic-Based Magnetic Semiconductor V[TCNE]x. Advanced Materials. 2002;14(17):1230-3.
66. Serri M, Wu W, Fleet LR, Harrison NM, Hirjibehedin CF, Kay CWM, et al. High-temperature antiferromagnetism in molecular semiconductor thin films and nanostructures. Nat Commun. 2014;5.
67. Gruber M, Ibrahim F, Boukari S, Joly L, Da Costa V, Studniarek M, et al. Spin-Dependent Hybridization between Molecule and Metal at Room Temperature through Interlayer Exchange Coupling. Nano Letters. 2015;15(12):7921-6.
68. Gruber M, Ibrahim F, Boukari S, Isshiki H, Joly L, Peter M, et al. Exchange bias and room-temperature magnetic order in molecular layers. Nat Mater. 2015;14(10):981-4.
69. Urdampilleta M, Klyatskaya S, Cleuziou JP, Ruben M, Wernsdorfer W. Supramolecular spin valves. Nat Mater. 2011;10(7):502-6.

70. Blundell S. Magnetism in condensed matter: Oxford Univ. Press; 2001.
71. Yang JL, Sullivan P, Schumann S, Hancox I, Jones TS. Organic photovoltaic cells based on unconventional electron donor fullerene and electron acceptor copper hexadecafluorophthalocyanine. Applied Physics Letters. 2012;100(2):3.
72. Smucker BW, Hudson JM, Omary MA, Dunbar KR. Structural, magnetic, and optoelectronic properties of (diimine)(dithiolato)platinum(II) and -palladium(II) complexes and their charge-transfer adducts with nitrile acceptors. Inorganic Chemistry. 2003;42(15):4714-23.
73. Suzuki A, Ohtsuki T, Oku T, Akiyama T. Fabrication and characterization of tetracyanoquinodimethane/phthalocyanine solar cells. Materials Science and Engineering: B. 2012;177(11):877-81.
74. Duong DT, Wang CC, Antono E, Toney MF, Salleo A. The chemical and structural origin of efficient p-type doping in P3HT. Organic Electronics. 2013;14(5):1330-6.
75. Gao W, Kahn A. Controlled p-doping of zinc phthalocyanine by coevaporation with tetrafluorotetracyanoquinodimethane: A direct and inverse photoemission study. Applied Physics Letters. 2001;79(24):4040-2.
76. Brown AR, de Leeuw DM, Lous EJ, Havinga EE. Organic n-type field-effect transistor. Synthetic Metals. 1994;66(3):257-61.
77. Menard E, Podzorov V, Hur SH, Gaur A, Gershenson ME, Rogers JA. High-performance n- and p-type single-crystal organic transistors with free-space gate dielectrics. Advanced Materials. 2004;16(23-24):2097-+.
78. Alves H, Molinari AS, Xie H, Morpurgo AF. Metallic conduction at organic charge-transfer interfaces. Nat Mater. 2008;7(7):574-80.
79. Ferraris J, Walatka V, Perlstei.Jh, Cowan DO. Electron-Transfer in a New Highly Conducting Donor-Aceeptor Complex. Journal of the American Chemical Society. 1973;95(3):948-9.
80. Miller JS. Tetracyanoethylene (TCNE): The Characteristic Geometries and Vibrational Absorptions of Its Numerous Structures. Angewandte Chemie International Edition. 2006;45(16):2508-25.
81. Kaim W, Moscherosch M. The coordination chemistry of TCNE, TCNQ and related polynitrileπ acceptors. Coordination Chemistry Reviews. 1994;129(1):157-93.

82. Clerac R, O'Kane S, Cowen J, Ouyang X, Heintz R, Zhao HH, et al. Glassy magnets composed of metals coordinated to 7,7,8,8-tetracyanoquinodimethane: M(TCNQ)(2) (M = Mn, Fe, Co, Ni). Chemistry of Materials. 2003;15(9):1840-50.
83. Pennelly RR, Eckhardt CJ. Quasi-metallic reflection spectra of TCNQ single crystals. Chemical Physics. 1976;12(1):89-105.
84. Merski J, Eckhardt CJ. Piezomodulation spectroscopy of molecular crystals. IV. The first singlet systems of TCNQ and BDP. The Journal of Chemical Physics. 1981;75(8):3731-42.
85. Girlanda R, Martino G, Mezzasalma AM, Mondio G, Perillo P, Saitta G. Optical properties of the semiconductor 7, 7′, 8, 8′, tetracyanoquinodimethane (TCNQ). Il Nuovo Cimento D. 1986;7(4):469-82.
86. Yanagimoto T, Takimiya K, Otsubo T, Ogura F. 11,11,12,12-Tetracyano-2,6-anthraquinodimethane (TANT) as a novel extensive electron acceptor. Journal of the Chemical Society, Chemical Communications. 1993(6):519-20.
87. Jonkman HT, Kommandeur J. The UV spectra and their calculation of TCNQ and its mono- and di-valent anion. Chemical Physics Letters. 1972;15(4):496-9.
88. Lü J-M, Rosokha SV, Kochi JK. Stable (Long-Bonded) Dimers via the Quantitative Self-Association of Different Cationic, Anionic, and Uncharged π-Radicals: Structures, Energetics, and Optical Transitions Journal of the American Chemical Society. 2003;125(40):12161-71.
89. Huang J, Kingsbury S, Kertesz M. Crystal packing of TCNQ anion [small pi]-radicals governed by intermolecular covalent [small pi]-[small pi] bonding: DFT calculations and statistical analysis of crystal structures. Physical Chemistry Chemical Physics. 2008;10(19):2625-35.
90. Garcia-Yoldi I, Miller JS, Novoa JJ. Theoretical Study of the Electronic Structure of [TCNQ]22− (TCNQ = 7,7,8,8-Tetracyano-p-quinodimethane) Dimers and Their Intradimer, Long, Multicenter Bond in Solution and the Solid State. The Journal of Physical Chemistry A. 2009;113(25):7124-32.
91. Lunelli B, Pecile C. Polarized Infrared Spectra of TCNQ and TCNQ-d4 Single Crystals. The Journal of Chemical Physics. 1970;52(5):2375-84.
92. Khatkale MS, Devlin JP. The vibrational and electronic spectra of the mono-, di-, and trianon salts of TCNQ. The Journal of Chemical Physics. 1979;70(4):1851-9.

93. Nanova D, Beck S, Fuchs A, Glaser T, Lennartz C, Kowalsky W, et al. Charge transfer in thin films of donor-acceptor complexes studied by infrared spectroscopy. Organic Electronics. 2012;13(7):1237-44.
94. Bozio R, Zanon I, Girlando A, Pecile C. Vibrational spectroscopy of molecular constituents of one-dimensional organic conductors. Tetrathiofulvalene (TTF), TTF+, and (TTF+) 2 dimer. The Journal of Chemical Physics. 1979;71(5):2282-93.
95. Kagoshima S, Ishiguro T, Anzai H. X-ray scattering study of phonon anomalies and superstructures in TTF-TCNQ. Journal of the Physical Society of Japan. 1976;41(6):2061-71.
96. Zhao H, Heintz RA, Dunbar KR, Rogers RD. Unprecedented Two-Dimensional Polymers of Mn(II) with TCNQ-• (TCNQ = 7,7,8,8-Tetracyanoquinodimethane). Journal of the American Chemical Society. 1996;118(50):12844-5.
97. Mikami S, Sugiura K-i, Miller JS, Sakata Y. Two-Dimensional Honeycomb Network Formed by Porphyrinatomanganese(III) and <I>μ</I>4-<I>σ</I>-Dimerized 7,7,8,8-Tetracyano-<I>p</I>-quinodimethane Dianion. Chemistry Letters. 1999;28(5):413-4.
98. Long RE, Sparks RA, Trueblood KN. The crystal and molecular structure of 7,7,8,8-tetracyanoquinodimethane. Acta Crystallographica. 1965;18(5):932-9.
99. Kadish KM, Smith KM. The Porphyrin Handbook: Academic Press; 2000.
100. Paulat F, Praneeth VKK, Näther C, Lehnert N. Quantum Chemistry-Based Analysis of the Vibrational Spectra of Five-Coordinate Metalloporphyrins [M(TPP)Cl]. Inorganic Chemistry. 2006;45(7):2835-56.
101. Gouterman M. Spectra of porphyrins. Journal of Molecular Spectroscopy. 1961;6(0):138-63.
102. Boucher LJ. Manganese porphyrin complexes. Coordination Chemistry Reviews. 1972;7(3):289-329.
103. Burawoy A. Licht-Absorption und Konstitution, I. Mitteil.: Homöopolare organische Verbindungen. Berichte der deutschen chemischen Gesellschaft (A and B Series). 1930;63(11):3155-72.
104. Boucher LJ. Manganese Porphyrin Complexes. Coordination Chemistry Review. 1972;9.

105. Edwards L, Dolphin DH, Gouterman M, Adler AD. Porphyrins XVII. Vapor absorption spectra and redox reactions: Tetraphenylporphins and porphin. Journal of Molecular Spectroscopy. 1971;38(1):16-32.
106. Mu XH, Schultz FA. Methanol bonding to and electron-transfer reactivity of chloro(tetraphenylporphinato)manganese(III). Inorganic Chemistry. 1992;31(16):3351-7.
107. Hoffman BM, Weschler CJ, Basolo F. The dioxygen adduct of meso-tetraphenylporphyrinmanganese(II), a synthetic oxygen carrier. Journal of the American Chemical Society. 1976;98(18):5473-82.
108. Jones DH, Hinman AS. In situ infrared spectroelectrochemical studies of tetraphenylporphyrin complexes containing manganese, iron and cobalt. Journal of the Chemical Society, Dalton Transactions. 1992(9):1503-8.
109. Urban MW, Nakamoto K, Basolo F. Infrared spectra of molecular oxygen adducts of (tetraphenylporphyrinato)manganese(II) in argon matrixes. Inorganic Chemistry. 1982;21(9):3406-8.
110. Beggan JP, Krasnikov SA, Sergeeva NN, Senge MO, Cafolla AA. Control of the axial coordination of a surface-confined manganese(III) porphyrin complex. Nanotechnology. 2012;23(23).
111. Murphy BE, Krasnikov SA, Sergeeva NN, Cafolla AA, Preobrajenski AB, Chaika AN, et al. Homolytic Cleavage of Molecular Oxygen by Manganese Porphyrins Supported on Ag(111). Acs Nano. 2014;8(5):5190-8.
112. Li XY, Czernuszewicz RS, Kincaid JR, Su YO, Spiro TG. Consistent porphyrin force field. 1. Normal-mode analysis for nickel porphine and nickel tetraphenylporphine from resonance Raman and infrared spectra and isotope shifts. The Journal of Physical Chemistry. 1990;94(1):31-47.
113. Behere DV, Marathe VR, Mitra S. Low-temperature magnetisation study on manganese(III) porphyrins. Chemical Physics Letters. 1981;81(1):57-61.
114. Behere DV, Mitra S. Magnetic susceptibility study and ground-state zero-field splitting in manganese(III) porphyrins. Inorganic Chemistry. 1980;19(4):992-5.
115. Dugad LB, Behere DV, Marathe VR, Mitra S. Magnetic properties and electronic structure of manganese(III) porphyrins. Chemical Physics Letters. 1984;104(4):353-6.

116. Goldberg DP, Telser J, Krzystek J, Montalban AG, Brunel LC, Barrett AGM, et al. EPR spectra from "EPR-silent" species: High-field EPR spectroscopy of manganese(III) porphyrins. Journal of the American Chemical Society. 1997;119(37):8722-3.
117. Hunter SC, Podlesnyak AA, Xue Z-L. Magnetic Excitations in Metalloporphyrins by Inelastic Neutron Scattering: Determination of Zero-Field Splittings in Iron, Manganese, and Chromium Complexes. Inorganic Chemistry. 2014;53(4):1955-61.
118. Krzystek J, Pardi LA, Brunel L-C, Goldberg DP, Hoffman BM, Licoccia S, et al. High-frequency and -field electron paramagnetic resonance of high-spin manganese(III) in tetrapyrrole complexes. Spectrochimica Acta Part A: Molecular and Biomolecular Spectroscopy. 2002;58(6):1113-27.
119. Cheng B, Scheidt WR. Chloro(5,10,15,20-tetraphenylporphyrinato)manganese(III) with 4/m Symmetry. Acta Crystallographica Section C. 1996;52(2):361-3.
120. Armstrong RS, Foran GJ, Hambley TW. Structure of chloro([alpha],[beta],[gamma],[delta]-tetraphenylporphinato)manganese(III) toluene solvate. Acta Crystallographica Section C. 1993;49(2):236-8.
121. Tulinsky A, Chen BML. The crystal and molecular structure of chloro-.alpha.,.beta.,.gamma.,.delta.-tetraphenylporphinatomanganese(III). Journal of the American Chemical Society. 1977;99(11):3647-51.
122. Djuric T, Ules T, Gusenleitner S, Kayunkid N, Plank H, Hlawacek G, et al. Substrate selected polymorphism of epitaxially aligned tetraphenyl-porphyrin thin films. Physical Chemistry Chemical Physics. 2012;14(1):262-72.
123. Mckeown NB. Phthalocyanine Materials - synthesis, structure and function.: Cambridge University Press; 1998.
124. Sauvage JP. Transition Metals in Supramolecular Chemistry: Wiley; 2008.
125. Wang H, Mauthoor S, Din S, Gardener JA, Chang R, Warner M, et al. Ultra long Copper Phthalocyanine Nanowires with New Crystal Structure and Broad Optical Absorption. Acs Nano. 2010;4(7):3921-6.
126. Brown CJ. Crystal structure of [small beta]-copper phthalocyanine. Journal of the Chemical Society A: Inorganic, Physical, Theoretical. 1968(0):2488-93.
127. Hoshino A, Takenaka Y, Miyaji H. Redetermination of the crystal structure of [alpha]-copper phthalocyanine grown on KCl. Acta Crystallographica Section B. 2003;59(3):393-403.

128. Barraclo.Cg, Gregson AK, Mitra S. Intepretation of Magnetic-Properties of Manganese (II) Phthalocyanine. Journal of Chemical Physics. 1974;60(3):962-8.
129. Barraclough CG, Martin RL, Mitra S. Diamagnetic Anisotropies of Metal-Free, Nickel(II), and Zinc(II) Phthalocyanines. The Journal of Chemical Physics. 1971;55(3):1426-9.
130. Barraclough CG, Martin RL, Mitra S, Sherwood RC. Paramagnetic Anisotropy, Low Temperature Magnetization, and Electronic Structure of Iron(II) Phthalocyanine. The Journal of Chemical Physics. 1970;53(5):1643-8.
131. Wu W, Kerridge A, Harker AH, Fisher AJ. Structure-dependent exchange in the organic magnets Cu(II)Pc and Mn(II)Pc. Physical Review B. 2008;77(18):12.
132. Heutz S, Mitra C, Wu W, Fisher AJ, Kerridge A, Stoneham M, et al. Molecular thin films: A new type of magnetic switch. Advanced Materials. 2007;19(21):3618-+.
133. Wang JH, Shi YS, Cao JX, Wu RQ. Magnetization and magnetic anisotropy of metallophthalocyanine molecules from the first principles calculations. Applied Physics Letters. 2009;94(12):3.
134. Bartolome J, Bartolome F, Garcia LM, Filoti G, Gredig T, Colesniuc CN, et al. Highly unquenched orbital moment in textured Fe-phthalocyanine thin films. Physical Review B. 2010;81(19).
135. Gredig T, Colesniuc CN, Crooker SA, Schuller IK. Substrate-controlled ferromagnetism in iron phthalocyanine films due to one-dimensional iron chains. Physical Review B. 2012;86(1):014409.
136. Wu Z. Magnetic Properties of Transition Metal Phthalocyanine Molecular Thin Films and Nanostructures.: Imperial College London; 2012.
137. Gredig T, Werber M, Guerra J, Silverstein E, Byrne M, Cacha B. Coercivity Control of Variable-Length Iron Chains in Phthalocyanine Thin Films. Journal of Superconductivity and Novel Magnetism. 2012;25(7):2199-203.
138. Pavia DL, Lampman GM, Kriz GS. Introduction to Spectroscopy (Third edition) Books/cole Thomson Learning; 2001.
139. Wright JD. Molecular Crystals: Cambridge University Press; 1995.
140. Woodruff DP, Delchar TA. Modern Techniques of Surface Science. Davis EA, Ward IM, Clarke DR, editors: Cambridge University Press; 1994.
141. Peter E, West P. Atomic Force Microscopy: Oxford University Press; 2010.

142. Barrett C, Massalski TB. Structure of Metals: Crystallographic Methods, Principles, and Data. Hopkins H, editor: Pergamon Press Ltd; 1980.
143. Clarke J, Braginski AI. The SQUID handbook: fundamentals and technology of SQUIDs and SQUID Systems, Volume I. Wiley-VCH Verlag GmbH&Co, KGaA, Weinheim; 2004.
144. Mydosh JA. Spin Glasses: An Experimental Introduction: Taylor & Francis; 1993.
145. Bain GA, Berry JF. Diamagnetic Corrections and Pascal's Constants. Journal of Chemical Education. 2008;85(4):532.
146. Sutter TPG, Hambright P, Thorpe AN, Quoc N. Diamagnetic Susceptibilities of Porphyrins. Inorganica Chimica Acta. 1992;195(2):131-2.
147. Kojima K, Maeda A, Ieda M, editors. Electrical properties of TCNQ evaporated thin films. Properties and Applications of Dielectric Materials, 1991, Proceedings of the 3rd International Conference on; 1991 8-12 Jul 1991.
148. Owen AE, Owen T. Fundamentals of UV-visible Spectroscopy: A Primer: Hewlett Packard; 1996.
149. Gao HJ, Xue ZQ, Wu QD, Pang SJ. 2D fractal pattern in fullerene doped polymer. Solid State Communications. 1996;97(7):579-82.
150. Gao HJ, Xue ZQ, Wang KZ, Wu QD, Pang S. Ionized-cluster-beam deposition and electrical bistability of C60–tetracyanoquinodimethane thin films. Applied Physics Letters. 1996;68(16):2192-4.
151. Li JC, Xue ZQ, Zeng Y, Liu WM, Wu QD, Song YL, et al. Growth and characterization of polyaniline 7,7,8,8-tetracyanoquino-dimethane (TCNQ) complex films grown by vacuum evaporation. Thin Solid Films. 2000;374(1):59-63.
152. Heutz S, Ferguson AJ, Rumbles G, Jones TS. Morphology, structure and photophysics of thin films of perylene-3,4,9,10-tetracarboxylic dianhydride. Organic Electronics. 2002;3(3–4):119-27.
153. Chen W, Huang H, Chen S, Chen L, Zhang HL, Gao XY, et al. Molecular orientation of 3, 4, 9, 10-perylene-tetracarboxylic-dianhydride thin films at organic heterojunction interfaces. Applied Physics Letters. 2007;91(11):114102.
154. Chen W, Qi D-C, Huang H, Gao X, Wee ATS. Organic–Organic Heterojunction Interfaces: Effect of Molecular Orientation. Advanced Functional Materials. 2011;21(3):410-24.

155. Heutz S, Jones TS. Structural and morphological modifications in double layer heterostructures containing H2Pc, perylene-3, 4, 9, 10-tetracarboxylic dianhydride and Alq(3). Journal of Applied Physics. 2002;92(6):3039-46.
156. Uyeda N, Murata Y, Kobayashi T, Suito E. Epitaxial growth of an organic semiconductor from the vapor phase — TCNQ on potassium chloride. Journal of Crystal Growth. 1974;26(2):267-76.
157. Willenbockel M, Stadtmüller B, Schönauer K, Bocquet FC, Lüftner D, Reinisch EM, et al. Energy offsets within a molecular monolayer: the influence of the molecular environment. New Journal of Physics. 2013;15(3):033017.
158. Glowacki ED, Irimia-Vladu M, Bauer S, Sariciftci NS. Hydrogen-bonds in molecular solids - from biological systems to organic electronics. Journal of Materials Chemistry B. 2013;1(31):3742-53.
159. Aakeroy CB, Seddon KR. The hydrogen bond and crystal engineering. Chemical Society Reviews. 1993;22(6):397-407.
160. Möbus M, Karl N, Kobayashi T. Structure of perylene-tetracarboxylic-dianhydride thin films on alkali halide crystal substrates. Journal of Crystal Growth. 1992;116(3–4):495-504.
161. Tsao JY. Materials Fundamentals of Molecular Beam Epitaxy: Elsevier Science; 2012.
162. Arasasingham RD, Bruice TC. Reaction of hydroxide ion with manganese(III) tetramesitylporphyrin and the oxidation states of manganese tetramesitylporphyrins. Inorganic Chemistry. 1990;29(7):1422-7.
163. Mirafzal GA, Bosse HM, Summer JM. An efficient method for the synthesis of manganese(III)meso-tetraarylporphyrins. Tetrahedron Letters. 1999;40(4):623-6.
164. Wagner C, Davis L, Zeller M, Taylor J, Raymond R, Gale L. Empirical atomic sensitivity factors for quantitative analysis by electron spectroscopy for chemical analysis. Surface and Interface Analysis. 1981;3(5):211-25.
165. Sugiura K-i, Mikami S, Iwasaki K, Hino S, Asato E, Sakata Y. Synthesis, properties, molecular structure and electron transfer salts of 13,13,14,14-tetracyano-1,6- and -1,8-pyrenoquinodimethanes (1,6-TCNP and 1,8-TCNP). Journal of Materials Chemistry. 2000;10(2):315-9.
166. Ewen RJ, Honeybourne CL. X-ray photoelectron spectroscopy of clean and gas-doped films of phthalocyanines. Journal of Physics: Condensed Matter. 1991;3(S):S303.

167. Tan BJ, Klabunde KJ, Sherwood PMA. XPS studies of solvated metal atom dispersed (SMAD) catalysts. Evidence for layered cobalt-manganese particles on alumina and silica. Journal of the American Chemical Society. 1991;113(3):855-61.
168. Nardi M, Verucchi R, Corradi C, Pola M, Casarin M, Vittadini A, et al. Tetraphenylporphyrin electronic properties: a combined theoretical and experimental study of thin films deposited by SuMBD. Physical Chemistry Chemical Physics. 2010;12(4):871-80.
169. Valentine JS, Quinn AE. Reaction of superoxide with the manganese(III) tetraphenylporphine cation. Inorganic Chemistry. 1976;15(8):1997-9.
170. Gonzalez B, Kouba J, Yee S, Reed CA. Manganese (II) Porphyrins - Synthesis, Structures, and Preference for 5-Coordinatio . Journal of the American Chemical Society. 1975;97(11):3247-9.
171. Oyamada T, Tanaka H, Matsushige K, Sasabe H, Adachi C. Switching effect in Cu:TCNQ charge transfer-complex thin films by vacuum codeposition. Applied Physics Letters. 2003;83(6):1252-4.
172. Lindner S, Knupfer M, Friedrich R, Hahn T, Kortus J. Hybrid States and Charge Transfer at a Phthalocyanine Heterojunction: ${\mathrm{MnPc}}^{\ensuremath{\delta}+}/{{\mathbf{F}}_{16}\mathrm{CoPc}}^{\ensuremath{\delta}-}$. Physical Review Letters. 2012;109(2):027601.
173. Lindner S, Mahns B, König A, Roth F, Knupfer M, Friedrich R, et al. Phthalocyanine dimers in a blend: Spectroscopic and theoretical studies of MnPcδ +/F16CoPcδ −. The Journal of Chemical Physics. 2013;138(2):024707.
174. Melby LR, Harder RJ, Hertler WR, Mahler W, Benson RE, Mochel WE. substuted Quinodimethans. II. Anion-radical Derivatives and Complexes of 7,7,8,8-Tetracyanoquinodimethan. Journal of the American Chemical Society. 1962;84(17):3374-87.
175. Jonkman H, Kommandeur J. The UV Spectra and Their Calculation of TCNQ and Its Mono- and Di-valent Anion. Chemical Physics Letters. 1972;15(4).
176. Bell SE, Field JS, Haines RJ, Moscherosch M, Matheis W, Kaim W. Novel and stable metal-metal-bonded diruthenium(I) complexes containing TCNX0/.bul.- in both the inner and the outer coordination sphere (TCNX = TCNE, TCNQ). A combined EPR/ENDOR-, UV/visible/near-IR-, and IR-spectroscopic and electrochemical investigation. Inorganic Chemistry. 1992;31(15):3269-76.

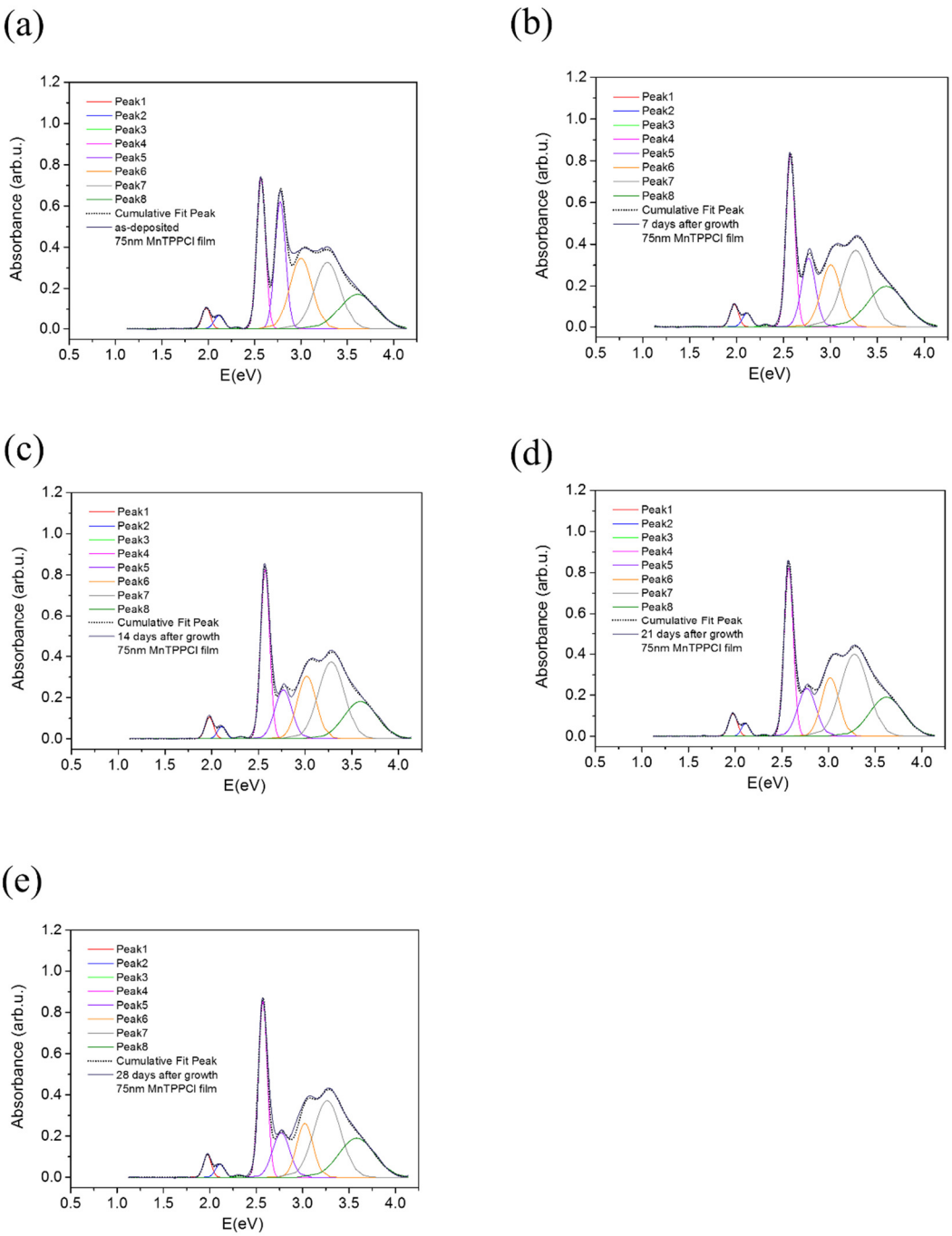
177. Herrmann H, Ziesak A, Wild U, Leingang S, Schrempp D, Wagner N, et al. Tetracyanoquinodimethane Reduction by Complexed Guanidinyl-Functionalized Aromatic Compounds. ChemPhysChem. 2014;15(2):351-65.
178. Ganesan V, Rosokha SV, Kochi JK. Isolation of the Latent Precursor Complex in Electron-Transfer Dynamics. Intermolecular Association and Self-Exchange with Acceptor Anion Radicals. Journal of the American Chemical Society. 2003;125(9):2559-71.
179. Jones DH, Hinman AS. Insitu Infrared Spectroelectrochemical Studies of Tetraphenylporphyrin Complexes Containing Manganese, Iron and Cobalt. Journal of the Chemical Society-Dalton Transactions. 1992(9):1503-8.
180. Furuhashi M, Yoshinobu J. Charge Transfer and Molecular Orientation of Tetrafluoro-tetracyanoquinodimethane on a Hydrogen-Terminated Si(111) Surface Prepared by a Wet Chemical Method. The Journal of Physical Chemistry Letters. 2010;1(10):1655-9.
181. Vickers EB, Giles ID, Miller JS. M[TCNQ]y-Based Magnets (M = Mn, Fe, Co, Ni; TCNQ = 7,7,8,8-tetracyano-p-quinodimethane). Chemistry of Materials. 2005;17(7):1667-72.
182. Spreer LO, Maliyackel AC, Holbrook S, Otvos JW, Calvin M. Synthesis and characterization of a manganese(III) porphyrin cation radical and its conversion to manganese(IV) by ligand metathesis. Journal of the American Chemical Society. 1986;108(8):1949-53.
183. Pecoraro VL, Baldwin MJ, Gelasco A. Interaction of Manganese with Dioxygen and Its Reduced Derivatives. Chemical Reviews. 1994;94(3):807-26.
184. Tseng T-C, Lin C, Shi X, Tait SL, Liu X, Starke U, et al. Two-dimensional metal-organic coordination networks of Mn-7,7,8,8-tetracyanoquinodimethane assembled on Cu(100): Structural, electronic, and magnetic properties. Physical Review B. 2009;80(15):155458.
185. Warner M, Mauthoor S, Felton S, Wu W, Gardener JA, Din S, et al. Spin-Based Diagnostic of Nanostructure in Copper Phthalocyanine-C-60 Solar Cell Blends. Acs Nano. 2012;6(12):10808-15.
186. Senapati T, Pichon C, Ababei R, Mathonière C, Clérac R. Cyanido-Bridged Fe(III)–Mn(III) Heterobimetallic Materials Built From Mn(III) Schiff Base Complexes and Di- or Tri-Cyanido Fe(III) Precursors. Inorganic Chemistry. 2012;51(6):3796-812.

187. Oshio H, Nihei M, Yoshida A, Nojiri H, Nakano M, Yamaguchi A, et al. A Dinuclear MnIII–CuII Single-Molecule Magnet. Chemistry – A European Journal. 2005;11(3):843-8.
188. Rittenberg DK, Miller JS. Observation of magnetic ordering as high as 28 K for meso-tetrakis(4-halophenyl)porphinatomanganese(III) tetracyanoethenide, MnTXPP TCNE (X = F, Br, I). Inorganic Chemistry. 1999;38(21):4838-48.
189. Drillon M, Coronado E, Georges R, Gianduzzo JC, Curely J. Ferrimagnetic Heisenberg chains [(1/2- \textit{S}] (\textit{S=1} to (5/2): Thermal and magnetic properties. Physical Review B. 1989;40(16):10992-8.
190. O'Connor CJ. Magnetochemistry—Advances in Theory and Experimentation. Progress in Inorganic Chemistry: John Wiley & Sons, Inc.; 2007. p. 203-83.
191. Myers BE, Berger L, Friedberg SA. Low - Temperature Magnetization of Cu(NO3)2·2.5H2O. Journal of Applied Physics. 1969;40(3):1149-51.
192. Johnson Mitchell T, Arif Atta M, Miller Joel S. Structure and Magnetic Properties of Tetrakis(3,4,5-trimethoxy-phenyl)porphinatomanganese(III) 2,3,5,6-Tetrafluoro-7,7,8,8-tetracyanoquinodimethenide: The First Example of an Isolated [TCNQF4]•−. European Journal of Inorganic Chemistry. 2000;2000(8):1781-7.
193. Brandon EJ, Kollmar C, Miller JS. Orbital Overlap and Antiferromagnetic Coupling in Substituted Tetraphenylporphinatomanganate(III) Tetracyanoethenide Based Magnets. The Importance of σ−dz2−pz Overlap. Journal of the American Chemical Society. 1998;120(8):1822-6.
194. Kim JI, Kwak HY, Yoon JH, Ryu DW, Yoo IY, Yang N, et al. Cyanide-Bridged FeIII−MnIII Bimetallic Complexes with Dimeric and Chain Structures Constructed from a Newly Made mer-Fe Tricyanide: Structures and Magnetic Properties. Inorganic Chemistry. 2009;48(7):2956-66.
195. Kwak HY, Ryu DW, Lee JW, Yoon JH, Kim HC, Koh EK, et al. Cyanide-Bridged Fe(III)−Mn(III) Bimetallic Systems Assembled from the fac-Fe Tricyanide and Mn Schiff bases: Structures, Magnetic Properties, and Density Functional Theory Calculations. Inorganic Chemistry. 2010;49(10):4632-42.
196. Caneschi A, Chiesi P, David L, Ferraro F, Gatteschi D, Sessoli R. Crystal structure and magnetic properties of two nitronyl nitroxide biradicals and of their copper(II) complexes. Inorganic Chemistry. 1993;32(8):1445-53.

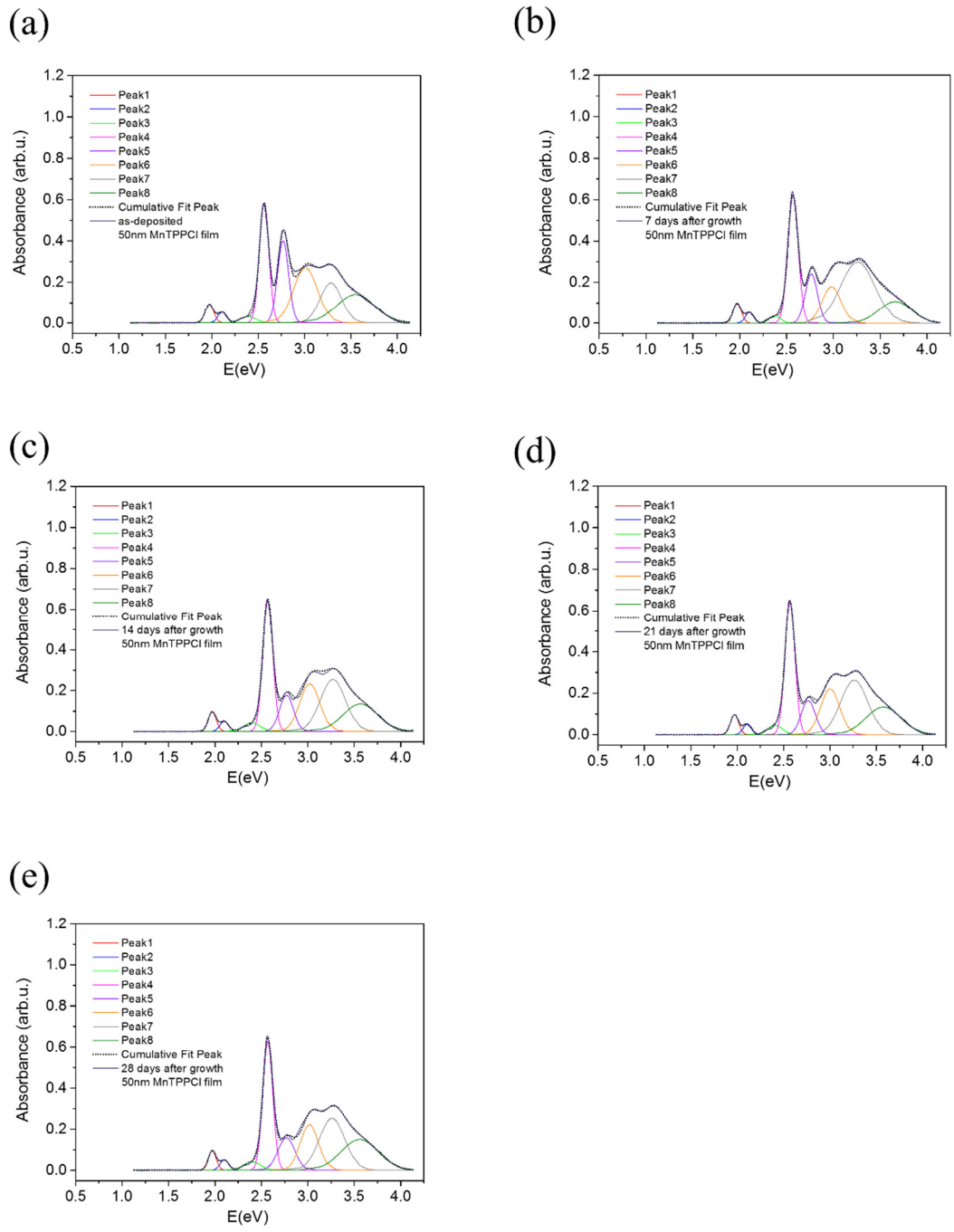
197. Kahn O. Dinuclear Complexes with Predictable Magnetic Properties. Angewandte Chemie International Edition in English. 1985;24(10):834-50.
198. Brandon EJ, Rittenberg DK, Arif AM, Miller JS. Ferrimagnetic Behavior of Multiple Phases and Solvates of (meso-Tetrakis(4-chlorophenyl)porphinato)manganese(III) Tetracyanoethenide, [MnTClPP]+[TCNE]•-. Enhancement of Magnetic Coupling by Thermal Annealing. Inorganic Chemistry. 1998;37(13):3376-84.
199. Gredig T, Werber M, Guerra JL, Silverstein EA, Byrne MP, Cacha BG. Coercivity Control of Variable-Length Iron Chains in Phthalocyanine Thin Films. Journal of Superconductivity and Novel Magnetism. 2012;25(7):2199-203.
200. Bałanda M, Falk K, Griesar K, Tomkowicz Z, Haase W. Characterization of magnetic ordering in porphyrin-based molecular magnets [Mn(R)4TPP][TCNE] (R=OC12H25, F, CN). Journal of Magnetism and Magnetic Materials. 1999;205(1):14-26.
201. Hom T, Kiszenik W, Post B. Accurate lattice constants from multiple reflection measurements. II. Lattice constants of germanium silicon, and diamond. Journal of Applied Crystallography. 1975;8(4):457-8.
202. Wyckoff RWG. Crystal Structures 1: Interscience Publishers, New York; 1963.
203. Gilchrist JB, Basey-Fisher TH, Chang SC, Scheltens F, McComb DW, Heutz S. Uncovering Buried Structure and Interfaces in Molecular Photovoltaics. Advanced Functional Materials. 2014;24(41):6473-83.
204. Bayliss SM, Heutz S, Rumbles G, Jones TS. Thin film properties and surface morphology of metal free phthalocyanine films grown by organic molecular beam deposition. Physical Chemistry Chemical Physics. 1999;1(15):3673-6.
205. Gredig T, Colesniuc CN, Crooker SA, Schuller IK. Substrate-controlled ferromagnetism in iron phthalocyanine films due to one-dimensional iron chains. Physical Review B. 2012;86(1):6.
206. Yim S, Jones TS. Anomalous scaling behavior and surface roughening in molecular thin-film deposition. Physical Review B. 2006;73(16):161305.

Appendix

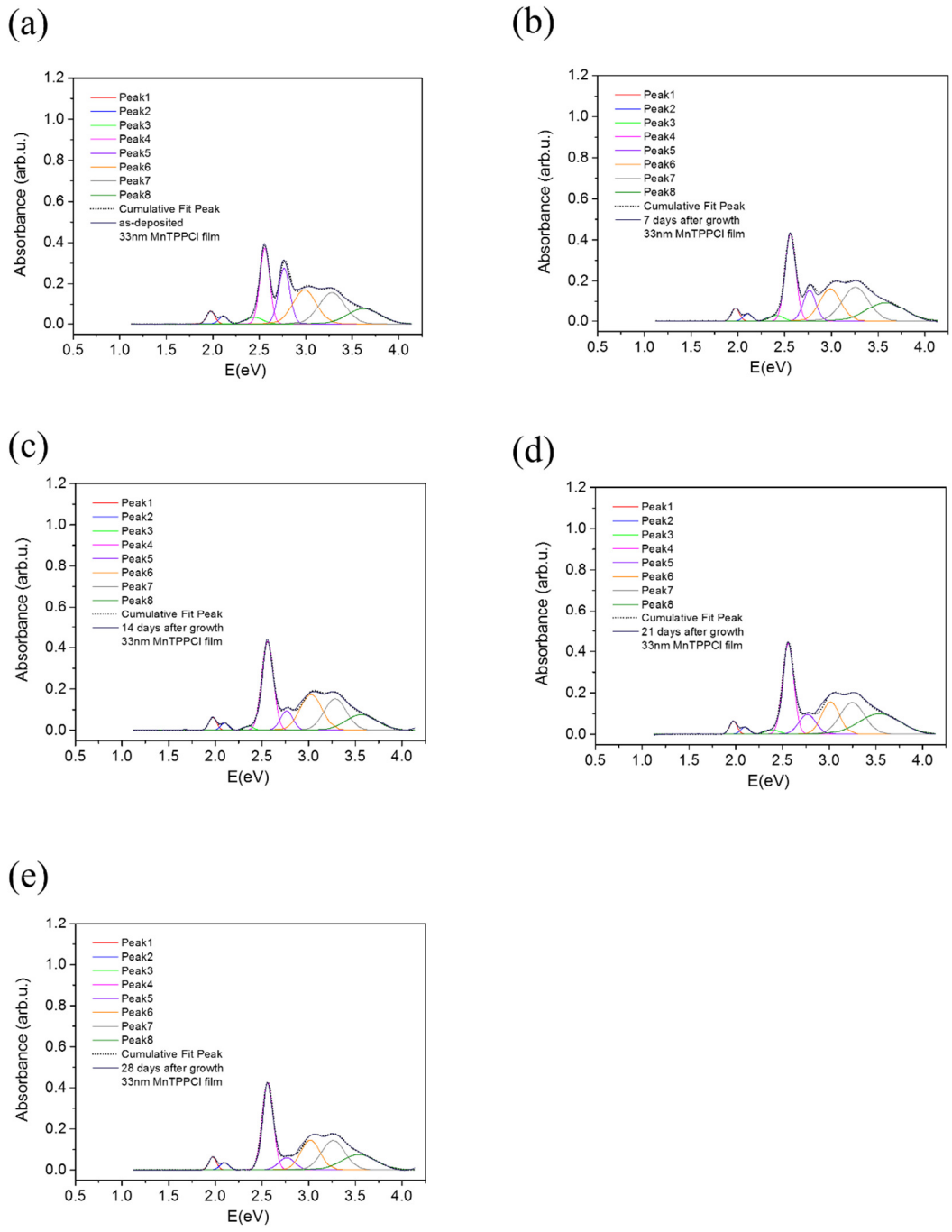
A.1 Electronic absorption spectra of MnTPPCl films



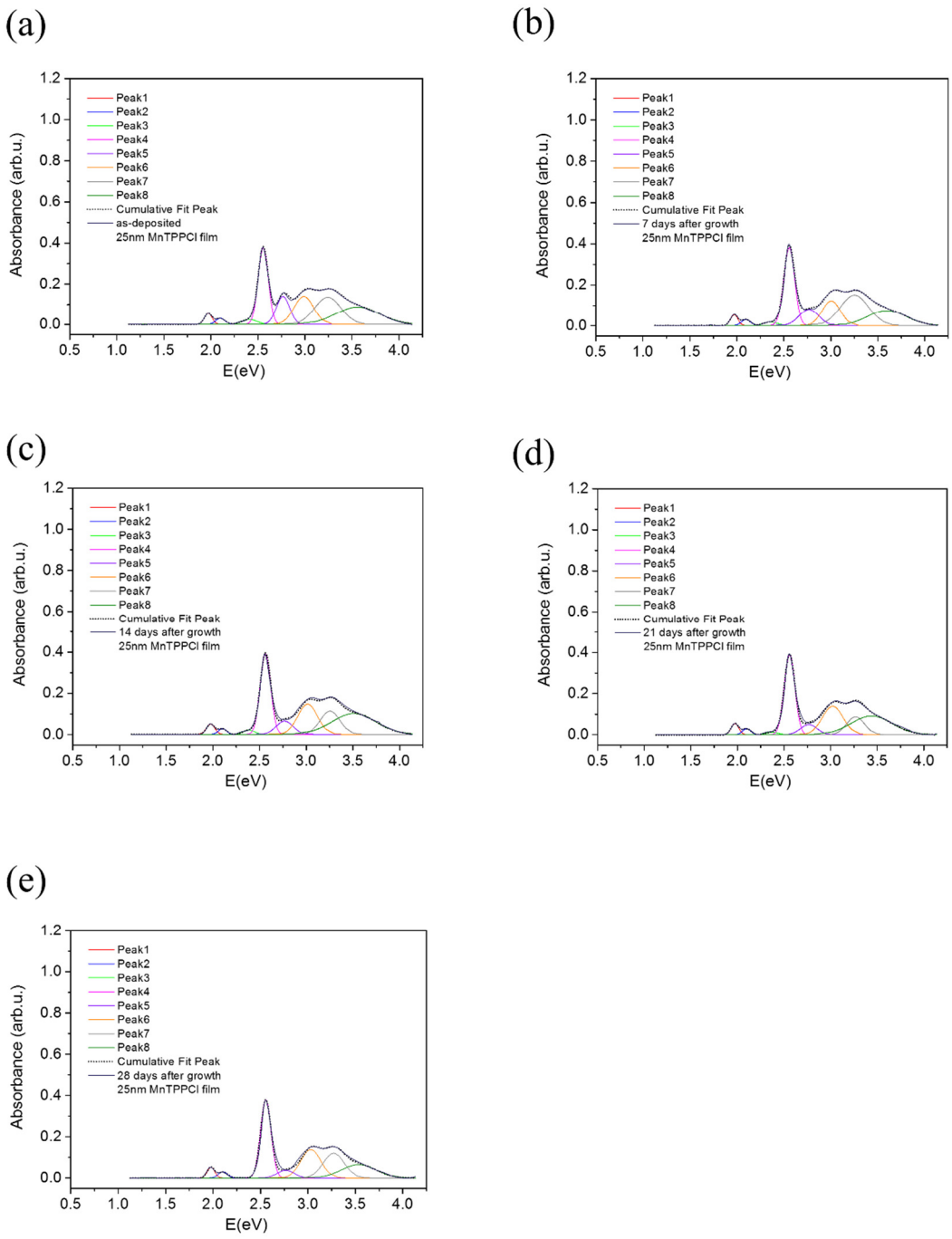
A.1.1 The optical spectra of a 75nm thick MnTPPCl film recorded at different times (a) as-deposited, (b) 7 days, (c) 14 days. (d) 21 days, and (e) 28 days after the film deposition (plotted in the scale of eV) shown with the Gaussian functions used for fitting.



A.1.2 The optical spectra of a 50nm thick MnTPPCl film recorded at different times (a) as-deposited, (b) 7 days, (c) 14 days. (d) 21 days, and (e) 28 days after the film deposition (plotted in the scale of eV) shown with the Gaussian functions used for fitting.



A.1.3 The optical spectra of a 33nm thick MnTPPCl film recorded at different times (a) as-deposited, (b) 7 days, (c) 14 days. (d) 21 days, and (e) 28 days after the film deposition (plotted in the scale of eV) shown with the Gaussian functions used for fitting.



A.1.4 The optical spectra of a 25nm thick MnTPPCl film recorded at different times (a) as-deposited, (b) 7 days, (c) 14 days. (d) 21 days, and (e) 28 days after the film deposition (plotted in the scale of eV) shown with the Gaussian functions used for fitting.

A.2 IR spectrum

Vibrational frequencies with the spectral assignments for the porphyrin-core in NiTPP[112].

	A_{1g}	B_{1g}	A_{2g}	B_{2g}	E_u
$\nu(C_mPh)$	1235			1269	1254
$\nu(C_\alpha C_m)_{asym}$		1594	1550		1568
$\nu(C_\beta C_\beta)$	1572	1504			1552
$\nu(C_\alpha C_m)_{sym}$	1470			1485	1473
ν(Pyr quarter-ring)			1341	1377	1403
ν(Pyr half-ring)$_{sym}$	1374	1302			1331
$\delta(C_mPh)$		238	255		233
$\nu(C_\beta C_m)_{sym}$	3101	3100			3100
ν(Pyr half-ring)$_{asym}$			1016	998	1003
$\nu(C_\beta C_m)_{asym}$			3096	3096	3097
δ(Pyr def)$_{asym}$			828	869	864
ν(Pyr breathing)	1004	1005			1023
δ(Pyr def)$_{sym}$	889	846			895
δ(Pyr rot.)			560	450	512
ν(NiN)	402	277			436
$\delta(C_\beta H)_{asym}$			1230	1190	1093
$\delta(C_\beta H)_{sym}$	1079	1084			1213
δ(Pyr transl)				109	306

A.3 FePc thin films

The roughness of the Al layers deposited on different substrates

Summary of the RMS values measured from the Al films deposited at the rate of 0.2 Å/s at room temperature on various substrates.

	Al (nm)	RMS (nm)
Glass	50	2.4
	100	4.6
Silicon	100	4.4
Kapton	100	5.5